TR 3600 S

STELLINGEN
Behorende by

De Zarshuran Goud Afzettingmodel toegepast in een Mineraalexploratie GIS in Iran

1. De Zagros Orogenetische Gordel van Iran is een van de meest actieve geodynamische zones van de wereld, en God heeft ons hiermee voorzien van een zone met een enorm onderzoek-en mineraalpotentieel.

2. Het is heel interesant om te zien dat een afzetting in Iran zoveel gemeen heeft met de Carlin-type afzettingen die gewoonlijk in Nevada voorkomen (commentaar van Alan Wallace, een in Nevada werkzaam geoloog, op het artikel Invisible Gold at Zarshuran, Iran)

3. De overeenkomst van Zarshuran met Carlin-type goudafzettingen, momenteel de leidende goudproducent in de Verenigde Staten, is een belangrijke motivatie om maar dergelijke belangrijke afzettingen in Iran, te speuren.

4. De hypothese van een sterke link tussen mineralisatie en magmatisme voor Carlin-type goudafzettingen wordt sterk ondersteund (dit inderzoek)

5. De omgeving die heeft geleid tot de vorming van goudmineralisatie in Zarshuran verschilt van de simpele geothermische omgeving in een gesloten systeem, die traditioneel voor Carlin-type goudafzettingen wordt gesuggereerd.

6. Overgang van een hoog temperatuur/druk hydrothermaal systeem naar een lage temperatuur/druk omgeving en daarop volgende vrijgave van een belangrijke hoeveelheid koolstof, als gevolg van de explosie van CO_2-rijke vloeistofinsluitsels, zorgden voor gunstige mineralisate condities in de Zarshuran Carlin-achtige goud afzetting.

7. GIS en remote sensing zijn zeer nuttige gereedschappen voor mineraalexploratie, maar afzettingen kunnen niet worden ontdekt door alleen maar deze gereedschappen te gebruiken vanachter een computer.

8. Denk conceptueel, plan structureel, en handel lokaal (dit onderzoek).

9. Het is moeilijk om eenvoudig te zijn, het is eenvoudig om moeilijk te zijn, en het is gewoon prachtig om ongecompliceerd te zijn.

10. Ik zie liever de toename van kennis dan toename van aanbidding (Profeet Mohammed).

PROPOSITIONS

Accompanying the thesis

The Zarshuran Gold Deposit Model Applied in a Mineral Exploration GIS in Iran

1. The Zagros Orogenic Belt of Iran is one of the most geodynamically active zones in the world, thanks to God for providing us such a zone with enormous research and mineral potentials.

2. It is very interesting to see a deposit in Iran has so much in common with Carlin-type deposits that commonly occur in Nevada (comment of Alan Wallace, a Nevada-based geologist, on the paper Invisible gold at Zarshuran, Iran).

3. Similarity of Zarshuran to the Carlin-type gold deposits, currently ranked as the leading gold producer in the United States, is an important motivation to search for such important deposits in Iran.

4. The hypothesis of a close link between mineralization and magmatism for Carlin-type gold deposits is strongly supported (this research).

5. The environment leading to the formation of gold mineralization at Zarshuran differs from a simple geothermal environment with a closed system, traditionally suggested for the Carlin-type gold deposit (this research).

6. Transition from a high pressure/temperature hydrothermal system to a low pressure/temperature environment and subsequent release of substantial amount of carbon, due to the explosion of CO_2-rich fluid inclusions by decompression, provided favourable conditions for mineralization at the Zarshuran Carlin-like gold deposit.

7. GIS and remote sensing are very useful tools for mineral exploration, but deposits can not be discovered by only using these tools whilst sitting in front of a computer.

8. Think conceptually, plan structurally and act locally (this research).

9. It is difficult to be simple, it is simple to be difficult, it is simply beautiful to be simple.

10. I cherish the increase of knowledge over the increase of worship (Prophet Mohammed).

3600
748384
TR 3600

The Zarshuran Gold Deposit Model Applied in a Mineral Exploration GIS in Iran

BIBLIOTHEEK TECHNISCHE UNIVERSITEIT
Prometheusgebouw
DELFT

PROEFSCHRIFT

ter verkrijging van de graad van doctor
aan de Technische Universiteit Delft,
op gezag van de Rector Magnificus prof. ir. K.F. Wakker,
voorzitter van het College voor Promoties,
in het openbaar te verdedigen op dinsdag 21 november 2000 om 13:30 uur

door

ASADI HARONI Hooshang
Master of Science in Mineral Exploration, ITC Delft
geboren te Shahrekord, Iran

Dit proefschrift is goedgekeurd door de promotor:

Prof. Dr. Martin Hale

Samenstelling promotiecommissie:

Rector Magnificus,	voorzitter
Prof. Dr. Martin Hale,	Technische Unversiteit Delft, promotor
Prof. Dr. S.B. Kroonenberg,	Technische Unversiteit Delft
Prof. Dr. F.D. van der Meer,	Technische Unversiteit Delft
Dr. J.H.L. Voncken,	Technische Unversiteit Delft
Prof. Dr. J.L.R. Touret,	Vrije Universiteit Amsterdam
Dr. H. de Boorder,	Rijks Universiteit Utrecht
Dr. R.A. Kuhnel,	ITC

The Zarshuran Gold Deposit Model Applied in a Mineral Exploration GIS in Iran

Thesis Delft University of Technology and ITC,
with ref. summary in Dutch.

The research presented in this thesis was financially supported by the Ministry of Science, Research and Technology of Iran and conducted at the Delft University of Technology and the International Institute for Aerospace Survey and Earth Sciences (ITC) in The Netherlands.

The cover is a 3D image (colour composite Landsat TM images draped on the DTM). The front page shows the alteration (orange pixels) associated with the Zarshuran gold deposit (on the southern flank of a large anticline) and its surroundings. Aghdarreh gold deposit can be distinguished as a dome structure in the back page.

Copyright © 2000 by H. Asadi Haroni
ITC Dissertation Number 78
ISBN 90 6164 185 3

To Marjan, Puya and Parya

Acknowledgments

Most of all, I am grateful to God for creating a beautiful world - full of mystery - to discover, for keeping me in good health and for giving me the ability to successfully conclude my PhD research. After a long journey, full of ups and downs, light and darkness, and sweet and bitter, I hope that I can now make ultimate use of my knowledge alongside His passion, toward brightening the lives of human beings.

This thesis explains four years of scientific research at ITC, Delft University of Technology and the Free University of Amsterdam and field work in Iran. With a great sense of appreciation, I take the opportunity to thank those people who have supported me along the way.

I am greatly indebted to my supervisor, Prof. Dr. Martin Hale, whose comments, valuable scientific discussions and critical ideas are highlights of various aspects of this research. Without his sound guidance, supervision, motivation, kindness and continual support this research would have not reached its present from. With his patience and encouragement, he gave me the confidence to publish most parts of this research. I also highly appreciate his support during field work in Iran, improving my scientific writing in English, as well as solving all the financial matters related to the research. Moreover, his personal qualities, inter-personal skills and good humour created an excellent working environment at ITC in Delft. Thank you.

I would like to express my gratitude to Dr. Jack Voncken for supporting my in-depth study of the minerals of Zarshuran. I thank him for providing technical assistance in working with the electron microprobe at the Department of Applied Earth Sciences at Delft University of Technology. His patience and creativity when working with me behind the microprobe led to the recognition of the mode of occurrence of gold at Zarshuran, as well as the identification of over 40 other minerals, seven of which were identified for the first time. I would like also to thank him for his work as co-author in publishing these findings.

I would also like to express my sincere thanks to Prof. Dr. Jacques Touret for introducing me to the amazing world of fluid inclusions, and for helping me to investigate the pressure and temperature conditions and environment of formation of gold mineralization at Zarshuran.

I am grateful to Dr. Radko Kühnel, who first introduced me to the beautiful world of ore microscopy and helped me to carry out the initial study of the minerals at Zarshuran. I wish to thank him for the effort he made to obtain chemical analyses of the Zarshuran samples. Fruitful discussions with him have improved the quality of this thesis.

I am also grateful to Dr. Edmund Sides for valuable discussions, comments and technical assistance, and in particular for improving my knowledge of 2D and 3D GIS. I especially thank him for his guidance on the spatial modelling and reserve estimation of the Zarshuran deposit. Ed, I learned many things from you and really enjoyed working with you since the beginning of my graduate studies at ITC. I only can say that I owe you a lot.

I would like to express my special thanks to Dr. Phil Westerhof for helpful discussions and comments on the geodynamic modelling of the Zagros Orogenic Belt. From my arrival at ITC, he played an important role in increasing my knowledge of the genesis and exploration of many types of mineral deposits.

I wish also to express my gratitude to drs. Boudewjin de Smeth for his support and encouragement during my stay in the Netherlands.

My special thanks to my PhD colleagues and other staff members of the Delft location of ITC. In particular, I thank Prof. Reeves for valuable comments related to the magnetic signatures at Zarshuran, Hans Erren for assistance with the processing and interpretation of the aeromagnetic data of the whole Iran, Senol Uzmutlu for teaching me how to work with Lynx software and apply a 3D visualization to different features of the Zarshuran deposit, Alok Porwal for discussions about weights of evidence analysis and my roommate Emmanuel John Carranza for assistance with the interpretation of stream sediment geochemical data of the Takab area.

I wish to convey my gratitude to Mrs. Ineke Theussing for her helpful administrative support, and for facilitating a pleasant stay for my family and me in the Netherlands.

In Iran, the many staff members of Ministry of Mines and Metals, Geological Survey, Atomic Energy Organization, Mineral Export Company and Shahid Beheshti University are thanked for supplying data to this research project, as well as supporting me during field work. I especially thank Mr. Kolahdoz, the deputy minister, Mr. Esmaeili, head of exploration division of the Ministry of Mines and Metals, Prof. Dr. Khakzad from Shaihd Beheshti University, Mr. Korehi, the head of Geological Survey, and Mr. Samani, the head of the exploration division of the Atomic Energy Organization.

I am very grateful to the Ministry of Culture and Higher Education of Iran for providing me with a scholarship to study abroad. I highly appreciate the administrative support of Dr. Sedighi, Director General of Scholarship and Student Affairs, and Mr. Padashi.

The successful completion of this research is also connected to the encouragement and cooperation of the following people who did not hesitate in offering their support: Dr. Elizabeth Kosters, Mr. Bahram Ojaghi, Mr. Tafazoli, Mr. Montazeri, Mr. Faez, Mr. Frank van Ruitenbeek, Mr. Bish Kewalder, Mr. Wim Zuiderwijk, Mrs. Dienke Mass Geesteranus, Mrs. Barnet Stern, Mrs. Margaret Volijk, Mrs. Willy Engelen, Mr. Henk Wilbrink, Mr. Stijn Staffhorst, Prof. Freek van der Meer, Dr. Tsehaie Woldai, Dr. Momenzadeh, Prof. Hans Shellekens and Mr. Piet van der Hulst.

I am grateful to my mother, my mother-in-law, sisters, brothers and other relatives in Iran for having endured our long absence from home.

And last but not least, I am indebted to my wife, Marjan, for her company, patience, scientific help and much needed moral support. She has made many personal sacrifices to make this journey possible. I also owe a lot to the understanding of my adorable son, Puya, and patience of my sweet daughter, Pariya, whilst I was away from them. You two are the sweetest memory of my stay in the Netherlands.

Furthermore, I would like to thank the members of the promotion committee.

Abstract

Genetic and spatial models have been developed for the gold and arsenic mineralization at Zarshuran, in the northwest part of the Zagros Orogenic Belt of Iran. Three stages of mineralization, related to the evolution of a single hydrothermal fluid, are distinguished. The early stage was weak pyrrhotite, pyrite and chalcopyrite mineralization deposited from a magmatic hydrothermal fluid at a pressure of about 1250 bars and a temperature of ±360°C. The main stage of mineralization was characterized by sudden release of pressure, which fell to 250 bars, due to uplift and opening of conduits. At this stage, with the temperature at 200-270°C, there was widespread precipitation of base-metal sulphides, lead-sulphosalt minerals, coloradoite, christite, stibnite, pyrite and massive-network arsenian pyrite. The pyrite and arsenian pyrite contain invisible gold in solid solution and/or as submicron-sized grains. The late stage of mineralization saw pressure restoration to 300-400 bars as a result of silicification of the system (conduit re-sealing) accompanied by further cooling and precipitation of orpiment, realgar, getchellite, cinnabar and gold-bearing colloform arsenian pyrite and colloform sphalerite.

The mineralization at Zarshuran lies on the flank of a large anticline and is associated with a highly-altered granitoid and an inferred subsurface intermediate or basic intrusion. An exceptional magnetic anomaly suggests that the core of the anticline is occupied by serpentinite, probably an altered ophiolitic remnant of Neo-Tethys oceanic crust and a likely source of metals that may have been leached by circulating hydrothermal fluids. Permeable and chemically-reactive carbonate and black shale formations acted as the main mineralization precipitation barriers, along with northeast-southwest high-angle extensional faults (formed by orogenic collapse after subduction) and their intersections with northwest-southeast structures. Hydrothermal alteration of the host rocks is manifested by silicification, decalcification, argillization and less extensive ferruginization.

The genetic and spatial models of the Zarshuran mineralization suggest six deposit recognition criteria (DRC) for comparable mineralizations in the same geodynamic setting. Within a GIS environment, evidential maps of these DRC throughout the 1800 km^2 Takab area surrounding Zarshuran were generated. Evidence of suitable host rocks (permeable and chemically-reactive sedimentary formations), heat sources (young igneous rocks) and metal sources (serpentinized ophiolites) were digitized from mapped geology and/or interpreted from aeromagnetic data. Evidence of hydrothermal alteration, in particular argillization and ferruginization, was extracted by processing Landsat-TM and aeromagnetic data, and validated by ground truthing and laboratory analysis. Favourable structures were digitized from geological maps and interpreted from Landsat-TM and aeromagnetic data. Evidence for the presence of minerals containing arsenic, antimony, mercury, thallium, zinc and tellurium was inferred by mapping stream sediment geochemistry. These evidential maps, combined in a weights-of-evidence model, yielded a mineral potential map that indicates further, undiscovered mineralization in the Takab area. Ground truthing in some of the high-potential areas confirmed the presence of previously-unknown mineralization or anomalous gold concentrations in rock and stream sediment samples.

Samenvatting

Voor de diffuse, in sedimenten aanwezige goud- en arseenmineralisatie in Zarshuran, in het noordwesten van de Zagros Orogenic Belt in Iran, zijn ruimtelijke en genetische modellen opgesteld. Drie stadia van mineralisatie kunnen in Zarshuran worden herkend, gerelateerd aan de evolutie van een enkele hydrothermale fluid. De vroege fase bestond uit zwakke mineralisatie met pyrrhotiet, pyriet en chalcopyriet, afgezet door een hydrothermaal fluid systeem, bij een druk van ongeveer 1250 bar een temperatuur van ± 360 °C. De hoofdfase van de mineralisatie werd gekarakteriseerd door een plotselinge verlaging van de druk tot 250 bar, als gevolg van opheffing en het openen van transportroutes. In deze fase, bij een temperatuur van 200-270 °C, vond wijdverbreide precipitatie plaats van base-metal sulfides, lood-sulfosalt mineralen, coloradoite, christiet, stibniet, pyriet en massieve/netwerk arseenhoudende pyriet. De pyriet en de arseenhoudende pyriet bevatten invisible gold zowel in solid solution als in sub-micron deeltjes. De late mineralisatiefase bracht drukherstel tot 300-400 bar als gevolg van silicificatie van het systeem (afdichten van de transportroutes), samen met verdere afkoeling en precipitatie van orpiment, realgaar, getchelliet, cinnaber, en colloforme goud- en arseenhoudende pyriet en colloforme sfaleriet.

De mineralisatie in Zarshuran bevindt zich op de flank van een grote anticline en is geassocieerd met een sterk omgezette granitoid en een veronderstelde intrusie van intermediair-basisch karakter in de ondergrond. Een exceptionele magnetische anomalie doet vermoeden dat de kern van de anticline wordt ingenomen door serpentiniet, waarschijnlijk een omgezet ophiolitisch overblijfsel van de Neo-Thetys oceanische korst, en een aannemelijke bron van metalen, die uitgeloogd kunnen zijn door circulerende hydrothermale fluids. Doorlatende en chemisch reactieve carbonaten en zwarte-schalie formaties fungeerden als de hoofdzakelijke mineralisatie-precipitatie barrières, tezamen met noordoost-zuidwest lopende high-angle extension faults (gevormd door orogenic collapse na subductie) and de intersecties hiervan met noordwest-zuidoost lopende structuren. Hydrothermale omzetting van de gastheergesteenten manifesteert zich door silicificatie, decalcificatie argillitisatie, en minder geprononceerde ferruginitisatie.

De ruimtelijke en genetische modellen van de Zarshuran mineralisatie wijzen op zes deposit recognition criteria (DRC) voor vergelijkbare mineralisaties in dezelfde geodynamische setting. Binnen een GIS omgeving zijn kaarten gegenereerd die aanwijzingen geven omtrent het voorkomen van deze DRC in het 1800 km^2 grote Takab gebied rondom Zarshuran. Aanwijzingen voor geschikte gastheergesteenten (permeabele en chemisch reactieve sedimentaire formaties), hittebonnnen (jonge stollingsgesteenten), en bronnen voor metalen (geserpentiniseerde ophiolieten) werden gedigitaliseerd van in kaart gebrachte geologie, en/of geïnterpreteerd van aeromagnetische data. Aanwijzingen voor hydrothermale omzetting, in het bijzonder argillitisatie en ferruginisatie, werden verkregen door processing van Landsat TM en aeromagnetische data, en

gevalideerd door controle in het veld en laboratorium analyse. Gunstige structuren werden gedigitaliseerd van geologische kaarten en geïnterpreteerd van Landsat TM en aeromagnetische data. Aanwijzingen voor de aanwezigheid van mineralen met arseen, antimoon, kwik, thallium, zink en tellurium, werden verkregen uit het in kaart brengen van stream sediment geochemie. De kaarten die verspreiding van de DRC aangeven werden gecombineerd in een weights-of-evidence model hetgeen resulteerde in een mineral potential kaart, welke andere, nog niet ontdekte, mineralisatie in het Takab gebied aanduidt. Controle in het veld in sommige van deze potentieel interessante gebieden bevestigde de aanwezigheid van voorheen onbekende mineralisatie dan wel anomale goudconcentraties in gesteente en stream sediment monsters.

CONTENTS

Acknowledgment.....I
Abstract.....III
Samenvatting.....IV

Chapter 1: Introduction.....1

1.1 Problem definition.....1
1.2 Objectives and aims.....2
1.2.1 Spatial model.....3
1.2.2 Genetic model.....3
1.2.3 Exploration model.....3
1.3 Background to the research.....4
1.3.1 Concepts.....5
1.3.2 Tools.....6
1.4..Methodology.....6
1.4.1 Phase One.....7
1.4.1 Phase Two.....7
1.5..Structure of the thesis.....7

Chapter 2: Geology, metallogeny and geodynamics of the Zagros Orogenic Belt.....**11**

2.1 Introduction.....11
2.2 Origin of the Zagros Orogenic Belt.....13
2.3 Geological sub-divisions of the Zagros Orogenic Belt.....13
2.2.1 Urumieh-Dokhtar Magmatic Assemblage.....14
2.2.2 Sanandaj-Sirjan Zone.....15
2.2.3 Zagros Simply Folded Belt.....16
2.3 Metallogeny of the Zagros Orogenic Belt.....17

2.4 Geodynamic re-interpretation of the Zagros Orogenic Belt....19
2.4.1 Lithology....19
2.4.2 Structure....22
2.4.3 Geodynamic model....24
2.5 Conclusions....26

Chapter 3: Using 2D GIS to assist 3D modelling of the Zarshuran deposit.... 29

3.1 Introduction....29
3.2 Modelling database....32
3.3 Geophysical data analysis....33
3.3.1 Qualitative analysis....33
3.3.2 Quantitative analysis....34
3.4 Geochemical data analysis....35
3.4.1 Qualitative analysis.... 35
3.4.2 Quantitative analysis....38
3.5 Three-dimensional interpretation.... 38
3.5.1 Geology.... 38
3.5.2 Mineral resource....39
3.7 Conclusions....41

Chapter 4: Petrography, mineralogy and geochemistry.... 43

4.1 Introduction....43
4.2 Methods....43
4.3 Petrography of the mineralized formation....46
4.4 Mineralization....49
4.5 Alteration.... 8
4.5 Paragenetic sequence....60
4.6 Discussion....63
4.7 Conclusions....64

Chapter 5: Invisible gold at Zarshuran, Iran....65

5.1 Introduction....65
5.2 Methods.... 66
5.3 Results....67
5.3.1 Occurrence of visible gold....67
5.3.2 Gold concentrations and associations....68
5.3.3 Occurrence of invisible gold....70
5.4 Discussion....74
5.5 Conclusions....75

Chapter 6: Sulphosalts at Zarshuran, implications for gold mineralization.....77

6.1 Introduction.....77
6.2 Methods.....78
6.3 Results.....78
6.3.1 Assemblage 1: As-Sb sulphide and sulphosalt minerals.....79
6.3.2 Assemblage 2: Pb-As-Sb sulphosalt minerals.....80
6.3.3 Assemblage 3: Cu-Hg-Tl-As sulphosalt minerals.....86
6.4 Discussion.....87
6.4.1 Arsenic-antimony substitution.....87
6.4.2 Sulphosalt crystallisation sequence and associated temperatures.....88
6.4.3 Occurrence of gold.....89
6.4.4 Evolution of the gold-mineralising fluid.....90
6.5 Conclusions.....91

Chapter 7: Mineralizing fluids.....93

7.1 Introduction.....93
7.2 Methods.....94
7.3 Sample description.....95
7.3.1 Mineralized samples.....97
7.3.1.1 Quartz intergrown with sulphides (main mineralization stage).....97
7.3.1.2 Fluorite intergrown with sphalerite (late mineralization stage).....98
7.3.1.3 Barite.....101
7.3.1.4 Sphalerite.....102
7.3.2 Weakly mineralized samples.....102
7.3.3 Unmineralized samples.....103
7.4 Microthermometric data.....103
7.4.1 Fluid types.....103
7.4.1.1 Water dominated inclusions (W types).....103
7.4.1.2 Gaseous inclusions.....105
7.4.2 Early stage fluid composition.....105
7.4.2.1 Aqueous inclusions (W1).....106
7.4.2.2 Gaseous inclusions.....106
7.4.3 Main stage fluid composition.....107
7. 4.3.1 Aqueous inclusions (W1 to W3).....107
7. 4.3.2 Gaseous inclusions.....108
7.4.4 Late stage fluid composition (W1 to W3).....108
7. 4.4.1 Aqueous inclusions.....108
7.4.3.2 Gaseous inclusions.....109
7.5 Interpretation: pressure and temperature of fluid entrapment.....110
7.5.1 Early stage.....110
7.5.2 Main stage.....111
7.5.3 Late stage.....111
7.6 Model.....112

7.7 Conclusion....114

Chapter 8: Genesis of gold mineralization, implications for deposit recognition criteria..115

1.1 Introduction....115
8.2 Genesis of the Zarshuran deposit....117
8.2.1 Igneous association (heat sources) 118
8.2.2 Age of mineralization....121
8.2.3 Sources of mineralizing hydrothermal solutions.... 121
8.2.4 Sources of gold in hydrothermal solutions....122
8.2.5 Environment of mineralization.... 122
8.2.6 A genetic model.... 123
8.2.7 Conclusions.... 124
8.2 Deposit recognition criteria....125

Chapter 9: Application of GIS and remote sensing for mapping DRC in Takab area.... 127

9.1 Introduction....128
9.2 Background....128
9.2.1 Geology....128
9.2.2 Mineralization.... 130
9.3 Deposit Recognition Criteria (DRC)....132
9.3.1 DRC in the Takab area.... 132
9.3.2 Sources of data for DRC maps....135
9.4 DRC maps....136
9.4.1. Map of favorable host lithologies....137
9.4.2 Map of heat sources....138
9.4.3 Map of hydrothermal alteration....139
9.4.3.1 Hydrothermal clay minerals....140
9.4.3.1 Iron oxide minerals....142
9.4.4 Map of structures....144
9.4.5 Map of favourable metal sources....145
9.4.6 Map of geochemical signatures of gold mineralization....146
9.4.6.1 Filtration of effects of factors irrelevant to mineralization.... 146
9.4.6.2 Determination of geochemical signature of mineral occurrences....148
9.5 Conclusions....151

Chapter 10: A predictive GIS model for mapping potential gold and base metal.....153

10.1 Introduction 153
10.2 Weights of evidence method 154
10.3 Weights of evidence analysis....156
.10.3.1 Analysis of host lithologies domain 156
.10.3.2 Analysis of heat-sources domain....157
.10.3.3 Analysis of hydrothermal alteration domain....157
.10.3.4 Analysis of structures domain....160
.10.3.5 Analysis of metal source domain 160
.10.3.6 Analysis of geochemical signatures of mineralization domain 161

.10.4 Test of conditional independence 161
.10.5 Prospectivity model 164
.10.6 Conclusions 165

Chapter 11: Conclusions and recommendations 167

11.1 Conclusions 167
11.1.1 Geodynamics of mineralization 167
11.1.2 Spatial controls on mineralization 168
11.1.3 Ore genesis 169
11.1.4 Deposit recognition criteria 170
11.2 Recommendations 171

References 173
Colour figures 185

Chapter 1

INTRODUCTION

1.1 PROBLEM DEFINITION

The Alpine-Himalayan orogenic-metallogenic belt extends for 2000 km across Iran, where it is known as the Zagros Orogenic Belt. In the northern part of the Zagros Orogenic Belt lies the Takab Shahin-Dez region, an area of 15,000 km^2 underlain by a geothermal system and long-recognized as hosting base-metal deposits of hydrothermal origin and epithermal mineralizations of arsenic, antimony and mercury (Fig. 1.1).

Recent exploration in the Takab Shahin-Dez region has delineated gold reserves at the previously-known arsenic deposit at Zarshuran. However, full realization of the gold potential of the region has been hampered by lack of conceptual models for mineralization and under-utilization of modern exploration tools.

Therefore two problems are addressed here. The first is the development, for Zarshuran, of a conceptual/genetic model. The second is the development, for the Takab Shahin-Dez region, of an exploration model in which the Zarshuran model constitutes a significant input.

Alongside these geoscientific problems is a wider macro-economic problem. The economy of Iran relies substantially on exploitation of the country's natural resources, in particular, petroleum. Dwindling reserves of petroleum, which at present generates the greater part of the country's foreign exchange, heightens the necessity of finding alternatives, such as gold resources.

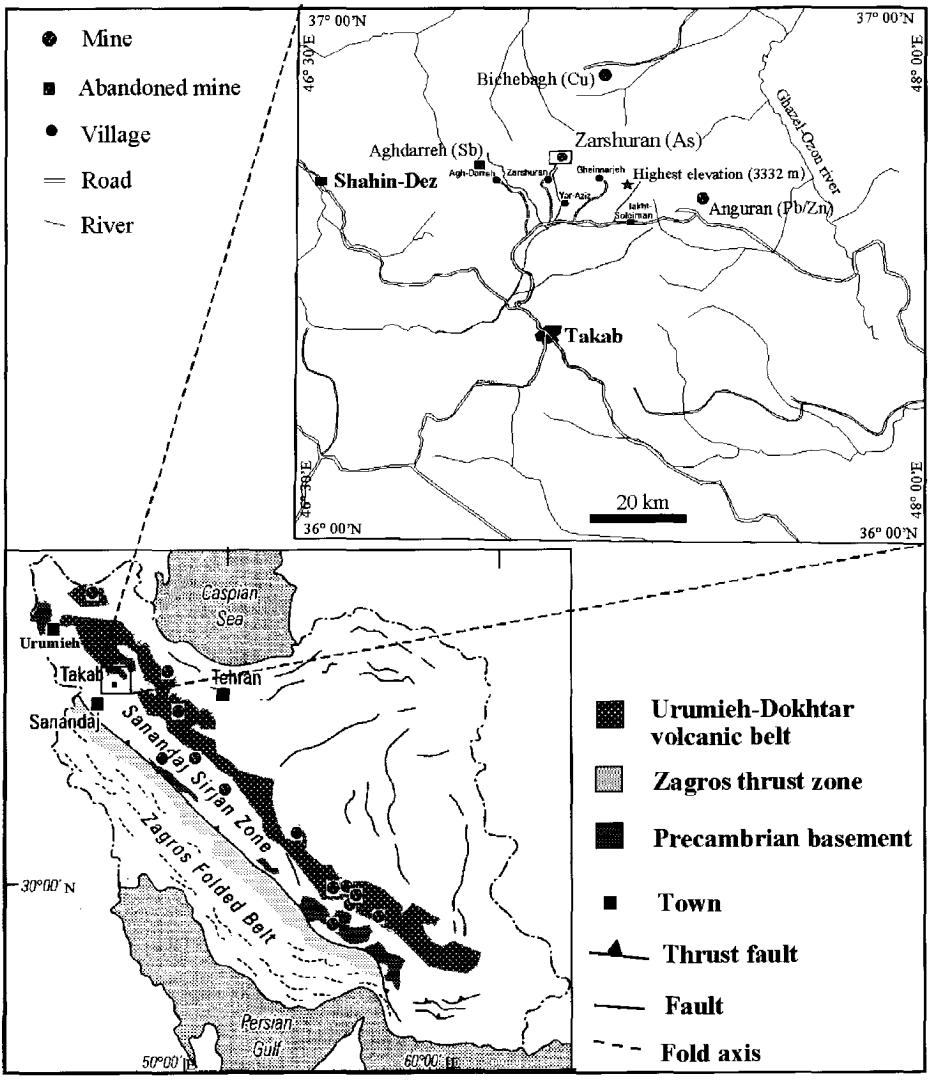

Fig. 1.1. Location in Iran of the Zagros Orogenic Belt (comprising, from southwest to northeast, the Zagros Folded Belt, Zagros Thrust Zone, Sanandaj Sirjan Zone and Urumieh-Dokhtar volcanic belt) and the Takab Shahin-Dez quadrangle

1.2 OBJECTIVES AND AIMS

The research sets out to apply both original mineral deposit genesis concepts and new exploration tools to the investigation of the gold potential of the Takab Shahin-Dez region. It has the following objectives:

1. to develop a spatial model of gold mineralization at Zarshuran;
2. to develop a genetic model of gold mineralization at Zarshuran; and
3. to show how the application of these models can be used in an exploration model to recognize the presence of similar mineralizations in the surrounding region.

1.2.1 Spatial model

There is limited subsurface data for Zarshuran. However, the morphology of subsurface gold-mineralized zones suggests that geologic boundaries confine the mineralization. Therefore spatial modelling has the following aims.

- Infer, from an interpretation of the 2D-3D spatial data, a 3D spatial model
- Determine the size and morphology of the deposit
- Identify the litho-structural controls on mineralization
- Determine the presence and spatial distribution of any metal zoning.

1.2.2 Genetic model

The genetic model suggests what geologic conditions and events favoured the process of mineralization at Zarshuran. Within the context of genetic modeling, the research has the following aims.

- Define the modes of occurrence of gold in the ore minerals
- Define the fabric (texture, structure and orientation) of the ore
- Determine the composition of the ore and associated minerals
- Determine the paragenesis of the ore and associated minerals
- Define the petrography of host formations and their role in gold precipitation
- Define the alteration assemblages
- Determine the temperature and depth of mineralization
- Determine the source of the mineralizing hydrothermal solutions
- Determine the heat source driving their circulation
- Determine the source of gold and associated metals

1.2.3 Exploration model

Gold mineralization of the type found at Zarshuran is not necessarily confined to Zarshuran. The aims of the research in relation to locating similar mineralization in the surrounding region are as follows.

- Use Zarshuran as a basis for defining deposit recognition criteria (DRC) that provide possible indications of unknown gold mineralization in the region
- Develop a regional GIS containing all available regional geodata layers from which DRC might be extracted (e.g., geological maps, Landsat TM satellite imagery, airborne magnetometry, airborne gamma-ray spectrometry, reconnaissance geochemistry, locations of mineral occurrences)
- Develop methods for querying the GIS for DRC
- Test the validity of the query results by ground truthing
- Refine the model into a predictive GIS for gold exploration in the region

1.3 BACKGROUND TO THE RESEARCH

Belts at the surface of the Earth where oceanic crust has been forced downward by the collision of tectonic plates are characterized by subduction zones and island arcs. These orogenic environments are prone to various styles of magmatic-hydrothermal mineralization. During the Mesozoic and Cenozoic eras, plate movements driving closure of the Tethys ocean created such environments along the length of the Alpine-Himalayan belt. Concomitant metallogenesis is conspicuous across the Alpine arc. From Italy through the Balkans to Turkey there are porphyry copper deposits, base-metal mesothermal vein deposits, volcanogenic massive sulphide deposits and epithermal mineralizations related to geothermal systems connected to ensialic Andean arc-type volcanism (Pirajno, 1992). In west-central Iran, the Alpine-Himalayan Zagros Orogenic Belt hosts porphyry copper deposits, other base-metal deposits of hydrothermal origin and epithermal arsenic and antimony deposits. Several deposits have proved to be economic and are, or have been, in production. In comparable geological settings elsewhere in the world, gold is associated with epithermal arsenic and antimony mineralizations.

Conceptual modeling of geothermal systems and their fossilized equivalents, epithermal gold deposits, is one of the major successes of the last 10-15 years in applied geological research (Fig. 1.2). Foster (1996) points out how conceptual modelling has been used to guide exploration of known palaeosystems and the search for undiscovered systems. Prediction of the palaeoelevation of an exposed epithermal system can be made from the thermal stability ranges of alteration minerals whilst prediction of the boiling zone, heat source, metal source and fluid-flow regime of the hydrothermal system can be made from fluid inclusion data and isotope data.

Related new exploration tools are exemplified by the approach of Harris and Pan (1991). They combined genetic factors related to epithermal gold mineralization in a control area with well-known features of epithermal gold and silver mineralization in the Walker Lake quadrangle of Nevada and California. They used these inputs to delineate further areas of high potential for gold and silver mineralization within the Walker Lake area.

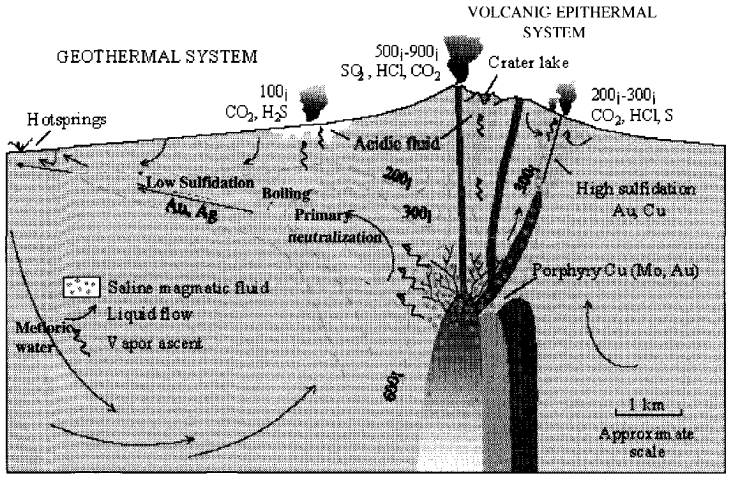

Fig. 1.2. Schematic cross-section showing shallow subvolcanic intrusions and associated stratovolcano, and the active hydrothermal environments deduced for the formation of epithermal ore deposits.

1.3.1 Concepts

Epithermal gold deposits, and in particular the carbonate-hosted disseminated type, are best known in the Basin and Range province of western North America. There are several large active gold mines exploiting this type of deposit in Nevada. Indeed deposits of this type currently rank as the leading gold producer in the United States and are an important exploration target. Deposits of this type have also been reported from southern China. In Iran, the mineralization at Zarshuran shares several characteristics with the carbonate-hosted disseminated epithermal gold deposits.

Research on different carbonate-hosted disseminated epithermal gold deposits has revealed several similarities in size, mineral associations, type and degree of alteration and host rock compositions which has provided a common "Carlin-type" model for them (Bagby and Berger, 1985; Berger and Bagby, 1991; Radtke, 1985; Bakken et al. 1989; and Kuehn and Rose; 1992). Nevertheless, for the genesis of this type of deposit, common agreement has not yet been achieved. Three contrasting genetic models have been suggested. The first proposes that Carlin-type deposits are associated with distal magmatism which drives hydrothermal circulation and supplies at least some of the fluid components and metals (Sillitoe and Bonham, 1990; Arehart et al., 1993; Radtke et al., 1980). The second invokes no link to magmatism but proposes that Carlin-type deposits are formed in terranes dominated by (meta-) sedimentary rocks that experienced crustal extension and regional fluid circulation (Ilchik and Baton, 1997). The third suggests that mineralizing hydrothermal fluids were derived from regional metamorphism of supercrustal rocks (Phillips and Powell, 1993).

This diversity of genetic models for Carlin-type deposits shows that several fundamental questions remain unresolved. What is the origin of mineralizing hydrothermal solutions? What is the source of gold and associated elements? What drives hydrothermal circulation? What, if any, is the relation between mineralization and magmatism? This research therefore asks whether, and in what ways, Zarshuran fits a Carlin-type model.

1.3.2 Tools

During the past several decades remote sensing has become an important tool for regional mineral exploration. It facilitates fast reconnaissance of large areas at relatively low cost. In the case of epithermal gold deposits, initial area selection can be rapidly achieved by using remote sensing technology for the detection of volcanic rocks, fracture and fault zones and areas of hydrothermal alteration. Moore and Guo (1990) analyzed the TM imagery data of part of southeast Spain and, using new image enhancement techniques, determined the presence of many hydrothermal alteration zones, which were interpreted as potential surface indicators of epithermal gold mineralization.

Often mineral deposits are not recognized by their responses in only one data set, but rather by superimposition of several subtle signals in different data sets (Ortega et al., 1990). The superimposition of geological, geophysical and geochemical data sets has been used by exploration geologists for a long time. Recently the Geographic Information System (GIS) has become an important tool to store, analyze and superimpose many different data sets with a speed and versatility that was formerly impossible. Approaches to exploration for gold mineralization using GIS have been applied in many areas, including the Joutel district in the Abitibi region of Quebec (Rheault et al., 1989), Stare Lake in Saskatchewan (Bonham-Carter et al., 1988), Nova Scotia (Tanaka and Segal, 1990), Round Mountain in Nevada (Watson and Rencz, 1989) and Tonopah district in Nevada (Lugaski et al., 1990).

Several regional geodata sets are available for parts of the Takab Shahin-Dez region. A GIS incorporating them is considered likely to lend itself to similar and appropriately adapted approaches.

1.4 METHODOLOGY

The research falls naturally into two phases. It rests on first proposing genetic and spatial models for the Zarshuran deposit. Then it goes on to use these models to structure the analysis of different geodata sets for gold exploration in the surrounding Takab Shahin-Dez region.

The research approach involves striving to maximize the usable information from different geodata sets in a number of ways. First, use is made of the spatial features related to the Zarshuran deposit (plus spatial features related to other known gold deposits) that are likely to be constraints on deposition of gold mineralization. Second, use is made of genetic

criteria from the Zarshuran deposit that are likely to be relevant to the formation of gold mineralization elsewhere in the region.

The spatial covariations in different geodata sets are taken into account and appropriate features in the different spatial geodata sets are enhanced, either separately or in combination. Finally there are elements of ground truthing and refining.

1.4.1 Phase One

The first phase involves investigations of the Zarshuran deposit in order to determine features that characterize its morphology and genesis. The results are compared with similar mineralizations elsewhere and evaluated to propose the spatial and genetic models. The spatial modeling is achieved through mapping surface and subsurface structural features, lithological units, alteration zones, geochemical anomalies and magnetic anomalies. The resulting data are analyzed in a GIS. Genetic modeling is based on laboratory investigations into ore mineralogy, ore mineral chemistry and the composition of fluid inclusions (Fig. 1.3).

1.4.1 Phase Two

The second phase involves determining how (some of) the spatial and genetic characteristics of the Zarshuran deposit may be recognized in regional geodata sets such as geology, stream sediment geochemistry, airborne magnetometry and Landsat TM imagery (Fig. 1.3). These geodata sets are then searched for anomalous features in an assessment of the regional gold potential of the surrounding Takab Shahin-Dez region. Ground truthing on the selected target areas is used to validate and refine the findings.

1.5 STRUCTURE OF THE THESIS

This thesis is mainly composed of scientific papers published by the author since 1998 in peer-reviewed international journals and international conference proceedings. In this thesis the content of these papers is slightly modified to avoid repetition and to obtain coherence between chapters.

Chapter 2 is an edited version of *Integrated analysis of remote sensing, aeromagnetic, geological and mineral occurrence data for the assessment of a subduction setting along the Zagros Orogenic Belt of Iran* (Asadi et al., 2000a). Remote sensing and GIS are used to characterize the geology and metallogeny of the Zagros orogenic belt, with emphasis on the Urumieh-Dokhtar arc and Sanandaj-Sirjan zone.

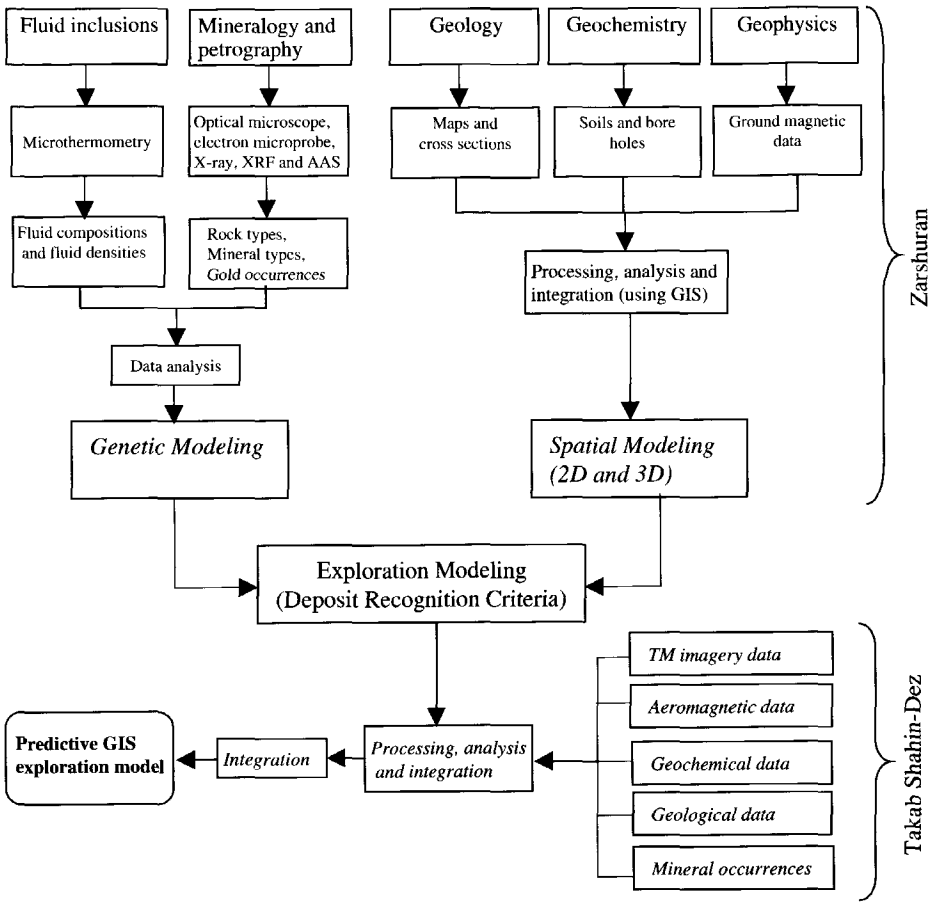

Fig. 1.3. Flow chart showing the general methodology of the research

Chapter 3 deals with the spatial modelling of the Zarshuran deposit, specifically *Using 2D GIS to assist 3D modelling of the Zarshuran gold deposit, Iran* (Asadi et al., 2000b). In order to define the spatial controls on gold mineralization, results of modelling with mainly 2D data are used to assess the 3D parameters of the deposit.

Chapter 4 describes the *Petrography, mineralogy and geochemistry of the Zarshuran Carlin-like gold deposit, NW Iran* (Asadi et al., 2000c). It proposes a mineral paragenetic sequence for the gold mineralizing hydrothermal fluids at Zarshuran and draws comparisons with those of Carlin-type gold deposits of the western United States.

Chapter 5 records the presence of *Invisible gold at Zarshuran, Iran* (Asadi et al., 1999). It explains in detail the mode of occurrences of gold, the gold-bearing minerals and also the association of gold with different elements and different rock types at Zarshuran.

Chapter 6 considers *Sulphosalts at the Zarshuran Carlin-like gold deposit, northwest Iran, implications for gold mineralization* (Asadi et al., 2001). It describes the sulphosalts and their association with gold mineralization at Zarshuran and proposes a model for the evolution of gold-mineralizing hydrothermal solutions. Part of this chapter was also presented as an extended abstract entitled *Gold mineralization at Zarshuran, NW Iran* (Asadi et al., 2000d)

Chapter 7 describes the Conditions for mineralization at the Zarshuran Carlin-like epithermal gold deposit through an investigation of the type, appearance and microthermometric characteristics of fluid inclusions that are present at Zarshuran. The results are used to explain the temperature and pressure conditions under which the Zarshuran ore has been formed.

Chapter 8 analyzes the evidence for a *Magmatic contribution to the Carlin-type gold deposit at Zarshuran, Iran* (Asadi and Hale, 1999a). It goes on to bring together the results from the spatial and genetic models of the Zarshuran deposit with the geology and metallogenic models of the Urumieh-Dokhtar arc and Sanandaj-Sirjan zone. These are used to identify the deposit recognition criteria (DRC) for gold exploration in the Takab Shahin-Dez quadrangle. The chapter is an edited version of *Application of Zarshuran Carlin-like deposit model for gold exploration GIS in NW Iran* (Asadi and Hale, 2000a).

Chapter 9 synthesizes an *Assessment of epithermal mineralization in northwest Iran using GIS* (Asadi et al., 1998a), *GIS and remote sensing for epithermal gold exploration in northwest Iran* (Asadi et al., 1998b) and *Integrated analysis of aeromagnetic, Landsat TM and mineral occurrence data for epithermal gold exploration in northwest Iran* (Asadi and Hale, 1999b). It shows how, for a test area of some 1800 km^2 within the Takab Shahin-Dez quadrangle, the identified DRC are reduced to mineral potential maps.

Chapter 10 is a modified version of *A predictive GIS model for potential mapping of gold and base-metal mineralization in Takab area, Iran* (Asadi and Hale, 1999c; Asadi and Hale, 2000a). A weights of evidence Baysian approach is used to develop an exploration model for the 1800 km^2 test area. Binary maps, representing diagnostic DRC, are combined to produce a predictive GIS exploration model for follow-up gold exploration.

Chapter 11 shows how the objectives of the research have been achieved, draws conclusions and establishes recommendations for future research.

Chapter 2

GEOLOGY, METALLOGENY AND GEODYNAMICS OF THE ZAGROS OROGENIC BELT

This chapter presents an integrated analysis of remote sensing, geological and mineral occurrence data of Iran within a country-scale GIS to test the hypothesis of subduction along the Zagros Orogenic Belt (ZOB), and to identify more precisely the subduction features inferred by earlier researchers. The interpretation of remote sensing data identifies several geological features resulting from the closure of the Tethys ocean, and their integration with the geology and known mineral occurrences defines a geodynamic setting for the Zagros belt that controls the occurrence of porphyry copper mineralizations and epithermal precious metal mineralizations. This geodynamic setting identifies some regional deposit recognition criteria for the occurrence on the regional scale of epithermal mineralizations in the Takab Shahin–Dez quadrangle This chapter is an edited version of *Integrated analysis of remote sensing, aeromagnetic, geological and mineral occurrence data for the assessment of a subduction setting along the Zagros orogenic belt of Iran*, published in Proceedings of. XIXth Conference of the International Society for Photogrammetry and Rremote Sensing (ISPRS 2000), Amsterdam, as paper TP VII-04-22 on CD ROM (Asadi et al., 2000a).

2.1 INTRODUCTION.

The Zarshuran gold deposit is located within the Takab Shahin-Dez quadrangle, Azarbaijan and Kordestan provinces, northwest Iran. The Takab Shahin-Dez quadrangle covers 15,000 km^2 between latitudes 36°N to 37°N and longitude 46°30'E to 48°E. Much of the quadrangle is characterized by geothermal systems, hot springs, travertine deposits and epithermal arsenic, antimony, mercury, gold and base-metal mineralizations. In terms of regional geology, the Takab Shahin-Dez quadrangle straddles the Zagros Orogenic Belt. A

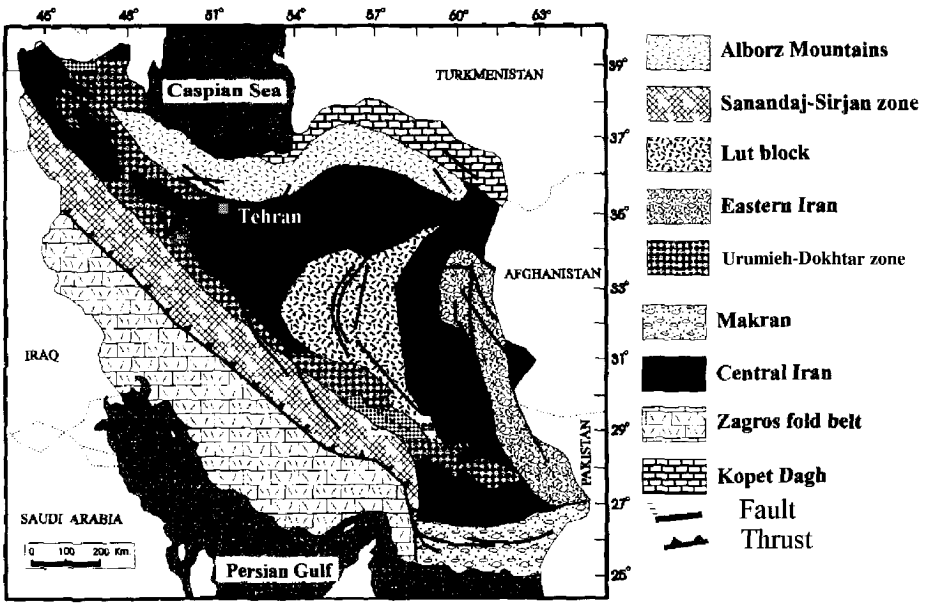

Fig. 2.1. Geological subdivisions of Iran (modified after Stocklin, 1977, and Shahabpour, 1994)

reliable model for the geology and metallogeny of this belt clearly has a bearing on the interpretation of the geology and mineralization of Zarshuran and the Takab Shahin-Dez quadrangle.

According to Stocklin (1977) and Shahabpour (1994), Iran is divided into nine litho-tectonic domains (Fig. 2.1): (1) the Central Iran Block; (2) the Alborz Mountains; (3) the Lut Block; (4) Eastern Iran; (5) Makran; (6) Kopet Dagh; (7) the Urumieh-Dokhtar zone; (8) the Sanandaj-Sirjan zone; and (9) the Zagros fold belt. The Central Iran Block comprises Palaeozoic platform sediments disrupted by late Triassic tectonic activity, horsts of Precambrian crystalline basement and Cambrian to Triassic cover rocks. The Alborz Mountains and Kopet Dagh mainly consist of Eocene volcanic and volcanoclastic rocks. The Lut Block is an old stable platform which is covered by thick Mesozoic sediments and Eocene volcanics. Eastern Iran and Makran are covered by post-Cretaceous flysh-mollasse sediments. The Urumieh-Dokhtar zone (or Sahand-Bazman zone), Sanandaj-Sirjan zone and Zagros fold belt together constitute the Zagros Orogenic Belt (Fig. 2.1). The Zagros Orogenic Belt extends over 2000 km in a northwest-southeast direction from the Eastern Anatolian Fault of eastern Turkey to the Oman Line in southern Iran (Alavi, 1994), and is part of the Alpine-Himalayan orogenic and metallogenic belt.

Although to date different parts of the Zagros Orogenic Belt (ZOB) have been subjected to detailed structural-metamorphic-magmatic studies, a synthesis of the geodynamic history of the entire belt is still far from complete. In this chapter, a review of the known geology and models for the origin of the ZOB is followed by analysis of geological, mineral occurrence, aeromagnetic and Advanced Very High Resolution Radiometric (AVHRR) data

using a country-scale GIS. One aim is to test the hypotheses of subduction *versus* continental rifting.

2.2 ORIGIN OF THE ZAGROS OROGENIC BELT

There is controversy amongst geologists about the tectonic setting and formation of the Zagros Orogenic Belt. Both a subduction model and a continental rifting model have been proposed.

In the subduction model, the ZOB is associated with the closure of the Tethys ocean. According to Alavi (1994), in the early Mesozoic a small continental block, the Central Iran Block, separated from the Gondwana landmass, forming the Iranian Plate. Newly-generated neo-Tethys oceanic crust was subducted below the Iranian Plate, until closure of the Tethys ocean led to collision of the Afro-Arabian and Iranian Plates.

Amongst those who support the subduction model there is, however, disagreement regarding certain spatial features and elements typical of a subduction setting, such as the precise location of the suture zone – with ophiolites – and its position in relation to the magmatic arc (Alavi, 1980, 1994; Takin, 1972; Cherven, 1986; Berberian and King, 1980). Such details are important because the geodynamic history defines the metallogenetic scenario and the role of the ZOB in the regional setting of mineralizations.

A rift model for the origin of the volcanic rocks and their geodynamic situation along the ZOB was proposed by Sabzehie (1974) and discussed by Amidi (1975) and Lescuyer and Rio (1976). They argued that the volcanic rocks of Urumieh-Dokhtar zone belong to the Central Iran Block and are mainly alkaline in origin. They believe that there is neither magmatic zonation nor K_2O enrichment, characteristics in both time and space of the volcanism related to subduction in this volcanic sequence. The inferred alkaline magmatism is linked to the rhythmic opening of a continental rift zone during the Eocene.

2.3 GEOLOGICAL SUB-DIVISIONS OF THE ZAGROS OROGENIC BELT

Since the pioneering work of Schröder (1944) and Stocklin (1968) the Zagros Orogenic Belt has always been divided into different tectono-metamorphic-magmatic domains. The generally-accepted way in which Alavi (1994) sub-divides the ZOB distinguishes three elongated parallel zones from northeast to southwest *viz.*, the Urumieh-Dokhtar Magmatic Assemblage (UDMA), the Sanandaj-Sirjan Zone (SSZ) and the Zagros Simply Folded Belt (ZSFB). Alavi (1994) postulates that the boundary between the UDMA and SSZ is formed by the Zagros Suture (ZS), characterized by some elongated, mylonitized and sheared ophiolite bodies. It represents the suture zone between the Afro-Arabian Plate and the Iranian Plate. The boundary between the SSZ and ZSFB is formed by the so-called Main Zagros Thrust (MZT). The intensely sheared and thrusted zone along the MZT is called the Zagros Thrust Zone (ZTZ; c.f., Stocklin, 1968). This zone grades into the lesser-deformed

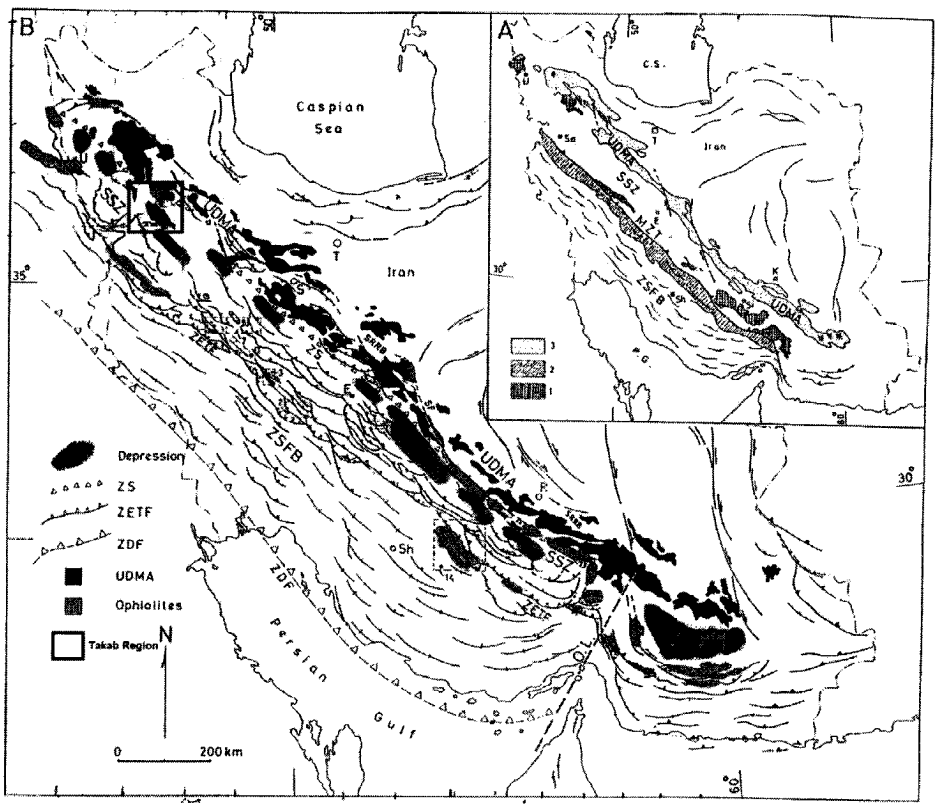

Fig. 2.2. Subdivisions of the Zagros Orogenic Belt according to (A) Stocklin (1968) and (B) Alavi (1994). 1 = Precambrian basement; 2 = Zagros Thrust Zone; 3, UDMA (black) = Urumieh-Dokhtar Magmatic Assemblage; MZT = Main Zagros Thrust; SSZ= Sanandaj-Sirjan Zone; ZSFB = Zagros Simply Folded Belt; ZDF = Zagros Deformation Front; ZETF = Zagros Exposed Thrust Front; ZS = Zagros Suture; O.L. = Oman Line; T = Tehran; U = Urumieh; Sh = Shirhaz.

ZSFB and eventually into the undeformed sediments of the Mesopotamian-Persian Gulf Basin (Fig. 2.2).

2.2.1 Urumieh-Dokhtar Magmatic Assemblage

The Urumieh Dokhtar Magmatic Assemblage (UDMA) or Urumieh-Dokhtar Zone according to Schröder (1944) comprises a linear magmatic arc which extends along the entire length of the ZOB. The UDMA has been attributed to both the Central Iran Block (Stocklin, 1968) and the ZOB (Alavi, 1994). There are several hypotheses about its formation. It is said to be an Andean-type magmatic arc formed by northeast subduction along the active continental margin of the Central Iran Block during the Alpine orogeny

(Takin, 1972; Sengor, 1990; Dewey et al., 1973; Berberian and King, 1980; Berberian et al., 1982; Forster, 1976). Alavi (1994) suggested that it is an Andean-type magmatic arc resulting from northeast subduction along the margin of the SSZ. Its formation has also been interpreted as post-collision magmatism (related to orogenic collapse), rather than subduction (Stocklin, 1974; Berberian and King, 1981). An alternative hypothesis is that the volcanism of the Urumieh-Dokhtar arc is not related to subduction but that it originated in a continental rift setting (Sabzehie, 1974; Amidi, 975)

Plutonic rocks are well-represented in UDMA and include diorite, granodiorite, gabbro and granitoids. Volcanic rocks are widespread as flows of trachy-basalt (locally shoshonitic), andesite and dacite. Other volcanic rocks include agglomerates, ignimbrites and tuffs (Alavi, 1980). Petrographic data suggest a generally calc-alkaline composition. Granitoid rocks of the UDMA are tentatively classified as calc-alkaline I-type Cordilleran-type products. Geological evidence indicates a post-Upper Jurassic to pre-Lower Cretaceous age of emplacement for the oldest plutons (Nabavi, 1972). Magmatic activity peaked during the Eocene, as manifested by the interlayering of large volumes of volcanic material and numulitic limestones. The youngest magmatic products comprise volcanic flows and pyroclastics of Quaternary age.

The UDMA coincides with a negative Bouguer gravity anomaly of –150 mGal, indicating a continental crust thickness of 45-50 km, some 5-10 km thicker than the crustal average of the Iranian lithospheric plate. Northeast-directed thrusting affected parts of the UDMA in the Tertiary.

2.2.2 Sanandaj-Sirjan Zone

The SSZ lies to the southwest of the UDMA and has a width of 150-250 km. From Sanandaj in the northwest to Sirjan in the southeast its southwestern boundary is formed by the parallel MZT and ZTZ. It joins the Taurus orogenic belt in Turkey. Rocks of the SSZ are essentially composed of Phanerozoic shallow-marine and continental shelf deposits comprising shales, carbonates and siliciclastics (mainly sandstones with subordinate arkoses and greywackes). Intraformational breccias and polymict conglomerates occur in places. The breccias are considered a manifestation of syn-sedimentary tectonics (slumping). The conglomerates, together with a hiatus in the stratigraphic column, point to temporary emergence and erosion. Magmatic rocks are scarce. These mainly comprise sub-volcanic lenses of diabase and narrow horizons of basalt and rhyolite that are interlayered with shallow marine Carboniferous, Permian and Lower Triassic sediments. Gabbro and granitoid plutons, associated with tholeiitic lavas, were emplaced during the Middle to Upper Triassic. A few narrow intercalations of coarse pyroclastics and fine tuffs, found high in the sequence (e.g., near the Takab and Nahavan area in the northwest of the SSZ), are possibly of Cretaceous but more likely of Tertiary age.

The combination of sedimentary and igneous rocks as described above indicates a prolonged history of intermittent crustal extension which started in the Carboniferous and probably culminated in the Jurassic, when the Iranian Plate broke away from the Afro-

Arabian Plate. Each phase of crustal extension resulted in crustal thinning, basaltic underplating and an increased heat flow. This, in turn, gave rise to limited bi-modal magmatism. Some of the Palaeozoic and Mesozoic rocks in the SSZ have been affected by low- to medium-grade greenschist facies metamorphism (Alavi, 1994). Thermal events during the Late Cretaceous and Middle to Late Triassic even reached medium- to high-grade greenschist facies conditions (e.g., Sabzehie, 1992), which coincided with an important phase of bi-modal magmatism. The metamorphic events may reflect the combined results of increased heat flow and detachment faulting.

A series of elongated depressions mark the northeastern boundary of the SSZ. Towards the southwest the SSZ shows a strong increase in elevation, associated with a negative Bouguer anomaly. From this, the depth to the moho can be calculated (Dehghani and Markis, 1983). It appears that from northeast to southwest the thickness of the SSZ increases from an average of ~40 km to ~55 km.

Alavi (1980, 1994) presents a number of examples all demonstrating that the increase in crustal thickness is caused by overthrusting and stacking of nappes. A synthesis of the structural data from a number of areas described in detail by Alavi (1994) (e.g., the Kuhrang, Chaghagorg, Nahavand, Malayer, Asadabad, Baft and Nayriz areas) indicate that the SSZ is characterized by numerous thrust masses that have been transported from northeast to southwest in a piggy-back style, forming small- and large-scale duplex and imbricate structures. Older duplex structures have been truncated and overthrusted by younger duplex and imbrication structures, giving rise to complex geometries. In places thrust masses of older rocks overly younger rocks. All structural elements – low-angle thrust planes, verging of drag folds and slickenslides – demonstrate tectonic transport towards the southwest.

Ophiolites are particularly abundant along the northeast and southwest contact of the SSZ. According to Alavi (1994), along the southwestern boundary ophiolites form an intricate part of the low-angle, southwest-verging thrust structures. Serpentinites in particular may act as lubricants between thrust masses. Along the northeast contact, ophiolites are found as sheared and mylonitized complexes bounded by steep, high-angle faults.

2.2.3 Zagros Simply Folded Belt

The ZSFB is characterized by northwest-southeast trending parallel anticlines and synclines. It consists of a thick pile of sediments overlying a high-grade metamorphic Precambrian basement. This basement is most probably an extension of the Neo-Proterozoic Arabian-Nubian Shield (a special geodynamic domain of the Afro-Arabian Plate), which dips with a low angle in a northeast direction below the Persian Gulf-Mesopotamian Basin and the ZSFB (Berberian et al., 1982). According to Giesse et al. (1983), the Arabian-Nubian Shield even extends northeastward below the SSZ.

According to Alavi (1994), the sedimentary cover sequence is 6-10 km thick and comprises three main sub-units: (1) a late Precambrian to early Cambrian evaporate-

dolomite unit which is overlain discontinuously by a sequence of shallow (epi-) continental shelf siliciclastic and carbonate rocks of Cambrian to Carboniferous age, generally similar to the chronologically-equivalent rock successions of the SSZ; (2) a succession of Carboniferous/Permian to late Cretaceous continental shelf/platform carbonates; and (3) a sequence of uppermost Cretaceous to Recent marine and non-marine carbonates and siliciclastics which show a pronounced southwestward migration of the depocentres through time (Koop and Stoneley, 1982). Fragments of the underlying basement are known from 'exotic' blocks in salt diapirs.

Structurally, the ZSFB is generally characterized by upright northwest-southeast trending, doubly- plunging fold structures. In places, anticlines are displaced along their southwestern flank by longitudinal, southwest-verging reverse faults. Elsewhere, folds are overturned and, again, verging southwest. Further southwestward the fold structures become more gentle and younger and eventually grade into flat-lying sediments of the Mesopotamian-Persian Gulf Basin. The amount of shortening since the Miocene, based on the geometry of the fold structures, is estimated to be approximately 100 km, and shortening is still continuing (Haynes and McQuillan, 1974; Mann and Vita-Finzi, 1982). Seismic activity in the ZSFB is limited to shallow focal depths (<20 km; e.g., Nowroozi, 1972, 1976; Niazi et al., 1978; Jackson, 1980; Jackson et al., 1981; Chandra, 1981; Asudeh, 1982, 1983; Ni and Barzangi, 1986). From this, it can be concluded that shortening of the sedimentary cover is not mirrored by shortening (e.g., by reverse thrusting) of the corresponding crystalline basement. The fold structures in the ZSFB thus represent 'décollement folds' detached from their crystalline basement. The basal evaporites have served as the detachment surface between cover and basement. Following this line of thinking, it can also be concluded that the basement of the ZSFB continues underneath the stacked nappe structures of the SSZ, a conclusion already reached by Giesse et al. (1983).

Traditionally, the MZT was considered as the boundary between the ZSFB and the SSZ. Its association with the ZTZ (a narrow zone of extreme deformation, 10-70 km wide) and the occurrence of numerous ophiolite complexes in this zone prompted many geologists to consider the MZT as the suture between the Afro-Arabian and Iranian Plates (e.g., Takin, 1972; Crawford, 1972; Dewey et al., 1973; Berberian and King, 1980; Berberian et al., 1982 and Sengor, 1990). However, recent structural field observations and stratigraphic correlation reveal no sharp boundary between the ZSPB and the SSZ (Alavi, 1994).

2.3 METALLOGENY OF THE ZAGROS OROGENIC BELT

The ZOB is part of the Alpine-Himalayan orogenic and metallogenic belt, and therefore has a high potential for different types of metallic minerals. The geological environment favours the occurrence of porphyry copper deposits, volcanogenic massive sulphide deposits, hydrothermal Pb-Zn-Ba deposits and occurrences of Au, Ag, As, Sb, Hg deposits related to epithermal systems connected to the Tertiary volcanism. These mineral deposits are mostly spatially associated with the UDMA and the western margin of the SSZ.

Calc-alkaline volcano-plutonic rocks of the UDMA host manto, porphyry and vein type base metal and precious metal deposits. Porphyry copper mineralization is the most widespread type, and in places there are associated gold and molybdenum mineralizations.

Porphyry copper deposits have been intensively studied in the Mesozoic-Cenozoic orogenic belts of the American Cordillera and East Pacific rim, and their genesis and exploration criteria are relatively well understood (Titley and Beane, 1981; Sillitoe, 1993). Nevertheless, there have been few scientific investigations of this style of mineralization in Iran. Some geologists believe that, in terms of time of formation, element association (e.g., gold- or molybdenum-rich) and igneous petrology (e.g., both basaltic and andesitic rocks rather than andesitic rocks alone), the style of porphyry copper mineralization in Iran is slightly different to that elsewhere in the world (e.g., Sillitoe, 1993; Khakzad, 1991; Karimpour, 1989).

All porphyry copper mineralization in Iran occurs in UDMA volcano-plutonic rocks of Tertiary age. There are about 500 copper occurrences, including about 100 deposits and, at present, five active copper mines. The active mines and most of the large deposits are located in the southeastern part of the UDMA and in its northwestern corner. The very large Sungun and Sar-Cheshmeh deposits are located in the northwest and southeast of the UDMA respectively. These and several sub-economic deposits are associated with mid- to late-Miocene diorite-granodiorite to quartz-monzonite stocks (Hezarkhani and Williams-Jones, 1998). Molybdenite is mainly present in the deposits of northwestern parts of the UDMA (e.g., Sungun) and gold in the southeastern parts (e.g., Sar-Cheshmeh and Darehzar) (Hezarkhani and Williams-Jones, 1998).

The SSZ hosts numerous occurrences of hydrothermal, massive sulphide and skarn base-metal mineralizations in carbonates. These deposits are very abundant in the western margin of the SSZ, near the ZTZ, as well as at the boundary of SSZ and UDMA. In this latter setting, at Anguran in the northwest sector of SSZ, is the carbonate-hosted hydrothermal Pb-Zn deposit (currently the largest Pb-Zn mine in Iran). Mineralization at Anguran is spatially associated with subsurface Tertiary igneous rocks (Asadi, 1995), which possibly provided the main heat sources to drive the migration of the hydrothermal solutions.

Ophiolitic rocks, including peridotite, serpentinite and coloured melanges as well as volcano-plutonic complexes (e.g., granitoids), occur in the western margin of the SSZ and/or along the ZTZ. These host chromium, titanium, manganese, nickel, tin, tungsten copper and platinum-group metals mineralizations.

In addition, within the SSZ there are several geothermal fields that host mineralizations of gold, arsenic, antimony and mercury as well as deposits of hydrothermal silica and travertine. One geothermal field lies in the Muteh area, to the north of the town of Esfahan, in the central part of the SSZ. The gold deposits in the Muteh geothermal field are hosted by Precambrian meta-sedimentary rocks. Muteh itself is the only active gold mine in Iran.

The Takab Shahin-Dez area, also underlain by an active geothermal system, lies on the northeast margin of the SSZ, near its contact with the UDMA. The geology of the area is a complex of repeated cycles of orogenic activities, including structural uplift, sedimentation, magmatism and metamorphism. There are a variety of geologic structures in the area that

resulted from the Alpine orogeny (Alavi et al., 1982). The geological formations mostly comprise Precambrian metamorphics, Tertiary volcanics (with subordinate granitoids), Tertiary sedimentary rocks, some outcrops of Mesozoic sedimentary rocks and Quaternary sediments. The area is potentially important for epithermal gold, arsenic, antimony, mercury and base-metal mineralizations. Known mineralization of these types are hosted by jasperoid, black shale, carbonates and partially-altered andesite. Those deposits hosted by sediments are usually found a short distance from volcano-plutonic rocks.

2.4 GEODYNAMIC RE-INTERPRETATION OF THE ZAGROS OROGENIC BELT

Geology (lithological and structural attributes) was digitized from three 1:1 000 000-scale map sheets covering the whole of the ZOB. Mineral occurrences (deposit type, deposit name, UTM coordinates, major commodities and size) were digitized from the same sheets.

Five bands of digital data with a 1000 x 1000 m pixel size from Advanced Very High Resolution Radiometric (AVHRR) satellite imagery covering the whole of Iran were calibrated and geometrically corrected for further processing and interpretation. Data of the two reflective bands (Bands 1 and 2) were calibrated to percent reflectance. Data of the two thermal bands (Bands 3 and 4) and one intermediate band (Band 5) were calibrated to brightness temperature in degrees Kelvin. A Polyconic projection was used to georeference the images.

Magnetic data from the nation-wide airborne reconnaissance survey (7.5-km line spacing), conducted in 1976, was digitized from total magnetic field contour maps. State of the art visualization and enhancement techniques have been applied to the aeromagnetic data set for interpretation.

The Digital Elevation Model (DTM) grid of Iran with 5 km resolution was downloaded from United States Geological Survey (USGS) web site and imported into the GIS. Visualization and enhancement techniques have been applied to the DEM grid to highlight geological features for interpretation.

Finally, all data sets were re-formatted to a uniform map projection (Lat-Long coordinates) and combined to create a GIS database covering the whole of the ZOB.

2.4.1 Lithology

Several colour composite combinations of processed AVHRR bands were created to differentiate major lithological domains of the ZOB. A colour composite combination of two thermal bands (bands 4 and 3) and the intermediate reflective-thermal band (band 2) proved to be the best colour composite image for mapping the different parallel northwest-southeast geologic domains of the ZOB across much of Iran. In this colour-composite combination, the UDMA, the northeastern part of the SSZ and the northeastern part of the ZSFB are characterized by dark blue, yellow and a mixture of yellow and light blue,

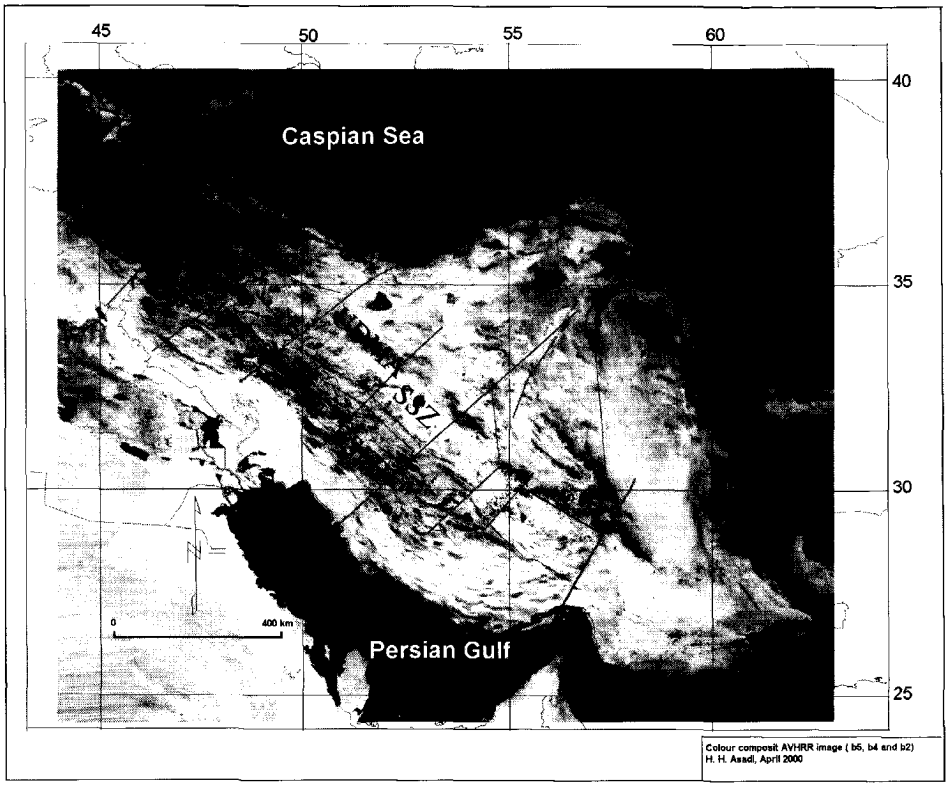

Fig. 2.3. Colour composite AVHRR image (Bands 4, 3, 2) showing UDMA, SSZ and ZSFB and also the interpreted major faults, trending in a northwest-southeast (black lines) and northeast-southwest (red lines), (see also the corresponding Fig. 2.3 in the colour figures).

respectively. By overlaying the previously-mapped Tertiary volcanic rocks of the UDMA on this image, some additional exposures of volcanic rocks, located along the axes of the known magmatic arc, were mapped. The boundary between the SSZ and UDMA is clearly visible in this image and coincides with the earlier interpretation. The spectral characteristics of the boundary between the ZSFB and SSZ along the MZT, proposed by Stoklin (1968), are not distinguishable in this image. There is a relatively sharp boundary, extending in a northwest-southeast direction, about 20-30 km to the northeast of the MZT within the SSZ. The deformation front along the western part of the ZSFB is characterized by featureless terrain and a yellow colour (Fig. 2.3). The zones along the ZOB with different spectral characteristics were screen digitized for use in data integration.

Most rock types have specific magnetic susceptibilities and therefore aeromagnetic measurements, when suitably processed, can distinguish different rock types. The analytic signal of the total magnetic field identifies anomalies associated with rocks of high magnetic susceptibility, both outcropping and at depth. Paterson and Reeves (1985) point out that one

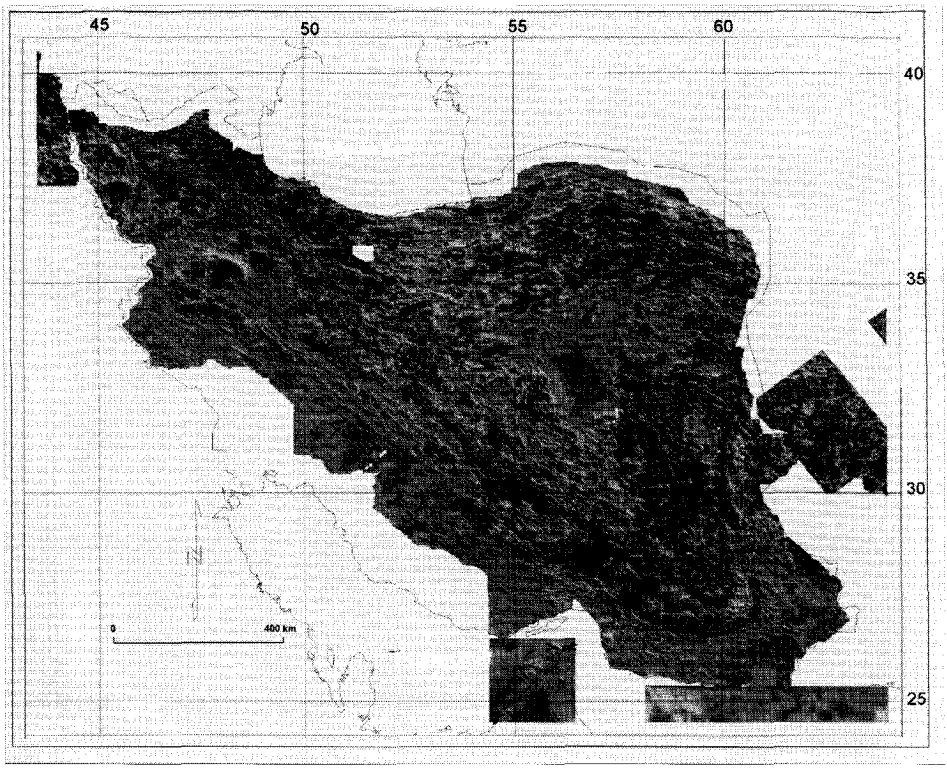

Fig. 2.4. Analytic signal map of Iran showing, as purple shades, the high amplitude analytic signal anomalies extending in a northwest-southeast direction; these are mainly associated with magmatic rocks of UDMA (purple) and ophiolites (grey shade) in the Sanandaj Sirjan Zone (SSZ), (see also the corresponding Fig. 2.4 in the colour figures).

advantage of the analytic signal is that magnetic information is displayed in a more interpretable manner than total magnetic intensity. Anomalies correlate directly with causative bodies and are positioned symmetrically over them. The analytic signal is independent of the inclination of the magnetic field; this has advantages over reduction to the pole in that the direction of magnetization does not need to be known (Qin, 1994).

Figure 2.4 is a shaded-relief analytic signal map of Iran in which anomalous high-amplitude signals appear in red. The strongest anomalies extend in a northwest-southeast direction and coincide with the UDMA. These anomalies mainly arise from the outcropping and sub-cropping igneous rocks. The igneous rocks in this region are extrusive and sub-volcanic rocks of mainly andesitic composition and the intermediate-to-deep intrusives of generally granodioritic composition. After overlaying the previously-mapped outcropping igneous rocks of the UDMA on this image, it was possible to map several other zones of surface and subsurface igneous rocks along the UDMA.

In addition, the magnetic signatures characterizing the exposed ophiolites of the ZOB were used to infer that certain elongated linear features represented unrecognized ophiolite

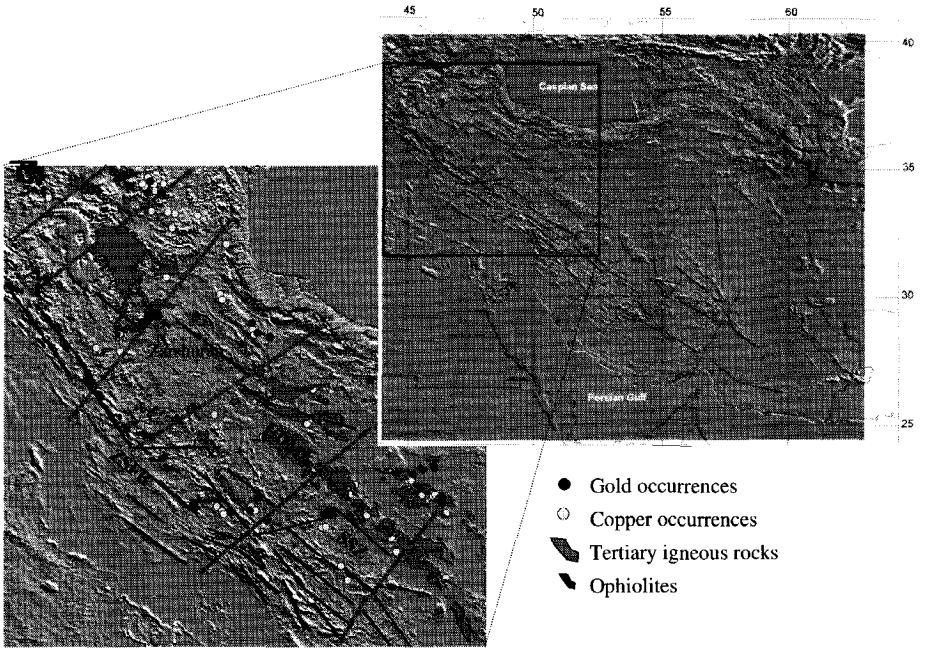

Fig. 2.5. Principal components image (PC1) overlain with interpreted structures and enlarged northwestern part (as indicated by black box), overlain with Tertiary igneous rocks, gold occurrences (black) and copper occurrences (grey).

bodies both at surface and at depth (Fig. 2.4). The ophiolitic rocks are characterized by narrow elongated medium-to-high magnetic anomalies which extend along northwest-southeast linear structures, mainly along the MZT and within the SSZ.

2.4.2 Structure

Structural data in the GIS came from digitizing geological maps and processing and interpretation of AVHRR and aeromagnetic data. The data digitized from geological maps included the main structural features attributed to the ZS (e.g., MZT and the contact of the SSZ and UDMA).

The colour-composite combination of AVHRR imagery used for lithological mapping highlights several sharply-defined parallel and elongated northwest-southeast structures along the ZTZ, in the western part of SSZ and at the contact of the SSZ and UDMA (Fig. 2.3). These structures were screen digitized and converted to a new format for data integration.

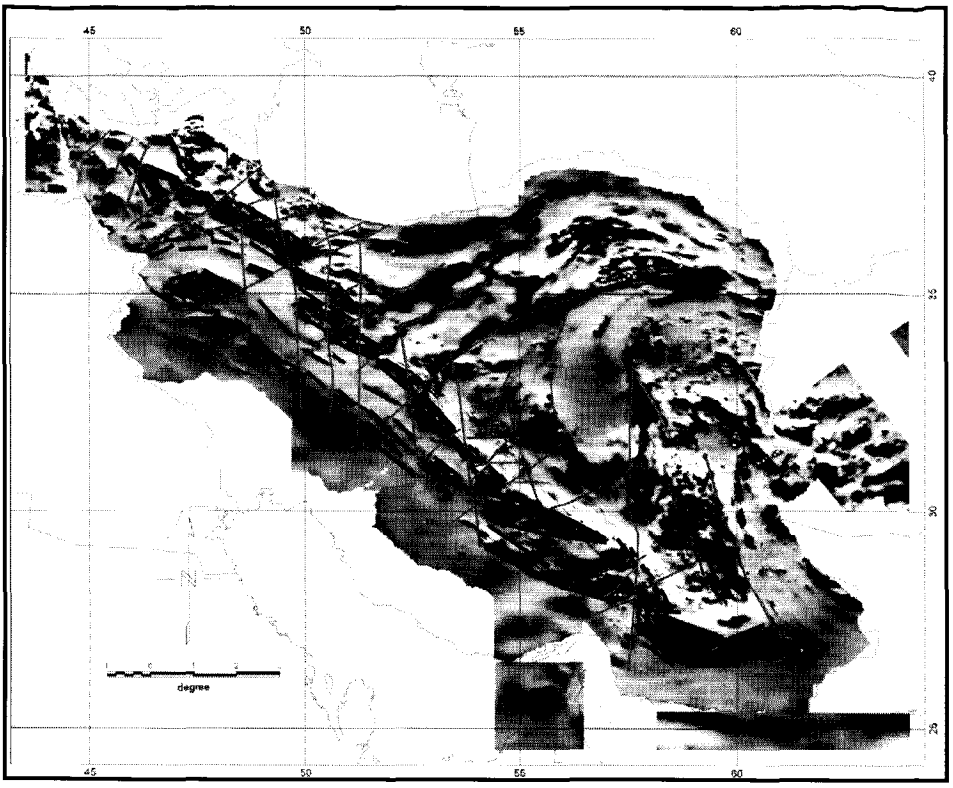

Fig. 2.6. Inverted grey-scale map of total magnetic field intensity showing linear structures: grey lines are interpreted northeast-southwest and north-south conjugate faults; black lines are northwest-southeast linear features.

A principal components (PC) transformation was applied to the five bands of the AVHRR imagery to highlight additional structural features. Two sets of lineaments, one trending in a northwest-southeast direction and the other in a northeast-southwest direction, were identified from the PC1 image by applying directional filtering. The alignments of relatively shorter lineaments were used to interpret several major structures running in the same two directions (Fig. 2.5). It appears that the northwest-southeast trending structures, particularly along the MZT, have been locally displaced by northeast-southwest structures extending into the SSZ and UDMA.

The Digital Elevation Model (DEM) of Iran was also used for structural mapping. Shaded relief maps of the DEM were created to map structures otherwise unmapped by the data already described. The parallel, elongated northwest-southeast structures along the ZTF, mapped by AVHRR imagery, were also clearly highlighted in the processed DEM maps. In addition, the DEM aided recognition of several elongated depression zones along the western margin of the SSZ.

Coloured and inverted grey-scale shaded-relief images of the total magnetic field and grey-scale 2nd vertical derivative maps of Iran were used for subsurface structural mapping along the ZOB. Figure 2.6 is an inverted grey-scale total magnetic field map in which high-amplitude magnetic anomalies appear in black. This map was used to identify northwest-southeast, northeast-southwest and north-south linear features. The northwest-southeast structures are mainly spatially associated with the ZTZ and extend into the SSZ. The boundary of the SSZ and UDMA is also marked by these structures. Two sets of northeast-southwest and north-south conjugate faults were also interpreted from this map. The conjugate faults appear to postdate the northwest-southeast structures. These two sets of structures displaced both the northwest-southeast structures as well as the magmatic rocks along the UDMA arc.

2.4.3 Geodynamic model

The results obtained from the interpretation of aeromagnetic data, AVHRR imagery and the DEM were integrated with the digitized geology and mineral occurrences of the ZOB in order to test the hypothesis of a subduction setting for the ZOB. Structures were digitized from processed aeromagnetic and AVHRR images and converted to suitable formats for data integration. The outline of the UDMA was re-mapped from the processed aeromagnetic and AVHRR images. The aeromagnetic images assisted the recognition of sub-outcropping igneous rocks along the UDMA and sub-outcropping ophiolite sheets along the MZT and into the SSZ.

Several elements of a subduction-related setting have been identified and the boundaries of the tectono-magmatic domains of the ZOB have been remapped with a much higher accuracy (Figs. 2.7 and 2.8). The results confirm the presence of a subduction zone along the ZOB and the occurrence of the suture zone probably along the boundary of UDMA arc and SSZ, as originally suggested by Alavi (1994), or somewhere in the western part of SSZ; the MZT which was traditionally suggested as the Zagros suture is just a thrust parallel to several similar other thrusts located within the SSZ.

Clearly distinguishable in aeromagnetic and AVHRR imagery data are the parallel tectono-magmatic domains of the ZOB. These include the passive margin sediments, magmatic arc, the elongated suture ophiolitic sheets, parallel-elongated structures up to 300 km long and the deformational front. Interpretation of the aeromagnetic data indicates the presence of many parallel linear sub-outcropping ophiolitic rocks along the MZT and in different parts of the SSZ. None of these linear ophiolites along the MZT can be singled out as the main suture zone between Iranian Plate and Afro-Arabian Plate; indeed, most of the inferred ophiolites do not coincide with the MZT.

Very strong magnetic anomalies not attributable to outcropping rocks along the UDMA are interpreted to reflect intermediate-basic volcano-plutonic rocks and/or oceanic crust beneath the UDMA. Outcropping elongated ophiolitic rocks at the contact of the SSZ and UDMA in the southeast and northwest of the ZOB exhibit very strong positive magnetic anomalies. Outcropping ophiolites in the southern sector and northern sector of the UDMA

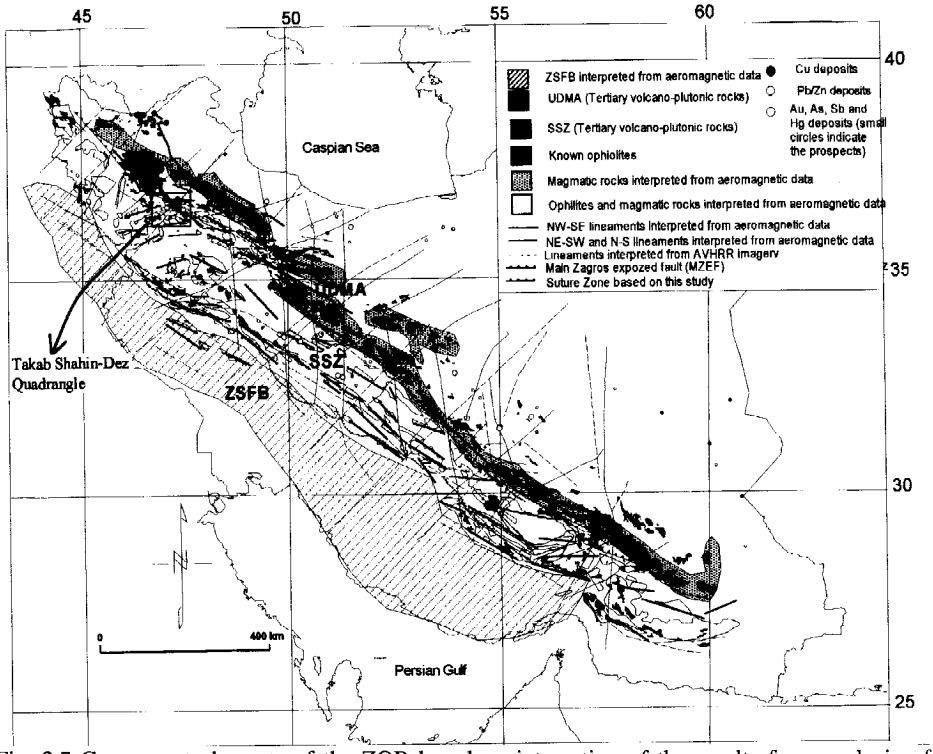

Fig. 2.7 Component elements of the ZOB based on integration of the results from analysis of AVHRR imagery, aeromagnetic, geological and mineral occurrence data (see also Fig 2.7 in the colour figures).

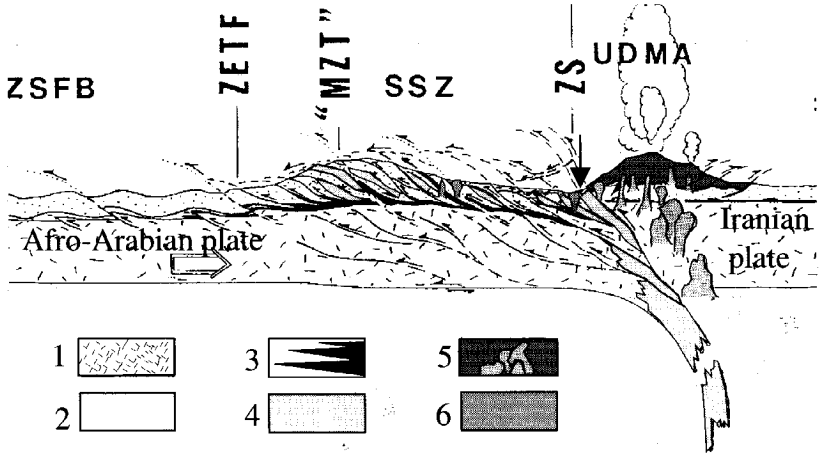

Fig. 2.8. Schematic cross-section across the ZOB (Fig. 2.7). 1 = Continental crust; 2 = Phanerozoic sedimentary cover; 3 = evaporites (white) and dolomites (black) at the base of the sedimentary cover; 4 = oceanic crust; 5 = intrusive and extrusive rocks of UDMA and 6 = igneous rocks of SSZ, arrow shows the location of Zarshuran deposit; based on this study and Alavi, 1994 (see also Fig. 2.8 in the colour figures).

can be magnetically traced into the SSZ at depth. This could indicate that remnants of oceanic crust have been moved from their original place, the boundary of the SSZ and UDMA, toward the southwest. Alavi (1994) suggested that this might have been achieved by reverse faulting.

Data integration yields three interpreted sets of faults in the ZOB, trending northwest-southeast, northeast-southwest and north-south. The northwest-southeast trending structures are mainly located in the SSZ and ZSFB, whilst the other two sets appear as conjugates that crosscut the UDMA, SSZ, ZSFB and northwest-southeast trending structures. The northwest-southeast trending structures are interpreted as compressional faults associated with subduction and the northeast-southwest and north-south trending structures are interpreted as extensional conjugate faults formed by orogenic collapse due to the reverse faulting and thickening of the crust during or after subduction.

Most mineral occurrences in the ZOB are spatially associated with the volcanic arc and ophiolites. They are typically controlled by major northwest-southeast trending structures which are crosscut and off-set by equally prominent northeast-southwest and north-south trending faults. The porphyry copper deposits are spatially associated with northwest-southeast trending structures and UDMA magmatic rocks, whilst the epithermal mineralizations, in particular those of the Takab Shahin-Dez area, are associated with northeast-southwest trending faults and their intersections with the northwest-southeast and north-south trending structures.

2.5 CONCLUSIONS

The evidence from data integration supports a subduction model for the ZOB. Furthermore, it supports the version of the subduction model which invokes a suture along the contact of the UDMA and SSZ, rather than along the MZT. The rift model is rejected due to the presence of three tectonically-related parallel zones of the ZOB extending from northwest to the southeast, the presence of widespread ophiolitic rocks, the remnants of oceanic crust within the SSZ and along the ZTZ, and several occurrences of porphyry copper and epithermal mineralizations, typical of a subduction-realted Andean-type geological setting.

Combining published ideas with the new interpretations described above, the following geodynamic history is proposed for the ZOB. During the opening of the Neo-Tethys ocean, the Iranian plate was breaking away from the Afro-Arabia plate. There was a peak in bi-modal magmatism in Late Cretaceous – Early Paleocene times, ca. 75 Ma (Davodzadeh and Schmidt, 1984). Closure of the Neo-Tethys oceanic basin was accompanied by subduction of oceanic crust beneath the Iranian Plate to the northeast (Eocene, 55-35 Ma, Cherven, 1986). Anatexis of the subducted material led to the formation of a magmatic arc (the UDMA) with associated porphyry copper mineralization. Subsequent collision of the Afro-Arabian and Iranian Plates resulted in southwestward thrusting and stacking of passive margin rocks forming an accretion wedge with suture materials (e.g., ophiolite fragments in the SSZ), thrusting of underlying basement beneath the SSZ and folding of the ZSFB cover.

This led to significant crustal thickening. Orogenic collapse of the thickened crust along the SSZ, together with bi-modal magmatism (mainly rhyolites, tuffs and basalt) and northeast-southwest and north-south extensional faulting, provided energy, sources and pathways for hydrothermal base-metal and epithermal precious-metal mineralizations.

Hydrothermal base-metal and epithermal precious-metal mineralizations are particularly pronounced in the sector of the ZOB straddled by the Takab Shahin-Dez quadrangle. The geodynamic setting of the ZOB indicates three regional deposit recognition criteria for these types of mineralization in this region: (1) proximity to the NW-SE trending ophiolitic rocks along the proposed suture zone at the boundary of the SSZ and UDMA; (2) proximity to the NE-SW trending faults and their intersections with the older NW-SE trending structures; and (3) proximity with the Tertiary igneous rocks extending in a NE-SW direction within the SSZ and their intersections with those igneous rocks, possibly connected to the UDMA, extending in a NW-SE direction. The existence of and potential for epithermal precious-metal mineralizations in this region is the subject of the subsequent chapters of this thesis. Where appropriate, this research takes advantage of the geodynamic setting and the related deposit recognition criteria deduced here.

Chapter 3

USING 2D GIS TO ASSIST 3D MODELLING OF THE ZARSHURAN DEPOSIT

This chapter uses a 2-dimensional (2D) GIS for analysis of the deposit-scale surface geo-information at Zarshuran in order to guide the initial phases of the preparation of a 3-dimensional (3D) model that embodies spatial controls on the deposit. Data of surface geology, geophysics and geochemistry are incorporated in a 2D GIS, in which a spatial model that highlights features associated with the mineralization is developed. The 3D sub-surface geological structures that control mineralization are then inferred from an interpretation of this 2D spatial model. The results are evaluated by a 3D model of the deposit using geological cross sections and assay data from 12 drillholes. The chapter is an edited version of *Using 2D GIS to assist 3D modelling of the Zarshuran gold deposit, Iran,* published in the Proceedings of. XIXth Conference of the International Society for Photogrammetry and Remote Sensing (ISPRS 2000), Amsterdam, as paper TP VII-04-22 on CD ROM (Asadi et al., 2000b)

3.1 INTRODUCTION

The Zarshuran mining district, north of the town of Takab in northwestern Iran, lies in the central part of the Takab Shahin-Dez quadrangle. The district is accessible by the Takab Takhte-Soleiman asphalt road. Zarshuran mine is accessible by a 42 km second class asphalt road and a 7 km track road via the villages of Yaraziz and Zarshuran (Fig. 3.1). This climate is moderate in the summer and very cold during the winter when the mining area is covered by thick snow.

The district is one of ancient arsenic and gold mining. Old workings and trenches in the area seem to be the remains of ancient gold mining activities (Mohajer et al., 1989). Large

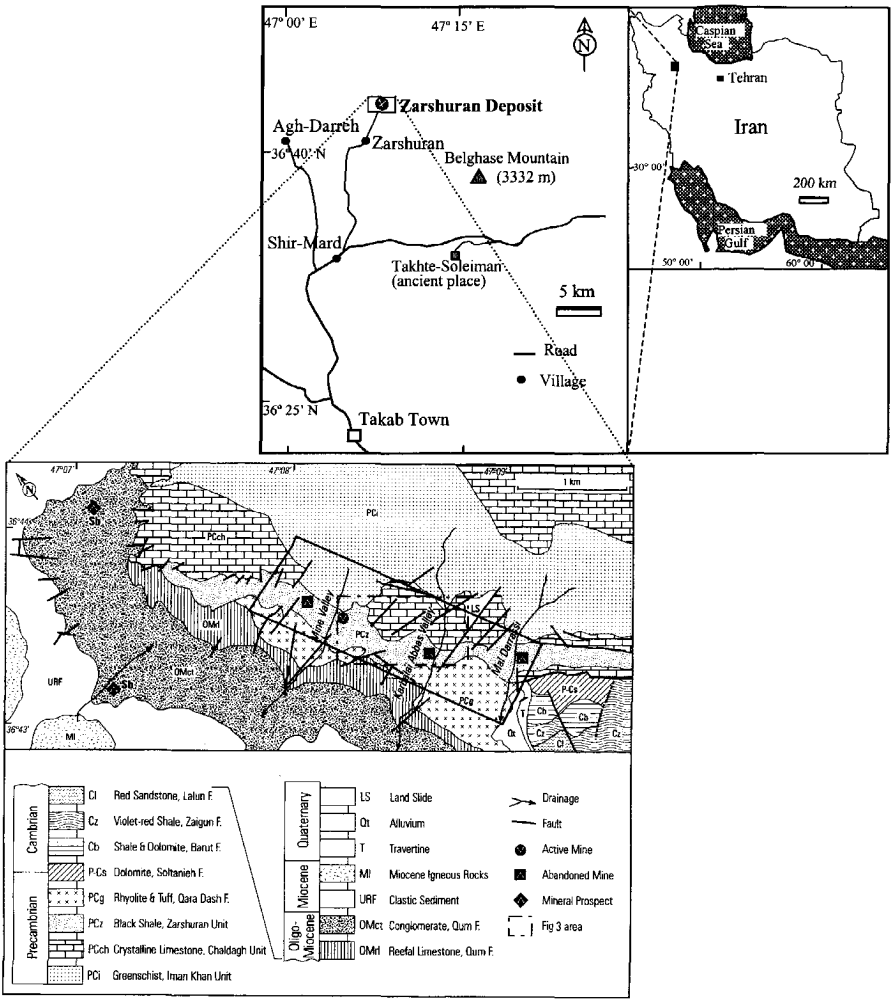

Fig. 3.1 Location and geological map of the Zarshuran district.

piles of rocks in the drainage downstream of the Zarshuran river are interpreted as a product of alluvial mining; the analysis of panned concentrate samples collected from the sediments near these alluvials revealed up to 1.5 ppm gold. In modern times orpiment and realgar have been mined for several decades on a small scale. Over the last few years an area of about 0.65 km^2 around the Zarshuran arsenic mine has been the subject of detailed geological mapping and systematic mineral exploration surveys for gold.

The principal geological features of the Zarshuran district are a late Precambrian basement high, overlain by Oligo-Miocene red beds, carbonates and acid/intermediate volcanics, through which Precambrian inliers are exposed. Shallow-dipping Quaternary

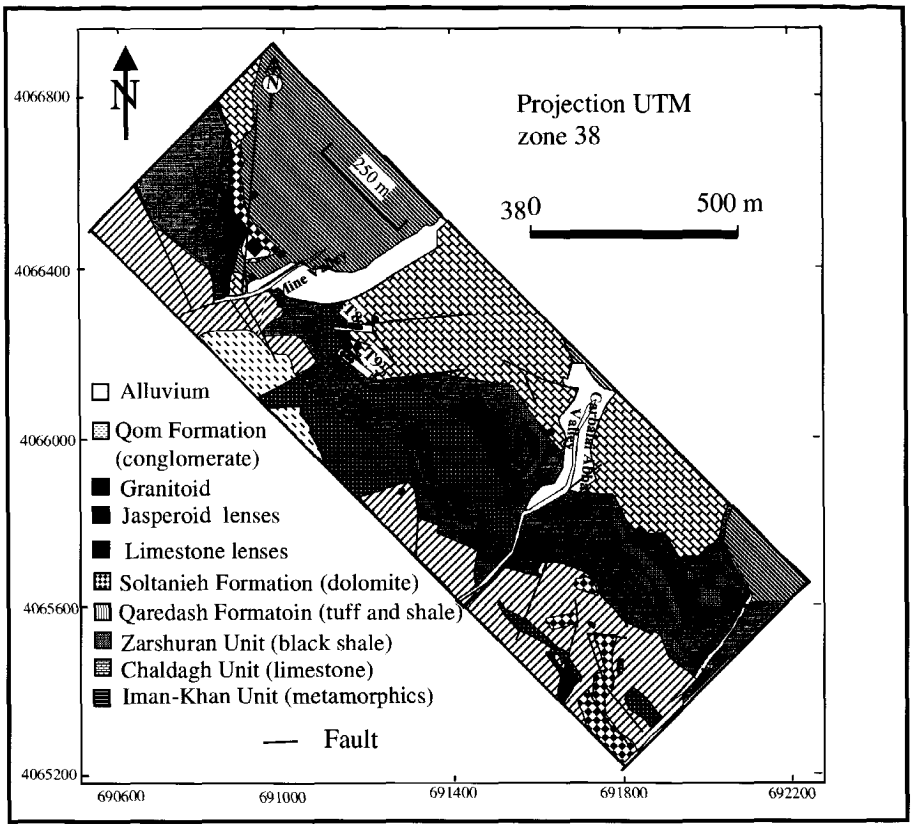

Fig. 3.2. Geological map of the Zarshuran deposit (modified after Ojaghi, 1995). The limit of this map is indicated by a box on Fig. 3.1.

travertine occurs in some places (Fig. 3.1). The stratigraphic units at Zarshuran are listed in Table 3.1 and mapped in Fig. 3.2. The oldest unit, the Iman-Khan unit, forms the core of the Iman-Khan anticline, plunging symmetrically NW-SE over some 6 km. The Iman-Khan unit mainly consists of chlorite-amphibole-schist and, locally, serpentinite. The Iman-Khan schist is followed upwards by the Chaldagh limestone, the Zarshuran black shale (with silica and carbonate intercalations) and the Qaradash shale, tuff and sandstone. An Oligo-Miocene granitoid, intruded into these Precambrian formations, is highly altered, mylonitized and weakly mineralized.

Gold occurs mainly as disseminations in carbonaceous, siliceous, and calcareous beds within the Zarshuran black shale. The main faults present at Zarshuran trend northeast-southwest and northwest-southeast in the Precambrian formation. The NW-SE trending faults are mainly marked by the juxtaposition of the Zarshuran and Chaldagh units. The NE-SW faults are mainly exposed along the valleys and intersect the mineralized host formation.

Table 3.1. Stratigraphic succession and rock types at Zarshuran.

ERA (Period)	FORMATION	DESCRIPTION
Quaternary	UNCONFORMITY	Travertine and alluvium.
Tertiary (Oligo-Miocene)	*Qom formation*	Volcano-sedimentary rocks and granitoid intrusive.
	UNCONFORMITY	
Palaeozoic (Cambrian)	*Soltanieh formation*	Crystalline dolomites with bands of chert, quartzite and shale.
	UNCONFORMITY	
Upper Proterozoic	*Qaradash unit*	Rhyolitic tuff, shale and sandstone.
	Zarshuran unit	Black shale with carbon enrichment, silicified veins and intercalations of limestone and dolomite; the main mineralized unit for gold, arsenic, antimony and mercury in the Zarshuran-Aghdarreh mining district.
	Chaldagh unit	Crystalline limestone with greyish colour and compact texture; gold-mineralized unit of secondary importance.
	Iman-Khan unit	Metamorphic rocks, including green schist, amphibolite, serpentinite and intercalations of black schist and marble; some horizons of hydrothermal alteration, including silicification and hematization.

In addition to geological mapping, systematic exploration work over Zarshuran has included geophysical and geochemical surveys and scout drilling. In a ground geophysics survey, total magnetic field intensity measurements were made by a proton magnetometer (IGS-4 Scintrex) at 10 m stations on a 50 m grid covering an area of about 1 km^2. In soil geochemistry surveys, samples were taken on two 100 x 20 m grids which together cover an area of about 9 km^2. The two grids have different orientations, *viz.*, 46° (lines 280W-90E) and 63° (lines 100E-320E). A total of 4500 soil samples were collected and analysed at the Karaj Geochemical Laboratory in Tehran, Iran, for Au, As, Sb, Ag, Tl, Hg, Cu, Pb and Zn by atomic absorption spectrophotometry (AAS). Scout drilling was also carried out at Zarshuran, and defined a possible resource tonnage of 2.5 million tonnes of ore with an average grade of 10g/t of gold (Samimi, 1992).

3.2 MODELLING DATABASE

Geological maps on a district scale (1:10,000) and deposit scale (1:2000), a topographic map at a scale of 1:2000, 19 geological cross sections on a deposit scale (1:2000) and the locations of 12 drillholes were digitized.

Data from the ground geophysical survey were captured from a contour map at a scale of 1:2000 by point digitizing UTM coordinates and total magnetic field intensity contour values along survey lines. This provides the closest approximation to the original data. The total magnetic field intensity data were gridded to provide uniform data distribution.

The soil geochemistry data were digitized by scanning. In order to facilitate subsequent processing the sample locations from the two grids were converted to UTM coordinates using a coordinate transformation option in the GIS.

The recorded parameters for bore holes included the hole number, the location (UTM coordinates), azimuth, elevation, dip and total depth. A total of 1799 assay results for Ag, As, Cu, Hg, Pb, Sb, Zn and Au were recorded in a spreadsheet. A bore hole log lithology description was also available for the research.

3.3 GEOPHYSICAL DATA ANALYSIS

Broad variations in total magnetic field intensity are potentially useful for mapping both exposed and unexposed lithologies based on their magnetic susceptibilities and hence ferrous iron contents. In particular, igneous rocks lend themselves to discrimination in magnetic data. More localized and subtler features in magnetic data often reflect the common deposition of iron minerals at discontinuities. Suitably processed magnetic data can therefore be used to map lineaments.

3.3.1 Qualitative analysis

The most striking feature of the contoured data of the ground magnetics survey at Zarshuran is the strength of the total magnetic field intensity over the Iman-Khan unit. The anomaly, of the order of 10,000 nT, generally extends in a NW-SE direction and corresponds to that seen in aeromagnetic data by Asadi and Hale (1999a), who demonstrated that the highest aeromagnetic anomalies in the Takab area are located around Zarshuran. Such large anomalies are typical of banded ironstones and serpentinites (C.V. Reeves, personal communication); the anomaly at Zarshuran is most logically attributed to serpentinized ophiolitic rocks. Elsewhere in the region, metamorphosed ophiolites have been mapped recently at the core of Iman-Khan anticline (Geological Survey of Iran, 1999).

The analytic signal of the total magnetic field intensity has the advantage of displaying magnetic information in such a way that anomalies correlate directly with causative bodies and are positioned symmetrically over them (Paterson and Reeves, 1985). The technique assumes constant directions of both the geomagnetic field and the crustal magnetization over a certain region, and the analytic signal is independent of the inclination of the magnetic field (Qin, 1994). An analytic signal image of total magnetic field intensity was created with a view to mapping igneous rocks at Zarshuran. The resulting analytic signal map (Fig. 3.3a) overlain on the geology shows that the zone that has the highest amplitude signals (purple shade) is located in the marginal part of the Iman-Khan metamorphic rocks comprising schist, amphibolite and serpentinite. This suggests one or more unexposed magnetic bodies at

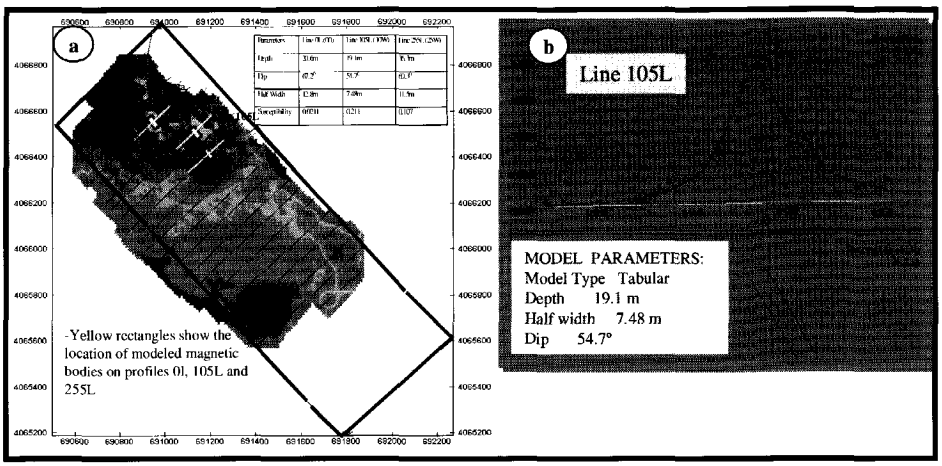

Fig. 3.3. Processed total magnetic field intensity data at the Zarshuran deposit: (a) analytic signal map overlain with Iman-Khan metamorphics (IM-Meta); (b) profile of results for quantitative modelling and inversion on survey line 105L (see also Fig. 3.3 in the colour

depth. Weak analytic signals (blue shade) are associated with Qaradash acidic volcanics and highly-altered Oligo-Miocene granitoid, both exposed in the southwest of the area.

The total magnetic field intensity data were also processed in ways aimed at revealing information about structure. Three directional (edge-enhancement) filters were applied to the total magnetic field intensity data. Maps generated with a horizontal and with a diagonal (45°) filter highlight several linear trends in a NW-SE direction, whereas a vertical filter reveals the presence of several NE-SW trending linear features. Together these images assisted identification of several NW-SE lineaments that are crosscut locally by NE-SW structures. Those interpreted lineaments that lie within the Iman-Khan unit are not recorded on the geological map, and are interpreted as fracturing and faulting within the Precambrian metamorphic rocks. This is related to a subsurface intrusion with high magnetic susceptibility or to the adjacent granitoid intrusion.

3.3.2 Quantitative analysis

Interactive magnetic anomaly modelling was used to quantify the morphology of the unexposed magnetic bodies detected on the margin of the Iman-Khan schist. The process of obtaining the "best fit" is carried out by adjusting the magnetization and geometric parameters such as depth, dip, thickness, magnetic susceptibility, main position and overall shape that are applicable to a chosen geometrical model for a magnetized body. Modelling was performed on three profiles from the area of the highest amplitude magnetic anomaly (Fig. 3.3a).

The results obtained suggest that the anomalies on all three profiles reflect the presence of a highly-magnetic body that is roughly tabular in shape, lying at an average depth of 25 m, and dipping in a northeast direction towards the core of Iman-Khan anticline. The magnetic body or bodies may be a stock or dykes with an intermediate-basic composition. The results obtained for survey line 105L are shown in Fig. 3.3b, and results for all three profiles are summarised in Table 3.2.

Table 3.2. Results of modelling and inversion of total magnetic field intensity data on three profiles at Zarshuran.

Parameters	**Line 0L (00)**	**Line 105L (10W)**	**Line 255L (25W)**
Depth	20.6m	19.1m	36.3m
Dip	67.2^0	54.7^0	60.3^0
Half Width	12.8m	7.48m	11.5m
Susceptibility	0.211	0.211	0.107

3.4 GEOCHEMICAL DATA ANALYSIS

Exploratory geochemical data analysis using statistical and spatial mapping methods was first carried out on the analytical results of all 4500 samples from the two grids covering Zarshuran and its surroundings (Ngonzi, 2000). For the research described here, a subset of the data covering the area immediately surrounding the Zarshuran deposit, and containing sample site coordinates and gold data only, was extracted and processed. This subset covers an area of around 3 km^2, surrounding the geographic limits shown in Fig. 3.2, and contains the results for 1214 samples.

3.4.1 Qualitative analysis

Data analysis, aimed at the delineation of gold-mineralized zones, was carried out using statistical and graphical methods. Statistical summaries were used to identify the number of valid (above detection limit) analyses, standard data ranges and the presence of outliers. These summaries revealed a few data entry errors which were corrected prior to further data analysis. Gold values showed a high skewness (10.25) and large differences between the arithmetic mean (842 ppb) and the median (33 ppb), indicating the presence of a log-normal distribution. Plotting of frequency histograms and cumulative probability plots confirmed the log-normal nature of the distribution and indicated the presence of at least two distinct log-normal populations (Fig. 3.4a). The inflexion point at 300 ppb was taken as a threshold value separating these two populations.

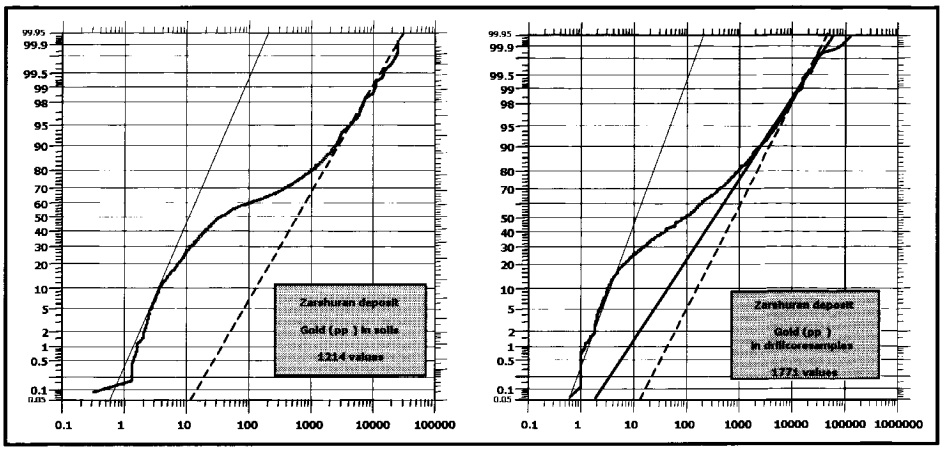

Fig. 3.4. Log-scaled cumulative probability plots for the gold distribution in: (a) soil samples; and (b) drillcore samples. Interpreted populations present are indicated by diagonal lines: thin black lines - low grade population common to both sample types; dashed lines - high grade population in soil samples; thick black line - high grade population in drillcore samples.

Grid plots of the gold values are used to indicate the spatial distribution of the two populations identified on the cumulative frequency curve. A simple three-class plot, based on the 300 ppb threshold value and 95th percentile concentration values (1500 ppb) indicates that the majority of the high-grade population samples fall within a single area corresponding with the outcrop area of the Chaldagh and Zarshuran units (Fig. 3.5a). This provides strong evidence of a significant degree of stratigraphic control on mineralization.

Contour maps of the gold values are used to identify relations between gold concentration in soil, underlying lithology and structural controls. Gold data were gridded using a quadrant search with an anisotropic search ellipse in order to avoid distortion due to the unequal sample spacing (along sample lines *versus* between sample lines). Several different gridding methods were tested in order to select the optimal approach for interpretation of geologically-related features in the data. Given the strongly-skewed distribution of gold values and the log-normal character of the two constituent populations, gridding of the natural logarithms of the gold values was eventually selected as giving the most readily-interpreted results. Anisotropic inverse distance squared weighting was applied in order to take account of a preferred continuity parallel to the NW-SE strike of the units. Various displays were used to create maps that provided the basis for data interpretation. The log-normal distribution of the data favoured a log scale of contour intervals. A colour-shaded map with closely spaced contours (Fig. 3.5b) highlights sharp discontinuities that reflect cross-cutting faults and/or geological contacts across which there are abrupt changes in gold concentrations (Fig. 3.6).

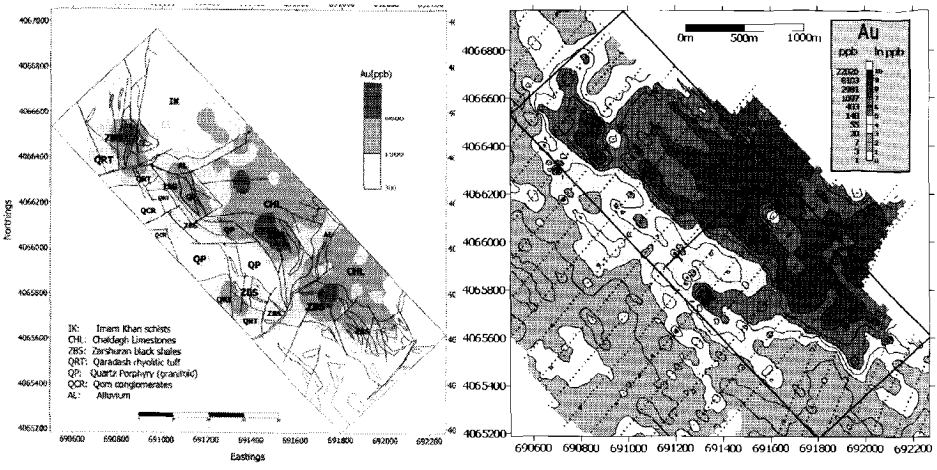

Fig. 3.5. Gold in soils at the Zarshuran deposit: (a) grid plot of three classes separated by the 300 ppb, and the 95th and 99th percentile Au concentration values, superimposed on geology; (b) colour-shaded contour plot with contours at regular log$_e$ ppb intervals (see also Fig 3.5 in the

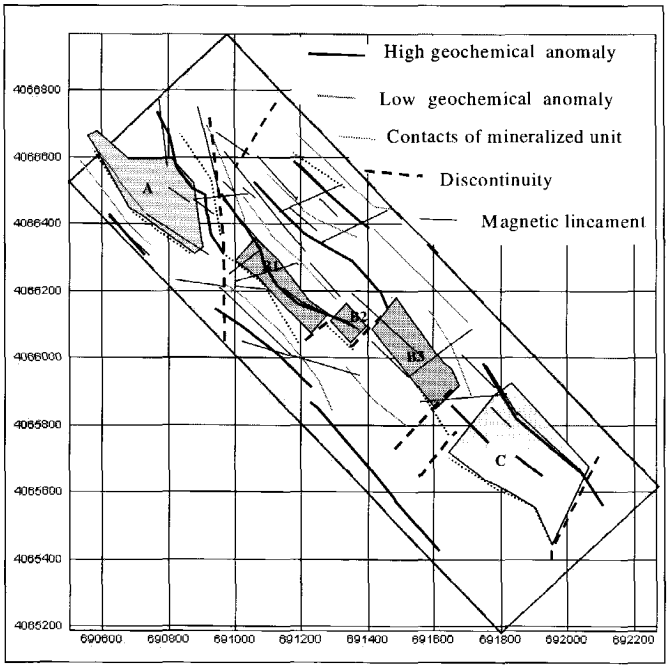

Fig. 3.6. Map showing the main soil-geochemical anomalies (A, B, C) overlaid with structural featu interpreted from gold in soils and processed total magnetic field intensity.

3.4.2 Quantitative analysis

Gold assay results from drillcore obtained from exploration drilling at Zarshuran in 1994 and 1995 were available for 12 drillholes. A comparison of the results from this limited campaign with those obtained from the more widespread soil geochemistry survey allows quantitative assessments of both how mineralization in bedrock is expressed in the soil and how the soil anomaly indicates the resource at depth.

A log-probability plot of the drillcore data again indicates the presence of two distinct populations (Fig. 3.4b). Comparison with the probability plot of the soil data (Fig. 3.4a) suggests that, whilst both data sets have more-or-less identical low-grade populations, there is a significant difference between the high-grade populations. The high-grade population in the soils has a higher average gold grade than that in the drillcore, although the two have similar variances. This is interpreted as reflecting moderate residual enrichment of gold in the soils.

The gold concentration in soil anomalies is approximately 1.5 times that in drillcore apparently corresponding to soil anomaly sources at depth. This figure is potentially useful in exploration modelling. The relationship is also used (below) to model the *in situ* gold resources in bedrock at Zarshuran.

3.5 THREE-DIMENSIONAL INTERPRETATION

3.5.1 Geology

Based on the results obtained from the interpretation of the 2D spatial data sets at Zarshuran, several important features of direct relevance to a 3D geological interpretation are identified.

- The main NW-SE stratigraphic trend is confirmed by linear anomalies identified in both the geophysical and geochemical data (Figs. 3.3a, 3.5b and 3.6).
- Several NE-SW linear features terminate or displace stratigraphic trends, and are therefore interpreted as late faults (Figs. 3.6).
- The high magnetic anomalies within the Zarshuran area arise from serpentinite, at the core of Iman-Khan anticline, and also indicate the presence, at a depth of about 25 m, of a stock or dykes of intermediate-basic composition, dipping northeast at around 60°, within or at the contact of the Iman-Khan unit (Fig. 3.3); these could have contributed energy or fluids to the mineralizing hydrothermal system.
- One of the low magnetic anomalies reflects a highly altered Oligo-Miocene granitoid, which is spatially associated with the mineralized jasperoids within the Zarshuran black

shale. This granitoid may also have contributed energy or fluids to the mineralizing hydrothermal system.

- The NW-SE magnetic anomaly, which has been modelled on line 255L, coincides with an inferred NW-SE structure identified from the geochemical data (Fig. 3.6). This may represent a previously-unmapped fault forming the western boundary of the Iman-Khan unit in this area. From the results of the quantitative geophysical modelling it is inferred to dip east at about 60°.
- Most of these deductions of sub-surface geology rest mainly on the interpretation of surface geophysical data. Any validation by means of scout drilling data is not possible, because all drillholes for which data are available are situated to the south of the main magnetic anomaly.

3.5.2 Mineral resource

Comparison of cross-sections of downhole and soil gold values highlights significant enrichment of gold in soils compared with corresponding grades in drillcore. For example the soil anomaly shown in Fig. 3.7 correlates well with the Zarshuran limestone, the mapped contact between the Chaldagh limestone and the granitoid. This profile shows a 200 m section with values in soil in excess of 1000 ppb gold, whereas in the drillhole which cuts the same units there are only four samples with values greater than 1000 ppb gold, representing a single 3 m intersection. In addition the soil geochemistry results suggest the presence of significant concentrations of gold in soils overlying the Chaldagh limestone, whereas at depth the Chaldagh limestone is not mineralized. The soil anomaly is interpreted as "smearing" of gold over units that were previously overlain by mineralized material, with gold having been concentrated in soils after erosion of their host rocks. This would account for the scarp-like topography of the main geochemical anomaly (sharp gradient on its southwest flank but gently-sloping plateau to the northeast) shown in Fig. 3.5. Calculated areas and average values of gold in soils for the main geochemical anomalies

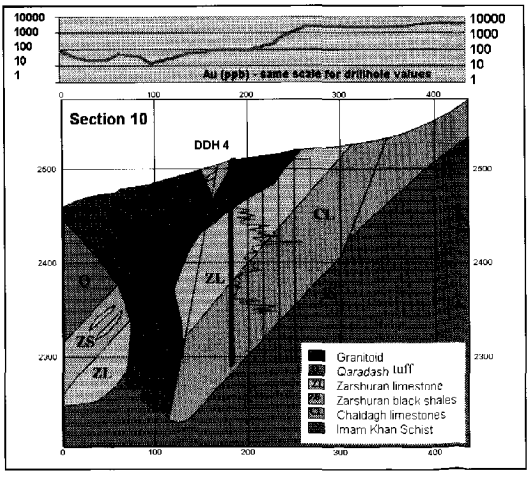

Fig. 3.7. Interpreted geology on drillhole cross-section no. 10 (see Fig. 3.5 for location), comparing drillcore gold values in drillhole no. 4 with gold values in soils (both profiles are log scaled starting at 1 ppb gold).

(Fig. 3.6) are used to predict the potential volume and grade of the resource *in-situ* in bedrock using the log-probability plots of Fig. 3.4. The results are summarized in Table 3.3.

Table 3.3. Bedrock resource potential inferred from gold anomalies in soils*.

(1) Anomaly	(2) Soils Au in ppb	(3) Soils Au ppb	(4) Rock Au ppb	(5) Area m^2	(6) Vol-100m Mm^3	(7)Vol_200m Mm^3	(8)Mass-100m Mt	(9)Mass-200m Mt
A	6.26	523	290	53125	5.31	10.62	13.28	26.55
B1	7.12	1236	800	24375	2.44	4.88	6.1	12.2
B2	7.98	2922	1970	6250	0.63	1.26	1.58	3.15
B3	7.88	2644	1890	32500	3.25	6.5	8.13	16.25
C	6.87	963	320	94375	9.44	18.88	23.6	47.2
TOTAL	**6.93**	**1201**	**840**	**210625**	**21.07**	**42.14**	**52.68**	**105.35**

*The average gold values of soil anomalies (columns 2, 3) are used to calculate *in situ* gold grades in bedrock (column 3) using the sample populations identified on the cumulative frequency plots (Fig. 3.4); anomaly areas (column 5) are used to calculate bedrock volumes to depths of 100 m and 200 m (columns 6, 7) from which the mass, or tonnage, of bedrock is calculated using a density of 2.5 t/m^3 for shales (columns 8, 9).

Table 3.4. Deposit Recognition Criteria (DRC) extracted from the spatial modelling of the Zarshuran deposit.

Geophysics	**Geochemistry**	**DRC**
Contour map and analytical signal map of the total magnetic field intensity data		Confirms NW-SE strike of Precambrian units, and indicate the presence of serpentinite associated with mineralization
	Symbol plots of >300 ppb gold population in soil confined to Chaldagh and Zarshuran units	Demonstrates stratigraphic control on mineralization
Late NE-SW faults displace stratigraphic units	Late NE-SW faults terminate geochemical anomalies	Demonstrates structural control on mineralization
- Intermediate-basic stock / dykes, dipping toward the Iman-Khan anticline, connected to a deep magma (fluid sources) - Highly-altered granitoids		Indicates igneous contribution as heat an/or fluid source for mineralization
	- One and half times enrichment of gold at surface - Value x area of gold soil anomaly indicates amount of gold in bedrock - Presence of significant concentrations of gold in soils overlying the Chaldagh limestone, which does not show significant mineralization at depth - Residual enrichment of gold led to placer deposits down stream of Zarshuran	Shows effect of weathering

3.7 CONCLUSIONS

Analysis and modelling in a 2D GIS of data for geology and total magnetic field intensity at Zarshuran allows the identification of several sub-surface geological structures likely to influence the morphology of sub-surface gold mineralized zones. Quantification of the degree of surface enrichment of gold in soils is achieved by comparison of the gold values in soils and gold assays from 12 drillholes in the same area. Based on this relationship, the size and magnitude of gold soil anomalies allows the calculation of the tonnage of *in-situ* gold mineralization present in bedrock.

Several deposit recognition criteria emerge from this investigation (Table 3.4). In particular it demonstrates the stratigraphic and structural controls on mineralization. It also indicates two possible heat and fluid sources for mineralization.

Chapter 4

PETROGRAPHY, MINERALOGY AND GEOCHEMISTRY

This chapter draws on the petrographic and mineralogic reports of Bariand (1962), Bariand et al. (1968), Karimi (1993) and Mehrabi et al. (1999) and adds descriptions of extensive original petrographic observations, geochemical analyses and mineralogical determinations. Collectively these provide data for proposing a paragenetic sequence of gold mineralizing hydrothermal solutions at Zarshuran. The chapter is an edited version of the paper entitled *Petrography, mineralogy and geochemistry of the Zarshuran Carlin-like gold deposit, NW Iran,* Mineralium Deposita, Springer, Issue 7, 35:672-682 (Asadi et al., 2000c).

4.1 INTRODUCTION

Gold mineralization at Zarshuran is hosted by Precambrian carbonate and black shale formations which are underlain by schist and are intruded by a Oligo-Miocene granitoid. A suite of 33 representative ore and rock samples was collected from these units by the author in 1996 and 1997 with the aim of characterizing their petrography, mineralogy and geochemistry.

4.2 METHODS

Observations on 17 thin sections, 5 polished thin sections and 28 polished sections were made on ore and rock samples from tunnels, trenches, bore holes and outcrops at Zarshuran (see Fig. 4.1 for sample locations). Descriptions of

Table 4.1. Descriptions of the samples used for chemical analysis, and petrographic and mineralogic studies

Sample No.	Rock Type/ Mineral	Location	Remarks
96100.	Calcite	50 m to the north of mine valley	Thin calcitic veins cutting Iman-Khan schist
96101	Iman-Khan metamorphic rocks	50 m to the north of mine valley	Green Schist, basement rock, core of Iman-Khan anticline
96102	Iman-Khan metamorphic rocks	200 m to the north of mine office	
96103	Chaldagh limestone	250 m northwest of mine office	Light grey crystalline limestone with compact texture
96104	Mylonitized Chaldagh limestone	Southeast of mine valley, close to the Tunnel 9	Brittle limestone collected at the lower contact with of the basement schist
96105	Zarshuran black shale	Karbalai-Abbas valley	Finely laminated carbon-rich shale
96106	Jasperoid	25 m to the northwest of mine office	Unmineralized carbon poor jasperoid with grey-white colour
96107	Jasperoid	150 m to the northwest of mine office	Unmineralized carbon poor jasperoid with grey-white colour
96108, 96109	Altered granitoid	Southeast of mine valley, near the bore hole No. 1	White rock containing large phenocrysts of quartz
96110	Powdery Chaldagh limestone	Southeast of mine valley, above the Tunnel 8	Sample collected on a fault zone at the upper contact with of Zarshuran Unit
96111	Alteration	Tunnel 8	Spare zones within the Zarshuran Unit
96112	Quartz veins	250 m to the northwest of mine office	Quartz veins containing barite and calcite located in the Chaldagh limestone.
96113	Oxidized quartz vein	Trench in Carbalai-Abbase valley	Fe-oxides are abundant in this rock
96114	Jasperoids	Tunnel 8	Mineralized quartz veins
96115	Jasperoids	Tunnel 8	Visible sphalerite and fluorite in hand specimen
96116	Altered granitoid	Southeast of mine valley	White rock with large quartz phenocrysts
96117	Quartz with orpiment	Tunnel 8	Mineralized rock
96118	Dense microcrystalline arsenic minerals	Tunnel 8	Arsenic ore with high gold content
96119	Crystalline arsenic mineral	Tunnel 8	Arsenic ore
96120	Carbon rich quartz veins	Tunnel 9	Carbonaceous ore with high gold content
96121	Carbon rich quartz veins	Tunnel 9	Carbonaceous ore with high gold content
96122	Carbon rich quart veins with arsenic minerals	Tunnel 8	Carbonaceous and arsenic ore
97201	Altered granitoid	Carbalai-Abbas valley	White rock with large quartz phenocrysts
97202	Quartz veins	Tunnel 8	Mineralized rock
97203	Black shale	Tunnel 8	Mineralized black shale with getchellite
97204	Quartz veins	TR2 trench, west of Carbalai-Abbas valley	Minerals are crystalline quartz, calcite and orpiment
97205	Quartz and pyrite	Tunnel 8	Visible pyrite grains taken from quartz veins
BH8-160	Mineralized limestone	160 m depth in bore hole no.8	Brittle limestone with visible pyrite grains (chemical analysis shows 20 ppm Au)
BH1-79	Black shale	79 m depth in bore hole no. 1	Finely laminated carbon-rich shale (carbonaceous ore)
BH1-135	Limestone	135 m depth in bore hole no. 10	Limestone intercalations in Zarshuran Unit
BH10-85	Limestone and As minerals	85 m depth in bore hole no. 10	Mineralized sample

the hand specimens from which these sections were prepared are given in Table 4.1. Petrographic and mineralogic examinations were carried out at the Department of Applied Earth Sciences of Delft University of Technology and

at the International Institute for Aerospace Survey and Earth Sciences, Delft, Netherlands.

Petrography was determined by optical examination of thin sections and polished thin sections using transmitted light microscopy, supported by recalculation of the compositions of representative host rock samples determined by total rock analyses by X-ray fluorescence and atomic absorption spectrophotometry, carried out at the Geological Survey, Teplice, Slovakia (Table 4.2). X-ray diffraction analyses with a Philips PW3710 X'pert system, Cukα X-ray radiation (λ= 1.5418) and a Ni filter were used to confirm the

Table 4.2. Total analysis and trace element analysis of representative host rocks at Zarshuran (in weight percent, except as stated)

Sample No.	**96103**	**BH1-135**	**BH1-79**	**96114**	**96108**	**96116**
SiO2	0.69	1.76	36.60	91.8	76.11	78.62
CaO	54.15	53.32	25.40	0.35	1.48	0.67
Al2O3	0.21	0.34	5.65	2.3	17.10	15.06
Fe2O3,FeO	0.28	0.84	4.16	0.85	1.16	1.32
MgO	0.47	0.56	0.97	0.06	0.24	0.30
Na2O	0.02	0.04	0.06	0.01	0.2	0.06
K2O	0.04	0.06	1.41	0.30	2.26	2.19
MnO	0.002	0.071	0.118	0.02	0.083	0.055
TiO2	0.01	0.02	0.77	0.02	0.14	0.24
P2O5	0.03	0.02	0.06	0.12	0.37	0.42
SO3	0.03	0.05	0.38	0.25	0.16	0.22
CO2 Total	43.65 100.01	42.46 100.10	23.35 100.45	0.16 100.09	0.53 100.15	0.20 100.14
		Trace	***Element***	***Analysis***		
Au (ppm)	0.16	0.36	9.57	2.42	0.15	0.14
As	0.25	0.12	0.06	3.22	0.08	0.04
Ag (ppm)	< 0.2	0.2	0.4	3.2	0.25	0.2
Sb	0.002	0.032	0.007	0.029	0.004	0.003
Te (ppm)	< 0.5	1.0	< 0.5	18.1	< 0.5	< 0.5
Tl (ppm)	1.3	1.6	20.5	8.0	2.3	1.4
Hg (ppm)	4.45	4.53	26.14	62.6	5.2	3.060
Zn	0.272	0.1	0.055	0.103	0.05	0.064
C	nd	nd	7.38	1.84	nd	nd
S	0.46	0.61	1.91	4.9	0.85	0.63

nd= not determined

identity of alteration minerals. A reflected light optical microscope was used for initial examination of polished sections and polished thin sections and mineral identifications were made with the aid of the so-called Delft System (Kühnel et al., 1980; Glass and Voncken, 1996). Qualitative criteria (colour, pleochroism, internal reflection, polishing hardness, shape and form) and estimated quantitative features (anisotropy, reflectance and Vickers microhardness) were used for mineral identification.

The compositions of selected minerals were determined on carbon-coated polished sections using a Jeol electron probe microanalyser (JXA-8800M) in qualitative, quantitative and X-ray scanning modes. The instrument is fitted with three wavelength dispersive spectrometers and with sets of LDE1/TAP and PET/LIF analysing crystals. Standards used for instrument calibration included native gold, iodyrite for silver, galena for lead and sulphur, sphalerite for zinc, marcasite for iron, cinnabar for mercury, a synthetic GaAs (gallium arsenide) compound for arsenic and Sb_2Te_3 for antimony and tellurium. Counting times for the concentrations of major elements were 20 to 50 seconds using an accelerating voltage of 20 KV and a beam current of 2 x 10^{-8} A. Analysis for gold was made with a counting time of 300 seconds on peak and background using an accelerating voltage of 40 KV and a beam current of 4 x 10^{-8} A, giving a detection limit of about 20 ppm. Details of Au-trace analysis by microprobe can be found in chapter 5. Atomic concentrations of elements and the number of atoms in the mineral formula were used to determine mineral compositions; computer software calculated the stoichiometry of each mineral.

4.3 PETROGRAPHY OF THE MINERALIZED FORMATION

The Zarshuran deposit is underlain mainly by rocks of Precambrian age. The oldest unit, the Iman Khan metamorphic rocks, is followed upwards by the Chaldagh limestone and the Zarshuran black shale, which contains up to 7.38% carbon. An Oligo-Miocene granitoid, intruded into the mineralized Precambrian formations, is highly altered and mylonitized (Fig. 4.1).

The lowermost unit in the area, the Iman Khan schist, is mainly chlorite-amphibole-schist (Table 4.1; sample 96101) and serpentinite (sample 96102). These metamorphic rocks are locally cut by carbonate veins (sample 96100).

The Chaldagh limestone is mainly composed of anhedral to subhedral calcite and dolomite (0.05-0.8 mm). It has a compact mosaic texture and light-grey colour imparted by traces of organic matter (sample 96103). The texture is locally laminated due to variations in carbon content. Pyrite, iron oxides,

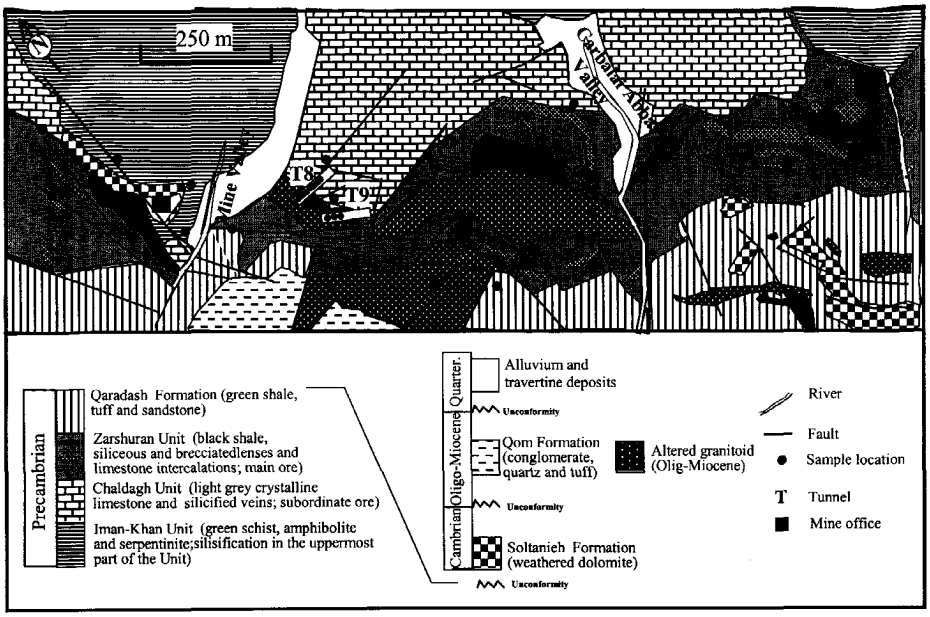

Fig. 4.1. Geology of the Zarshuran deposit (modified after Ojaghi, 1995); see also Fig. 4.1 (a-c) in colour figures.

barite and quartz are disseminated in the carbonate matrix. At its base the limestone grades into calc-schist which is strongly mylonitized and shows evidence of hydrothermal mineralization; calcite and dolomite are partially dissolved and replaced by silica (Fig. 4.2).

The finely laminated Zarshuran black shale comprises 45-55% calcite, 25-35% quartz (0.1-0.2 mm), 5% dolomite, 5-10% micaceous minerals, <3% opaque minerals, mainly pyrite, zircon and rutile, and ~ 1% detrital potassium feldspar (Fig. 4.3). The calcite and dolomite are partially replaced by silica. The shale owes its colour to the presence of a substantial amount of organic matter (sample BH1-79). The shale contains jasperoid lenses and dolomitic limestone intercalations in which the dolomite and calcite have a granoblastic texture and which contain minor iron oxides and disseminated opaque minerals such as pyrite, sphalerite and galena (samples BH1-135, BH10-85).

The granitoid dyke or stock contains large phenocrysts of quartz in a white cryptocrystalline groundmass. Its mineral composition is 40-45 vol. % quartz (50 μm-8 mm), 10-15 vol. % sericitized feldspars (40 μm-0.1 mm) and < 5% elongated mica and opaque minerals in a matrix of fragmented quartz and sericite (40-45 vol. %). On the basis of the fragmented nature of much of the quartz, its very strong undulous/wavy extinction (Fig. 4.4) and its close contact with some of the sericitized feldspar, the granitoid can be described as



Fig. 4.2. Photograph of Chaldagh limestone (ca, calcite) replaced by hydrothermal quartz (qz), (Sample 96104). Width of the picture is 0.35 mm.

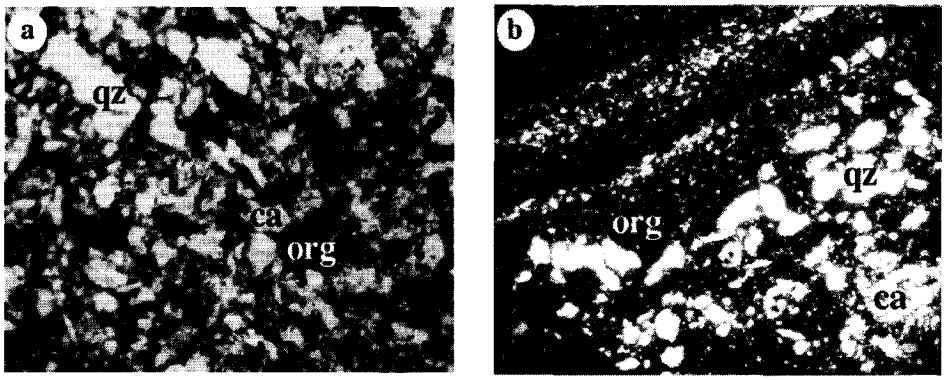

Fig. 4.3. Photographs of black shale: (a) angular quartz grains (qz, bright), calcite (ca, white-grey) and hydrocarbons (org, dark seams), (b) concentration of quartz grains and flooding of hydrocarbons along bedding (Sample BH1-79). Width of each photograph is 0.35 mm.

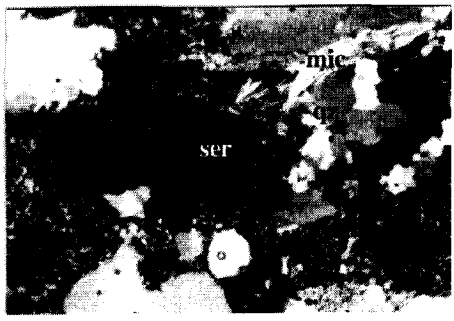

Fig. 4.4. Strongly altered granitoid rock with quartz (qz) showing undulatory extinction, sericite matrix (ser) and elongated mica (mic) (Sample 96109). Width of the photograph is 0.55 mm.

mylonite or an ultramylonite. Analysis by XRD revealed the presence of kaolinite and qualitative electron microprobe analyses revealed the presence of pyrite, cinnabar, iron oxides, mica and accessory minerals such as zircon, apatite and xenotime, some of which occur within very small fractures in sericite. Whole rock analysis showed an average of 77.36% SiO_2, 16.1% Al_2O_3, 2.23% K_2O, 1.24% (Fe_2O_3+FeO) and 1.1% CaO (samples 96108, 96116, Table 4.2). The mineralogic and geochemical data suggest that the parent granitoid was probably a quartz porphyry.

4.4 MINERALIZATION

Mineralization at Zarshuran occurs in the Zarshuran black shale and Chaldagh limestone, extending in a north-northwest direction over some 6 km along the southeastern flank of the Iman-Khan anticline. The highly mineralized zone, which extends over about 1 km, dips approximately 45° to the southwest and is intersected by two sets of high angle faults trending NW-SE and E-W (Fig. 4.1). The Iman Khan schist is only weakly mineralized over a few metres at its upper contact with the Chaldagh limestone. In the Chaldagh limestone gold is concentrated in quartz veins up to 3 m wide and cross cutting veinlets that occur throughout the Chaldagh limestone. The limestone also contains disseminated mineralization over about 10 m at its lower contact with the schist and at its upper contact with the Zarshuran unit. Gold is disseminated through the 5-75 m thick Zarshuran black shale, with the richest mineralization occurring in calcareous, carbonaceous and siliceous intercalations and veins.

Mineralization is accompanied by silicification. Quartz veins occupying the NW-SE and E-W high angle faults cut the mineralized formations and quartz partially replaces carbonates. The quartz veins in the Chaldagh limestone contain cross-cutting barite and microscopic pyrite, arsenian pyrite, sphalerite and iron oxides (sample 96112). The mineralized quartz veins and jasperoid lenses in the Zarshuran black shale contain arsenic-antimony sulphides, pyrite, arsenian pyrite, base metal sulphides, lead-sulphosalts, barite, fluorite and iron oxides. The altered granitoid is weakly mineralized and closely associated with the mineralized jasperoid lenses in the Zarshuran black shale.

About 30 sulphide minerals and sulphosalts have now been identified at Zarshuran. Those recognized by Bariand (1962), Bariand et al. (1968), Karimi (1993) and Mehrabi et al. (1999) are included in Table 4.3 along with those now identified for the first time and described below.

Table 4.3. Alphabetic List of minerals identified so far in the Zarshuran gold deposit

Mineral	Composition	Reference I	Method II	Abundance III
Aktashite(*)	$Cu_6Hg_3As_4S_{12}$	4	EPMA	R
Apatite	$Ca_5(PO_4)_3(OH,F,Cl)$	1,3,4	EPMA	R
As/Sb oxides	As_2O_3 , Sb_2O_3	1,2,4	EPMA	R
Baumhauerite(*)	$Pb_3(As)_4S_9$	4	EPMA	R
Barite	$BaSO_4$	1,2,3,4	EPMA, M	C
Boulangerite(*)	$8[Pb_5Sb_4S_{11}]$	1,2,4	Re	R
Calcite	$CaCO_3$	1,2,3,4	EPMA,M, F	C
Chalcopyrite	$CuFeS_2$	1,2,3,4	M	R
Christite (uncertain)	$TlHgAsS_3$	4	EPMA	R
Cinnabar	HgS	1,2,3,4	EPMA, M	R
Coloradoite	HgTe	4	EPMA, M	R
Covellite	CuS	1,3	Re	R
Dolomite	$(Ca,Mg)CO_3$	1,2,3,4	M, EPMA	C
Fluorite	CaF_2	1,2,3,4	EPMA, M	A
Galena	PbS	1,2,3,4	EMPA, M	R-S
Galkhaite	$[(Hg,Cu,Zn,Tl,Fe)_6(Cs,Tl)(As,Sb)_4S_{12}]$	3	Re	R
Geocronite (*)	$Pb_5(As, Sb)_2S_8$	1,3,4	EPMA, M	R
Getchellite	$AsSbS_3$	1,2,3,4	EPMA, M	R
Goethite	FeO(OH)	1,2,3,4	F	C
Gold	Au	2,3,4	EPMA, M	R
Gypsum	$CaSO_4.2H_2O$	1,2,3,4	F	C
Illite	$KAl_4[Si_4O_{10}](OH)$	1,2,3,4	XRD	
Jarosite	$KFe_3(SO_4)_2(OH)_6$	1,2	Re	
K-Feldspar	$KAlSi_3O_8$	1,2,3,4	EPMA, M	C
Kaolinite	$Al_4[Si_4O_{10}](OH)$	1,2,3,4	XRD	C
Kermesite	Sb_2S_2O	1,2	Re	
Lautite	(Cu,As,Fe)S	3	Re	R
Limonite	$FeO(OH).nH_2O$	1,2,3,4	F	C
Lorandite	$TlAsS_2$	1,2,3,4	XRD	R
Marcasite	FeS_2	1,2,3,4	M	R
Melnikovite	FeS1-2	1,2,4	EPMA, M	R
Metacinnabar	(HgFeZn)S	1	Re	
Orpiment	As_2S_3	1,2,3,4	EPMA, M	A
Plagionite(*)	$Pb_5Sb_8S_{17}$	4	EPMA	R
Pyrite	FeS_2	1,2,3,4	EMPA, M	A
Pyrrhotite	$Fe_{1-x}S$	1,2	Re	R
Quartz	SiO_2	1,2,3,4	EPMA, M	C
Realgar	AsS	1,2,3,4	EPMA, M	S
Rutile	TiO_2	1,3,4	EPMA	R
Scorodite	$(Fe,As)O_4.2H_2O$	1,2,3	Re	
Semseyite(*)	$(Pb_9Sb_8S_{21})$	4	EPMA	R
Sericite	$K_2Al_4[Si_6Al_2O_{20}](OH\ F)_4$	1,2,3,4	M	C
Simonite	$(TlHgAs_3S_6)$	3	Re	R
Sphalerite	ZnS	1,2,3,4	EPMA, M	S
Stibnite	Sb_2S_3	1,2,3,4	EPMA, M	S
Twinnite(*)	$Pb(As, Sb)_2S_4$	4	EPMA	R
Xenotime	YPO_4	3,4	EPMA	R
Zircon	$ZrSiO_4$	3,4	EPMA	R

(I). 1=Bariand (1962, 1965), 2=Karimi (1993), 3= Mehrabi et al. (1999) and 4=present study. (II) EPMA= Electron Probe Micro Analysis, M= polarizing microscope, F= field observation, XRD= X-ray Diffraction, Re= reported. (III) C= common A= abundant, S= subordinate, R= rare. (*) : mineral phase discussed in chapter 6.

Pyrite is one of the most abundant sulphides associated with ore and gangue minerals in the Zarshuran black shale and the Chaldagh limestone. Both diagenetic and hydrothermal pyrites are present. Diagenetic pyrites lack gold and arsenic in their composition, and occur as euhedral to subhedral crystals (<0.1 mm), mainly along the bedding planes in the Zarshuran black shale unit, and as minor framboidal aggregates typically a few micrometers, but in some cases up to several tens of micrometers in diameter. In the unmineralized parts of the Chaldagh limestone, diagenetic pyrite occurs mainly as isolated framboidal aggregates and as disseminated crystals of ~5 μm in size.

In the mineralized parts of the Zarshuran and Chaldagh formations, hydrothermal pyrite has different modes of occurrence. Pyrite that is anhedral is relatively pure and in some cases has inclusions of pyrrhotite (Karimi, 1993). However, the principal mode of occurrence is disseminated euhedral to subhedral crystals in quartz (Fig. 4.5a) and, less commonly, in fluorite, barite, calcite, sphalerite, and arsenic and antimony minerals. High resolution optical microscopy and electron microprobe analyses show that some of the large grains of euhedral pyrite (5-300 μm) have a zoning of arsenic, mercury, antimony and gold (Fig. 4.5b, 4.6c). An arsenic-rich zone (up to 6.5% As) appears brighter on a back-scattered image than pyrite of low arsenic content (Fig. 4.5d, 4.6e). Often surrounding zoned pyrite are network and massive arsenian pyrite, which are considered to be late hydrothermal pyrites. Some pyrite has a colloform texture and contains up to 4.5% As (Fig. 4.5f). This colloform arsenian pyrite is intimately intergrown with massive and colloform sphalerite. The arsenian pyrites are directly associated with gold mineralization.

In altered granitoid, hydrothermal pyrite occurs as very fine grains (<1 μm) precipitated along the quartz grain boundaries, in fractures in quartz and on the surfaces of clay minerals (Fig. 4.6a). The pyrite precipitated along the quartz grain boundaries has the appearance of veinlets when viewed at low magnification. This pyrite occurs in close association with grains of cinnabar.

Anhedral grains of marcasite (20-50 μm) occur in minor quantities in close association with pyrite in the mineralized black shale. Although Oberthur et al. (1997) interpret marcasite as a primary constituent of ores precipitated during the waning stages of hydrothermal mineralization, its mode of occurrence and interrelations at Zarshuran suggest that it is a supergene alteration product replacing pyrite.

Sphalerite is the most abundant base metal sulphide. It occurs in jasperoids and black shale in one of two habits. Anhedral grains (<1 mm), intimately intergrown with galena (Fig. 4.6b) and lead-sulphosalts, are found in association with pyrite; in places pyrite inclusions (2-3 μm) occur in

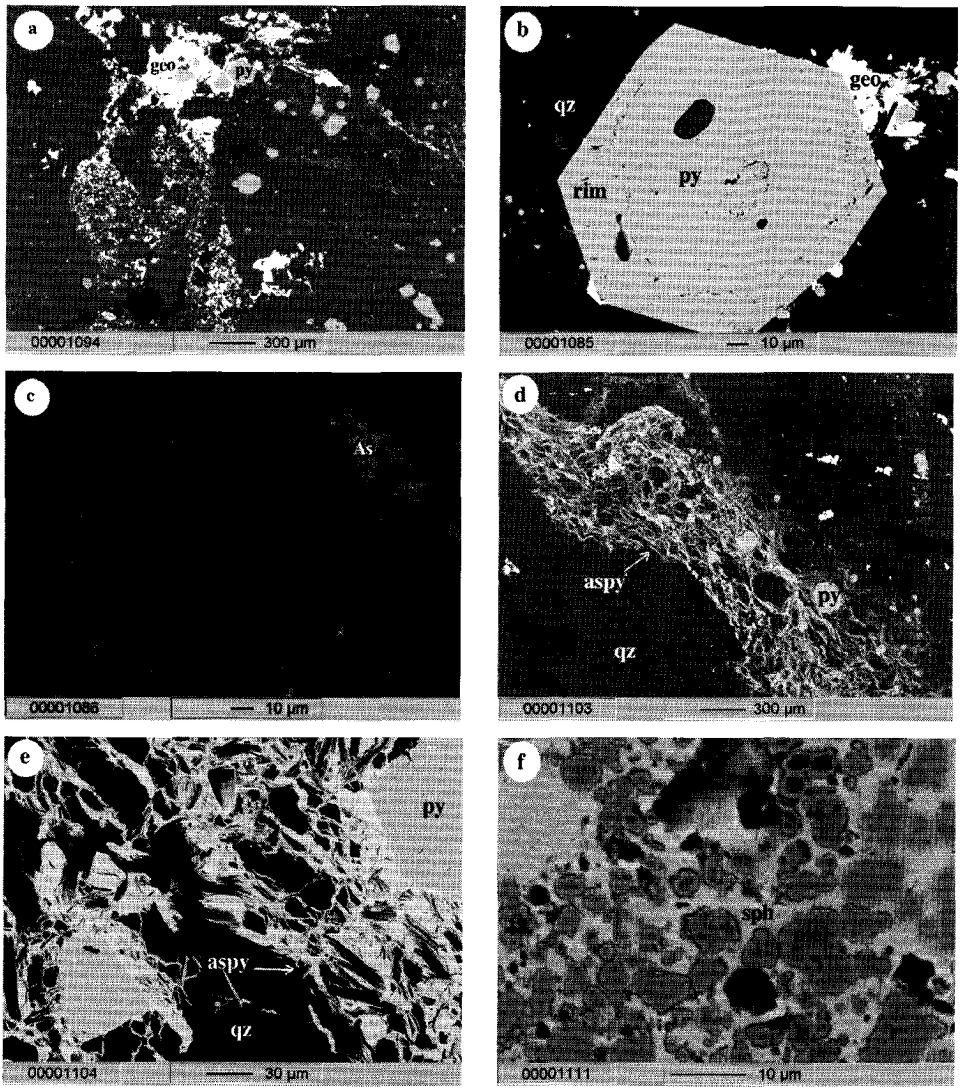

Fig. 4.5. Back-scattered electron micrographs of pyrite and arsenian pyrite in the quartz matrix: (a) overview of disseminated pyrite (py, light grey), replaced by geocronite (geo, white); (b) detailed disseminated pyrite showing zoned texture, white mineral around the pyrite is geocronite (geo); (c) X-ray image of zoned pyrite showing the As concentration in bright colour; (d) overview network arsenian pyrite (aspy); (e) detailed network arsenian pyrite and zoned pyrite; (f) Colloform arsenian pyrite or melnicovite (mel, grey) surrounded by massive sphalerite (sph, white grey). Samples 96117, 96115 and 96114.

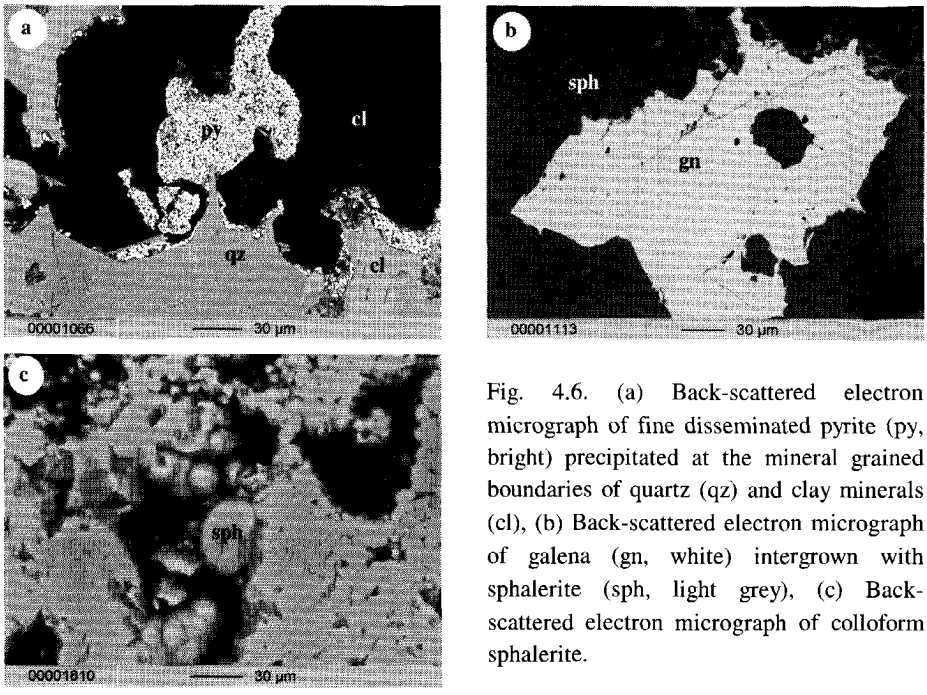

Fig. 4.6. (a) Back-scattered electron micrograph of fine disseminated pyrite (py, bright) precipitated at the mineral grained boundaries of quartz (qz) and clay minerals (cl), (b) Back-scattered electron micrograph of galena (gn, white) intergrown with sphalerite (sph, light grey), (c) Back-scattered electron micrograph of colloform sphalerite.

sphalerite. Massive and colloform sphalerite is associated with quartz, orpiment, stibnite and colloform arsenian pyrite, and less commonly with carbonate, barite and fluorite (Fig. 5f and 6c). Electron microprobe analyses indicate substantial amounts of gold in colloform sphalerite. Details on mode of occurrences of gold at Zarshuran are given in Chapter 5.

Other base metal sulphides at Zarshuran are galena and chalcopyrite. Galena is rare and often intergrown with sphalerite (Fig. 4.6b), closely associated with lead-sulphosalts and pyrite within a quartz matrix. It occurs in patches, as subhedral and anhedral grains (20-300 µm). Pyrite inclusions (2-3 µm) are occasionally observed in galena. Chalcopyrite is also rare but occurs as a few anhedral crystals (10-250 µm) in close association with pyrite in silicified rocks.

Orpiment (As_2S_3) is the most abundant sulphide at Zarshuran and the main arsenic ore mineral (Fig. 4.1b). It occurs in small veins, veinlets, fracture fillings and lenses (up to 3 m) within silicifed black shale as massive and coarsely crystalline aggregates of flaky crystals which are randomly oriented and partly deformed (Fig. 4.7a). The orpiment typically contains antimony and tellurium (Fig. 4.7b, 4.7c, Table 4.4); electron microprobe analyses revealed up to 0.24% Te and 9% Sb. Antimony probably substitutes for arsenic

Table 4.4. Average microprobe analysis (wt %) in orpiment, realgar, stibnite and getchellite minerals showing As/Sb variations and Te content

Mineral	As	Sb	S	Te (ppm)	Total	N	Empirical Formula
Orpiment	57.25	4.71	38.70	870*	100.66	16	$As_{1.94}Sb_{0.12}S_{2.98}$
Realgar	71.97	0.004	27.81	133	99.80	3	$As_{1.02}S_{0.98}$
Stibnite	3.97	67.57	29.07	0.00	100.61	4	$Sb_{1.84}As_{0.17}S_{2.95}$
Getchellite	24.14	42.43	33.07		99.64	4	$As_{0.98}Sb_{0.99}S_{3.03}$

N= number of analyses, * N = 13

(Dickson et al., 1975; Radtke et al., 1973). Massive orpiment contains inclusions of pyrite, thallium-bearing minerals, stibnite (Fig. 4.7d) and minute grains of metallic gold which can be seen by optical microscopy (Fig. 4.8) but remain undetected by quantitative electron microprobe analyses with a 20 ppm detection limit. Coarsely crystalline orpiment has inclusions of coloradoite aggregates and anhedral arsenian pyrite. Many of the other ore minerals are commonly associated with orpiment.

Realgar (AsS) is a subordinate arsenic mineral (<5%), occurring as anhedral crystals associated with orpiment, from which it can be differentiated by slightly lower reflectance, more pronounced bi-reflectance, greyer colour and intense red internal reflections. Realgar crystals in the Zarshuran black shale are often deformed (Fig. 4.7c). They contain traces of tellurium but, compared with orpiment, little antimony (Table 4.4).

Stibnite (Sb_2S_3) is found as irregular grains, needles (<50 μm) and needle-shaped aggregates within the orpiment matrix and is in places replaced by massive orpiment (Fig. 4.7d, 4.7e). It also occurs as inclusions in orpiment, getchellite and sphalerite. Inclusions of pyrite and sphalerite are found within stibnite aggregates. Electron microprobe analyses of stibnite grains yielded an average of 3.97 wt. % As, probably precipitated as solid solution (Dickson et al., 1975) or present as very fine grains of arsenic minerals (Table 4.4).

Rare getchellite ($AsSbS_3$) is closely associated with quartz, carbonate, stibnite and twinnite (Table 4.4). Inclusions of pyrite and fine lamellae of twinnite are found in the matrix of deformed getchellite (Fig. 4.9a) and elongated crystals of getchellite intersect the dark grey silicifed limestone host rock (Fig. 4.9b). Getchellite is formed when the arsenic-antimony ratio in the hydrothermal solution reaches 1:1 (Bariand et al., 1968).

Lorandite ($TlAsS_2$) was detected by X-ray diffraction analysis of massive orpiment. Another thallium-bearing mineral, suspected to be christite,

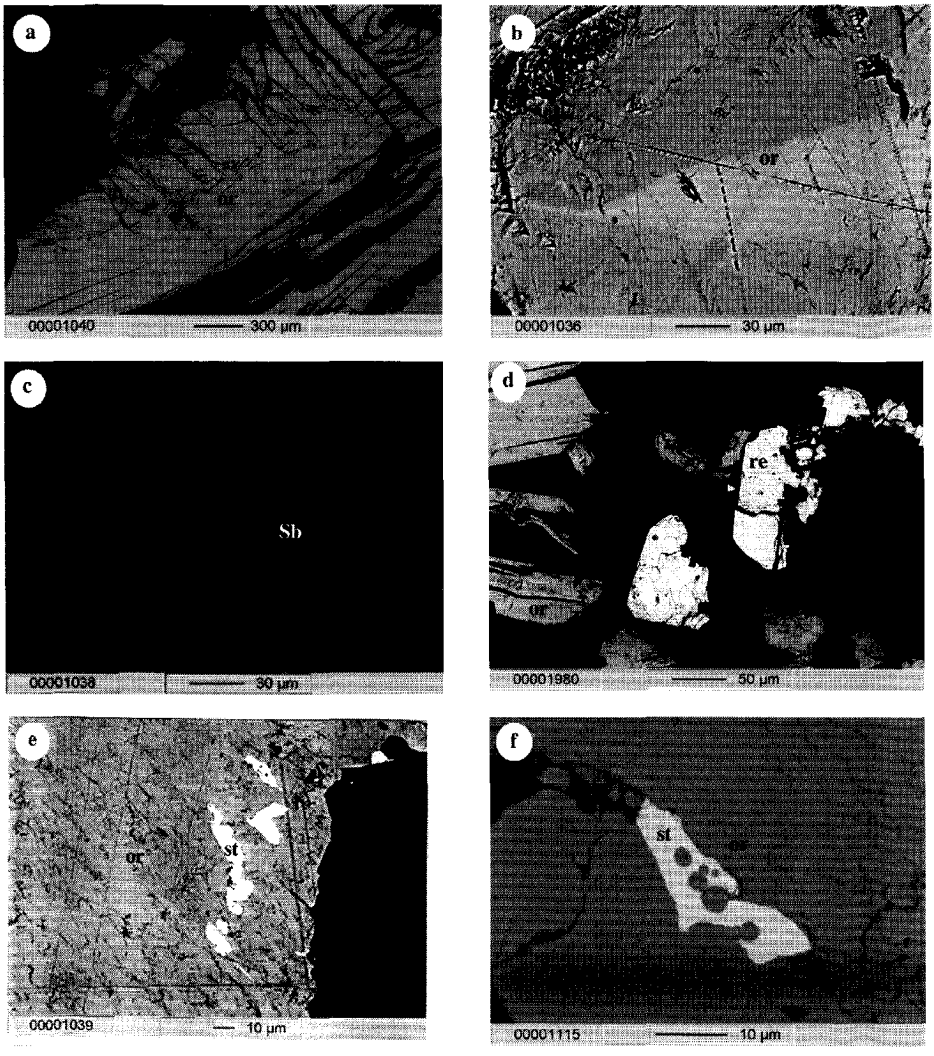

Fig. 4.7. Back-scattered electron micrographs of Orpiment, realgar and stibnite: (a) deformed orpiment crystal (or, grey); (b) massive microcrystalline orpiment, bright zone contains higher Sb as shown on X-ray image (map c); (d) realgar aggregates occurring with orpiment in the carbon rich quartz matrix; (e) stibnite grains (st, white) occurring in microcrystalline orpiment; (f) detailed stibnite (st, white-grey) replaced by orpiment. Samples: 96118, 96119 and BH1-79.

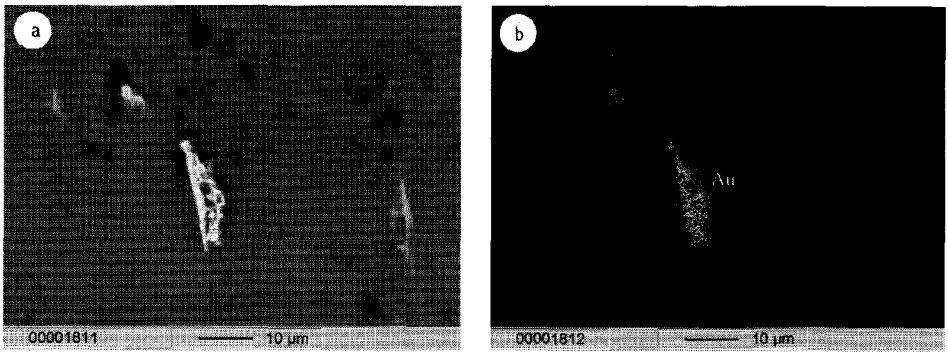

Fig. 4.8. Scarce native gold at Zarshuran: (a) back-scattered electron micrograph of dendritic gold grain in microcrytalline orpiment matrix; and (b) corresponding X-ray image showing Au concentration.

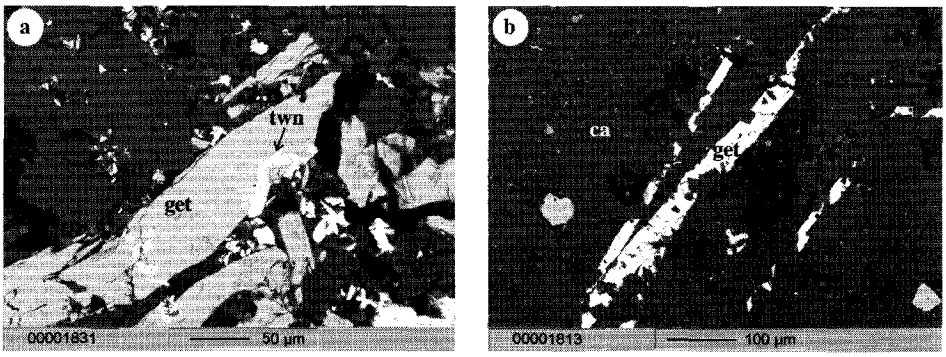

Fig. 4.9. (a) Back-scattered electron micrograph of elongated and foliated getchellite (get, white) intersecting the carbonate minerals, (b) needle inclusions and lamellas of twinnite occurring in getchellite. Samples 97203.

($TlHgAsS_3$) was observed (by back-scattered electron imagery) in massive orpiment as bright needle-shaped inclusions, too small (<5 µm) to be analysed quantitatively (Fig. 4.10). The X-ray images and spectrum of this mineral are presumed to correspond with those of christite. Christite is a very rare mineral, and was first recognized at the Carlin gold deposit (Radtke et al., 1977).

Cinnabar is a minor mineral at Zarshuran, mainly encountered in the highly altered and mylonitized granitoid. Trails of cinnabar inclusions (<2 µm) and anhedral grains (<15 µm) are located along quartz grain boundaries and in close association with argillic alteration (Fig. 4.11). Karimi (1993)

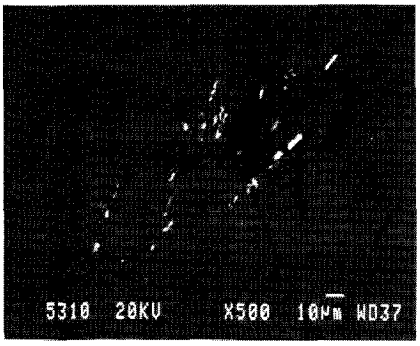

Fig 4.10. Back-scattered electron micrograph of oriented needles of the mineral assumed to be christite (bright needles) occurring in orpiment matrix. Sample 96118.

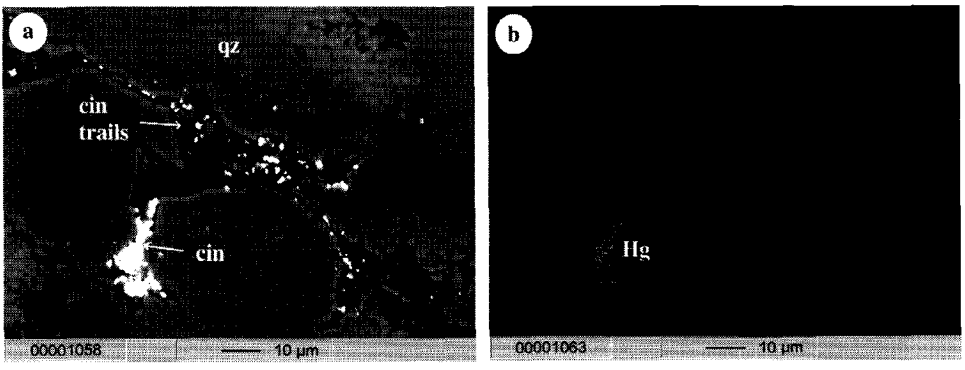

Fig. 4.11. (a) Back-scattered electron micrograph of accumulation of fine inclusions (cin, bright) and trails of cinnabar (cin. trails, bright) precipitated along the mineral grained boundaries of quartz (qz, grey) and clay minerals (cl, dark grey and light grey), (b) Corresponding X-ray image showing the Hg concentration in cinnabar. Sample 97201.

Table 4.5. Stoichiometry of coloradoite

	Analysis 1 atom %	**Analysis 2 atom %**	**Analysis 3 atom %**	**Analysis 4 atom %**	**Analysis 5 tom %**	**Average atom %**
Hg	49.41	49.27	49.23	49.00	48.65	49.11
Te	49.93	50.08	50.03	50.31	50.46	50.16
Total	**99.34**	**99.35**	**99.25**	**99.31**	**99.11**	**99.27**
No. atoms in formula	2	2	2	2	2	2
Hg	0.99	0.99	0.99	0.99	0.98	0.99
Te	1.01	1.01	1.01	1.01	1.02	1.01

Average analytical formula: $Hg_{0.99}Te_{1.01}$
Ideal formula: HgTe

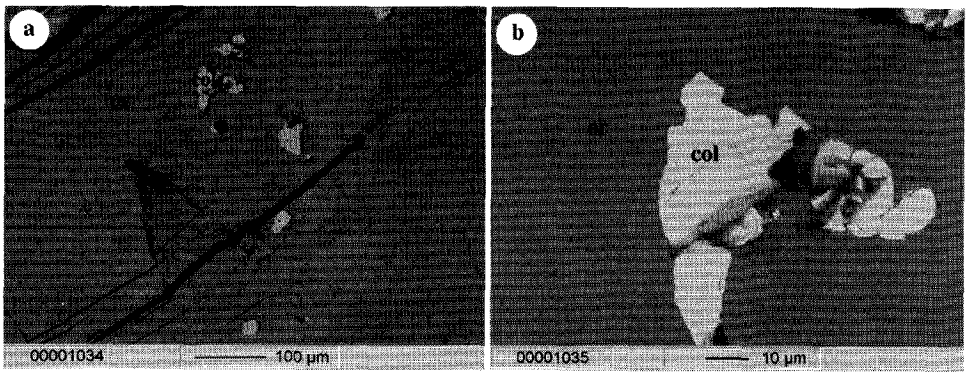

Fig. 4.12. Back-scattered electron micrographs of coloradoite grains (col, white) in orpiment matrix: (a) overview image and (b) detail image. Sample 96119.

mentions metallic gold in cinnabar at Zarshuran, but microprobe analyses of several cinnabar grains failed to confirm this.

Coloradoite (HgTe) is the only telluride so far identified at Zarshuran (Table 4.5). It is found as rare patches of fine diamond-like grains (<50 µm) in coarsely crystalline orpiment (Fig. 4.12a, 4.12b).

4.5 ALTERATION

Three types of hydrothermal alteration have been identified at Zarshuran; decalcification, silicification and argillization. There has also been a late oxidation and acid leaching event.

The calcite and dolomite in both black shale and limestone intercalations are replaced to varying degrees by hydrothermal silica, in extreme cases forming jasperoid with up to 95 vol. % of cryptocrystalline quartz. Unmineralized jasperoids occur as white siliceous lenses (samples 96106, 96107) and mineralized jasperoids occur as grey siliceous lenses and veins (samples 96114, 96117, 96120, 96121, 96122, 97202, 97204, 97205).

Decalcification, a partial replacement of carbonate by silica, is conspicuous in a fault zone at the contact of the Chaldagh limestone and Zarshuran black shale, where a powdery limestone has been formed (sample 96110). It is also found in the carbonate horizons of the black shale.

Silicification is the most widespread alteration at Zarshuran and is attributed to neutralization of acidic silica-rich solutions by carbonates accompanied by precipitation of silica in voids; subsequently the precipitated silica recrystalized into chalcedony and quartz. The intensity of silicification varies from weak to the total replacement of the original rock by jasperoid. It

is best developed in the Zarshuran black shale, where there are jasperoid veins and lenses. The Chaldagh limestone is locally silicified along faults and fractures. Highly altered granitoid and carbonate at the contact of the Chaldagh limestone and Zarshuran black shale, and near an E-W trending fault, also shows a siliceous alteration. Massive cryptocrystalline quartz and hydrothermal quartz with idomorphic hexagonal crystals (1 μm to 500 μm) are the main components of siliceous alteration, and are visible on most of the polished and thin sections from silicified zones of the Zarshuran black shale. Two generations of silicification can be recognized: an early, massive silicification with which no mineralization is associated; and a later, pervasive and vein-type silicification with which mineralization is associated. The unmineralized silicified rocks are white and contain fewer sulphides, and then mainly pyrite, compared to the mineralized rocks. Arsenian pyrite and sphalerite, arsenic-antimony-thallium sulphides, lead-sulphosalts, iron oxides and gangue minerals are commonly present in the mineralized jasperoids. The presence of 3-5 μm in size metallic gold in jasperoids was reported by Karimi (1993), but this has not been confirmed by the present study. Detrital or sedimentary quartz crystals, disseminated in the matrix of unmineralized carbonate rocks, are typically much coarser (0.4 mm) than the hydrothermal quartz.

Argillization, alteration of feldspars to phyllosilicates and quartz, extends throughout and beyond the zones of gold mineralization. This alteration is best developed in the granitoid and the Zarshuran black shale where it is pervasive and intimately associated with mineralization. Intensely argillized black shale comprises fine-grained kaolinite, illite, sericite, quartz, calcite, pyrite, cinnabar and orpiment (samples 96108, 96109, 96116, 97201, 97206). Sericite forms about 50 vol. % of the altered granitoid.

Weak mylonitization generated further fragmentation and caused additional

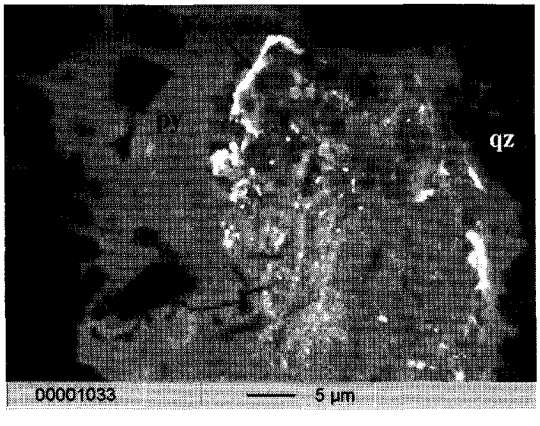

Fig. 4.13. Back-scattered electron micrograph of gradual oxidation of pyrite to hematite (sample 97113).

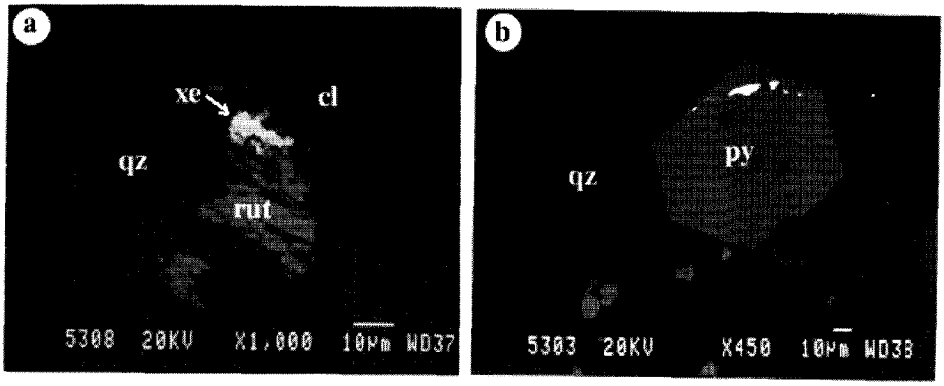

Fig. 4.14. Back-scattered electron micrographs of accessory minerals: (a) xenotime (xe, bright) and rutile (rut, grey) associated with clay minerals and quartz; (b) apatite (ap, bright) inclusion within the rim of pyrite, and rutile inclusion (rut, dark grey spot) in the core of pyrite. Samples 96108, 96114.

porosity and opened pathways for penetration of air; cool fluids may also have moved downward along these pathways. This air and fluid penetration led to oxidation and acid leaching along fractures and faults. This is manifested by the oxidation of pyrite and other ferruginous sulphides to hematite and goethite (Fig. 4.13), and by the formation of secondary oxides containing sulphur, iron and arsenic, such as anhydrite, jarosite, scorodite and arsenic oxides. A fracture zone, 5 m wide, affected by oxidation and acid leaching is found to the southeast of Zarshuran, along the Carbalai-Abbas valley. Kuehn and Rose (1992, 1995) attribute similar oxidation and acid leaching in sediment-hosted gold deposits of Nevada to deep weathering, although they are often considered to be hypogene processes, coinciding with the later stages of hydrothermal mineralization (Radtke, 1985).

Some of the accessory minerals in the granitoid at Zarshuran are found in association with hydrothermal alteration and mineralization. Xenotime (YPO_4) and rutile (TiO_2) are found in altered granitoid (Fig. 4.14a). Xenotime often contains erbium, cerium, and other rare earth elements, as well as thorium, uranium, aluminium, calcium, beryllium, zirconium; it occurs as an accessory mineral in granites and pegmatites (Bate and Jackson, 1980). Rutile also occurs as inclusions in the core of zoned pyrite crystals in the black shale (Fig. 4.14b). Apatite ($Ca_5(PO_4)_3(OH,F,Cl)$)is found as inclusions in the arsenic-rich rims of zoned pyrites.

Gangue minerals introduced with the mineralization include barite, fluorite, calcite and dolomite. They occur in minor amounts as single minerals, patches, veins and veinlets in close association with late hydrothermal quartz.

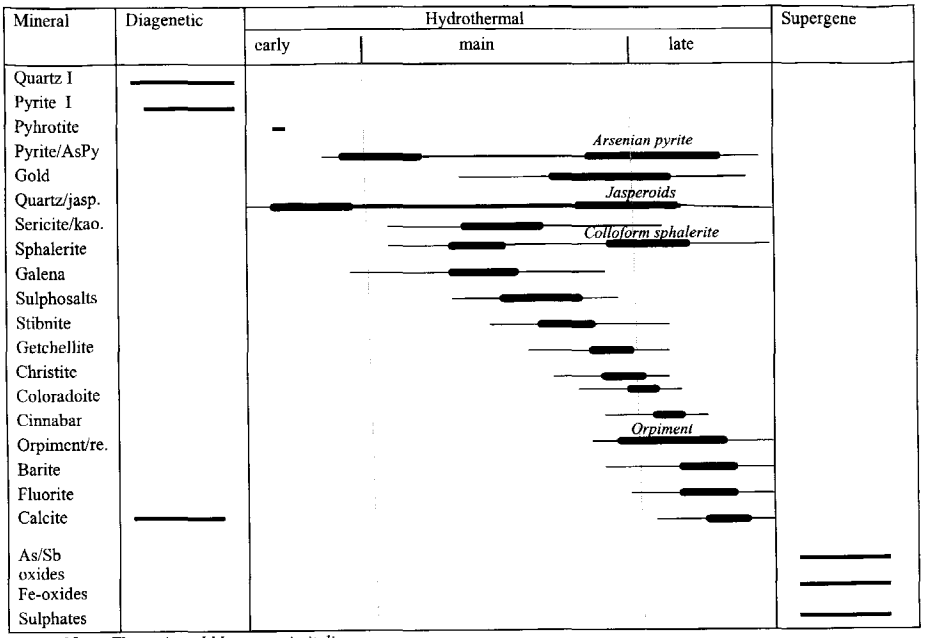

Note: *The main gold hosts are in italics*

Fig. 4.15. Paragenetic sequence in the Zarshuran gold deposit

4.5 PARAGENETIC SEQUENCE

Mineral assemblages at Zarshuran include minerals of up to four different origins: primary host rock minerals; minerals formed from primary minerals by replacement due to the hydrothermal solutions; minerals formed by direct crystallization from hydrothermal solutions; and secondary minerals resulting from weathering of hydrothermal minerals. The paragenetic sequence is complicated by the recognition of three different assemblages related to hydrothermal processes. The mineral assemblages are shown in their inferred paragenetic sequence in Fig. 4.15.

Primary assemblage. Unaltered rocks are rare and primary minerals are remnants within altered rocks. Those in the sedimentary rocks are detrital quartz (Quartz I), calcite, and diagenetic pyrite (Pyrite I). Both quartz and pyrite occur as anhedral grains along bedding planes in black shale and as framboids disseminated in the matrix of carbonate rocks. Those in the granitoid are quartz, feldspar, zircon, xenotime and rutile.

Early hydrothermal assemblage. This comprises quartz (Quartz II), sericite, illite, kaolinite, pyrite (Pyrite II) and pyrrhotite. In the granitoid the predominant minerals are clays resulting from feldspars alteration whilst the carbonate and black shale are characterized by weak argillic alteration and the

introduction of large quantities of silica at the expense of calcite. Pyrrhotite inclusions in this pyrite (Karimi, 1993) are interpreted as the earliest sulphide minerals at Zarshuran, precipitating from a hydrothermal solution that contained insufficient sulphur to precipitate pyrite. There is no gold in the minerals of this assemblage.

Main hydrothermal assemblage. In carbonates and black shale, this is marked by the precipitation of a wide range of sulphides and sulphosalts and the continuation of silicification and argillic alteration. The zinc and lead introduced by these fluids precipitated anhedral-euhedral grains of sphalerite (Sphalerite I) and galena. The arsenic formed anhedral-euhedral grains of arsenian pyrite and overgrowths of arsenian pyrite on pre-existing pyrite (Pyrite I and Pyrite II). The arsenian pyrite contains traces of gold, antimony and mercury. Gold also precipitated as micrometer-sized grains of metallic gold, which are found in jasperoids, along with hydrocarbons and gold-bearing arsenian pyrite, and as inclusions in later orpiment. Evolution of the fluid resulted in the precipitation of lead-sulphosalts, replacing both sphalerite and arsenian pyrite rims. Still later the hydrothermal solution, now enriched in antimony, precipitated stibnite. Subsequent depletion of antimony led to precipitation of getchellite, which is often intergrown with stibnite and occurs as open space fillings in both quartz and calcite (which in places it cross cuts). The thallium in the fluids then precipitated as christite and lorandite, and the tellurium precipitated as coloradoite. In the granitoid there is weak pyrite (Pyrite II) and cinnabar mineralization.

Late hydrothermal assemblage. Large quantities of orpiment and realgar were deposited as veins, veinlets, small lenses and open space fillings. Network and massive arsenian pyrite enclosing arsenian pyrite rims and colloform arsenian pyrite intimately intergrown with massive and colloform sphalerite (sphalerite II) were formed in late quartz (Quartz II) veins. The fluids were enriched in gold, resulting in the precipitation of invisible gold in late arsenian pyrite and colloform sphalerite. Barite, quartz (Quartz II), calcite and fluorite were also precipitated, mainly as veins, veinlets and open-space fillings.

Weathering assemblage. Oxidation of pyrite, orpiment and stibnite formed oxides of iron, arsenic and antimony and liberated SO_4^{2-}. This reacted with Ca^{2+}, Fe^{2+}, Ca^{2+}, Ba^{2+} and Al^{3+} to form sulphates.

4.6 DISCUSSION

The petrological and mineralogical characteristics of the Carlin-type sediment-hosted disseminated gold deposits of the western United States and

southeastern China have been described by Radtke et al. (1972), Wells and Mullens (1973), Bagby and Berger (1985), Radtke (1985), Bakken et al. (1989, 1991), Berger and Bagby (1991), Kuehn and Rose (1992) and Arehart et al. (1993). A comparison of the characteristics of the Carlin-type deposits with those of the Zarshuran gold deposit reveals much in common, e.g.,

- finely laminated black shale and silicified carbonate host rocks
- abundant organic matter in host rocks
- widespread decalcification, silicification and argillization
- disseminated mineralization
- sulphide minerals with colloform texture occupying open spaces
- abundance of arsenic minerals, but scarcity of arsenopyrite
- high concentrations of antimony in orpiment and occurrence of getchellite
- high concentrations of zinc associated with mineralization
- low concentrations of copper associated with mineralization
- occurrence of christite, lorandite and lead-sulphosalts
- association of arsenic, antimony, mercury and thallium with gold
- rare native gold in orpiment, realgar and silica
- invisible gold in arsenian pyrite.

On the other hand, Zarshuran has some characteristics that it does not share with the Carlin-type sediment-hosted disseminated gold deposits of the western United States and southeastern China, e.g.,

- presence of a mylonitized, highly altered and weakly mineralized granitoid
- presence of tellurium in arsenic minerals and as coloradoite
- occurrence of significant amounts of invisible gold in colloform sphalerite

The mylonitized and weakly mineralized granitoid intrusion at Zarshuran contrasts with the setting of typical sediment-hosted disseminated gold deposits. The unmineralized granitoid contains 140 ppb Au, compared with 80 ppb in the Iman Khan schist and 70 ppb in the Eocene volcanics located 3 km to the southwest. Its emplacement led to faulting, fracturing and an increase in porosity of the Precambrian formations, in particular the Chaldagh limestone and Zarshuran black shale. As a result, these formations were able to provide channels along which the weakly acid fluid associated with the intrusion invaded the black shale and limestone. According to Radtke (1985) and Berger and Bagby (1991) fluid circulation in the carbonate host formations causes decalcification and further increases porosity and permeability, thus preparing more favourable conditions for mineralization. Into rocks so prepared at

Zarshuran, hydrothermal solutions introduced silica, arsenic, base metals and gold, whilst in the mylonitized granitoid the same solutions effected sericitization, argillization and silicification and precipitated pyrite and cinnabar.

Telluride minerals have not been reported from the sediment-hosted disseminated gold deposits of the western United States and southeastern China. Their presence in the mineralization at Zarshuran, taken alongside the likelihood of hydrothermal solutions from the nearby granitoid permeating the host rocks, has implications for the origin of the mineralizing fluids. These are examined further in Chapter 8.

The organic matter in the sediment-hosted disseminated gold deposits is derived from the dissolution of carbonate rocks by hydrothermal solutions (Taylor, 1986) or an igneous source (Kuehn and Rose, 1995). Both possibilities exist at Zarshuran. At Carlin, Radtke (1985) found that the mineralized rocks contain significantly more organic carbon than unmineralized rock; when the organic content of the ore exceeds 0.3 wt. %, there is a high gold concentration associated with organic matter, indicating that organic carbon plays an important role in the deposition of gold (Radtke and Scheiner, 1970). There is certainly a spatial relation between organic carbon and gold at Zarshuran. Hausen and Park (1986) found that the ores at Getchell and Alligator Ridge contain bituminous matter that was emplaced in the host rocks prior to gold mineralization and mobilized locally by hydrothermal solutions. Similarly the Zarshuran black shale represents a source of organic matter that could have been locally mobilized by hydrothermal solutions.

4.7 CONCLUSIONS

From petrography, mineralogy and trace-element geochemistry it is possible to distinguish five mineral assemblages at Zarshuran, including three of hydrothermal origin. The Zarshuran gold deposit exhibits many similarities with the sediment-hosted disseminated gold deposits of the southwestern USA, from which it seems reasonable to conclude that Zarshuran can be regarded as a Carlin-like deposit. There are also differences that may be of significance. In particular the proximity of the Zarshuran deposit to a granitoid intrusion, the presence of tellurium in concentrations sufficient to precipitate telluride minerals and the occurrence of gold-bearing colloform sphalerite deserve further attention.

Chapter 5

INVISIBLE GOLD AT ZARSHURAN, IRAN

The Zarshuran deposit has, in the past decades, proved economic for its arsenic mineralization rather than its gold mineralization. Failure to recognize its gold potential until recently had been due to the near-absence of visible gold. This chapter establishes the ways in which gold occurs and in what forms it is concentrated to ore grade. It is an edited version of the paper, *Invisible Gold at Zarshuran, Iran* published in Economic Geology, Vol. 94, pp. 1367-1374 (Asadi et al., 1999).

5.1 INTRODUCTION

At Zarshuran disseminated gold occurs mainly in Precambrian sedimentary rocks. In the Chaldagh limestone it is found in hydrothermal veins of massive quartz (jasperoid) and quartz veinlets formed by carbonate replacement along high-angle faults that trend NW-SE and E-W. Gold also occurs as disseminations in the carbonaceous, siliceous and calcareous beds within the Zarshuran black shale. The Chaldagh limestone is mineralized at its contacts with the underlying Iman Khan schist and with the overlying Zarshuran unit. Also weakly mineralized and in close spatial association with the mineralized Precambrian rocks is a highly-altered Oligo-Miocene granitoid stock. Recent exploration for gold has established a probable reserve of 2.5 million tonnes of ore with an average grade of 10 g/t gold (Samimi, 1992).

Quartz, calcite, dolomite and clays are the principal gangue minerals of the host rocks. Decalcification, silicification, and argillization characterize mineralized rocks. Decalcification increased the porosity and permeability of the host rocks and thus provided favourable sites for hydrothermal

mineralization. The ore consists mainly of orpiment and pyrite, and to a lesser extent sphalerite, galena, realgar and stibnite, with subordinate cinnabar, HgS, lorandite, $TlAsS_2$, christite, $TlHgAsS_3$, coloradoite, HgTe, getchellite, $AsSbS_3$, aktashite, $Cu_6Hg_3As_4S_{12}$, baumhauerite, $Pb_3As_4S_9$, boulangerite, $Pb_5Sb_4S_{11}$, geochronite, $Pb_{14}(Sb, As)_6S_{23}$, plagionite, $Pb_5Sb_8S_{17}$ and twinnite, $Pb(Sb, As)_2S_4$ (Asadi et al., 2000c). Sulphide oxidation is mainly confined to veins, veinlets, and fracture zones. Quartz, calcite, fluorite, hematite and barite are the main gangue minerals. Accessory minerals include apatite, $Ca_5(PO_4)_3$ (OH, F, Cl), rutile, TiO_2, zircon, $ZrSiO_2$, and xenotime, YPO_4. There are no gold minerals except for rare native gold, which is present in quantities insufficient to explain the gold grade established by exploration trenches, boreholes and tunnels.

Many characteristics of the Zarshuran deposit are similar to other disseminated gold deposits hosted by sedimentary rocks. In those of the western United States, gold is rarely visible but occurs invisibly in a number of mineral phases (Bakken et al., 1991; Arehart et al., 1993). In order to determine if similar invisible gold occurs at Zarshuran, trace-element analyses of 15 mineralized samples from outcrops, trenches, boreholes, and tunnels were carried out by electron microprobe analysis. Bulk chemical analyses for ore and ore-related trace elements were performed on corresponding subsamples.

5.2 METHODS

Trace levels of gold in other minerals can be determined by electron microprobe analysis provided the X-ray intensity of the microprobe is maximized and the peak-to-background ratio for the X-ray line under consideration is optimized. These operating characteristics require maximum achievable accelerating voltage, highest possible beam current, and long counting times (Graham et al., 1989; Gervilla et al., 1997; Johansen and Kojonen, 1996; Cook and Chryssoulis, 1990; Kojonen and Johansen, 1997; Robinson and Graham, 1992).

Electron microprobe analyses of the Zarshuran samples were performed with a JEOL 8800 instrument at the Department of Applied Earth Sciences, Delft University of Technology. The analytical conditions were: (a) 40 KV accelerating voltage; (b) 3.8×10^{-8} A beam current; (c) X-ray line of Au-Lα on the LIF-crystal; (d) counting times of 300 seconds on peak and background; and (e) native gold as analytical standard. Measurements were carried out first on the peak and subsequently on the upper and lower background positions. The applied alternating peak and background measurements require

special software which was available for our instrument. However, it was found that the instrument was fairly stable under these conditions, so that errors due to drift were minimal. The detection limit for gold is 20 ppm according to the calculation made by the instrument software, i.e.,

$$D.L. = 3/nc * \sqrt{2 * IB/tB} * wt$$

where D.L. = detection limit, nc = net count (cps) of the standard specimen, IB = mean background intensity (cps) of unknown specimen, tB = measurement time (sec) at background position, and wt = weight percent of standard specimen. The detection limit calculated according to the Zieboldt equation (Zieboldt, 1967) is slightly lower. In similar work, Johansen and Kojonen (1996) report a detection limit of 15 ppm gold.

The 15 samples studied by electron microprobe analysis were also analyzed for Au, As, Ag, Sb, Hg, Tl, Te, Zn, S, and C by atomic absorption spectrophotometry (AAS) at the Geological Laboratory in Teplice, Slovakia (table 1). These data were used primarily to support the electron microprobe analyses results. These AAS results were merged with the AAS results from 838 borehole samples and 47 other representative mineralized and unmineralized rock samples from outcrops, trenches, and tunnels at Zarshuran to create a geochemical database of 900 samples. This database was used to prepare bar charts showing the ranges of gold concentrations in different rock types and to identify correlations between gold and other elements.

5.3 RESULTS

Arsenian pyrite occurs as overgrowths on large euhedral pyrite crystals. A later network and massive arsenian pyrite encloses the overgrowth rims. The latest generation of arsenian pyrite is colloform in texture and intimately intergrown with massive and colloform sphalerite.

5.3.1 Occurrence of visible gold

Karimi (1992) reported the occurrence of micron-size gold in the silicified ores. Nevertheless, examination by high-resolution optical microscopy and electron microprobe of several silicified ore samples, including those found by chemical analyses to have the highest gold concentrations, failed to reveal any native gold associated with silica. Sparse gold was found only in close association with an arsenic-mercury-thallium sulphide, both occurring as inclusions in a matrix of microcrystalline orpiment. These inclusions were first observed by optical microscopy and subsequently confirmed by electron

microprobe analysis (chapter 4, Fig. 4.8). Qualitative microprobe analysis of a gold grain gave no indication of the presence of other metals commonly found with gold (e.g., Ag, Te, Se).

5.3.2 Gold concentrations and associations

Gold at Zarshuran is hosted mainly by the jasperoid, silicified shale, and silicified limestone (Fig. 5.1). Within these rock types, high gold concentrations tend to be found in samples that contain visible pyrite and orpiment. Gold shows strong positive correlations with arsenic and mercury, and weaker positive correlations with antimony and zinc (Fig. 5.2). It has no significant correlation with other elements. Arsenic has a very strong positive correlation with mercury and antimony, and a weaker positive correlation with zinc. Among the samples examined by electron microprobe, bulk gold contents determined by AAS ranged from 0.08 to 26.53 ppm. The highest gold concentrations were found in samples containing visible pyrite, orpiment and sphalerite (Table 5.1).

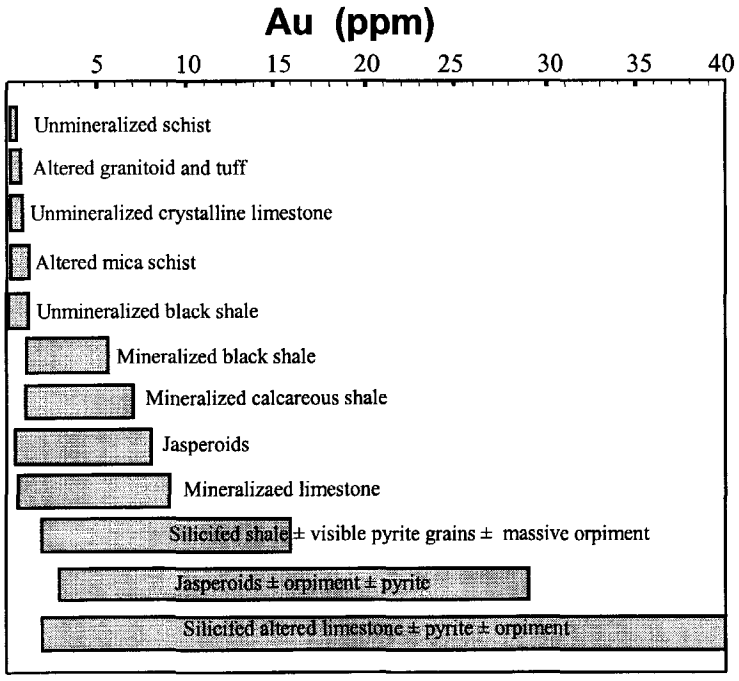

Fig. 5.1. Distribution of gold in different rock types at Zarshuran, based on analyses of 900 samples by Atomic Absorption Spectrophotometry (AAS).

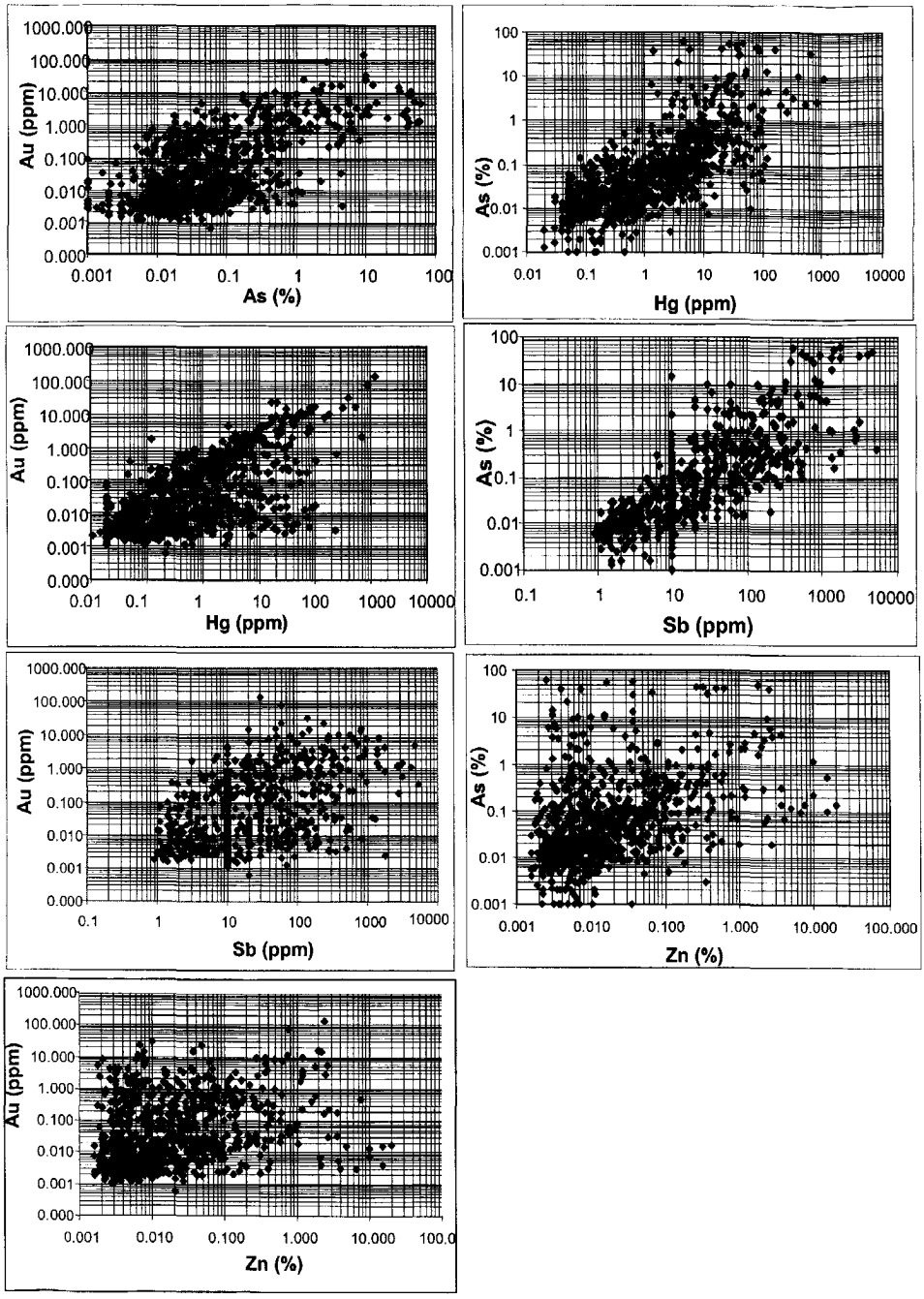

Fig. 5.2. Scatter diagrams (logarithmic axes) for Au-As, Au-Hg, Au-Sb, Au-Zn, As-Hg, As-Sb and As-Zn at Zarshuran, based on analyses of 900 samples by AAS.

Table 5.1. Bulk chemical analyses of 15 samples (in ppm, except as stated)

Description	Sample	Au	Ag	As%	Sb %	Tl	Hg	Te	Zn %	S %
Unmineralized Rocks										
Schist	15486	0.08	< 0.2	0.05	0.002	0.5	0.64	< 0.5	0.041	1.00
Andesite	15483	0.10	< 0.2	0.02	0.013	4.5	4.89	< 0.5	0.101	0.72
Altered granitoid	15485	0.14	0.2	0.04	0.003	1.4	3.06	< 0.5	0.064	0.63
Dense limestone	15487	0.18	0.2	0.05	0.002	5.7	1.46	< 0.5	0.067	2.77
Altered limestone	15491	0.16	< 0.2	0.25	0.002	1.3	4.45	< 0.5	0.272	0.46
Weakly silicified limestone	15493	0.36	0.2	0.12	0.032	1.6	4.53	1.0	0.100	0.61
Mineralized Rocks										
Black shale	15488	0.18	5.8	0.22	0.040	8.8	14.66	1.8	0.960	9.09
Black shale	15492	9.57	0.4	0.06	0.007	20.5	26.14	< 0.5	0.055	1.91
Black shale + getchellite + py	15489	15.24	2.2	3.14	3.100	360	606.6	9.0	4.818	10.00
Jasperoid + orpiment	15494	0.64	10.0	18.00	0.70	50.0	43.8	55.3	0.780	13.51
Jasperoid + sph + fl	15484	0.58	210.4	0.47	0.750	12.6	499.3	5.7	30.813	19.74
Jasperoid + barite	15481	2.42	3.2	3.22	0.029	8.0	62.60	18.1	0.103	4.90
Jasperoid + py + sph	15482	10.75	17.2	1.05	0.627	185	142.2	18.2	23.625	25.05
Jasperoid + py + orp	15490	26.53	10.0	16.85	1.940	14.9	327.7	125	0.410	11.91
Massive orpiment and realgar	15480	0.14	1.2	58.50	2.250	1.6	8.78	316	nd	38.58

Detection limits: Ag = 0.2 ppm; Te = 0.5 ppm. Analytical method = Atomic Absorption Spectrophotometry
Abbreviations: py = pyrite; sph = sphalerite; fl = fluorite; orp = orpiment; nd = not determined..

5.3.3 Occurrence of invisible gold

The scarcity of visible gold, coupled with the high concentrations of gold in the mineralized rocks at Zarshuran, lends credence to the occurrence of invisible gold. The positive correlations between gold and arsenic, mercury, antimony, and zinc guided the search for this gold to the arsenic, mercury, antimony, and zinc sulphides (orpiment, realgar, arsenian pyrite, cinnabar, stibnite, and sphalerite). Where applicable, a distinction was made between different textures (and therefore possibly different generations) of the same mineral. The search was also extended to pyrite and lead-sulphosalts such as

getchellite. The results of electron microprobe analyses of these minerals for trace gold are summarized in Table 5.2.

Table 5.2. Ranges of concentrations of gold, arsenic and mercury in sulphide and sulphosalt minerals in 15 samples examined by electron microprobe analysis

Mineral / phase	No. analyses	Au (ppm)	As (%)	Hg (ppm)	Observations
Orpiment	15	< 20		< 250 - 710	Rare (sub)micron-size grains of metallic gold
Realgar	7	< 20		< 250 - 660	
Stibnite, getchellite and Pb-sulphosalts	10	< 20			
Euhedral pyrite	5	< 20	< 0.04, 0.22	< 250	Core of pyrite with overgrowth rims; quartz matrix. One analysis only 0.22% As
Anhedral pyrite	10	40 – 100	0.04 - 2.4	< 250	Occurs in orpiment matrix
Overgrowth, network and massive arsenian pyrite	8	< 20 – 140	1.08 – 3.4	< 250 - 5400	Overgrowths on euhedral pyrite, network and massive varieties adjacent; quartz matrix; Au, As and Hg content variable.
Colloform arsenian pyrite (melnicovite)	10	1060 - 1300	3.16 - 4.73	4420 - 5940	Late stage mineral occurring in quartz and sometimes intimately intergrown with massive and colloform sphalerite.
Colloform and massive sphalerite	10	110 - 390	< 0.04 - 0.65	<250 - 1970	Iron-rich colloform and massive sphalerite intimately intergrown with colloform pyrite; Au content correlates with Fe content

Detection limits: Au = 20 ppm; Hg = 250 ppm and As = 0.045 %

After orpiment, pyrite and arsenian pyrite are the most abundant sulphide minerals at Zarshuran. Euhedral to subhedral pyrite commonly occurs as fine-grained crystals in quartz and occasionally in fluorite, barite, calcite and sphalerite. In this variety of pyrite, gold and, in most cases, arsenic were found to be below detection limit.

Anhedral pyrite grains commonly occur in an orpiment matrix, and electron microprobe analysis revealed that this variety of pyrite contains 40-100 ppm gold, an average of 0.19 % arsenic and up to 2.4% arsenic. Where arsenic concentrations exceed 1%, this pyrite can be considered to be arsenian pyrite. The gold concentration in this type of pyrite displays a positive

correlation with the arsenic concentration. Owing to the combination of its relative abundance and typically high gold content, arsenian pyrite is the most important gold-bearing mineral at Zarshuran. Three types of arsenian pyrite are recognized.

The earliest gold-bearing arsenian pyrite is very abundant in association with sphalerite, euhedral pyrite, and lead-sulphosalts (mainly geochronite and baumhauerite) in quartz. This arsenian pyrite occurs as overgrowths on some large (5-300 μm) euhedral pyrite crystals (chapter 4, Fig. 4.5b and 4.5c). These overgrowth rims, identified by high-resolution optical microscopy (1000x magnification, oil immersion lens) and confirmed by microprobe analysis, vary in thickness from 1 to 20 μm. Geochronite and baumhauerite occasionally enclose the overgrowth rims. Electron microprobe analyses of these rims pinpoint high arsenic concentrations (1.08-1.65%), high mercury concentrations (<250-480 ppm), and gold concentrations of up to 140 ppm. These concentrations compare with low arsenic (<0.04%, one analysis 0.22%), and gold and mercury concentrations below the 20 ppm and 350 ppm detection limits respectively, in the euhedral pyrite core. Within the rim, the highest arsenic and gold concentrations were detected by electron microprobe analyses at the boundary of the overgrowth rims with the euhedral pyrite core. This boundary exhibits a brighter colour than the rest of the rims in the back-scattered electron microphotograph.

A second type of arsenian pyrite encloses the overgrowth rim and, due to its high arsenic and mercury contents (up to 3.4% and 5940 ppm respectively), appears bright in a back-scattered electron microphotograph. This type of arsenian pyrite shows a network and massive texture attributed to its precipitation from hydrothermal solutions percolating through microfractures

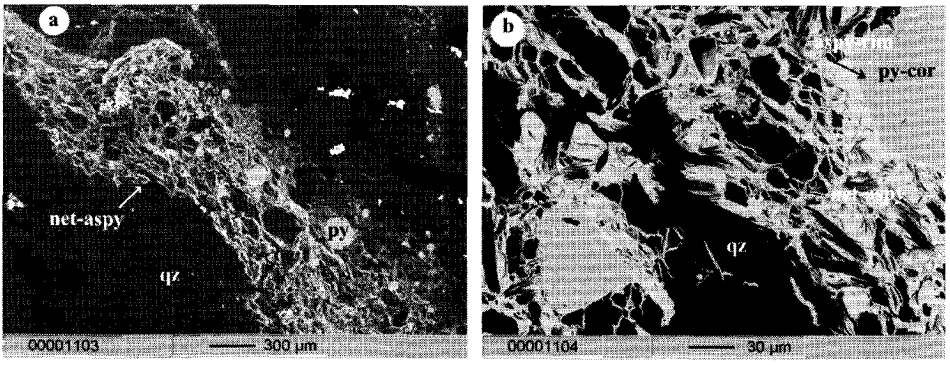

Fig. 5.3. Back-scattered electron microphotographs of network arsenian pyrite (net-aspy) in quartz matrix: (a) overview; (b) detail showing the bright net-aspy surrounding rimmed pyrite (py)

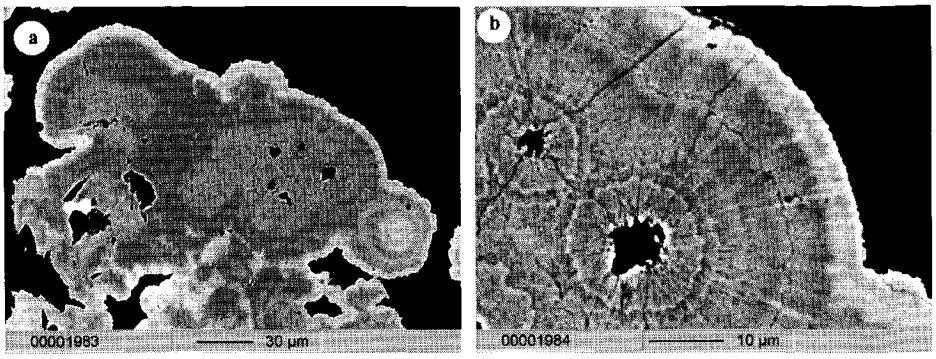

Fig. 5.4. Back-scattered electron microphotographs of colloform arsenian pyrite (melnicovite): (a) overview; (b) detail showing bright rims rich in arsenic and with higher gold concentration

in quartz (Fig. 5.3). It is occasionally intergrown with massive sphalerite in quartz. Microprobe analyses show an average higher gold concentration in this type of arsenian pyrite (116 ppm) compared to overgrowth rims (90 ppm).

A third type of arsenian pyrite exhibits a colloform texture. Colloform arsenian pyrite, or melnicovite, contains 1030-1300 ppm gold and up to 4.73% arsenic. The highest concentrations of gold, arsenic and mercury tend to be found in the rim (Fig. 5.4, Table 5.2). Melnicovite occurs in the hydrothermal silica matrix and commonly is intimately intergrown with massive and colloform sphalerite.

Sphalerite, the most abundant sulphide after orpiment, pyrite and arsenian pyrite, is present as individual anhedral grains associated with galena and also as massive and colloform sphalerite intergrown with massive arsenian pyrite and melnicovite (Fig. 5.5). Gold was detected in massive and colloform

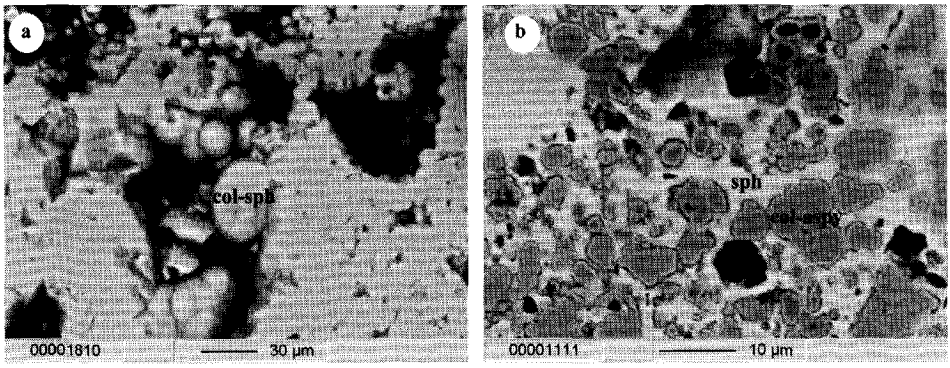

Fig. 5. 7. Back-scattered electron microphotographs of sphalerite: (a) colloform sphalerite (col-sph); and (b) massive sphalerite (sph, light grey) intimately intergrown with colloform arsenian pyrite (col-aspy, dark grey)

sphalerite in concentrations from 110 to 390 ppm. The highest gold values are found in massive and colloform sphalerite that also contains elevated arsenic and mercury concentrations. A sample of jasperoid with anhedral sphalerite and fluorite (sample 15484) was found by AAS to contain 0.58 ppm gold and 0.47% arsenic, whereas a sample of jasperoid with massive sphalerite and pyrite (sample 15482) was found to contain 10.75 ppm gold and 1.05 % arsenic (Table 5.1).

Orpiment and realgar are very abundant at Zarshuran, and constitute an arsenic ore that currently is worked on a small scale. These minerals mainly occur as massive grains associated with jasperoid and carbonate minerals. Whereas electron microprobe analyses of orpiment and realgar did not reveal any gold concentration above the 20 ppm detection limit, bulk chemical analyses of dense microcrystalline orpiment occasionally yielded high gold concentrations, up to 158 ppm, presumably due to the presence of rare native gold and of gold-bearing pyrite in orpiment.

5.4 DISCUSSION

Gold in rocks altered to hydrothermal silica at Zarshuran is incorporated mainly into arsenian pyrite. By electron microprobe analyses this gold is traced to three sites: (1) the arsenian pyrite overgrowth rims on euhedral pyrite; (2) the network and massive arsenian pyrite associated with such overgrowth rims; and (3) colloform arsenian pyrite. On a microscale, gold concentrations increase from a barren euhedral pyritic core into an arsenian pyrite rim, and then further increase into the surrounding network, massive, and colloform arsenian pyrite. The occurrence of a gold-rich periphery on barren pyrite has been noted at sediment-hosted disseminated gold deposits in Nevada: Radtke et al. (1972) and Wells and Mullens (1973) reported gold on the surfaces of pyrite at Carlin; and Radtke (1985) found enrichments of arsenic, mercury, antimony, and gold on the rims of some of the large pyrite grains at both Carlin and Cortez. Similarly, mercury at Zarshuran is concentrated with gold in the arsenian pyrite overgrowth rims. From their examination of five sediment-hosted disseminated gold deposits in Nevada, Arehart et al. (1993) suggested that gold was deposited with arsenic as coupled solid solution in arsenian pyrite. Comparable associations at Zarshuran suggest that this also may be the principal mechanism of gold deposition there.

Orpiment is the most abundant sulphide at Zarshuran and is an important gold carrier. Although Dickson et al. (1974) found that synthetic orpiment and realgar may contain 200 ppm gold as submicron-size particles and up to

2000 ppm gold as solid solution, electron microprobe analyses of Zarshuran orpiment and realgar revealed less than 20 ppm gold in these minerals. Rather gold is attributed to scarce micron-sized native gold and gold-bearing anhedral pyrite in the orpiment matrix. At the sediment-hosted disseminated gold deposit at Carlin, Nevada, Bakken et al. (1989) noted submicron-size gold in pyrite and cinnabar.

Radtke et al. (1972) and Wells and Mullens (1973) reported gold in sphalerite at Carlin. At Zarshuran, almost all massive and colloform sphalerite studied by electron microprobe showed a significant quantity of gold. The zoned texture and chemical variations of the colloform sphalerite suggest that layers of sphalerite alternate with layers of melnicovite. Thus the gold-hosting role of this sphalerite may owe much to its intimate association with melnicovite, the host for the highest concentrations of gold at Zarshuran.

5.5 CONCLUSIONS

Electron microprobe quantitative point analyses of sulphide and sulphosalt minerals from Zarshuran have demonstrated the presence of invisible gold. It occurs in four minerals:

- melnicovite (up to 1300 ppm Au) associated with hydrothermal silica;
- massive and colloform sphalerite (up to 390 ppm Au) associated with hydrothermal silica;
- arsenian pyrite overgrowth rims (up to 140 ppm Au) on euhedral pyrite; and
- anhedral pyrite (up to 100 ppm Au) in the orpiment matrix.

Gold in these forms adequately explains the measured gold concentrations at Zarshuran. The invisible gold owes its origin to solid solution deposition and/or encapsulation of submicron-size particles of metallic gold. Micron-size visible gold, found in inclusions in microcrystalline orpiment, makes an insignificant contribution to the total gold concentration.

Several of the modes of occurrence of gold at Zarshuran have been recorded previously in sediment-hosted disseminated gold deposits in Nevada. This adds further support to the hypothesis that Zarshuran is a sediment-hosted disseminated gold deposit.

Chapter 6

SULPHOSALTS AT ZARSHURAN, IMPLICATIONS FOR GOLD MINERALIZATION

This chapter describes various sulphosalt minerals, their paragenesis and their association with gold at Zarshuran. Using their temperatures of formation and paragenetic sequences, further evidence is brought forward for the origin of the mineralization. This chapter is edited versions of: (a) *Sulphosalts at the Zarshuran Carlin-like gold deposit, northwest Iran: implications for gold mineralization,* in review in the Transactions of the Institution of Mining and Metallurgy, Section B (Asadi et al., 2001); and (b) *Gold mineralization at Zarshuran, NW Iran,* published as extended abstract in the MSF Mini-Symposium, Espoo, Finland, Modern Approaches to Ore and Environmental Mineralogy, pp. 1-2 (Asadi et al., 2000d).

6.1 INTRODUCTION

At Zarshuran, the principal ore minerals are pyrite, orpiment, realgar, stibnite, sphalerite and galena (Asadi et al., 2000c). Gold mainly occurs as invisible gold associated with the arsenian pyrite and sphalerite; visible gold is rare and occurs in orpiment and silica (Asadi et al., 1999). During scientific investigations of the sulphide minerals (Chapter 4) and gold (Chapter 5), trace quantities of several sulphosalt minerals were observed in close association with the sulphide minerals and gold. In order to investigate their significance, 30 samples of ore and host rocks, collected for mineralogical studies from tunnels, trenches, bore holes and outcrops at Zarshuran, were

studied using ore microscopy and electron probe microanalyses (EPMA) at the Department of Applied Earth Sciences, Delft University of Technology.

6.2 METHODS

Thirty samples of ore and host rocks were collected for mineralogical studies from tunnels, trenches, boreholes and outcrops at the Zarshuran gold deposit. Polished sections were prepared and investigated using ore microscopy and electron microprobe analyses. These analyses were carried out in the Department of Applied Earth Sciences of Delft University of Technology.

Selected minerals in polished sections were analysed by EPMA using a JEOL Electron Probe Micro Analyser (JXA-8800M). The instrument is fitted with two wavelength-dispersive spectrometers and with sets of LDE1/TAP and PET/LIF analysing crystals. Qualitative, quantitative and X-ray scanning analyses were carried out to detect mineral compositions. Counting times during analysis for concentrations of the major elements were 20-50 s, using an accelerating voltage of 20 KV and a beam current of 20 nA.

To identify sulphosalt minerals, qualitative and quantitative microprobe analyses were carried out to determine Pb, As, Au, Sb, Ag, Hg, Cu, Bi, Fe, Te, Tl and Cl, which are common components of sulphosalts. During quantitative analysis, standards used for instrument calibration were metallic Au for gold, iodyrite for Ag, galena for Pb and S, sphalerite for Zn, marcasite for Fe, cinnabar for Hg, a synthetic compound of GaAs for arsenic, Sb_2Te_3 for Te and Sb, Bi_2Se_3 for Bi, metallic copper for Cu and tugtupite for Cl. Thallium was not determined quantitatively, due to the lack of a suitable standard. Atomic concentrations of elements in a mineral as well as the number of atoms in the mineral formula were used to calculate the stoichiometry of sulphosalt minerals. The calculated stoichiometry and the Pb:(As+Sb) ratio, which is fixed in lead sulphosalts, was used for the determination.

Routine X-ray diffraction analyses (diffractometer) were carried out with a Philips PW3710 X'pert system, Cu-Kα radiation (λ= 1.5418) and a Ni filter. The XRD results were compared with identifications made by optical microscopy and EPMA.

6.3 RESULTS

Optical microscopy and EPMA of the polished sections led to the recognition of several sulphosalt minerals containing various quantities of

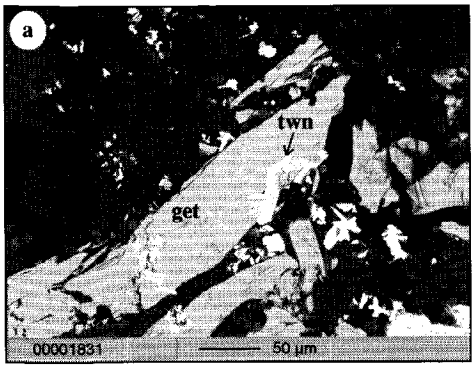

6.1. Backscattered electron micrograph of getchellite (get, white) with needle inclusions and lamellae of twinnite

lead, arsenic, antimony, mercury, thallium, copper and sulphur. Mineral identification was assisted in some cases by XRD analysis. In the case of the composition determined for one Pb-Sb-As-sulphosalt, it proved impossible to attribute a mineral name.

Based on the paragenetic observations of sulphosalts and sulphides by optical microscopy and EPMA, three types of mineral assemblages were identified.

6.3.1 Assemblage 1: As-Sb sulphide and sulphosalt minerals

Four As-Sb sulphide and sulphosalt minerals were identified at Zarshuran, namely orpiment, realgar, stibnite and getchellite. Their bulk compositions and trace element contents are shown in Table 6. 1. Orpiment, and to a lesser extent realgar, are relatively abundant, being arsenic ore minerals at Zarshuran.

Orpiment (As_2S_3) occurs as massive and coarsely-crystalline aggregates of flaky crystals in small veins, veinlets, fracture fillings and lenses within silicifed black shale. The orpiment typically contains Sb and Te; microprobe analyses reveal up to 9% Sb and 0.24% Te. Antimony probably substitutes for As, as at Carlin (Dickson et al., 1975; Radtke et al., 1973). Massive orpiment contains inclusions of Tl-bearing minerals, stibnite and minute grains of metallic gold, which can be seen by optical microscopy. Coarsely-crystalline orpiment has inclusions of coloradoite aggregates and anhedral arsenian pyrite. Many other ore minerals are commonly associated with orpiment (Asadi et al., 2000c).

Realgar (AsS) is a subordinate arsenic ore mineral (<5%) at Zarshuran, occurring as anhedral crystals associated with orpiment. Realgar crystals in

the Zarshuran black shale are often deformed. They contain traces of Te but, compared with orpiment, little Sb.

Stibnite (Sb_2S_3) is found as irregular grains, needles and needle-shaped aggregates within the orpiment matrix. Locally stibnite is replaced by massive orpiment. It also occurs as needle-like inclusions in orpiment and getchellite. Microprobe analyses of stibnite grains show an average 3.97 wt. % As. By analogy with Carlin, this As precipitated as solid solution (Dickson et al., 1974) or as very fine grains of As-minerals.

Table 6. 1. Average contents (determined by microprobe analyses) of As, Sb, S (wt %) and Te ppm) in orpiment, realgar, stibnite and getchellite at Zarshuran.

Mineral	N	As	Sb	S	Total	Te (ppm)
Orpiment	16	57.25	4.71	38.70	100.66	870*
Realgar	3	71.97	0.004	27.81	99.80	133
Stibnite	4	3.97	67.57	29.07	100.61	< L.D.
Getchellite	4	24.14	42.43	33.07	99.64	< L.D.

*N= number of analyses; * N = 13. L.D. = limit of detection = 50 ppm*

Getchellite ($AsSbS_3$) is rare at Zarshuran but was nevertheless identified some time ago by Bariand et al. (1968). It is closely associated with quartz, carbonate and stibnite. Inclusions of star-shaped aggregates of twinnite are found in the matrix of deformed getchellite (Fig. 6.1). Elongated crystals of getchellite intersect the dark grey silicifed limestone host rock. Getchellite is formed when the As:Sb ratio in the hydrothermal solution reaches 1:1.

6.3.2 Assemblage 2: Pb-As-Sb sulphosalt minerals

Geocronite ($Pb_{14}(Sb, As)_6 S_{23}$) was first observed under the polarising microscope at the periphery of a zoned arsenian pyrite. Atomic concentrations of elements resulting from quantitative microprobe analysis were used to calculate the stoichiometry of this mineral (Table 6.2). Geocronite mainly occurs as anhedral crystals in close association with sphalerite crystals and also as needles and anhedral grains around the gold-bearing zoned arsenian pyrite grains dispersed throughout the quartz veins in Zarshuran (Asadi et al, 2000c). Anhedral geocronite replaces sphalerite and intergrows intimately with baumhauerite (Fig. 6.2). It occasionally shows twin lamellae in only one direction (Fig. 6.2b). In places, massive and needle-shaped aggregates of geocronite have been replaced by aktashite. Geocronite occurs in many hydrothermal deposits where Pb, As and Sb mineralization is present (Birnie and Burnham, 1976).



Fig. 6.2. Back-scattered electron micrographs of geocronite: (a) overview of mixed phases of geocronite (geo, light grey) and baumhauerite (bm, light grey), and sphalerite (sph, dark grey) occurring in a quartz matrix (qz, dark), (b) enlarged central part of image showing massive geocronite intergrown intimately with needle-shaped aggregates of baumhauerite. Sample 97203.

Table 2. Composition (weight %) and atomic proportions (%) of mineral identified as geocronite

Sample	Hg	Sb	Pb	S	As	Ag	Cl	Cu	Total
Composition									
97203-1	0.03	8.61	66.94	17.97	6.06	0.02	0.05	0.02	99.67
96114-1	0.03	8.77	66.57	17.40	3.98	0.02	nm	nm	97.02
96114-2	0.02	9.14	68.30	17.37	4.02	0.01	nm	nm	99.03
96114-3	0.02	9.43	66.22	17.79	3.93	0.01	nm	nm	98.40
Atomic proportions									
97203-1		6.82	31.15	54.05	7.80				
96114-1		7.36	32.38	54.49	5.45				
96114-2		7.50	32.86	54.00	5.35				
96114-3		7.58	31.28	54.29	5.13				
Average		7.31	31.92	54.21	5.93				
Ratio		0.07	0.321	0.546	0.06				

nm = not measured

Number of atoms in mineral formula of geocronite = 43
Element 1 (Pb) : 0.321 * 43 = 13.81
Element 2 (Sb) : 0.074 * 43 = 3.18
Element 3 (As) : 0.060 * 43 = 2.58
Element 5 (S) : 0.546 * 43 =23.48
Analytical formula = $(Pb)_{13.81}(Sb, As)_{5.76}S_{23.48}$
Idealized formula = $Pb_{14}(Sb,As)_6S_{23}$

Baumhauerite ($Pb_3(As,Sb)_4S_9$) is characterized by lower reflectance than geocronite. During the microprobe analysis of geocronite a dark phase was identified occurring in close association with geocronite. Further quantitative microprobe point analyses of this mineral led to the identification of this as baumhauerite. The stoichiometry of baumhauerite was calculated as shown in Table 6.3. Microprobe analysis of baumhauerite shows up to 7.5% Sb in its

composition. This Sb was probably precipitated as solid solution. It occurs as needle-shaped crystals (fine lamellar twinning) that are arranged in sub-parallel groups. It always intergrows with geocronite, and it is only possible to differentiate it from geocronite by high resolution backscattered electron micrographs (Fig. 6.2).

Table 6.3. Composition (weight %) and atomic proportions (%) of mineral identified as baumhauerite

Sample	Hg	Sb	Pb	S	As	Ag	Cl	Cu	Total
Composition									
97202-18	0.06	7.83	47.34	24.10	19.26	0.00	nm	nm	98.93
9720-19	0.09	7.19	46.15	24.26	19.44	0.00	nm	nm	97.27
97202-20	0.03	7.28	48.08	23.80	19.53	0.01	nm	nm	98.90
97203-3	0.01	7.55	48.40	23.65	18.92	0.00	nm	nm	98.98
96115-1	0.03	7.28	47.38	24.32	19.69	0.02	nm	nm	98.84
Atomic proportions									
97202-18		4.92	17.48	57.51	19.67				
9720-19		4.69	17.60	57.55	19.86				
97202-20		4.61	17.89	57.21	20.10				
97203-3		4.80	18.08	57.08	19.55				
96115-1		4.56	17.42	57.79	20.02				
Average		4.72	17.69	57.43	19.84				
Ratio		0.047	0.178	0.576	0.199				

nm = not measured

Number of atoms in mineral formula of baumhauerite =16
Element 1 (Pb) : 0.178 * 16 = 2.85
Element 2 (Sb) : 0.047 * 16 = 0.75
Element 3 (As) : 0.199 * 16 = 3.19
Element 4 (S) : 0.576 * 16 = 9.22
Analytical formula = $(Pb)_{2.85}(As, Sb)_{3.94} S_{9.22}$
Idealized formula = $Pb_3(As,Sb)_4S_9$

Semseyite ($Pb_9Sb_8S_{21}$) occurs as anhedral, massive, lath-like and needle-shaped crystals and commonly intergrows with plagionite (Fig. 6.3a). Semseyite, galena, plagionite and twinnite often occur as four separate phases in a single, irregularly-shaped crystal (Fig. 6.3b). In this example, massive semseyite grains and galena form the core of the crystal and both are surrounded by plagionite and twinnite, which are described below. Galena in the core is replaced by semseyite. Semseyite itself is often replaced by plagionite and twinnite. The calculation of its stoichiometry is shown in Table 6. 4.

Plagionite ($Pb_5 Sb_8 S_{17}$) occurs as anhedral tabular crystals in the periphery of semseyite crystals. It commonly replaces the rims of semseyite and occasionally extends into the semseyite as lath-like crystals and veinlets (Figs. 6.5 and 6.6). Its stoichiometry is shown in Table 6. 5.

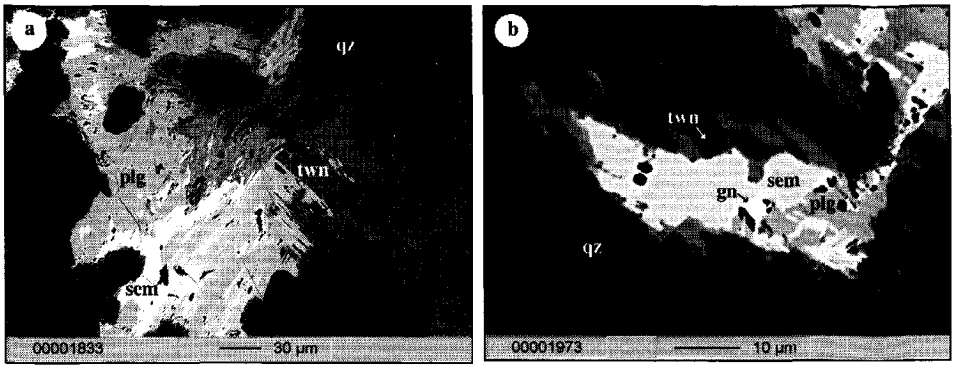

Fig. 6.3. Back-scattered electron micrographs of: (a) lath-like and needle-shaped semseyite (sem, bright) intimately intergrown with plagionite (plg, light grey) and dark grey twinnite (twn, dark grey); (b) galena (gn, bright), semseyite (sem, white), plagionite (plg, light grey) and twinnite (twn, dark grey) in an agglomerated grain. Sample 97202.

Twinnite ($Pb(Sb, As)_2 S_4$) is formed as anhedral and tabular grains, and as parallel polysynthetic twins, in the periphery of plagionite. It commonly extends into plagionite in the form of parallel veinlets. Twinnite often replaces plagionite and occasionally intimately intergrows with it. It never has direct contact with galena, and rarely has contact with semseyite (Fig. 6.3). In a backscattered image, twinnite exhibits a lower backscatter coefficient and thus a paler grey colour compared to semseyite and plagionite. This is due to the arsenic content of twinnite. Arsenic is not present in semseyite and plagionite. The calculation of its stoichiometry is shown in Table 6.6.

Table 6.4. Composition (weight %) and atomic proportions (%) of mineral identified as semseyite

Sample	Hg	Sb	Pb	S	As	Ag	Cl	Cu	Total
Composition									
97202-12	0.00	28.33	51.88	19.51	0.0	0.00	0.03	0.03	99.78
97202-13	0.00	28.04	52.34	19.34	0.0	0.00	0.06	0.03	99.80
97202-14	0.03	28.44	51.06	19.63	0.1	0.00	0.03	0.00	99.29
97202-15	0.07	27.93	51.61	19.22	0.0	0.00	0.03	0.01	98.86
97202-16	0.01	27.33	52.57	19.06	0.0	0.00	0.03	0.02	99.02
97202-17	0.02	27.81	52.43	1923	0.0	0.00	0.03	.001	99.53
Atomic proportion									
97202-12		21.28	22.91	55.68					
97202-13		21.16	23.21	55.43					
97202-14		21.34	22.51	55.94					
97202-15		21.26	23.08	55.54					
97202-16		20.91	23.63	55.36					
97202-17		21.11	23.38	55.41					
Average		21.28	23.07	55.50					
Ratio		0.21	0.23	0.56					

Number of atoms in mineral formula of semseyite = 38
Element 1 (Pb) : 0.23 * 38 = 8.74
Element 2 (Sb) : 0.21 * 38 = 7.98
Element 4 (S) : 0.56 * 38 = 21.28
Analytical formula = $Pb_{8.74}\ Sb_{7.98}\ S_{21.28}$
Idealized formula = $Pb_9Sb_8\ S_{21}$

Table 6. 5. Composition (weight %) and atomic proportions (%) of mineral identified as plagionite

Sample	Hg	Sb	Pb	S	As	Ag	Cl	Cu	Total
Composition									
97202-4	0.09	39.13	39.60	21.21	0.08	0.01	nm	0.10	100.3
97202-5	0.09	37.53	39.7	21.90	0.70	0.00	0.02	0.00	99.94
97203-2	0.08	38.40	39.51	21.40	0.37	0.00	0.01	0.00	99.77
Atomic proportions									
97202-4		27.26	16.21	56.10	0.09				
97202-5		25.45	16.25	57.43	0.78				
97203-2		26.75	16.17	56.61	0.36				
Average		26.49	16.21	56.71	0.41				
Ratio		0.265	0.162	0.568	0.004				

nm = not measured

Number of atoms in mineral formula of plagionite = 30
Element 1 (Pb) : 0.162 * 30 = 4.87
Element 2 (Sb) : 0.265 * 30 = 7.96
Element 2 (As) : 0.004 * 30 = 0.12
Element 4 (S) : 0.568 * 30 = 17.04
Analytical formula = $Pb_{4.87}\ (Sb,As)_{8.08}\ S_{17.04}$
Idealized formula = $Pb_5Sb_8S_{17}$

A further sulphosalt was also recognized, to which it proved difficult to attribute a name. It is a white mineral observed as individual grains in three different polished sections. The only other sulphosalt observed in association with this mineral was twinnite, and then in only one of the three polished sections. The unidentified sulphosalt shows a higher reflectance than geocronite. It occurs as anhedral grains enclosed with massive quartz and exhibits weak-to-moderate anisotropy and weak pleochroism. The results of quantitative microprobe analyses of this mineral do not yield a match with any other known sulphosalt minerals. The closest similar minerals are guettardite and twinnite, but the chemical data and microscopic characteristics are not the same. For instance, the Sb:As ratios in guettardite and twinnite are 10:9 and

3:2 respectively (Jambor, 1967), whilst the As:Sb ratio in the unidentified mineral is 1:2, which appears quite characteristic. The stoichiometry of this mineral corresponds to the ideal formula of $Pb(As, Sb)_2 S_4$ (Table 6.7).

Table 6. 6. Composition (weight %) and atomic proportions (%) of mineral identified as twinnite

Sample	Hg	Sb	Pb	S	As	Ag	Cl	Cu	Total
Composition									
97202-18	0.04	33.39	32.52	24.25	9.02	0.24	nm	0.25	99.75
97202-19	0.12	43.06	32.52	22.80	0.71	0.03	0.02	0.34	99.47
97202-20	0.11	41.73	32.48	22.67	1.20	0.02	0.02	0.43	98.67
97203-3	0.09	32.53	39.79	21.90	4.70	0.00	0.02	0.00	99.03
96115-2	0.00	27.94	41.21	23.56	8.76	0.00	mn	0.01	101.6
Atomic proportions									
97202-18		20.75	12.63	57.41	9.15				
97202-19		28.62	12.63	57.50	0.76				
97202-20		27.85	12.74	57.46	1.30				
97203-3		22.15	15.92	56.63	5.20				
96115-2		19.43	16.41	57.77	6.11				
Average		22.78	14.31	57.35	5.27				
Ratio		0.228	0.144	0.575	0.05				

nm = not measured

Number of atoms in mineral formula of twinnite = 7

Element 1 (Pb) : 0.144 * 7 = 1.01

Element 2 (Sb) : 0.228 * 7 = 1.60

Element 3 (As) : 0.053 * 7 = 0.37

Element 4 (S) : 0.575 * 7 = 4.03

Analytical formula = $Pb_{1.01}$ (As, Sb) $_{1.97}$ $S_{4.03}$ (with Sb:As $\cong$ 4.3:1)

Idealized formula = $Pb(Sb,As)_2S_4$

Table 6.7. Composition (weight %) and atomic proportions (%) of unidentified sulphosalt mineral

Sample	Hg	Sb	Pb	S	As	Ag	Cl	Cu	Total
Composition									
96115-4	0.00	13.87	43.87	23.34	18.36	0.00	nm	0.01	99.99
96115-5	0.00	14.02	42.88	24.69	17.73	0.00	nm	0.02	99.95
96117-1	0.04	14.38	41.23	26.23	17.46	0.00	nm	nm	99.41
Atomic proportions									
96115-4		8.62	14.53	59.73	17.02				
96115-5		8.70	16.14	55.64	18.73				
96117-1		8.61	15.48	57.57	17.69				
Average		8.64	15.38	57.65	17.81				
Ratio		0.087	0.155	0.58	0.179				

nm = not measured

Apparent number of atoms in mineral formula = 7
Element 1 (Pb) : 0.155 * 7 = 1.085
Element 2 (Sb) : 0.087 * 7 = 0.61
Element 3 (As) : 0.179 * 7 = 1.25
Element 4 (S) : 0.58 * 7 = 4.06
Analytical formula = $Pb_{1.085}(As,Sb)_{1.86}S_{4.06}$ (with As:Sb $\cong$ 2:1)
Idealized formula = $Pb(As,Sb)_2S_4$

6.3.3 Assemblage 3: Cu-Hg-Tl-As sulphosalt minerals

Copper and thallium concentrations in the Zarshuran ore are quite low. Copper occurs in rare chalcopyrite ($CuFeS_2$) and rare aktashite ($Cu_6Hg_3As_4S_{12}$). Thallium occurs in lorandite ($TlAsS_2$) and a mineral presumed to be christite ($TlHgAsS_3$). Mehrabi et al. (1999) mention the occurrence at Zarshuran of simonite ($TlHgAs_3S_6$), a mineral similar in composition to christite. Mercury is not only incorporated in aktashite and the Tl-minerals (christite and simonite). It is found as cinnabar (HgS), rare coloradoite (HgTe) and quantitative microprobe point analysis of gold-bearing arsenian pyrite shows up to 6000 ppm Hg. There is a strong correlation between Au and Hg confirmed by quantitative microprobe analyses and 900 chemical analyses of samples from bore holes, trenches, tunnels and outcrops.

Aktashite occurs as anhedral grains in close association with geocronite. It replaces the periphery of both anhedral and needle-shaped geocronite grains (Figs. 6.5). The stoichiometry of aktashite was calculated as shown in Table 6.8.

Christite ($TlHgAsS_3$) was suspected as the mineral observed in backscattered electron imagery in massive orpiment as bright needle-shaped inclusions, too small (<5 μm) to be analysed quantitatively (chapter 4). Christite is a very rare mineral, and was first recognized at the Carlin gold deposit (Radtke et al., 1977). Mehrabi et al. (1999) mentioned another thallium-bearing mineral at Zarshuran, galkhaite $(Hg,Cu,Zn,Tl,Fe)_6(Cs,Tl)(As,Sb)_4S_{12}$.

Lorandite ($TlAsS_2$), previously described at Zarshuran by Karimi (1993) and Mehrabi et al. (1999), was also suspected. Its presence was confirmed by XRD analysis.

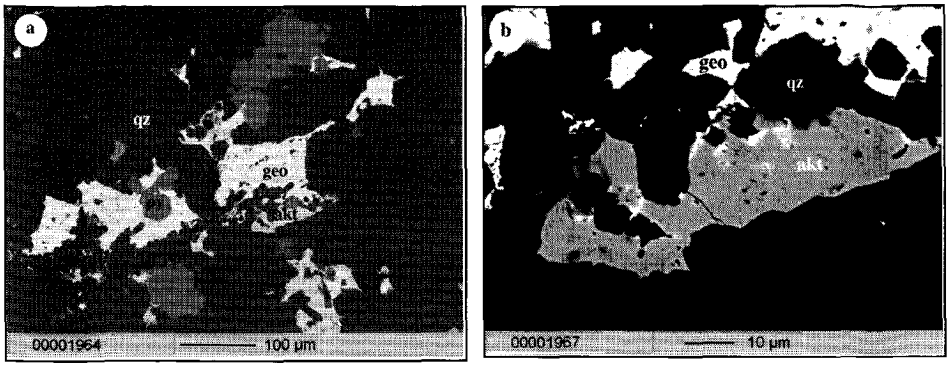

6.5. Back-scattered electron micrograph of aktashite and geocronite: (a) overview of anhedral aktashite (akt, light grey) and anhedral geocronite (geo, white) both occurring at the periphery of Au-As bearing pyrite (b) enlarged central part of map (a) showing the association of

Table 6. 8. Composition (weight %) and atomic proportions (%) of mineral identified as aktashite

	Sample	Hg	Sb	Pb	S	As	Ag	Cl	Cu	Total
Composition										
	97202-1	34.17	0.42	0.00	23.86	18.69	0.07	0.00	23.03	100.24
	97202-2	34.90	0.40	0.00	23.67	18.84	0.04	0.01	23.00	100.86
	97202-3	32.85	0.49	0.00	23.42	18.56	0.04	0.00	22.32	97.70
Atomic proportions										
	97202-1	11.13			48.63	16.30			23.67	
	97202-2	11.37			48.27	16.44			23.65	
	97202-3	10.93			48.77	16.54			23.45	
	Average	11.14			48.56	16.43			23.59	
	Ratio	0.112			0.487	0.165			0.237	

Number of atoms in mineral formula of aktashite = 25
Element 1 (Cu) : 0.237 * 25 = 5.93
Element 2 (Hg) : 0.112 * 25 = 2.8
Element 2 (As) : 0.165 * 25 = 4.13
Element 4 (S) : 0.487 * 25 = 12.18
Analytical formula = $Cu_{5.93}$ $Hg_{2.8}$ $As_{4.13}S_{12.18}$
Idealized formula = $Cu_6Hg_3As_4S_{12}$

6.4 DISCUSSION

The precipitation sequence of sulphosalt minerals can be used to determine the evolution of their parent hydrothermal fluid in terms of composition and temperature. Due to the close association between sulphosalts and gold at Zarshuran, the sulphosalt sequence can be used to infer information about the genesis of the mineralization

6.4.1 *Arsenic-antimony substitution*

In the Zarshuran arsenic ore As-Sb substitution is variable. This has been recognized in orpiment, realgar, stibnite and getchellite.

Preliminary experimental studies by Dickson et al. (1975) on the As-Sb-S system demonstrate the existence of incomplete solid solution series between orpiment and stibnite. According to Dickson et al. (1975), synthetic and natural stibnite and orpiment (from Nevada and Utah) contain up to 7 wt % As in stibnite and 1.5 wt % Sb in orpiment. The As-Sb sulphide solid solution was studied in hydrothermal conditions by Nakai et al. (1986) at temperatures of 250, 300, 350 and 400°C and a pressure of 100 bars for 1-3 weeks. They found that orpiment and getchellite formed only at 250 and 300°C respectively.

Synthetic orpiment formed at 250°C shows more Sb substitution than that formed at 300°C with the same raw material. Getchellite formed at higher temperature (300°C) deviates from the ideal $AsSbS_3$ toward the As-rich side (Nakai et al., 1986). The high antimony content of orpiment (up to 3%) and the presence of getchellite at Zarshuran suggests that they formed at relatively low temperatures. According to Weissberg (1965), the chemical composition of getchellite was first reported to be $As_{0.98}Sb_{1.01}S_3$, which is idealized as $AsSbS_3$. Subsequently getchellite has been believed to have an As:Sb ratio fixed at 1 (Nakai et al., 1986). The As:Sb ratio of the Zarshuran getchellite is around 1.

Synthetic stibnite shows up to 24 mol% As_2S_3 and crystals that form at higher temperature show a narrower Sb-As substitution range (Nakai et al., 1986). Stibnite formed at Zarshuran is heterogenous and shows a high As concentration.

6.4.2 *Sulphosalt crystallization sequence and associated temperatures*

Phase diagrams are established for the PbS-As_2S_3, Pb-As-S, PbS-Sb_2S_3 and Pb-Sb-S systems, but at Zarshuran there are also intermediate Pb-(As-Sb) compounds, for which in general no such temperature data are available. Petrographic observations show semseyite to follow galena, plagionite to follow semseyite, and twinnite to follow plagionite. For semseyite a stability range of about 350–400°C is mentioned by Moëlo (1983), based on literature reviews. The sequence galena, semseyite, plagionite, twinnite and baumhauerite is consistent with their phase relations given by Chang and Bever (1973). On the basis of petrographic observations we consider

geocronite and baumhauerite to be more-or-less contemporaneous (Fig. 6.2) and on the basis of Sb content we place geocronite after twinnite. According to Jambor (1968), copper-bearing sulphosalt minerals generally precede lead sulphosalts, but this is contradicted by our observations (Fig. 6.5). We position aktashite after baumhauerite. Finally, according to the relations described by Chang and Bever (1973), stibnite, orpiment and realgar should be at the end of the Pb-Sb-As-S mineral sequence.

Thallium-bearing minerals have been found as inclusions in, or associated with, orpiment but not with stibnite or getchellite (Mehrabi et al., 1999; Asadi et al., 2000c). They must therefore have a place in the sequence somewhere between stibnite and orpiment. This is in accordance with experimental work on these minerals indicating that their stability range must be at temperatures of 150–260°C (Radtke et al., 1974; Radtke et al., 1977). Getchellite probably postdates stibnite, but precedes or is contemporaneous with orpiment, on the basis of both observations here and those of Bariand et al. (1968). This is also in agreement with the descriptions by Weissberg (1965) of getchellite-bearing samples from the type locality in Nevada. Weissberg (1965) synthesized getchellite at 260°C and 1 kbar. Nakai et al. (1986) synthesized getchellite at 300°C. The phase diagram for the systems As_2S_3-PbS (as given by Chang and Bever, 1973) shows that orpiment may be formed at temperatures <315°C.

6.4.3 Occurrence of gold

Sparse metallic gold was only found in close association with an arsenic-mercury-thallium sulphosalt mineral, both occurring as inclusions in a matrix of microcrystalline orpiment. These inclusions were first observed by optical microscopy and subsequently confirmed by EPMA (chapter 4).

Anhedral pyrite grains commonly occur in an orpiment matrix, and EPMA revealed that this variety of pyrite contains 40-100 ppm invisible gold, an average of 0.19% arsenic and up to 2.4% arsenic. The gold concentration in this type of pyrite displays a positive correlation with the arsenic concentration. Owing to the combination of its relative abundance and typically high gold content, arsenian pyrite is the most important gold-bearing mineral at Zarshuran. Three types of arsenian pyrite are recognized.

The earliest gold-bearing arsenian pyrite is very abundant in association with sphalerite, euhedral pyrite, and lead sulphosalts (mainly geochronite, baumhauerite and semseyite) in quartz. This arsenian pyrite occurs as overgrowths on some large (5-300 μm) euhedral pyrite crystals. A sulphosalt phase consists of geochronite and baumhauerite occasionally enclosing the

overgrowth rims (chapter 4). Electron microprobe analyses of these rims pinpoint high arsenic concentrations (1.08-1.65%), high mercury concentrations (<250-480 ppm) and gold concentrations of up to 140 ppm. These concentrations compare with low concentrations of arsenic (< 0.04%), mercury (<350 ppm) and gold (<20 ppm) in the euhedral pyrite core.

A second type of arsenian pyrite encloses the overgrowth rim and geochronite, baumhauerite and semseyite. It contains a higher arsenic and mercury concentration (up to 3.4% and 5940 ppm respectively). This type of arsenian pyrite shows a network and massive texture. Microprobe analyses show a higher average gold concentration in this type of arsenian pyrite (116 ppm) compared to overgrowth rims (90 ppm).

A third type of late stage arsenian pyrite exhibits a colloform texture. Colloform arsenian pyrite contains 1030-1300 ppm gold and up to 4.73% arsenic. The highest concentrations of gold, arsenic and mercury tend to be found in the rim. It occurs in the hydrothermal silica matrix and commonly is intimately intergrown with massive and colloform sphalerite which contains up to 390 ppm gold. Colloform and massive sphalerite often replaces geochronite, baumhauerite and semseyite.

6.4.4 Evolution of the gold-mineralizing fluid

The Pb-(As-Sb)-sulphosalts are known to crystallize in a very narrow temperature range. Figure 6.6 shows the crystallization sequence and temperatures of formation of these minerals and some other associated minerals, established on the basis of mineral paragenesis and published sources (McKinstry and Kennedy, 1957; Chang and Bever, 1973; Couto et al., 1990; Moëlo, 1983; Jambor, 1968).

Apparently we are dealing with a temperature range of from at least 400°C down to 250-150°C for the minerals under discussion. From petrographic observations it is clear that the first phase of gold mineralization in Zarshuran (gold in rims of arsenian pyrite grown on barren pyrite) must precede sulphosalt formation. This is inferred from the occurrence of a combination of Pb-As-Sb sulphosalts around the rimmed Au-bearing zoned arsenian pyrite (chapter 4). It is not possible to indicate an accurate temperature for this first phase of mineralization. The well-known arsenopyrite geothermometer (Kretschmar and Scott, 1976) applies only to arsenopyrites, not to pyrites containing only a few weight percent of arsenic. Phase relations provide no definite clue to the stability ranges of geocronite, aktashite and galena. But it is possible to compare the results with data from Couto et al. (1991) who

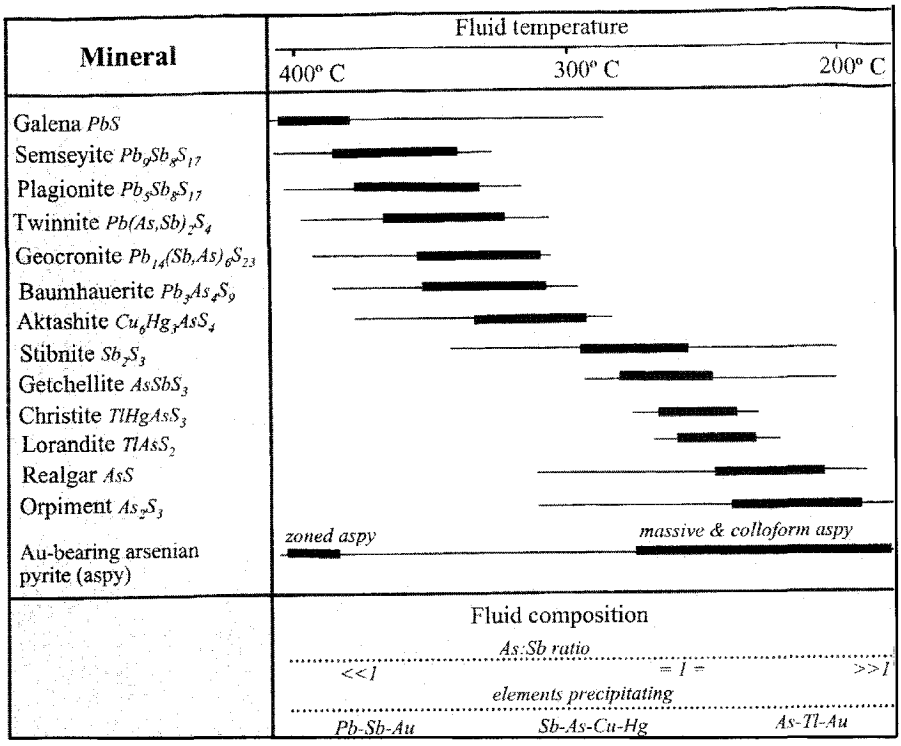

6.6. Paragenetic sequences of sulphosalt crystallization at Zarshuran and relationship with gold mineralization.

presented a range of 580 °C down to less than 340°C for sulphosalt-containing gold mineralization with arsenopyrite in Portugal. The second mineralization phase at Zarshuran, with network, massive and colloform arsenian pyrite and colloform sphalerite, postdates the sulphosalt mineralization phase. Studies of fluid inclusions in quartz associated with this gold mineralization indicate a trapping temperature of 200-270°C (chapter 7).

Although it is clear that there are two phases of gold mineralization at Zarshuran, there appears to be no need to invoke the two fluid phases suggested by Mehrabi et al. (1999). It is perfectly possible that the observed mineralization and the described mineral sequence are the result of only one evolving fluid. In the following paragraph a model is tentatively suggested for this evolution.

The original hydrothermal fluid, containing gold and arsenic in aqueous complexes, encountered barren pyrite. Being out of equilibrium, this pyrite and fluid reacted, forming arsenian pyrite rims around the barren core. The mobilized Fe destabilized the aqueous gold complex and subsequently gold precipitated in the arsenian pyrite rims. Temperatures were probably above

350°C. At the moment that these rims acquired a critical thickness, only diffusion of arsenic through this rim could lead to formation of more arsenian pyrite. Diffusion became slower and slower, so that eventually the reaction stopped. Any gold or arsenic still in solution would then remain in solution. The fluid then crystallized the observed sequence of minerals, and only later precipitated gold again, when gold-bearing colloform pyrite and colloform sphalerite formed at about 200°C (Asadi et al, 1999).

6.5 CONCLUSIONS

The sulphosalt assemblage at Zarshuran (getchellite, geocronite, aktashite, semseyite, plagionite, twinnite, baumhauerite, Tl-bearing minerals and an unidentified Pb-As-Sb-sulphosalt) precipitated in the temperature range <400°C to approximately 200°C. The sulphosalt mineral sequence and its changing As:Sb ratio suggest the evolution of a single mineralizing hydrothermal fluid from which gold precipitated prior to and subsequent to the main sulphosalt precipitation phase. The first phase of gold mineralization was derived from an antimony-rich and arsenic-poor fluid at a temperature higher than 300°C. The second phase of gold mineralization was derived from an arsenic-rich fluid at a temperature range of 150-250°C.

Chapter 7

MINERALIZING FLUIDS

In this chapter data from microthermometric analysis of fluid inclusions observed in eleven doubly-polished sections, prepared from unmineralized and mineralized rocks, are used to explain the physical and chemical conditions of the formation of ore and associated minerals at Zarshuran. These genetic concepts are then used to identify some exploration guidelines (i.e., depth of mineralization, sources of gold and associated elements in the mineralizing hydrothermal solutions and information about the heat sources driving the migration of the hydrothermal solutions) in order to guide the search for similar mineralization in the neighbouring areas.

7.1 INTRODUCTION

At Zarshuran, the hydrothermal solution introduced a large amount of silica to the host rocks at the expense of CaO and CO_2. Large sterile jasperoid bodies precipitated from the early hydrothermal solution, whilst mineralized quartz veins with variable carbon content were deposited during the main and late periods of hydrothermal solution evolution. The mineralized hydrothermal quartz contains arsenian pyrite, massive and colloform sphalerite and arsenic sulphides, which are the main host minerals for gold mineralization. Small amounts of very fine-grained native gold, found as inclusions in late quartz and orpiment, probably precipitated from this solution during the period in which the main hydrothermal assemblage was formed.

Other minerals of hydrothermal origin (and potentially containing fluid inclusions) include fluorite, barite and sphalerite. Fluorite crystallized in veins, veinlets and open-space

fillings during the main and late stages of hydrothermal mineralization. Barite crosscuts the carbon-rich mineralized jasperoid and appears to occur at the end of main stage. Sphalerite shows a massive and colloform texture and occurs in close association with fluorite, quartz and gold-bearing arsenian pyrite, at the end of the main stage or at the late stage. Paragenetic sequences at Zarshuran are discussed in detail by Asadi et al. (1999).

The study of fluid inclusions at Zarshuran is intended to determine fluid compositions and fluid densities. These data provide information about the chemical environment, pressure and temperature (PT) at the time of mineralization and fluid entrapment (Roedder, 1984). Based on a combination of the fluid inclusion data, mineral paragenesis, mineral stability and geologic evidences, the likely pressure-temperature conditions during gold mineralization are proposed.

7.2 METHODS

Analyses of fluid inclusions can involve a number of tests, in particular heating and freezing measurements (Goldstein and Reynolds, 1994). Doubly-polished wafers, about 100 μm thick, of the ore, host rocks and veins at Zarshuran, were prepared and used for fluid inclusion studies in fluorite, quartz, barite and sphalerite, following the standard procedure commonly applied in microthermometric laboratories (Shepherd et al., 1985). Following the procedure described by Touret (1977), the first step of the analysis was to make drawings and descriptions of the occurrence and distribution of fluid inclusions as observed under the microscope during the petrographic studies. A microthermometric study was then carried out to determine the phase changes in fluid inclusions under controlled conditions of heating and cooling.

Temperatures measured for aqueous inclusions during the phase transitions include: (a) first ice melting or eutectic temperature (T_e); final ice melting (T_m); CO_2–clathrate (T_{clat}); and total homogenization temperature (T_h). Details of the procedure and technique of interpretation are described by Roedder (1984) and Goldstein and Reynolds (1994).

Microthermometric measurements on fluid inclusions were carried out the Department of Earth Sciences, Free University of Amsterdam, using a Linkam 600 heating/freezing stage provided with a thermal control (TMS-90, TP-91) and an Olympus microscope (BH-2) with a maximum magnification of 625. The stage is connected to a video system to allow monitoring of inclusions on a video screen. For cooling and heating, liquid nitrogen and a thermal resistor are used, respectively. The stage is calibrated with natural standards (CO_2 inclusions for –56.6°C and solutions of known salinities for temperature around 0°C).

Of particular importance are the temperatures of phase transitions, *viz.*, initial ice-melting or eutectic temperature (T_e), final ice-melting temperature (T_m), and homogenization temperature (T_h). In order to define the temperature of ice melting, first the inclusions are cooled until the vapour bubbles freeze, then the temperature is raised until the vapour bubbles reappear. During heating the occurrence of the first droplet of liquid corresponds to the first ice melting temperature (T_e) and could reflect the type of salt (i.e.,

NaCl, KCl, MgCl or $CaCl_2$) in fluids. The temperature at which the last solid crystal disappears and the vapour bubbles reappear is the final ice-melting temperature (T_m), which yields information on the chemical composition of the system. The final ice melting temperatures are used to estimate the salinity, which usually is measured in equivalent NaCl (weight %). Fluids of given salinities may then be tentatively related to the different mineralization events.

The other important temperature to be measured is the homogenization temperature (T_h) at which the liquid or vapour disappears. This can occur either by expansion of the vapour (T_{hv}), by expansion of the liquid (T_{hl}), or by sudden changes around the vapour bubble, without any expansion of the liquid/vapour phase (T_c). If, in a measurement, only homogenization to liquid is observed, this indicates fluids of relatively high density. For good measurements the rate of heating is very important. Inclusions are heated at a controlled rate of initially 50°C per minute, then the rate is reduced to 1°C per minute as the temperature is approached at which the vapour bubble disappears. This temperature is recorded as the homogenization temperature (T_h) which, combined with the composition, indicates the density (or molar volume) of the fluid.

For an inclusion of a known composition, the homogenization temperature defines the position on the fluid isochore at the time of trapping (in the case of homogeneous fluid).

7.3 SAMPLE DESCRIPTION

Fourteen samples of ore, quartz veins and veinlets, silicified black shale and carbonate host rocks and altered igneous rocks were collected from exploration tunnels, trenches, outcrops and bore holes at Zarshuran gold deposit for fluid inclusion studies. Based on earlier mineralogic studies (chapter 4) and additional microscopic studies, three types of mineralized, weakly mineralized and unmineralized samples were identified. Descriptions of the samples based on their examination under the microscope are given in Table 7.1.

Petrographic studies of thin and polished sections revealed that 11 samples contained fluid inclusions. Eleven doubly-polished wafers (80-100 μm) were prepared from those parts of these samples that best showed a close association between ore minerals and the transparent gangue minerals that could host fluids. Drawings and descriptions were made of the occurrence and distribution of fluid inclusions as observed under the microscope. The following minerals were identified as hosts of fluid inclusions:

(1) fluorite in patches associated with sphalerite in unoxidized silicified ore located in close association with orpiment and realgar veins (sample 96115);
(2) barite cross-cutting the carbon-rich jasperoid in highly mineralized ore (sample 9701);
(3) quartz intergrown with orpiment and realgar in a silicifed vein within the black shale host rock (samples 96117, 96118, BH1-79);
(4) quartz enriched in carbon associated with orpiment, colloform and massive arsenian pyrite (main gold-bearing minerals), sphalerite and sulphosalts (sample 96122);

(5) quartz phenocrysts of a mylonitized and altered granitoid (samples 96108, 96109);
(6) weakly mineralized carbon-poor, milky quartz from the central part of a vein (sample 9702);
(7) quartz of large outcropping bodies of unmineralized jasperoids (96106);
(8) unmineralized quartz associated with a tuff (sample 96116); and
(9) sphalerite associated with fluorite (sample 96115).

Table 7.1. Description of the samples used for fluid inclusion studies

Sample No.	Rock Type/ Mineral	Location	Remarks
Mineralized			
96122	Carbon rich jasperoid	Tunnel 8	Occurrence of carbon-rich quartz and milky quartz associated with visible orpiment and massive colloform arsenian pyrite, the main host for gold. Cavities of up to 1 cm present in the black shale, which are filled with orpiment and idiomorphic microcrystalline quartz
96117 96118	Quartz with orpiment	Tunnel 8	Occurring in the quartz veins, arsenic ore
BH1-79	Black shale	79 m depth in bore hole no. 1	Finely laminated carbon-rich silicified shale (carbonaceous ore) with visible orpiment
BH10-85	Limestone and As minerals	85 m depth in bore hole no. 10	Limestone with visible orpiment and pyrite
96115	Jasperoid	Tunnel 8	Visible sphalerite and fluorite in hand specimen
9701	Black shale	Tunnel 9	Carbon-rich silicifed shale with cross cutting barite
96112	Quart veins	50 m to the northwest of mine office	Quartz veins containing barite, calcite and pyrite located in the Chaldagh limestone
Weakly-Mineralized			
96105	Silicified black shale	Karbalai-Abbas river	Finely laminated carbon-rich shale
96108 96109	Altered granitoid	Southeast of the mine river, near the bore hole no. 1 and also Karbalai-Abbas river	White rock with large quartz phenocrysts occurring in the matrix of fragmented sericite and clay minerals, weakly mineralized by pyrite and cinnabar; low Au content
9702	Quartz vein	10 m to the west of Tunnel 9	Quartz vein occurring at the contact of Chaldagh limestone and black shale unit. Milky quartz associated with carbon-rich quartz. White spots within the samples are possibly evidence of hydrothermal alteration. Sample partially shows ferrogenization (red spots)
Unmineralized			
96106	Jasperoid	25 m to the west of mine office	Carbon poor jasperoid with grey-white colour
96116	Quartz veins	150 m to the west of tunnel 9	Quartz veins cutting through the Qaredash formation

Inclusions in unmineralized quartz associated with tuff, in orpiment and in calcite are relatively rare, and smaller in size. This makes measurements difficult and none were attempted.

Examination of the doubly-polished wafers under both reflected and transmitted light, combined with mineralogic and petrographic data from electron microprobe analysis of the same samples (chapters 4, 5 and 6) suggests three stages (early, main and late) of hydrothermal mineralization. It appears that the unmineralized carbon-free quartz and possibly weakly-mineralized quartz phenocrysts of altered granitoid rocks were formed in the early stage. The main stage is characterized by the widespread occurrence of carbon-rich quartz associated with different sulphides and sulphosalts. Sphalerite shows a massive and colloform texture and occurs in close association with fluorite, carbon-rich quartz and gold-bearing arsenian pyrite. Colloform sphalerite, colloform arsenian pyrite and fluorite appear to form at the end of the main stage or at the late stage hydrothermal mineralization. Barite crosscuts the mineralized carbon-rich quartz and appears to have formed at the late stage hydrothermal mineralization.

7.3.1 Mineralized samples

The studies of the four wafers of mineralized samples of main stage of hydrothermal mineralization (samples 96117, 96118, 96122) and the late stage of hydrothermal mineralization (sample 96115) confirmed the abundance of fluids in: (a) carbon-rich quartz intergrown with massive orpiment, massive arsenian pyrite; (b) fluorite associated with massive sphalerite; (c) barite associated with the carbon-rich jasperoid and pyrite grains; and (d) sphalerite. Fluids observed in orpiment were rare and it proved difficult to make microthermometric measurements on them.

7.3.1.1 Quartz intergrown with sulphides (main mineralization stage)

Hydrothermal quartz associated with orpiment, arsenian pyrite, pyrite and sphalerite (samples 96117, 96118, 96122) contains liquid-rich fluid inclusions. Four types can be distinguished.

(1) Randomly-distributed liquid-rich primary inclusions (5-50 μm). The relative proportion of vapour bubbles to liquid varies in different samples. Most contain 5-30 percent vapour bubbles (Fig 7.1). These inclusions often show irregular shapes and occasionally show necking-down features which could be a sign for the beginning of decrepitation (Barrie and Touret, 1999)

(2) Naturally decrepitated (exploded) inclusions and/or leaked inclusions occur in quartz associated with sulphide minerals (arsenian pyrite, orpiment, base metal sulphides) and sulphosalt minerals. These inclusions are related to syngenetic depositional decompression of the host quartz during uplift and opening of the veins during quartz precipitation from hydrothermal fluids. The decrepitation

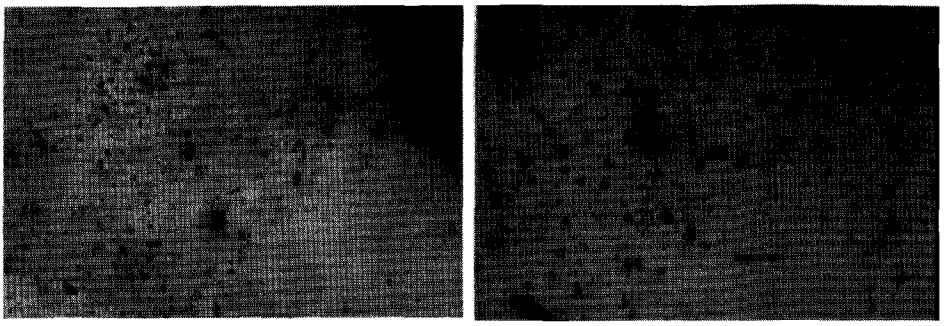

Fig. 7.1. Randomly-distributed liquid-rich primary inclusions in the mineralized quartz (right: overview, left: detail), black spots are decrepitated inclusions (sample 96102). Scale bar = 30 μm.

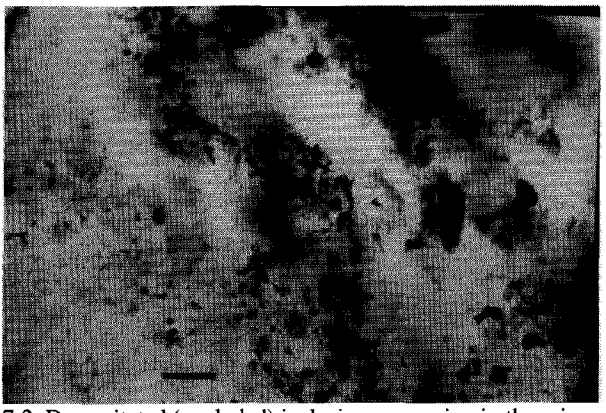

7.2. Decrepitated (exploded) inclusions occurring in the mineralized quartz (sample 96102). Scale bar = 30 μm.

phenomena is manifested by clusters of black, star-shape, empty inclusions distributed throughout the quartz (Fig. 7.2).

(3) Small inclusions (2-15 μm) preserved in the growth zonation of idomorphic quartz. These are mostly homogeneous, liquid-rich inclusions that are primary and formed during quartz precipitation from hydrothermal fluids.

(4) Secondary trails of liquid-rich inclusions (2-15 μm). These inclusions contain <10 percent vapour bubbles.

7.3.1.2 Fluorite intergrown with sphalerite (late mineralization stage)

There are numerous large fluid inclusions of different generations in fluorite associated with sphalerite that contains up to 390 ppm gold (sample 96115). Fluids occurring in fluorite are mainly liquid dominated. Many of them are isolated and randomly distributed throughout the fluorite, suggesting that they may be of primary origin There are also fluids

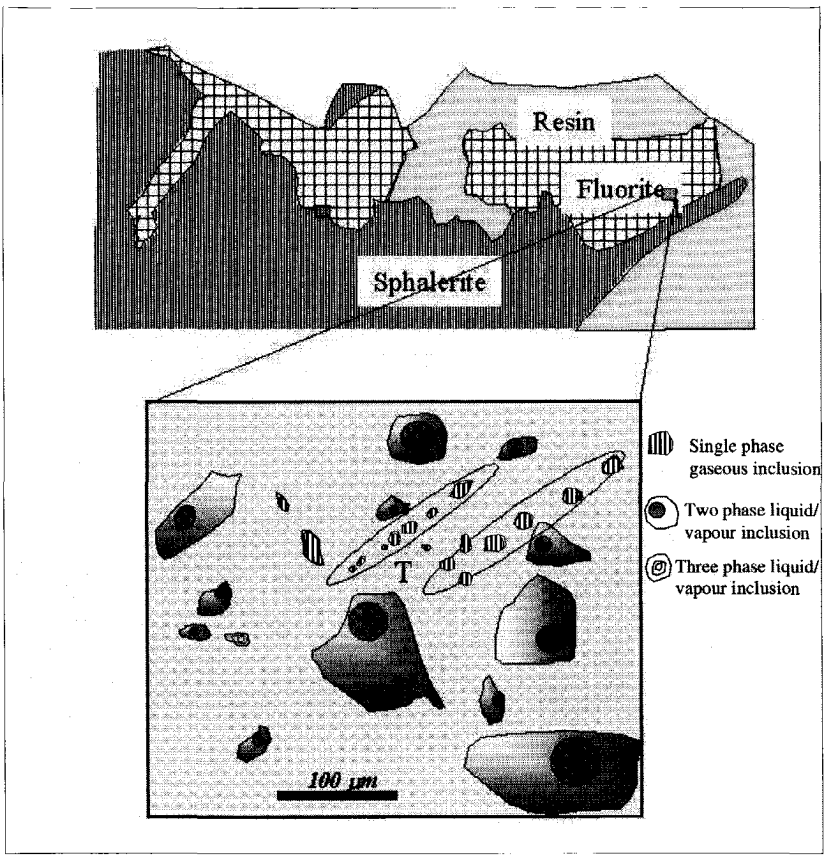

Fig. 7.3. Distribution of large, isolated liquid-rich inclusions and trails of pseudosecondary gas-rich inclusions (T) in fluorite (sample 96115)

in planar groups and in fractures of fluorite suggesting pseudosecondary and secondary origins, respectively.

Two major types of liquid-dominated and vapour-dominated fluids occur in fluorite (Fig. 7.3). In terms of chronology or origin, these two major types are manifested by four subtypes.

1) Randomly distributed liquid-rich fluid inclusions (1a) mostly occur as negative crystals, contain both liquid and vapour phases and appear to be primary in origin. They are generally homogeneous; the liquid-vapour ratio in most of these fluids is almost constant (about 15-25 volume percent of the fluids are filled with vapour bubbles). The size of these inclusions varies from <5 μm to 150 μm (Figs 7.4). When frozen, a pale-yellow colour may sometimes appear.
2) Pseudosecondary trails of liquid-rich inclusions (1b), forming trails, are the most abundant type in fluorite (Fig. 7.5). Their size varies between <5 and 50 μm and

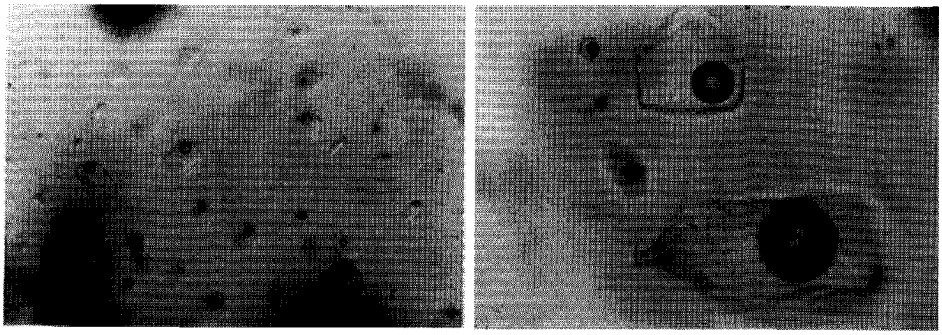

7 4. Primary aqueous inclusions in fluorite (left: overview, right: detail), sample 96115. Scale bar = 50 μm.

their liquid-vapour ratio varies across a comparatively wide range (heterogeneous), with about 15-40 volume percent of an inclusion filled with vapour bubbles.

3) Pseudosecondary trails or clusters of gas-rich inclusions (2a) are found parallel to and in close association with the trails of liquid-rich pseudosecondary inclusions (Fig 7.5) or sometimes occur near the large, isolated liquid-rich fluid inclusions (Fig. 7.6). These inclusions are mostly less than 15 μm in size. Most are mono-phase vapour inclusions; the vapour and liquid phases are not clearly separable. Some contain 70-95 volume percent vapour bubbles. Smaller trails of vapour-rich pseudosecondary inclusions are also found in close association with large, isolated liquid-rich inclusions. This type of inclusion occasionally exhibits three phases (at room temperature two concentric bubbles floating in a liquid). These correspond to the well known (Roedder, 1984) H_2O-CO_2 inclusions (from the centre to the wall of the cavity, CO_2-gas, CO_2-liquid and H_2O-liquid).
4) Secondary trails of small liquid-rich inclusions (<5–15 μm) occur in fractures and intersect the mineral grain boundaries. These could post-date the precipitation of the fluorite. The gas bubble is very small or absent; therefore they appear to be dominantly mono phase liquid inclusions.

Also visible in fluorite is a transition from one inclusion type to another. Near the contact with massive sphalerite there are a few primary liquid-rich fluids in the fluorite. Further into the fluorite, these give way to numerous trails of pseudosecondary inclusions (both liquid-rich and vapour-rich).

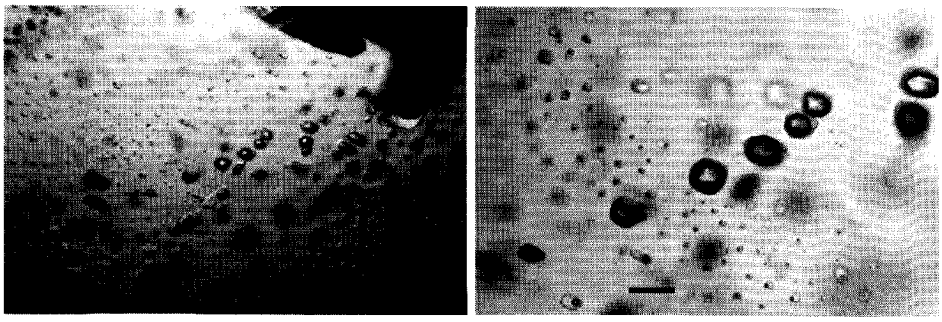

Fig. 7.5. Trails of pseudosecondary vapour-rich inclusions and aqueous inclusions in fluorite, sample 96115. Scale bar = 30 μm.

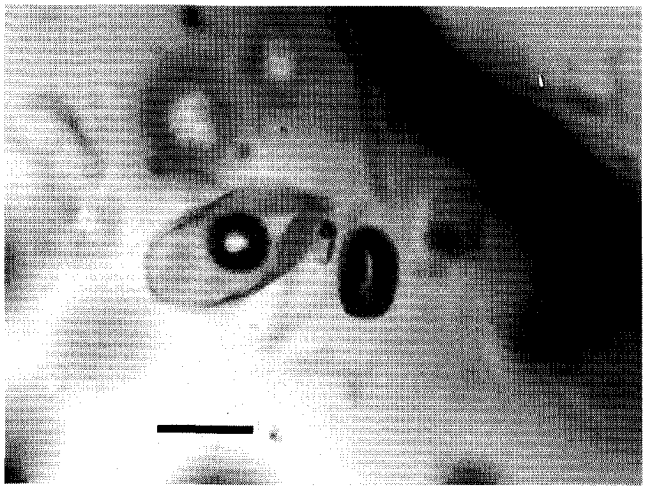

Fig. 7.6. Occurrence of isolated two phase liquid-rich inclusion and single phase gas-rich inclusion (black) in fluorite, sample 96115.

7.3.1.3 Barite

Barite containing fluid inclusions is associated with gold-mineralizing zones in carbon-rich jasperoidal silica (samples 9701, 96112). This barite contains two types of inclusions, liquid-rich and vapour-rich.

Liquid-dominated inclusions are rare and have both liquid and vapour phases. The liquid-vapour ratio is not constant and some inclusions contain only five volume percent vapour bubbles. These inclusions are randomly distributed and appear to be primary.

Vapour-dominated inclusions are more abundant and are found as both isolated inclusions and trails. The liquid-vapour ratio is similarly not constant; some inclusions contain more than 95 volume percent vapour bubbles.

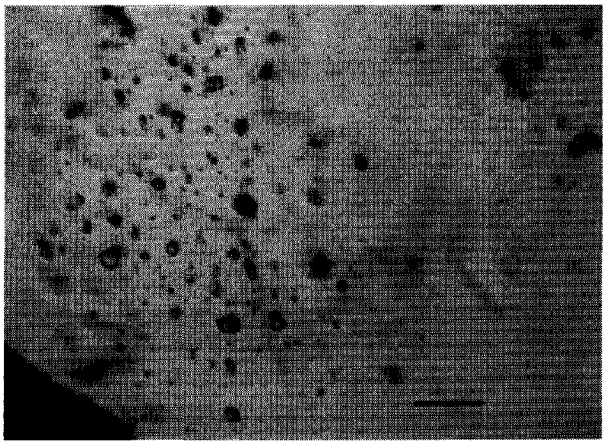

Fig. 7.7. Primary gaseous-rich and aqueous inclusions in weakly-mineralized quartz (sample 9702). Scale bar = 50 μm.

7.3.1.4 Sphalerite

Fluid inclusions are found in a few sphalerite grains (sample 96115). There are a few large isolated liquid-rich primary inclusions (up to 30 μm) and several trails of small liquid-rich inclusions. Some primary inclusions are located along the growth zonation of sphalerite. The trails do not intersect the mineral grain boundaries, and so can be considered as pseudo-secondary inclusions.

7.3.2 Weakly mineralized samples

The studies of four doubly-polished wafers confirmed the presence of measurable fluids in the weakly-mineralized carbon-free milky quartz of veins (Sample 9702) and the quartz phenocrysts of weakly-mineralized, altered granitoids (96108 and 96109). Two main types of aqueous fluids (5-40 μm) and vapour-rich fluids (2-20 μm) were observed. Both are isolated and randomly distributed in the quartz, suggesting a primary origin. These inclusions are very abundant in the weakly-mineralized milky quartz (sample 9702, Fig 7.7). The aqueous fluids are homogeneous (degree of fill 0.85-0.75). Vapour-rich inclusions are characterized by 70 percent vapour bubbles up to nearly pure CO_2 inclusions. There are also numerous three-phase inclusions in the milky quartz (sample 9702). The relative proportion of H_2O and CO_2 in the three-phase inclusions are nearly constant (V. CO_2 = 35-40%). All three-phase inclusions appear two-phase at 25°C, with CO_2 only separate as a vapour bubble below 10°C. Secondary trails of H_2O-rich inclusions (2-10 μm) and vapour-rich inclusions (2-15 μm) are also present in this type of quartz.

7.3.3 Unmineralized samples

The fluid inclusions in the unmineralized quartz (samples 96106, 96112 and 96116) are relatively smaller in size and compared to the weakly-mineralized quartz it is rather difficult to perform microthermometric measurements on them. Two major types of liquid-rich inclusions and vapour-rich inclusions, which are isolated and randomly distributed, are found in this quartz. These inclusions are very similar to those observed in the weakly-mineralized quartz.

7.4 MICROTHERMOMETRIC DATA

7.4.1 Fluid types

Based on the constituent phases at room temperature and on microthermometric behaviour, two major compositional types of fluid inclusions (with subtypes) were recognized in quartz, fluorite, barite and sphalerite: (1) aqueous and (2) gaseous (CO_2-rich). Table 7.2 summarizes their characteristics.

7.4.1.1 Water dominated inclusions (W types)

Aqueous or liquid-dominated inclusions can be identified by their transparent colour. They range in size from <5 to 150 μm. At room temperature, there are two types of inclusions, monophase aqueous type and biphase aqueous-gaseous type. In terms of compositions (salinity), these inclusions can be divided into three subtypes.

1) Low salinity aqueous inclusions (W_1), characterized by final melting close to 0°C, are mostly small and appear to be pseudosecondary. They sometimes occur as monophase aqueous inclusions. Compared to the other aqueous inclusions, they often show a low homogenization temperature.
2) High salinity aqueous inclusions (W_2) are characterized by a low final ice melting temperature (T_m). The size of the vapour phase in these inclusions varies but makes up less than 20 percent of total volume. They are very abundant and occur both as trails and randomly-distributed inclusions in fluorite, quartz, barite and sphalerite.
3) A third type of aqueous inclusion (W_3) contains a small halite cube at room temperature. These inclusions are large, isolated inclusions occurring in fluorite and in mineralized quartz. They sometimes show traces of black materials that could be organic matter. The vapour phase makes up 20-25 percent of the total volume. Compared to the other aqueous-rich inclusions, they often show relatively higher homogenization (T_h) temperatures.

Table 7.2. Major compositional types of fluid inclusions at Zarshuran

Sample	Fluid type		T_e °C	T_m°C (H_2O)	T_m°C (hyd.)	T_m°C (CO_2)	T_h°C (CO_2)	T_h°C total	Density gr/cm^3	Salinity wt%NaCl equival.
Early Stage										
9702, 96108 96122	Aqueous (W1 in quartz)	Min Max N Mean		-0.3 -5.7 22 -2.3				170 350 73 251	0.72 0.87 8 0.79	0.5 8.8 22 3.8
9702 96108 96122	Gaseous (quartz)	Min Max N Mean				-57.8 -56.4 13 -56.8	12.5 21.5 12 17.8	229 360 18 286		
Main Stage										
9701 96117 96118 96122 Bh1-79	Aqueous (quartz)	Min Max N Mean	-25 -50 13 -41	-1.2 -22.2 34 -7.8	-22.2 -21.1 8 -21.5			150 330 82 215	0.68 0.96 12 0.85	1.8 21.4 34 11.5
96115	Aqueous (sphaleri-te)	Min Max N Mean		-1.2 -8.9 8 -5.1				140 235 47 192	0.75 0.86 3 0.8	 7.8
Late Stage										
96115	Aqueous (W1 and W2 in fluorite)	Min Max N Mean		-0.5 -11.5 125 -5.75				120 258 112 196	0.6 0.85 12 0.74	0.9 15.8 125 10.1
96115	Aqueous (W3 in fluorite)	Min Max N Mean	- 52 -35 47 -46.4	-7.1 -20 80 -11.3	-24.5 -5.0 30 -17.1			160 300 95 213	0.75 0.88 15 0.82	10.6 22.7 80 15.6
96115	Aqueous (two phase in fluorite)	Min Max N Mean		-11.5 -2.0 26 -5.4				194 286 5 234		
96115	Gaseous (in fluorite)	Min Max N Mean				-56.9 -56.4 9 -56.7	11.5 13.6 5 12.4	245 335 18 266		
96115	Gaseous (mono phase in fluorite)	Min Max N Mean				-56.9 -56.5 12 -56.7	10.0 13.3 6 12.5			

7.4.1.2 Gaseous inclusions

These fluids are present in fluorite, weakly-mineralized quartz, unmineralized quartz and barite. In the mineralized quartz these are all decrepitated or totally leaked out. Naturally-decrepitated and/or leaked inclusions occur commonly in the quartz associated with pyrite, arsenian pyrite, orpiment and realgar. On the basis of optical properties and microthermometric data, three subtypes of gaseous inclusions were identified.

1) Monophase inclusions in fluorite are medium size (10-35 μm) with a negative crystal, tabular to equant shape, but smaller in quartz (3-10 μm) with equant shape. They nucleate a vapour bubble below 10°C. In fluorite and barite they are pseudosecondary with medium relief and dark appearance, but in weakly-mineralized quartz they are minute and primary. Upon cooling, freezing of these fluids often occurs between –85 and –95°C. Upon heating (after freezing) melting occurs close to the CO_2 triple point (-56.6°C). They show an average clathrate temperature at 11°C.
2) Mixed (aqueous-gaseous) inclusions are identified by a liquid-vapour phase separation below 10°C (CO_2 gas, CO_2 liquid and H_2O). They occasionally occur in fluorite and are abundant in weakly-mineralized quartz. Melting of these fluids occurs slightly below the CO_2 triple-point temperature, indicating the presence of additional components such as $CH_4 \pm N_2$ (Roedder, 1984).
3) Gaseous-rich or vapour-dominated inclusions contain both a liquid and a vapour phase, but the volume of the vapour phase exceeds that of the liquid phase and is typically 65-80 percent of the total volume of the inclusion. They show an average clathrate temperature at 10°C and commonly exhibit higher total homogenization temperatures than the aqueous-rich inclusions. These inclusions only occur as pseudosecondary trails in fluorite.

7.4.2 Early stage fluid composition

Two types of isolated and randomly-distributed aqueous-rich inclusions and gaseous-rich inclusions are observed in the unmineralized quartz and weakly-mineralized quartz. These aqueous inclusions show a low salinity (W_1), a similar distribution and microthermometric behaviour in both types of quartz. The size of inclusions in the unmineralized quartz is slightly smaller. The microthermometric measurements of fluids from these two types of quartz are therefore combined and used for determination of fluid composition in the early stage of hydrothermal mineralization.

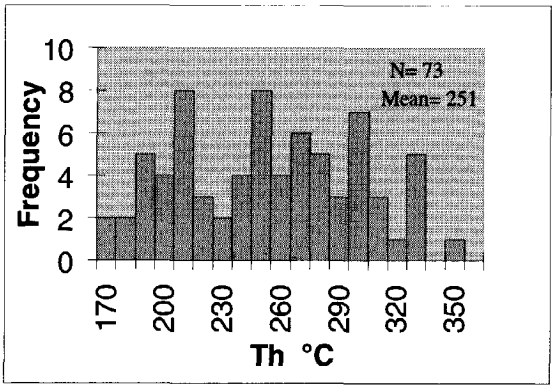

7.8 Frequency histogram of the homogenization temperatures in aqueous inclusions in unmineralized and weakly-mineralized quartz, (samples 9705, 96108, 96105, 96106)

7.4.2.1 Aqueous inclusions (W_l)

The size of these inclusions in unmineralized and weakly-mineralized quartz is relatively small and therefore it is very difficult to measure first ice melting temperatures. Final ice melting temperatures, measured from 22 inclusions in three samples of weakly-mineralized quartz, indicated a low salinity (T_m ranging from –0.3 to –5.7, with an average of –2.3).

The homogenization temperature of aqueous inclusions was rather easier to measure. These inclusions in unmineralized and weakly-mineralized quartz have homogenization temperatures that belong to one of two populations, a higher-temperature population, ranging between 230-350°C, and a lower-temperature population, ranging between 170-220°C (Fig. 7.8).

Salinities of these inclusions, calculated in the system H_2O-NaCl on the basis of final ice melting temperatures (T_m) (Potter et al. 1978), range form 0.5 to 8.8.wt% NaCl equivalent (with a mode at 3.8 wt% NaCl equivalent). These fluids show bulk densities of 0.82 to 0.97 g/cm^3.

7.4.2.2 Gaseous inclusions

Both three-phase gaseous-rich and monophase inclusions are observed in the unmineralized and weakly-mineralized quartz. These two types of inclusions show a triple-point melting temperature (T_hCO_2) ranging between -57.5 and -56.8°C, indicating the presence of CO_2 as the dominant gas with traces of CH_4 and/or N_2 in the system. In the three phases inclusions, which are the dominant gaseous inclusions, the CO_2 vapour phase homogenizes to CO_2 liquid at temperatures in the range of 12.5-21.5°C and both CO_2 phases homogenize to liquid (disappearance of CO_2 interface) at temperatures in the range of 229-360°C. These inclusions show an average clathrate temperature of 8.1°C, an average partial CO_2 homogenization temperature of 17.8°C and an average total homogenization

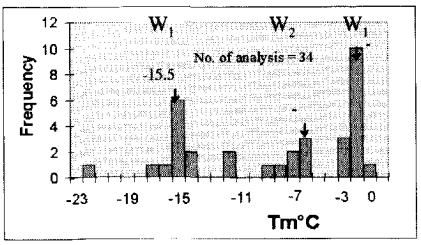

Fig. 7.9. Frequency histogram of the final ice melting temperatures of the aqueous inclusions in the mineralized quartz, labeled values represent averages and the values in brackets represent salinities in wt% NaCl

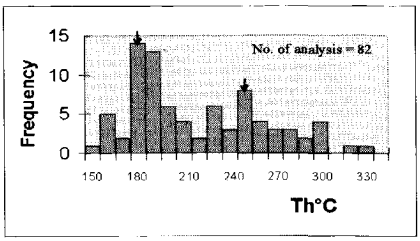

Fig. 7.10. Frequency histogram of the homogenization temperatures of the aqueous inclusions in the mineralized quartz, labeled values represent averages (samples 9701, 96122, 96117)

temperature of 286°C. Three phase gaseous inclusions show a bulk density of 0.94 g/cm^3 and a molar volume of 23.03 cm^3/mole (Touret, 1977 and Roedder, 1984).

Both fluid types (CO_2-rich and low salinity aqueous) can not be synchronous in a given sample. Detailed observation shows that the CO_2-rich fluids are early compared to later low salinity aqueous fluids.

7.4.3 Main stage fluid composition

First ice melting temperature (T_e), final ice melting temperature (T_m) and homogenization temperature (T_h) were used to analyze the chemical composition of the aqueous-rich inclusions in the (main stage) mineralized quartz. T_m and T_h were only measured on the aqueous inclusions trapped in mineralized quartz, barite and sphalerite. For these fluids T_m varies from –22 to -0.5°C, indicating a relatively wide range of salinity.

7. 4.3.1 Aqueous inclusions (W_1 to W_3)

First ice melting temperature (T_e) of the aqueous-rich inclusions in the (main stage) mineralized quartz was found to be, in most cases, difficult to measure. A few measurements from a few aqueous-rich fluids with small halite cube (W_3) showed first ice melting temperatures from –25 to -50°C. These inclusions often show an average hydrohalite melting temperature of about –21.5 °C in quartz.

Final meting varies on a wide range characterizing the three different types of aqueous-rich inclusions (W_1, W_2 and W_3) (Fig. 7.9). These fluids have an average Tm –7.8°C. Some of the large inclusions (W_3) show an average hydrohalite melting temperature –21.5°C. The ranges of T_m determined from these fluids correspond to salinities between 1.8 and 21.4

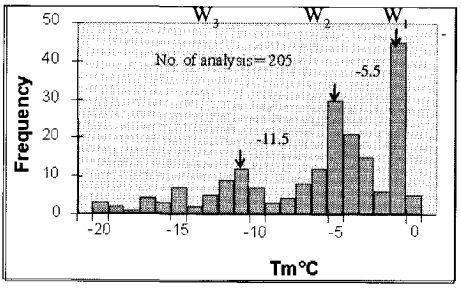

Fig. 7.11. Frequency histogram of the final ice melting temperatures of the aqueous inclusions in the fluorite, the values in brackets represent salinities in wt% NaCl (sample 96115)

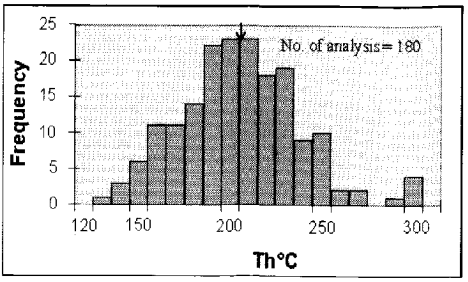

Fig. 7.12. Frequency histogram of the homogenization temperatures of the aqueous inclusions in the fluorite (sample 96115)

wt% NaCl equivalent. Three salinities calculated for different modes T_m are shown in Figure 7.9. These inclusions show densities between 0.68 and 0.90 g/cm^3.

Figure 7.10 shows the histogram of the homogenization temperatures (T_h) in the different subtypes. These fluids show two populations and an average T_h 215°C.

7. 4.3.2 Gaseous inclusions

In the (main stage) mineralized quartz, the gaseous-rich inclusions are commonly decrepitated. Those that are not did not show any phase changes during the microthermometric analysis.

7.4.4 Late stage fluid composition (W_1 to W_3)

7. 4.4.1 Aqueous inclusions

A few measurements, although not very clear, from the low salinity inclusions (W_1) and high salinity inclusions (W_2) in (late stage) fluorite showed inconsistent first ice melting temperatures (T_e) from -20 to 50°C. It was possible to measure a clear and accurate T_e from several inclusions with small salt cubes (W_3). These inclusions when frozen commonly show a pale-yellow colour and a T_e between -35 to -52°C. Comparing these measurements with the eutectic temperature of chlorides (Barrie and Touret, 1999) indicates the presence of salts other than NaCl, possibly $CaCl_2$, in the system. These inclusions often show an average hydrohalite melting temperature of about –17°C. They often show a wide range of T_m from –7.1 to –20°C.

Aqueous fluids in fluorite show a wide range of T_m characterizing the three different types of aqueous-rich inclusions (W_1, W_2 and W_3) (Fig. 7.11). The histogram of the final ice

melting temperatures of the aqueous-rich fluids in (late stage) fluorite shows three populations (Fig. 7.11). The first population corresponds to the low salinity inclusions (W_1), with T_m near to pure water (T_m -0.5 to -3.5°C). The second shows relatively high T_m (-3.8 to -8°C) corresponding to the high salinity aqueous-rich inclusions (W_2). The third shows a relatively very high salinity with Tm ranging from -8 to -20°C corresponding to the aqueous-rich inclusions with small salt cubes (W_3).

All these inclusions homogenize to a liquid phase at temperatures in the range of 130–300°C, with a mode at 201°C (Fig. 7.12). The ranges of T_m on these fluids correspond to salinities between 1.7.and 22.7 wt% NaCl equivalent. The calculated salinities corresponding to each fluid population are shown in Figure 7.11. These inclusions show bulk densities between 0.7 and 0.92 g/cm^3.

In addition, T_m and T_h were also measured from a few inclusions of this type in sphalerite. These inclusions show an average T_m of –5.1°C and T_h of 192°C. These correspond to a salinity of 7.8 wt% NaCl equivalent and a density of 0.8 g/cm^3.

Figure 7.13 is a diagram showing T_m versus T_h in this type of fluid in fluorite. This diagram indicates that the cooler fluids exhibit higher salinities.

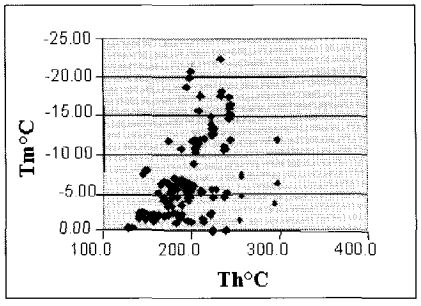

Fig. 7.13. Diagram of final ice melting temperatures versus homogenization temperatures in aqueous inclusions in fluorite.

7.4.3.2 Gaseous inclusions

In fluorite gaseous-rich inclusions show a triple point melting temperature (T_hCO_2) of -56.9 to -56.5°C. These temperatures indicate the presence of CO_2 as the dominant gas and possibly the presence of traces of CH_4 and/or N_2 in the system. These inclusions show a clathrate temperature of ± 11°C and an average partial CO_2 homogenization temperature (by vapour disappearance or homogenization to CO_2 liquid) of 12.7°C. Total homogenization temperatures (homogenization to H_2O) of these inclusions range between 245-335°C (with an average of 266°C). These inclusions show an average bulk density of 0.82 g/cm^3 and a molar volume of 39.2 cm^3/mole (Touret, 1977 and Roedder, 1984).

7.5 DISCUSSION: PRESSURE AND TEMPERATURE OF FLUID ENTRAPMENT

When, in a given mineral, synchronous generations of aqueous and gaseous inclusions coexist, it is theoretically possible to determine P-T conditions of trapping by "crossing" the representative isochores (e.g., Touret, 1977), provided that no equilibration has occurred after the initial trapping. This can be done, notably, for the late stage of mineralization. For the early stage of mineralization, presence of a homogeneous fluid system (mainly three phase CO_2-rich inclusions) and for the main stage, the absence of gaseous-rich inclusions (decrepitated) in the mineralized quartz make this construction impossible.

For the late stage, the key values determined from the T_m and T_h histograms were used for the determination of the isochore in a H_2O-NaCl system. Microthermometric data of the aqueous-rich and gaseous-rich fluids are used to calculate the isochores and P-T conditions for the late stage.

7.5.1 Early stage

Early stage mineralization is characterized by a homogeneous fluid system (mainly three- phase homogeneous gaseous-rich fluids) occurring in the unmineralized and weakly-mineralized quartz (samples 9702, 96108, 96122 and 96106). There are also aqueous fluids (late fluids) which appear that have occurred from immiscibility of the gaseous-rich fluids (but, then, gaseous phases disappeared). For the first type of fluid, pressure and temperature conditions were estimated, from the H_2O-CO_2 system (Touret, 1977; Touret, 1979 and Roedder, 1984).

The aqueous fluids are characterized by a moderate to relatively high homogenization temperature (170-350°C), with a mode at 250°C, and low salinity. The three-phase gaseous inclusions show an average partial CO_2 melting temperature of 17.86°C and total homogenization temperatures ranging between 229 and 360°C (with a mode at 286°C). For the homogeneous system, in this case three phase-gaseous inclusions, the maximum measured total-homogenization temperature is a minimum trapping temperature (Touret, 1977). On the basis of H_2O-CO_2 system, for three phase-gaseous inclusions, minimum pressure-temperature conditions of trapping at the early stage correspond to ±360°C and about 1.3 kb, respectively.

At the Carlin deposit, Kuehn and Rose (1995) attributed the mineralizing fluid pressure of 800±400 bars to a depth of 3.8±1.9 km (considering 80 to 85 percent lithostatic pressure). Using the criteria of Kuehn and Rose (1995), a depth of about 5 km is estimated for early stage mineralization at Zarshuran. Mehrabi et al. (1999) attributed such a depth to the main stage of hydrothermal mineralization at Zarshuran.

The CO_2-rich fluids at this stage can be related to either magmatic or metamorphic activities. Due the presence of outcropping granitoid and subsurface intermediate-basic intrusive rocks (chapter 3), associated with highly mineralized zones, it is reasonable to

imply a magmatic origin for CO_2-rich fluids. Only a weak mineralization is related to the early stage.

7.5.2 Main stage

Main stage mineralization is characterized by a heterogeneous fluid system (H_2O-rich and gaseous inclusions). The nature of the gas is unknown as all the gaseous inclusions were decrepitated, with subsequent deposition of abundance carbonic materials. Measurable fluid inclusions related to the main stage of mineralization are rare, due to the decompression phenomena and decrepitation of the fluids.

The histogram of homogenization temperatures of the aqueous inclusions in the (early stage) mineralized quartz (samples 9701, 96117, 96122 and BH1-79) show two populations with peaks at 180°C and 250°C. The higher-temperature population is very similar to the lower-temperature population in the early stage mineralization.

Decompression, manifested by decrepitation of fluid inclusions in the mineralized quartz, interrupted the early stage. It appears that the pressure was then much lower than in the early stage, but not low enough to provide boiling in the aqueous system. Due to the absence of gaseous inclusions, minimum trapping temperatures are estimated by homogenization temperatures (T_h) of aqueous inclusions at 250 and 180°C, respectively. These temperatures are probably close to real trapping temperatures, as the pressure must have been low because of widespread decrepitation. However, the inferred pressure was above the two-phase line (e.g., >200 bars) for the aqueous system (Roedder, 1984). Otherwise the aqueous system would have boiled which is not the case. In addition, according to Touret (personal communication), pressure release to decrepitate the gaseous inclusion should be at least 1 kb. Thus, compared to the early stage with an estimated pressure of 1250 bars, the best estimate of the pressure for the main stage hydrothermal mineralization could be about 250 bars.

At this stage fluid circulation began at a discrete maximum T_h, and then followed by successive fluid pulses at decreasing temperature. Unmixing of fluids from the early stage is certainly the main source of fluids at the main stage mineralization. Unmixing provokes destabilization of metal complexes leading to massive metal precipitation. Massive metal deposition in the main stage mineralization is manifested by the occurrence of massive and network arsenian pyrite, and intimately intergrowths of several sulphosalts in agglomerated grains.

7.5.3 Late stage

At the late stage pressure was restored by silicification. Contemporaneous occurrence of two relatively low-temperature fluid systems (CO_2 and H_2O inclusions) in sample 96115 (from the fluorite patches in the mineralized quartz vein zone) provide the opportunity to

determine isochore intersections and thus estimate the P-T conditions. The inferred P-T conditions, constrained by the isochore intersection (Touret, 1997; Roedder, 1984) of these two fluids in fluorite are 300-400 bars (roughly corresponding to a depth of 1.5±0.5 km) and 210±50°C (Table 7.3).

Table 7.3 P-T conditions at three stages of mineralization at Zarshuran

Sample No.	Stage	Salinity (wt %NaCl equivalent)	Pressure (bars)	Temperature (°C)
9702, 96108, 96122 and 96106	Early stage	0.5-8.8 (average 4.4)	±1250	> 360
9701, 96117, 96122 and BH1-79	Main stage	1.8-21.4 (average 12.4)	±250	about 200-270
96115	Late stage	1.7-22.7 (average 13.6)	300-400	210±50°C

7.6 MODEL

Fluid inclusion data confirm the three stages of hydrothermal mineralization (early, main and late) at Zarshuran, which were discussed earlier in chapter 5. The P-T conditions at the different stages of mineralization are shown in Table 7.3. Figure 7.14 illustrates the different types of fluids characterizing the three stages of mineralization.

At the early stage a significant magmatic contribution is suggested by the abundance of homogeneous gaseous-rich inclusions in unmineralized quartz, weakly-mineralized quartz

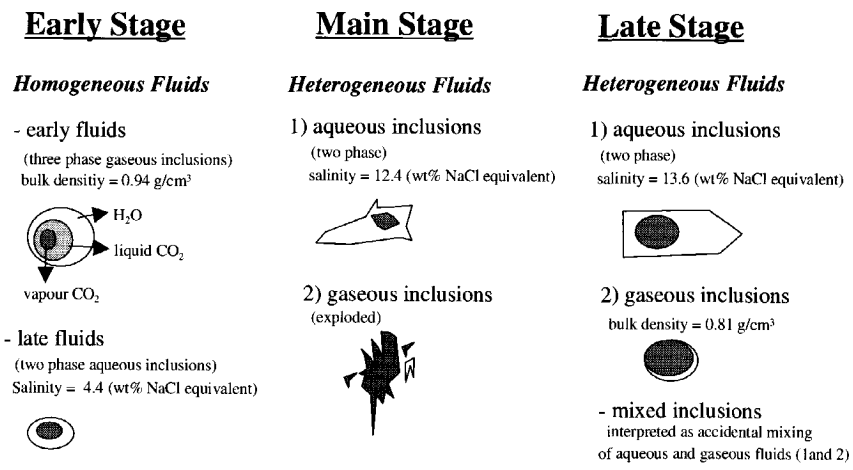

Fig.7.14. Fluids characterizing three stages of hydrothermal mineralization at Zarshuran

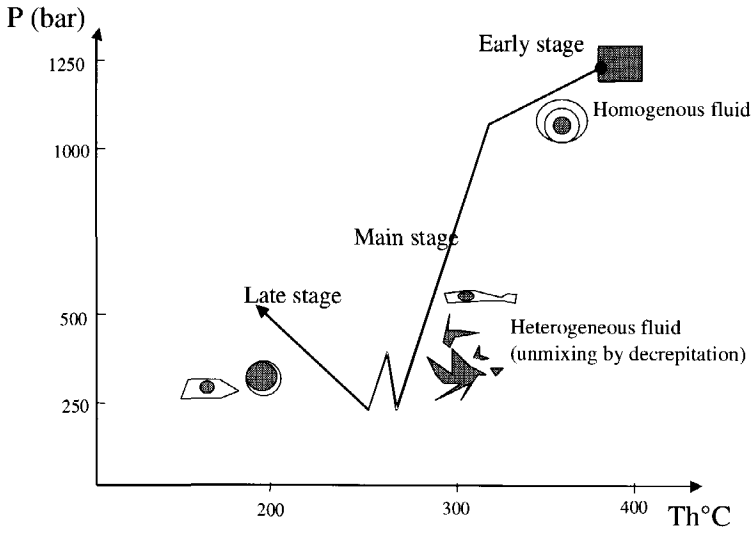

Fig. 7.15. Diagram showing the temperature/pressure conditions at three stages of hydrothermal mineralization in Zarshuran.

and quartz phenocrysts from weakly-mineralized granitoid. High fluid temperatures, abundance of primary CO_2 inclusions, hot low-salinity fluids and rarity of inclusion decrepitation (explosion) in the quartz indicate that the system was under relatively high pressure, which favoured no more than weak mineralization.

At the main stage mineralization fluid inclusions are decrepitated. The decrepitation is indicative of pressure release. Textural relationships (e.g., widespread randomly-distributed dark empty inclusions in the matrix of the quartz) suggest that decrepitated inclusions are related to syn-depositional decompression of the host quartz during uplift. This uplift was likely responsible for the formation of the Iman Khan anticline and for opening space for the introduction of hydrothermal quartz. A large amount of carbon was released by the decrepitation of CO_2-rich inclusions during uplift. Then it precipitated as amorphous carbon, which was likely a control on gold precipitation. Resealing of the fluid conduits with hydrothermal quartz gradually restored higher pressure.

The aqueous fluids which coexist with the decrepitated gaseous inclusions show only minor signs of decrepitation. This is due to the fact that aqueous fluid isochores, much steeper than gaseous isochores, remained roughly parallel to the metamorphic pressure-temperature path (Fig. 7.15). Both fluid types correspond to a heterogeneous fluid system, resulting from unmixing of the early stage homogeneous fluid.

Fluids trapped in inclusions in fluorite represent late mineralizing fluids. At this period, pressure was completely restored and there is no sign of decrepitation or leakage phenomena in the inclusions. Fluids show only one population of homogenization temperatures representing a consistent trapping temperature.

In conclusion, fluid inclusion data indicate that the whole evolution of the Zarshuran hydrothermal system has occurred in a temperature range of 350-200°C. Initially a fluid system derived from magmatic sources at about 5 km depth and a trapping temperature of ±360°C. This temperature is related to very weak hydrothermal mineralization, evidenced by the presence of pyrite and hydrothermal alteration. This fluid was unmixed by sudden pressure release, due to uplift, fracture opening and a transition in lithostatic/hydrostatic pressure. This led to high permeability, formation of network veins and veinlets accompanied by massive metal deposition. Silicification of the system (vein filling) causes pressure restoration and a decrease in permeability. Final cooling of the system occurred at about 200°C. Figure 7.15 illustrates the pressure/temperature conditions of mineralization at Zarshuran.

7.7 CONCLUSION

Hydrothermal fluid circulation, uplift, decompression, release of substantial amounts of carbon, and silicification leading to restoration of pressure provided favourable conditions for mineralization at Zarshuran. The earliest high-temperature hydrothermal fluid had a significant CO_2 component, possibly of magmatic origin, but this fluid was responsible for little or no mineralization.

The main mineralization was linked with fluid immiscibility, caused by a strong pressure decrease. It resulted in the destruction of metal-bearing complexes, stable in the homogeneous fluid, and metal deposition. This occurred in a temperature range of 200-270°C, at a pressure of approximately 250 bars (a depth of about 1 km), in a strong reducing environment.

The relation of fluids with magmatic rocks (possibly a basic intrusion) and the inferred depth of mineralization are important recognition criteria for exploration in the area surrounding Zarshuran.

Chapter 8

GENESIS OF GOLD MINERALIZATION, IMPLICATIONS FOR DEPOSIT RECOGNITION CRITERIA

The results presented and discussed in the earlier chapters are evaluated and combined with some new information to constrain a genetic model of mineralization for the Zarshuran Carlin-like deposit. The essential components for genesis of the Zarshuran deposit (e.g., heat sources, sources of hydrothermal fluids and metals, timing and environment of mineralization) are discussed and compared with the genetic characteristics of Carlin-type deposits. The results obtained from the genetic model are evaluated to determine the deposit recognition criteria for gold exploration in the surrounding region. This chapter is an edited version of papers entitled *A magmatic contribution to the Carlin-type gold deposit at Zarshuran, Iran,* published in the proceedings of SGA-IAGOD Conference, London, Mineral Deposits - Processes to Processing, Vol. 1, pp. 463-466 (Asadi and Hale, 1999a) and *Application of Zarshuran Carlin-like deposit model for gold exploration GIS in NW Iran,* published in the proceedings of The Fourteenth International Conference on Applied Geologic Remote Sensing, Las Vegas, Nevada, 6-8 November 2000 (Asadi and Hale, 2000a).

1.1 INTRODUCTION

Sediment-hosted disseminated gold deposits were considered as mesothermal deposits by Lindgren (1933). Subsequent research led to their classification as Carlin-type low to medium pressure and low temperature epithermal deposits.

The understanding of epithermal deposits today differs from that of earlier researchers. In general, epithermal deposits form by ascending hot aqueous solutions of uncertain origin into a shallow environment, where they undergo abrupt physical (pressure and temperature) and chemical changes. Research in recent years on epithermal gold and silver deposits has led to

the recognition of three principal varieties: 1) volcanic rock related adularia-sericite (illite) type or low sulphidation type; 2) alunite-kaolinite ± pyrophillite type or high sulphidation type hosted by either volcanic or sedimentary rocks; and 3) sedimentary rock hosted Carlin-type deposit (Berger and Henley, 1989; White and Hedinquist, 1990).

According to Berger and Bagby (1991), igneous rocks occur in the vicinity of most of the Carlin-type gold deposits of the western United States. They suggest that Carlin-type deposits are distal, magma-related, replacement deposits. Others point out that the genetic association between magmatic rocks and gold mineralization is unproven (Thorman and Christensen, 1991). Highly altered granodiorite or granite is found as stocks or dykes in the Getchell, Gold Acres, Goldstrike and White Caps deposits. Magnetic anomalies suggest large granitic bodies beneath some other deposits such as Carlin (Grauch, 1988). It has been suggested that sediment-hosted disseminated gold deposits formed above active, deep-penetrating extensional faults, where plutons provided magmatic hydrothermal fluid (Sillitoe and Bonham, 1990; Berger and Bagby, 1991). This implies a hydrothermal system similar to those that commonly form tungsten-skarn deposits and skarn and porphyry-type molybdenum deposits (Berger and Bagby, 1991). As the temporal and spatial association of most of the sediment-hosted disseminated gold deposits with magmatism is not well defined, Sillitoe and Bonham (1990) considered them to be a distal product of a magmatic hydrothermal system.

Geochronologic studies of the Carlin-type deposits along the Carlin trend have yielded no definitive age for mineralization. From K/Ar dates on alunite at Alligator Ridge (Ilchik, 1990) it appears that mineralization occurred during middle-late Tertiary and/or Cretaceous (e.g., Bonham 1985). Miocene igneous activity is considered by some to have been the heat source driving hydrothermal systems in north central Nevada (Radtke et al., 1980; Radtke, 1985; Rye, 1985). However Arehart et al. (1993) and Bonham (1985) indicate that the gold mineralization occurred earlier, possibly in the early Cretaceous (~117 Ma.). The scatter in the data may imply mineralization during two intervals, Late Cretaceous and Middle Tertiary (Bagby and Berger, 1985). Thorman and Christensen (1991) consider that mineralization has continued to the present time, but at fewer sites.

The depth of mineralization is variable within a narrow range. On the basis of the suite of trace elements (Au, As, Sb, Hg and Tl) present in many epithermal and hot spring deposits, vuggy and open space filling textures, a maximum depth of formation of 300 m is inferred at Getchell (Joralemon, 1975). A maximum depth of formation of 500 m for the Carlin deposit is based on boiling inferred from fluid inclusions (Radtke, 1985). Although such shallow environments have been suggested for Carlin-type gold deposits, Kuehn and Rose (1995) calculated a depth of 3.8±1.9 km (800±400 bar pressure) for mineralization at Carlin itself. Deep ore (>500 m) has been discovered in Carlin-type gold deposits at Post-Betz (Bettles 1989) and Getchell (Berger 1985).

A unique genetic model has not yet been established for the Carlin-type deposits. Many aspects of the genesis are still controversial including the source(s) of ore components, the

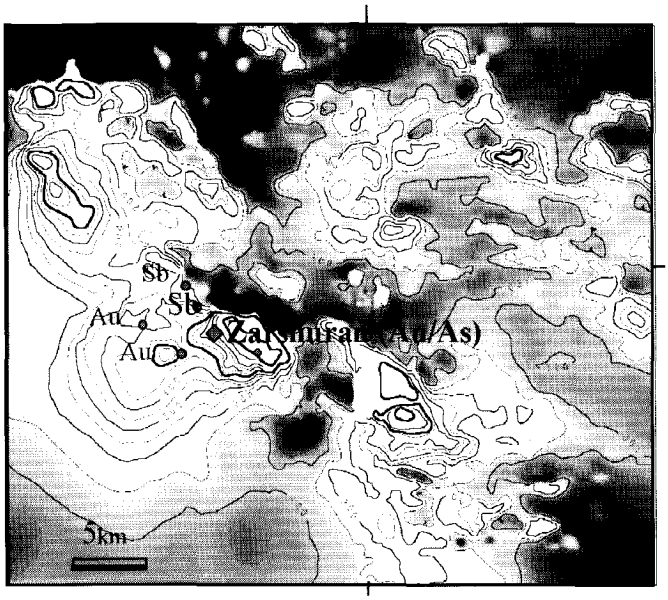

Fig. 8.1. Contours and shaded relief of total magnetic field intensity of the Takab region surrounding Zarshuran.

age of mineralization, the thermal and compositional characteristics of the hydrothermal fluid(s), the relationship between alteration and mineralization, the mechanism(s) of gold transport and precipitation, the heat source(s) driving the hydrothermal system and the depth of mineralization. Many researchers have proposed that gold was scavenged from sedimentary rocks and redeposited in a late Cenozoic geothermal system with boiling as the main deposition mechanism (Radtke et al., 1980; Radtke, 1985; Hofstra et al., 1988). Kuehn and Rose (1995) question the geothermal model and suggest that gold was deposited without boiling at a depth of 2-5 km.

8.2 GENESIS OF THE ZARSHURAN DEPOSIT

Disseminated gold mineralization at Zarshuran is hosted by Precambrian carbonates and black shales. The mineralization comprises mainly sulphides of arsenic, iron and, to a lesser extent, antimony and base metals, with subordinate cinnabar (HgS), lorandite ($TlAsS_2$), christite ($TlHgAsS_3$), coloradoite (HgTe), aktashite ($Cu_6Hg_3As_4S1_2$) and various lead-sulphosalts (Asadi et al., 2000c). Gold mainly occurs as invisible gold incorporated into the arsenian pyrite and sphalerite; visible gold is rare and occasionally occurs in orpiment (Asadi et al. 1999). Hydrothermal alteration associated with the mineralization is manifested as decalcification, silicification and argillization.

The essential components for genesis of the Zarshuran gold deposit are sources of heats, fluids and metals as well as suitable conditions to permit fluid flow and fluid circulation, fluid enrichments and metal deposition.

8.2.1 Igneous association (heat sources)

Zarshuran is one of many mineral deposits close to the boundary of the Urumieh-Dokhtar volcanic arc and the Sanandag-Sirjan volcano-sedimentary zone, both of which extend over 2000 km in a NW-SE direction across much of Iran. This boundary is interpreted as the suture zone between the Afro-Arabian plate and the Iranian plate. The widespread Tertiary volcanism of the Urumieh-Dokhtar arc is attributed to northeast-dipping subduction along this boundary (see chapter 2).

The area around Zarshuran has experienced repeated cycles of orogenic activity, including structural uplift, sedimentation, magmatism and metamorphism. The geological formations comprise late Precambrian metamorphics overlain by Eocene andesites, some of which are weakly mineralized, Oligocene-Miocene red beds, carbonates and intermediate igneous rocks, and Quaternary sediments. The Tertiary volcanics, which are partially altered throughout the area, are located in the immediate vicinity of not only the Zarshuran gold deposit but also a number of less significant hydrothermal Au, As and Sb mineralizations.

High resolution aeromagnetic data of a 1700 km^2 region including Zarshuran and the surrounding area have been used to re-map the main geological units and infer the subsurface geology (Asadi and Hale, 1998). Within this area, high amplitude magnetic anomalies are

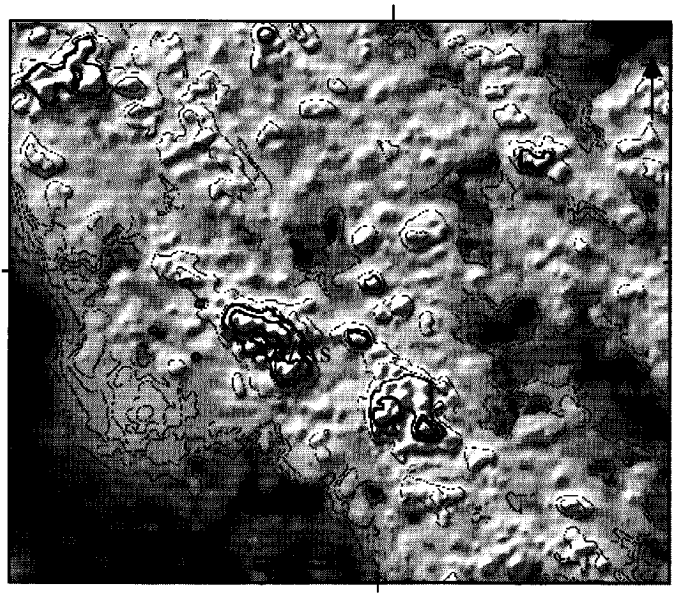

Fig. 8.2. Grey scale analytical signal map of Takab region surrounding Zarshuran. Bright shades show high amplitude processed signal anomalies, thick black contours indicate the highest anomalies.

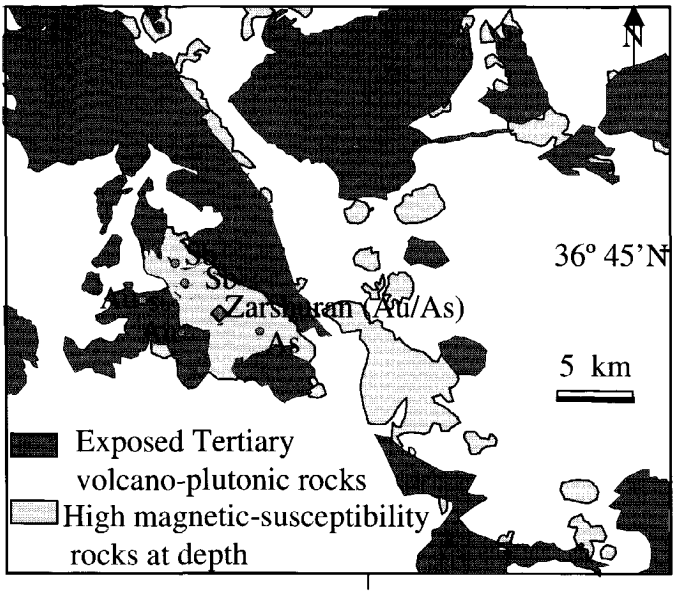

Fig. 8.3. Map showing the combination of exposed Tertiary igneous rocks overlain on the subsurface igneous rocks mapped by the analytical signal technique.

likely to be caused by the high magnetic susceptibility of igneous rocks. The highest anomalies are located in the central part of the area and coincide with the location of the Zarshuran deposit and its surroundings (Fig. 8.1). At a distance of 2-3 km from Zarshuran these anomalies can be ascribed to widespread outcropping Eocene volcanics.

In the immediate vicinity of Zarshuran, however, the rocks seen at outcrop are mainly Precambrian sediments and schists. High amplitude analytical signal anomalies of total magnetic intensities here suggest the presence of igneous intrusive rocks beneath the Zarshuran deposit and adjacent mineralizations (Asadi and Hale, 1998) (Fig. 8.2). The high amplitude analytical signal anomalies associated with high magnetic-susceptibility rocks beneath sediment cover have been digitized from the colour analytical signal image and overlain on the geological map of outcropping Eocene volcanics. This reveals the spatial association between mineralization and igneous activity in the Zarshuran area (Fig. 8.3).

Qualitative analysis of total magnetic field intensity of ground magnetic data at Zarshuran showed a strong magnetic anomaly over the Iman-Khan schist, which is most probably attributed to serpentinized ophiolitic rocks. Exposed metamorphosed ophiolites have been mapped recently at the central part of the doubly-plunging Iman-Khan anticline. In addition, this analysis revealed negative magnetic anomalies mainly associated with granitoid dykes and stocks (see Chapter 3).

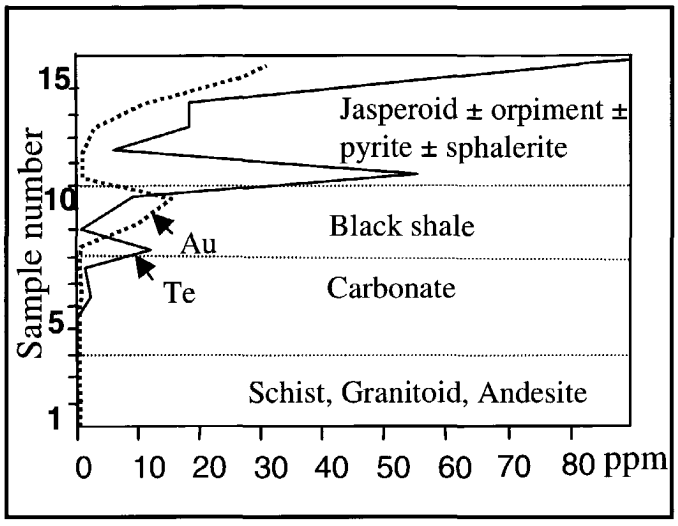

Fig. 8.4. Relation of Au and Te concentration at Zarshuran

Quantitative analysis of the ground magnetic data indicated the presence of subsurface intermediate to basic intrusive dykes or stocks at depth, dipping in a northeast direction towards the core of Iman-Khan anticline. These inferred dykes or stocks could be connected to a deep magmatic body at the core of anticline, below the ophiolites, which could be responsible for the main heat sources deriving the migration of hydrothermal solutions (see Chapter 3).

At the Zarshuran deposit a highly-altered intrusive occurs in close spatial association with the highly-mineralized zones hosted by Precambrian black shale and carbonates. The intrusive is a granitoid dyke or stock comprising large phenocrysts of quartz in a white cryptocrystalline groundmass. Qualitative microprobe analysis reveals the presence of pyrite and cinnabar in this rock. This granitoid, which is highly altered and shows evidence of subsequent mineralization, could have acted as a conduit for hydrothermal solutions from the deep, intermediate-basic magma present at the core of the anticline.

In addition, the geochemical and mineralogic study (Chapter 4) provided some evidence of igneous association at Zarshuran. Coloradoite (HgTe) is the only telluride so far identified at Zarshuran. It is found as rare patches of fine diamond-like grains (<50 μm) in coarsely-crystalline orpiment. The bulk trace element analyses of representative host rocks indicate a higher tellurium content in the samples that contain higher gold concentrations (Fig. 8.4). These analyses show that massive orpiment contains the highest Te and Au concentrations (up to 316 ppm Te and 148 ppm Au) and other gold-bearing minerals at Zarshuran usually reveal at least a trace of Te.

Telluride minerals have not been reported from most sediment-hosted disseminated gold deposits of the western United States and south-eastern China. Gold ore from Carlin contains

only traces of Te (<0.6 ppm) and no telluride minerals have been found (Radtke, 1985). Coloradoite, accompanied by several gold tellurides, was reported by Callow and Worley (1965) from the epithermal volcanic-hosted Acupan gold deposit in the Philippines, and the Te at Acupan is attributed to a magmatic source (Cooke et al., 1996). Thus the presence of coloradoite and the relatively high Te content in As minerals at Zarshuran represents geochemical evidence of a magmatic component in the hydrothermal fluids, whilst the absence of gold tellurides is attributed to a low Te fugacity.

The interpretation of regional geology and aeromagnetic data indicate that the outcropping Tertiary volcanic rocks of the Zarshuran district are associated with a deep magma (Asadi and Hale, 1999a). This information coupled with interpretation of the ground magnetic data as well as the presence of telluride and high tellurium concentration in the ore suggest that a deep magma supplied the main heat for the hydrothermal system responsible for the formation of gold mineralization at Zarshuran. This magma is connected to the nearby volcanics and possibly created the Iman-khan anticline and now is present at the core of the anticline.

8.2.2 Age of mineralization

Mehrabi et al. (1998) carried out geochronological studies at Zarshuran, using K/Ar dating of argillic alteration associated with gold mineralization. They reported that K/Ar ages of mineralized rock are in the range 14.2±0.3 to 26.1±0.8 Ma. Analysis of hydrothermal illite-sericite in limestone gave ages of 14.25±0.4 which they believed to be the best estimate of the true age of hydrothermal mineralization. They also reported that K/Ar and Ar/Ar dating of Miocene volcanic rocks, located 2-3 km to the east of the Zarshuran deposit, yielded ages in the range 11.1±0.3 to 16.4±0.3 Ma. The volcanics and the mineralization appear to be coeval and thus there may be a genetic link. A Miocene age was suggested by Radtke (1985) from igneous rocks which represent the possible heat source for the Carlin deposit and by Ilchik (1990) from K/Ar dates on alunite at Alligator Ridge.

8.2.3 Sources of mineralizing hydrothermal solutions

Giggenbach (1986) suggested that mineralizing hydrothermal fluids in the active geothermal systems of the Taupo Volcanic Zone, New Zealand, obtain CO_2 and H_2S from magmatic sources. There is also a common agreement on participation of meteoric fluid in geothermal systems and hydrothermal ore deposits (Radtke, 1985).

Fluid inclusion data at Zarshuran indicate two types of fluids were involved in mineralization, gaseous-rich (mainly CO_2) and aqueous-rich (chapter 7). During the early stage of hydrothermal mineralization, the aqueous fluid (low salinity) was possibly produced

by the unmixing of a homogeneous CO_2-rich fluid that had acquired CO_2 from magmatic components. During the main stage of mineralization, neighbouring aqueous inclusions with a wide range of salinities occurring alongside decrepitated gaseous inclusions provide evidence for unmixing of fluids because of pressure release as well as decalcification processes. During the late stage, similarly the presence of a wide range of salinities (e.g., the presence of very low salinity, low temperature fluids) may reflect the end members of involved fluids, for instance meteoric water and magmatic gas input.

Mehrabi et al. (1998) report the presence of H_2S in the fluids at Zarshuran. This too represents an indication of a magmatic source for (some of) the mineralizing solutions.

8.2.4 Sources of gold in hydrothermal solutions

Geochemical analysis shows that the unmineralized altered granitoid at Zarshuran contains 140 ppb Au, compared to 80 ppb in the Precambrian Iman Khan schist and 70 ppb in the Miocene volcanics located 3 km to the west. Taddaion (1991) reported 384 ppb gold in the metamorphic rocks. The spatial modelling of the Zarshuran deposit revealed a close association between metamorphosed ophiolitic rocks (serpentinite) and zones of high gold mineralization. If, at the early stage, the hydrothermal system was under high pressure (preventing mineral precipitation) and the Zarshuran black shale and Chaldagh limestone acted as a pressure seal (in addition to being a geochemical barrier), the volatile fluid, rich in CO_2 and H_2S may have leached gold from the granitoid and Precambrian metamorphic rocks (e.g., metamorphosed ophiolites). The deep magma itself may also be a source for gold and associated elements.

8.2.5 Environment of mineralization

Two major types of fluids, aqueous-rich and gaseous-rich, are present at Zarshuran. On the basis of the isochore intersections of these two fluids, a trapping pressure of approximately 1250 bars (corresponding to a depth of about 5 km) for the early stage of mineralization, ±250 bars (depth of about 1 km) for the late main stage and 300-400 bars (depth of about 1.5 ± 5 km) have been calculated (Chapter 7). The entire evolution of the hydrothermal and mineralization at Zarshuran system occurred in a temperature range of 350-200°C. It appears that the main mineralization occurred during two periods with temperatures fluctuating from 200-270°C. This could indicate the presence of two periods of mineralization evidenced by a sudden decompression and a later pressure restoration due to the silicification and filling of the veins. Colloform arsenian pyrite, colloform sphalerite and orpiment, the main hosts for gold, appear to occur at the end of the main stage (beginning of pressure restoration) and/or at the beginning of the late stage.

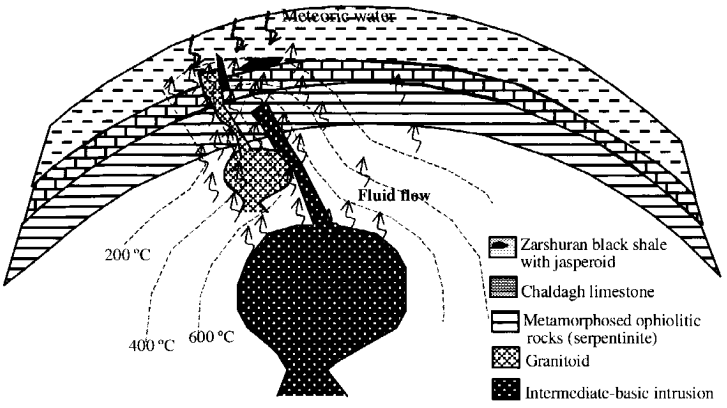

Fig. 8.5. Schematic model for the formation of mineralization at Zarshuran

From the trapping pressure and depth of mineralization, it is concluded that at the earliest, high-temperature and low-salinity, stage of hydrothermal mineralization the system was under a high pressure (chapter 7). The hydrothermal fluid at this stage seems likely to have had a significant magmatic component, but was responsible for no mineralization other than weak mineralization of the granitoid. The main stage of hydrothermal mineralization is characterized by uplift, possibly related to the formation of the Iman-Khan anticline, decompression and release of substantial amounts of carbon. At the end of the main stage and beginning of the late stage, silicification leading to restoration of pressure provided favourable conditions for mineralization.

8.2.6 A genetic model

Figure 8.5 is a schematic cross section illustrating the formation of mineralization at the Zarshuran gold deposit. Initially a hydrothermal system, below the Zarshuran black shale and Chaldagh limestone (pressure seals), was driven by an intermediate-basic magma at about 5 km depth. This system, low-salinity and high temperature (±350°C), was under too high pressure to precipitate minerals, and thus its volatile constituents had time to leach gold from the granitoids and metamorphosed ophiolitic rocks (serpentinite). Intrusion of the magma caused the uplift of the Iman-Khan anticline, with concomitant faulting, fracturing and fragmentation of granitoids, metamorphic rocks and the overlying Chaldagh limestone and Zarshuran black shale. The uplift, faulting, opening of veins and decompression, caused significant pressure release, migration of hot, low salinity fluids from a high-pressure system to a low-pressure system, and release of substantial amounts of carbon. The main mineralization was linked with fluid unmixing, caused by a strong decompression resulting in destabilizing metal-bearing complexes and metal precipitation. This occurred in a temperature range of 200-270°C, at pressure of approximately 250 bars (depth of about 1

km), in a strong reducing environment. Gradual pressure restoration, due to the silicification, and further migration of mineralizing hydrothermal fluids (gas-rich, high salinity, low to moderate temperature) into the chemically-reactive Chaldagh limestone and Zarshuran black shale provided favourable conditions for the precipitation of mineralization.

8.2.7 Conclusions

In terms of host rocks, mineral assemblages, the presence of As-Sb-Hg-Tl, hydrothermal alteration and the occurrence of invisible gold in arsenian pyrite, Zarshuran is very similar to the classic Carlin-type sediment-hosted disseminated gold deposits of the western United States and south-eastern China. Nevertheless, Zarshuran has some features that are not common to the classic Carlin-type gold deposits.

In terms of genetic components of mineralization at Zarshuran explained earlier, the following conclusions can be made.

1) The whole evolution of the Zarshuran hydrothermal system occurred in a temperature range of 350-200°C. Ore deposition occurred within the chemically-reactive black shale and carbonate barriers in a transitional condition from a high pressure system (1250 bars) to low pressure system (±250), followed by pressure restoration; the low pressure system and pressure restoration correspond to the main and late stage mineralizing events, respectively.
2) Gas-rich and aqueous-rich fluids were involved during the main stage and late stage of hydrothermal mineralization at Zarshuran. The salinity of the mineralizing fluids was moderate to high. The estimated temperature and pressure during the main mineralization event were about 200-270°C and 250 bars.
3) Major decompression (evidenced by fluid decrepitation and temperature fluctuations) occurred before the major mineralizing period at Zarshuran, but has not been reported elsewhere in the Carlin-type deposits. This phenomena coupled with low to moderate temperature (200-270°C) and a low to moderate pressure (250-400 bars), during the main and late stage mineralization periods, leads to an inferred depth of mineralization of about 1-1.8 km. This is consistent with a moderately deep environment for gold mineralization. This contrasts with the presence of very deep environment suggested by Mehrabi et al. (1998) for Zarshuran and by Kuehn and Rose (1995) for the Carlin deposit in Nevada. The maximum depth of gold mineralization at Zarshuran, observed in the boreholes used for spatial modelling of the deposit, is 250 m (chapter 3).
4) The presence of a substantial amount of invisible gold in sphalerite, which is often closely associated with gold-bearing arsenian pyrite, is unique to Zarshuran.

5) The presence of Te (evidenced by high tellurium concentrations in the ore and occurrence of coloradoite) suggests a larger magmatic component in the mineralizing hydrothermal solution at Zarshuran than is typical for most Carlin-type deposits. Abundance of gaseous inclusions associated with mineralization is suggestive of a large contribution of magmatic components in the fluids.
6) The main mineralization event occurs by transition from a high-pressure hydrothermal system (significant leaching of gold from serpentinite and granitoid) into a low-pressure system (release of carbon) and then gradual pressure restoration.

8.2 DEPOSIT RECOGNITION CRITERIA

On the basis of the model for genesis of mineralization at Zarshuran, it is concluded that Zarshuran is a Carlin-like deposit. The significance of the genetic model of mineralization is that it provides deposit recognition criteria (DRC) that can be used in exploration for similar deposits. Using the genetic model of the Zarshuran Carlin-like deposit, the following recognition criteria are proposed for exploration of similar mineralization in the surrounding region:

1) deep intermediate-basic magma, being the main heat source to drive the migration of mineralizing hydrothermal solutions. (such a body could be evidenced by nearby outcropping volcanics);
2) outcropping altered granitoid rock, intrusion of which is important for ground preparation for penetration of mineralizing hydrothermal solutions (the granitoids might also be important sources for gold and associated elements);
3) geochemically-reactive black shale and/or carbonate barriers (organic matter in the carbonate rocks could be also an important control on gold mineralization);
4) zones of hydrothermal alteration (silicification, decalcification and argillization);
5) dome structures, such as the Iman-Khan anticline, which could have resulted by uplift;
6) high angle faults, trending in a NE-SW and NW-SE direction, associated with dome structures (during uplift) or created due to the intrusions of granitoid into the host formations; and
7) the epithermal element suite of As-Sb-Hg-Tl and also for Zn and Te, in view of their close association with gold mineralization (e.g., occurrence of gold in sphalerite, presence of coloradoite and high concentration of Te in orpiment hosting rare visible gold).

Chapter 9

APPLICATION OF GIS AND REMOTE SENSING FOR MAPPING DEPOSIT RECOGNITION CRITERIA IN THE TAKAB AREA

This chapter first explains the geologic setting and mineralization of a test area of some 1800 km^2, surrounding the Zarshuran gold deposit, within the Takab Shahin-Dez quadrangle. It then reviews the recognition criteria for epithermal gold, arsenic, antimony and base metal mineralizations deduced from the geodynamic model of the Zagros orogenic belt (chapter 2), the metallogeny of the Takab Shahin-Dez quadrangle and the genetic and spatial models of the Zarshuran deposit (chapters 3, 8). The application of GIS and spectral and geophysical remote sensing tools are then used for mapping the recognition criteria characterizing Zarshuran and other known mineral deposits of the test area. It finally shows how the identified deposit recognition criteria are reduced to six evidence maps of mineral potential. The chapter is composed of edited versions of the papers, *Assessment of epithermal mineralization in northwest Iran using GIS northwest Iran,* published in the proceedings of 5th Cartographic Conference on GIS, Tehran, pp. 29-47 (Asadi, Carranza and Hale, 1998a), *GIS and remote sensing for epithermal gold exploration in northwest Iran,* published in the proceedings of Conference on GIS for Earth Science Applications, Lublijana, (Asadi, Carranza and Hale, 1998b) and *Integrated analysis of aeromagnetic, Landsat-TM and mineral occurrence data for epithermal gold exploration in northwest Iran,* published

in proceedings of 13th International Conference on Applied Geologic Remote Sensing, Vancouver, Canada (Asadi and Hale, 1999b).

9.1 INTRODUCTION

The Takab area is a sparsely-vegetated, semi-arid, mountainous region of 1800 km^2, located to the north of the town of Takab, northwest Iran. It is one of the most important gold-mineralized regions of Iran and includes an active arsenic mine (Zarshuran), two known gold deposits (Zarshuran and Aghdarreh), the largest lead-zinc mine in Iran (Anguran), another smaller lead-zinc mine (Alamkandy), a large copper mine (Baiche-Bagh) and evidence of several ancient mining activities for gold, arsenic, antimony and base metals (Figs 9.1, 9.2). The mineral occurrences of arsenic, antimony and base metals commonly contain considerable amounts of gold and silver.

Spectral and geophysical remote sensing and image processing techniques are important tools for defining subtle anomalies associated with mineral deposits. Geographic Information Systems provide an important tool to store, analyze and superimpose geological, spectral, geophysical and other mineral exploration data sets (e.g., Bonham-Carter et al., 1988; Lugaski et al., 1990; and Tanaka and Segal, 1990).

These tools are applied to the Takab area in order to reveal deposit recognition criteria (DRC). Procedures are described to extract information on alteration, structures, lithologies and geochemical signatures.

Data analysis was carried out in three steps: (1) compiling the data in digital format and integrating them in a GIS; (2) processing these to reveal DRC; and (3) creating six mineral-potential evidential maps (to be used to calculate a map of further gold and base-metal potential in the Takab area).

9.2 BACKGROUND

9.2.1 Geology

The Takab Shahin-Dez quadrangle is located in Azerbaijan and Kordestan provinces, northwest Iran. It covers some 15,000 km^2 between latitudes 36° N to 37° N and longitudes 46° 30' E to 48° E. It lies in the western sector of Sanandaj-Sirjan zone (SSZ), on/close to the western contact of Urumieh-Dokhtar volcanic arc (UDMA) of the Zagros Orogenic Belt (ZOB). The boundary between the SSZ and UDMA is interpreted as the suture zone

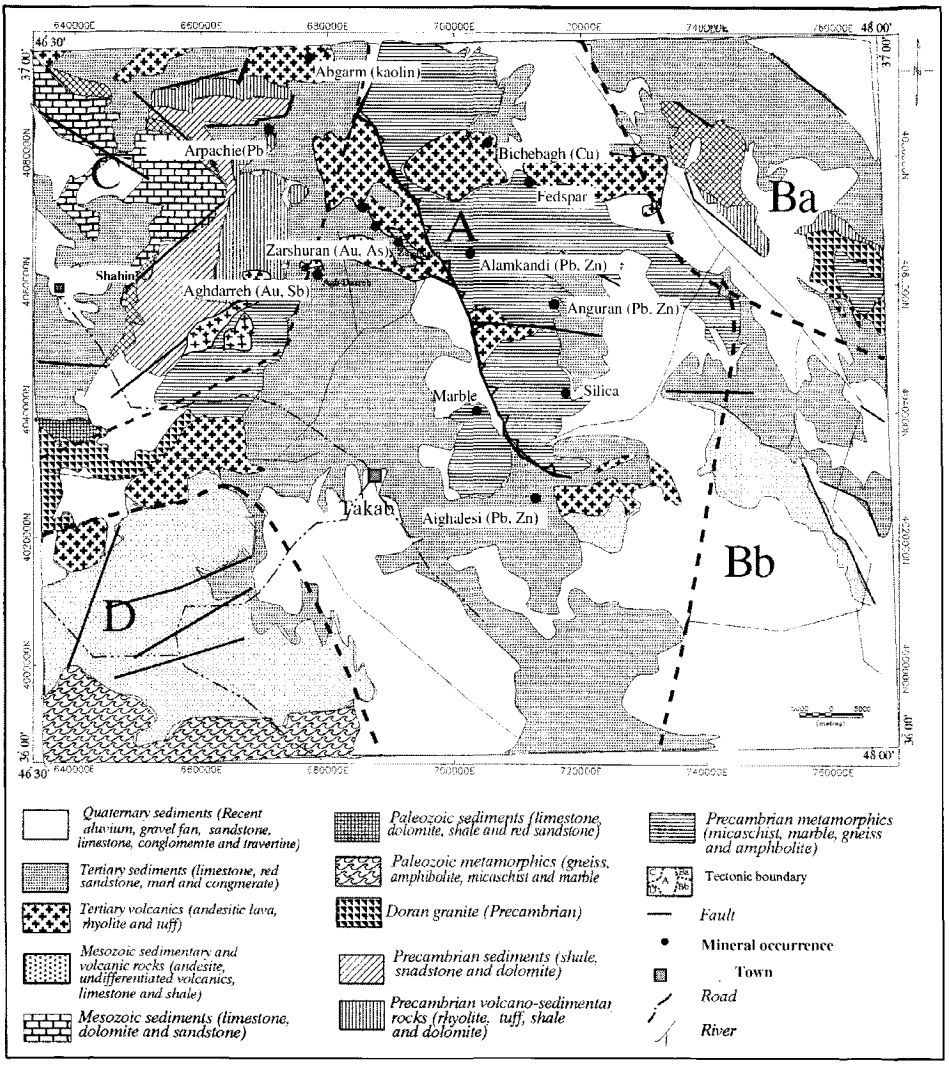

Fig. 9.1. Geological map of Takab Shahin-Dez quadrangle; the Takab area (test area) is located in the north-central part of the quadrangle; for explanation of zones A-D, see text.

between the Afro-Arabian and Iranian plates. It is characterized by a series of structural depressions, sheared and mylonitized ophiolitic rock sequences, and high-angle, northeast-dipping shear planes. The widespread Tertiary volcanism of the UDMA is attributed to northeast-dipping subduction of the Arabian plate under the Iranian plate (see chapter 2).

The quadrangle has experienced repeated cycles of orogenic activity, including structural uplift, sedimentation, magmatism and metamorphism

(Alavi et al., 1982). There are a variety of geologic structures that resulted from the Alpine orogenies (Alavi et al., 1982). According to Alavi et al. (1982), the Quadrangle can be divided into four separate structural zones (A, B, C and D), based on differences in faulting, folding, and the strike and lithology of various geological formations as shown in Fig. 9.1.

The test area (Takab area) is located in the north-central part of Takab Shahin-Dez quadrangle within Zone A (central), surrounding the Zarshuran gold deposit. Zone A, extending from north to south, consists of highly metamorphosed Precambrian basement and late Tertiary (Neogene) volcano-plutonic and sedimentary rocks. There is a lack of any sedimentary sequence from Precambrian to Oligocene in this zone. The rocks are mainly trending northwest-southeast, parallel to the NW-SE structural trend of the ZOB. The northwest-southeast trending faults put metamorphic rocks in juxtaposition with the Tertiary rocks in the middle of the zone.

In 1999, lithological mapping of the Takab area was carried out at the scale of 1:100,000 by the Geological Survey of Iran. The mapped geological formations are mostly Precambrian metamorphics, Tertiary volcanics (with subordinate granitoids), Tertiary sedimentary rocks and Quaternary sediments. Tertiary volcano-plutonic rocks underlie about 30% of the area and the volcanics are partially altered throughout the area. A major northwest-southeast trending fault puts the Precambrian metamorphics in juxtaposition with the Tertiary rocks in the middle of the area. Several small, elongated outcrops of metamorphosed ophiolitic rocks are also present in this area. Two major sets of NW-SE and NE-SW trending structures are present in the region. The NW-SE trending structures extend parallel to the major litho-structural subdivisions of the Zagros Orogenic Belt (ZOB). The NE-SW trending faults are located in proximity to or along the main conjugate faults across the ZOB interpreted from aeromagnetic data of Iran (chapter 2)

9.2.2 Mineralization

The known gold, arsenic, antimony and base metal mineralizations of the test area are mainly epithermal in origin and are hosted by jasperoid, black shale, carbonates and partially-altered andesite. Those deposits hosted by sediments are usually found a short distance from volcano-plutonic rocks.

Zarshuran, the largest gold deposit of the area, is a Carlin-like disseminated gold deposit hosted by Precambrian black shale and carbonates, which have been intruded by a weakly mineralized, highly altered granitoid. This intrusion fractured the host formation and provided a favourable condition for circulation mineralizing hydrothermal solutions. Decalcification,

silicification sericitization and kaolinitization are the principal alterations. The mineralizing hydrothermal solution, associated with an inferred deep basic-intermediate magma, leached gold and its associated elements from the granitoids and metamorphosed ophiolitic rocks and precipitated them in chemically-reactive black shale and carbonate rocks at a pressure 500-650 bar corresponding to a depth 1.7-2.7 km. The mineralization is mainly controlled by NE-SW trending high angle faults intersecting the southwest limb of a NW-SE plunging anticline. The gold mainly occurs as invisible gold associated with arsenic-bearing pyrite and sphalerite; visible gold is rare and occurs in orpiment and silica (Asadi et al., 1999). Compared to the Carlin-type deposits, the presence of higher tellurium concentrations in the ore and close association with igneous rocks at Zarshuran indicate a larger than typical magmatic component in the mineralizing hydrothermal solutions (Asadi and Hale, 1999a). The high concentration of invisible gold in sphalerite is unique to Zarshuran.

Aghdarreh, the second biggest gold deposit in the Takab area, occurs in a domed, locally-thickened Oligo-Miocene limestone. It comprises two separate areas of shallow mineralization about 1.5 km apart, prominently marked by the occurrence of jasperoid veins and lenses trending NE-SW and NNE-SSW (Middleton, 1994). Tuffaceous volcanic lenses are present at the top of the limestone, and may be related to volcanic rocks located 4-5 km to the northeast (toward Zarshuran). The richest mineralization occurs in jasperoid lenses in the upper part of the limestone and in underlying horizons, conformable with the limestone bedding and rich in iron and manganese oxides. The jasperoids and the iron-manganese oxide horizons are enriched to economic proportions in gold with accompanying arsenic, antimony, zinc, lead, silver and barium. According to Daliran et al. (1999), the mineralization is epithermal in origin.

There are also a number of less significant arsenic, antimony and gold prospects in the vicinity of Zarshuran and Aghdarreh. Arsenic is being worked on a small scale from NE-SW trending silicified veins and lenses in the Zarshuran Precambrian black shale unit. At Baldir-Ghanee, about 2 km northwest of Zarshuran, there are traces of antimony mineralization. This mineralization is characterized by massive silicification in Oligo-Miocene limestone and shale, and is closely associated with Miocene volcanics. At Bighair-Bolaghi, located 1 km north of Baldir-Ghanee, there are several indications of antimony mineralization in the carbonate rocks, which are intruded by altered Oligo-Miocene andesite dykes (Karimi, 1993). A few km to the west of Zarshuran there are several old workings at Chaldaghi and Kalaki, where small mineralized quartz veins occur at the top of Miocene volcanic sequences. Mohajer et al. (1989) reported up to 5.4 ppm gold from a quartz

vein at Kalaki. A small abandoned antimony mine is located about 2 km to the north of Aghdarreh. The stibnite mineralization at this mine is hosted by ferruginous carbonate, marl and black shale and appears to be controlled by NE-SW trending faults. Highly altered granitoid rocks are widespread about 2 km to the north of the mineralized area.

The Anguran lead-zinc mine is the largest mine in the area. The ore body is hosted by fractured, Oligo-Miocene calcareous rocks, which overlie Precambrian metamorphic and metavolcanic rocks. The dominant structure of the deposit is an ENE-SSW trending anticline intersected by NW-SE and E-W trending faults which control the mineralization. Ore minerals are mainly sphalerite and galena in the lower part of the ore body and smithsonite, hemimorphite, zincite, sericite, and iron oxides in the upper part. Oligo-Miocene andesitic rocks are located in the immediate vicinity of this deposit.

There are additional lead and zinc occurrences at Alamkandy and Arpachi. Mineralization at Alamkandy is hosted by ferruginous carbonates located along their contact with Precambrian metamorphic rocks. The mineralized rocks extend in a NW-SE direction. Vein type mineralization at Arpachi is hosted by Oligo-Miocene carbonates located close to an altered Miocene andesite. The mineralization is controlled by NE-SW trending faults.

Vein copper mineralization occurs in fractured and faulted zones in altered Oligo-Miocene andesite at Baiche-Bagh. The main NNE-SSW structural trend controls the mineralization in this area. Silica, kaolinite, sericite and limonite are the main alteration products. The silicifed veins 0.5-1.5 m thick and up to 2 km long, commonly contain chalcopyrite, tetrahedrite, arsenopyrite, pyrite, sphalerite, galena, and bismuthinite. Bulk chemical analyses of a few samples indicated high gold and silver concentrations (Zanjani, 1945) and Bariand (1962) reported the presence of native gold associated with arsenopyrite.

There are further copper occurrences, most of them old workings within the altered Oligo-Miocene andesite in the northwest of the Takab area. Mineralization in these occurrences is mainly controlled by E-W and NE-SW trending structures.

9.3 DEPOSIT RECOGNITION CRITERIA (DRC)

9.3.1 DRC in the Takab area

Sediment-hosted epithermal mineralizations are scattered throughout the Takab area. Based on the geodynamic setting of the ZOB, the geology and metallogeny of the Takab Shahin-Dez quadrangle, and the genetic and spatial models of the Zarshuran deposit, the characteristic DRC for mineralizations of

the Takab area appear to be: (1) host rock lithology; (2) association with volcano-plutonic rocks; (3) hydrothermal alteration; (4) geologic structures; (5) presence of an epithermal element suite (As-Sb-Hg-Tl-Te-Zn); and (6) proximity to metamorphosed ophiolitic rocks (e.g., serpentinite). The first four criteria are those also exhibited by Carlin-type deposits.

According to Berger and Bagby (1985), high permeability and chemical reactivity in the host formations provide favourable conditions for the precipitation from mineralizing hydrothermal solutions of Carlin-type gold deposits. In the Takab area these conditions occur in the calcareous and carbonaceous shale, carbonates and marls, which together host most of the known mineralization in the area. The spatial model of the Zarshuran gold deposit demonstrated a stratigraphic control (Zarshuran black shale and Chaldagh limestone) on mineralization (chapter 3). The genetic modelling at Zarshuran (chapter 8) indicated that black shale and carbonate played an important role as the geochemically-reactive barriers to precipitate gold and associated elements.

Berger and Bagby (1985) point out that nearly all of the Carlin-type gold deposits in Nevada are spatially associated with intermediate to acid igneous rocks that are either exposed at surface or concealed at depth. Hydrothermal base-metal and epithermal precious-metal mineralizations are particularly pronounced in the eastern sector of the SSZ straddled by the Takab Shahin-Dez quadrangle. The geodynamic model of the ZOB developed in chapter 2 indicates that proximity with the Tertiary igneous rocks extending in a NE-SW direction within the SSZ and their intersections with NW-SE trending igneous rocks possibly connected to the UDMA is an important regional recognition criterion for these mineralizations.

Asadi and Hale (1999b) attribute high amplitude aeromagnetic anomalies within the Takab area to high magnetic-susceptibility igneous rocks. The highest anomalies are located in the central part of the area and coincide with the location of the Zarshuran deposit and its surroundings. At a distance of 2-3 km from Zarshuran these anomalies can be ascribed to widespread outcrops of Miocene volcanics, some of which are mineralized. In the immediate vicinity of Zarshuran, however, surface exposures are limited to Precambrian and Oligo-Miocene sediments, but high amplitude magnetic anomalies here suggest the presence of igneous intrusive rocks beneath the Zarshuran deposit and other nearby arsenic and antimony mineralizations. There are partially-altered andesites and highly altered granitoid rocks in the immediate vicinity of the Zarshuran gold deposit as well as near most of the other hydrothermal gold, arsenic, antimony and base-metal mineralizations in the area. Interpretation of ground magnetic data at Zarshuran suggests the presence of some subsurface intermediate-basic intrusive dykes or stocks dipping toward

the core of the Iman-Khan anticline. Miocene volcanic rocks and granitoids appear to have provided the main heat sources for the hydrothermal systems responsible for gold, arsenic, antimony, and base metal mineralization, and have also been a source of gold-bearing hydrothermal solutions (see chapter 8). Some igneous bodies in the area, and granitoids at Zarshuran, have been altered and mineralized, indicating that the hydrothermal systems post-dated associated magmatic events. The genetic model of mineralization at Zarshuran suggests the presence of an intermediate-basic magma at depth which is the main heat source driving the migration of mineralizing hydrothermal solutions (chapter 8).

The presence of hydrothermally-altered zones is an important guide to epithermal deposits of the area. Two types of hydrothermal alteration, argillic and iron oxide, are associated with most of the known mineral deposits of the area (Asadi and Hale, 1999b) and each provides an important deposit recognition criterion. For example, the Zarshuran gold deposit is characterized by argillic hydrothermal alteration, whilst the Aghdarreh gold deposit is characterized by iron oxide hydrothermal alteration. Zones of hydrothermal argillic alteration usually surround central zones of silicification or quartz veining, which are commonly mineralized (MacMillan and Panteleyev, 1988). This feature is also manifested in Zarshuran. In addition, zones of argillic alteration are weakly mineralized.

Structures, and particularly structural intersections, are also important for controlling magmatism, hydrothermal fluid flow and mineral deposition in the Takab area. Based on the geodynamic setting of the ZOB, proximity to the NE-SW trending faults and their intersections with the older NW-SE trending structures are important regional recognition criteria controlling epithermal precious-metal and hydrothermal base-metal mineralizations in the SSZ, including the Takab Shahin-Dez quadrangle.

At the district and deposit scale the NE-SW and NW-SE trending faults and their intersections appear to control the location of most of the known deposits of the Takab area. Asadi et al. (1998b) show that most of the known mineral deposits of the area are located in a 500 m buffer zone adjacent to the NE-SW trending lineaments interpreted from Landsat-TM data. Spatial modelling at Zarshuran revealed that late NE-SW faults displace stratigraphic units and also terminate the soil geochemical anomalies. The NE-SW faults and their intersections with NW-SE faults are the major structural controls on mineralization.

The geodynamic setting of the ZOB indicates that there is a spatial proximity between epithermal precious-metal and hydrothermal base-metal mineralizations and the NW-SE trending sheared and mylonitized ophiolitic rocks along the proposed suture zone at the boundary of the SSZ and UDMA

(chapter 2). Spatial modelling of the Zarshuran deposit reveals the presence of metamorphosed ophiolitic rocks (serpentinite) in the vicinity of the highly mineralized zones at Zarshuran (chapter 3). The genetic model of Zarshuran indicates that these metamorphosed ophiolitic rocks could be the source for (part of) the gold and associated elements (chapter 8).

9.3.2 Sources of data for DRC maps

The geophysical, geochemical, geological, satellite remote sensing and mineral occurrence data of the Takab Shahin-Dez quadrangle were processed and converted to new formats for interpretation. A database, with UTM coordinates, tables and standard processed maps, was created for the aeromagnetic, gamma-ray spectrometry data, Thematic Mapper (TM) imagery, stream sediment geochemistry, geology, mineral occurrences and DEM coverage of the Takab Shahin-Dez quadrangle. These datasets were captured in a GIS as tabulated in Table 9.1.

In 1978, a semi-high resolution aeromagnetic survey was carried out in the 1:250,000 scale map sheet of Takab Shahin-Dez Quadrangle. The flight lines were oriented north-south with a spacing of 500 m and a nominal terrain clearance of 120 m. The aeromagnetic data were retrieved from twenty four analogue aeromagnetic total intensity contour maps (1:50,000); the data retrieved extend beyond the Takab area (covering the whole Takab Shahin-Dez quadrangle) in order to avoid truncation of magnetic anomalies within the Takab area. The contour maps were digitized by capturing UTM coordinates (X and Y values) and total magnetic field intensity contour values (Z values) along flight lines, which provide the closest approximation to the original data.

The six reflective bands of digital TM imagery, acquired October 1987, were radiometrically and geometrically corrected. A submap for each band of the satellite data that covers the 1785 km^2 Takab area was extracted from a complete scene covering much of the Takab Shahin-Dez quadrangle. These map data were processed and interpreted in order to identify hydrothermal alteration and spectral features that characterize Zarshuran and other known deposits.

A regional stream sediment geochemical survey was carried out by the Geological Survey of Iran over two areas covered by two 1:100,000 scale map sheets (Takhte-Soleiman and Shahin-Dez). The survey yielded 1500 samples from which a subset of 194 samples was used to characterize much of the Takab area. Samples were analysed by X-ray fluorescence (XRF) for B, Co, Pb, Zn, As, Cd, Sn, Cr, Sr, Ba and Cu.

A digital database of known mineral deposits and likely controls on mineralization of the Takab area was established. Most of the known mineral deposits of the area were digitized from the mineral occurrence map of the Takab Shahin-Dez quadrangle (1:250,000 scale) published by the Ministry of Mines and Metals of Iran (1994). Some of the small occurrences were digitized from the 1:100,000 scale geological map of the Takab area published by the Geological Survey of Iran (1998), and also from the district scale geological maps of Zarshuran and Aghdarreh mining area (Samimi, 1992; Mineral Export Company, 1995). The database consists of 19 mineral occurrences extracted from these maps.

In addition, the contour elevation lines and drainage channels were digitized from the topographic map of the Quadrangle (1:250,000). The contour elevations were used to create a digital elevation model (DEM). The DEM and the rasterized drainage channels were used to automatically generate the sample catchment basins, labelled with geochemical sample numbers, representing the area of influence for each sample site. Also the map of sample catchment basins was crossed with the map of bedrock geology to produce a dataset containing areal proportions of rock units occurring in each basin.

Table 9.1. Data layers integrated in the GIS of the Takab area

Dataset	Type	Capture	Attributes	Remarks
Bedrock geology (1:250,000)	Polygons and lines	Table digitized	Rock types and structural features	Takab Shahin-Dez quadrangle
Bedrock geology (1:100,000)	Polygons and lines	Table digitized	Rock types and structural features	Takab area
Rivers	lines	Table digitized		
Mineral Occurrences (1:250000)	Points	ASCII file with UTM coordinates	Metal	Au, As, Sb, Pb/Zn, Fe, Cu, etc.
Topography (1:250,000)	Contour lines	Table digitized	Elevation	DEM creation
Landsat TM	Raster, grey scale and colour composite	Computer-compatible CD	6 spectral bands and 1 thermal band	Full scene
Airborne magnetics (semi-high resolution)	Raster and grey scale	Table digitized from 24 map sheets of 1:50,000 scale	Total magnetic field intensity values	500 m line spacing and 120 m terrain clearance
Stream sediment geochemistry	Catchment basin	ASCII file with UTM coordinates and stream sediment analytical results	Element content	Two 100,000 scale map of Takab and Shahin-Dez areas

9.4 DRC MAPS

The controls on mineralization consist of: (1) suitable host lithologies, digitized from the 1:100,000 scale geological map of the area published by the

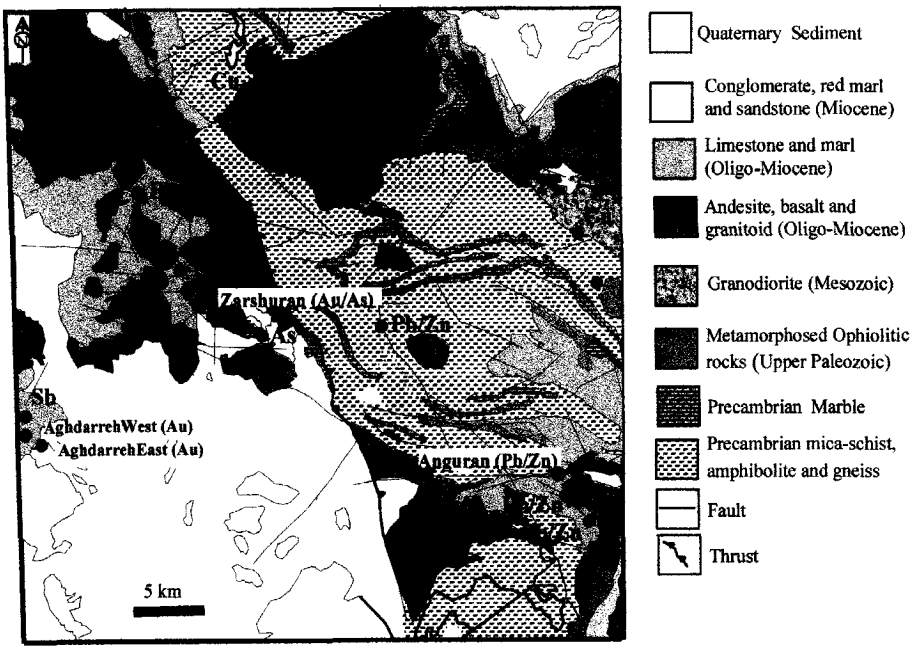

Fig. 9.2. Geological and mineral occurrence map of Takab area.

Geological Survey of Iran (1998); (2) volcano-plutonic heat sources, digitized from the same geological map and interpreted from the analytical signal image of the total magnetic field intensity; (3) hydrothermal alteration zones interpreted from the selected Landsat-TM bands and reduction to the pole of aeromagnetic data; (4) lineaments digitized from the 1:100,000 geological map and derived from the shaded relief image of total magnetic field intensity and the first principal component (PC) of six reflective TM bands; (5) metamorphosed ophiolitic rocks likely important sources for gold and associated metals, digitized from the 1:100,000 scale geological map of the area; and (6) stream sediment geochemical anomalies of As-Sb-Hg-Tl-Zn-Te are important DRC, nevertheless, the stream sediment samples were not analyzed for Sb, Hg, Te and Tl.

9.4.1. Map of favourable host lithologies

In the Takab area, most of the gold and base metal mineralizations, most obviously in the Zarshuran and Aghdarreh gold deposits and the Anguran lead-zinc deposit are hosted by chemically-reactive and permeable sedimentary

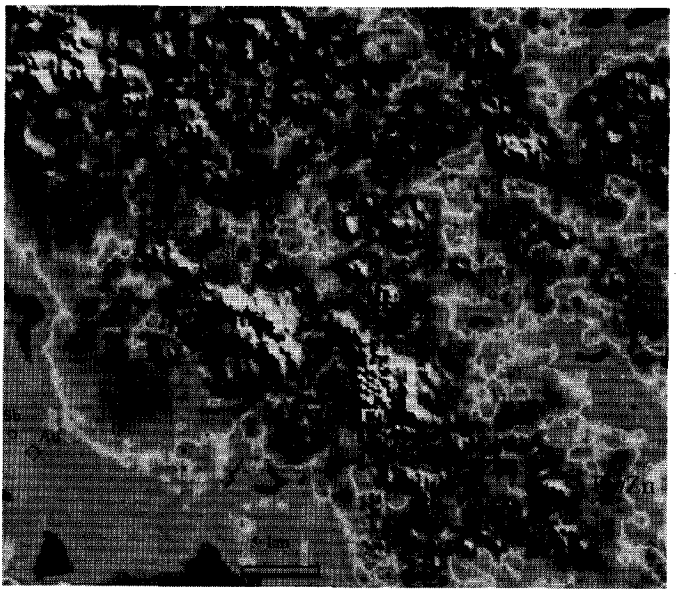

Fig. 9.3. Colour shaded relief map of the analytical signal of the total magnetic field intensity with the known deposits of the Takab area overlaid (see also Fig. 9.3 in colour figures).

formations. These include Precambrian black shales and carbonates, fractured Oligo-Miocene calcareous shales, karsted limestones, ferruginous carbonates and marls. The mapped outlines of these units were digitized from the 1:100,000 scale geological map of the area (Fig. 9.2) and converted to raster format (chapter 10).

9.4.2 Map of heat sources

Heat sources for hydrothermal systems include outcropping and concealed Oligo-Miocene volcano-plutonic rocks (i.e., andesites, granitoids and intermediate-basic intrusions). These outcrop over 21.4% of the Takab area. Still more lie beneath the surface. High resolution aeromagnetic data of the Takab area were used to re-map the main geological units and infer the subsurface geology.

Figure 9.3 is the colour shaded relief map of the analytical signal of the total magnetic field intensity of the Takab area, in which anomalously high-amplitude anomalies appear as purple shades. Most of these anomalies can be ascribed to widespread outcrops of Tertiary andesites. Others are interpreted with high-confidence as subsurface extensions of exposed Tertiary andesites.

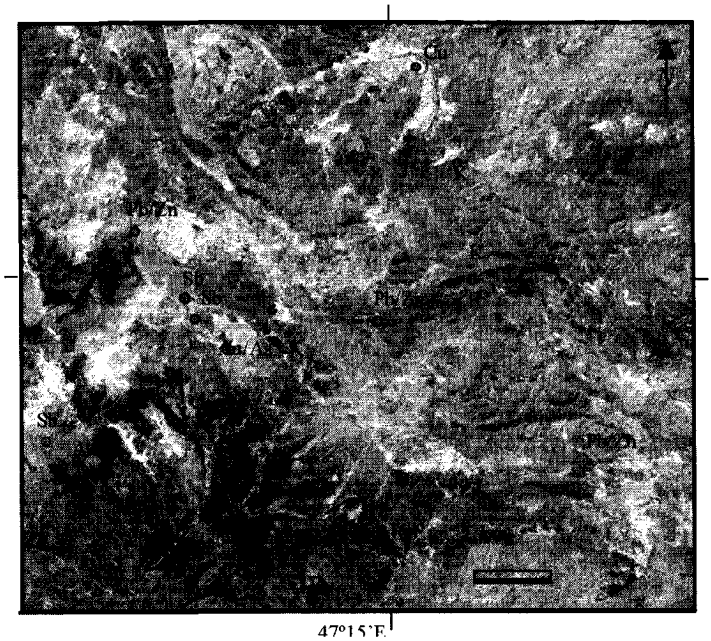

Fig. 9.4. Negated PC4 (Hydroxyl Image) showing hydroxyl-bearing minerals as bright zones.

The mapped subsurface igneous rocks represent 6.8% of the Takab area. The Tertiary andesites are partially mineralized and spatially associated with most of the known mineral deposits in the area (chapters 8 and 10).

9.4.3 Map of hydrothermal alteration

Landsat-TM imagery has picture elements that represent approximately 30m x 30m on the ground, excellent radiometric qualities and excellent geometric qualities (Richard, 1993). Six of the seven spectral channels (bands 1-5 and 7) represent terrain in terms of reflected radiation, in the wavelength ranges between 0.45 and 2.35 micrometers. According to Moore and Guo (1990), the most useful bands for general geological applications are band TM 5 (1.55-1.75 μm) and 'clay band' TM 7 (2.08-2.35 μm), whilst TM 1 (0.45-0.52 μm) and TM 3 (0.63-0.69 μm) are useful for mapping mafic rocks and iron-rich materials and soils. Landsat-TM imagery of the Takab area was enhanced and processed in order to map iron oxides and hydroxyl-bearing clay

minerals, which might reflect hydrothermal alteration associated with mineralization.

The method of principal component analysis proposed by Crosta and Moore (1989) was used here for the recognition of hydrothermal alteration (hydroxyl-bearing clay minerals and iron oxides). This technique has been successfully applied for alteration mapping associated with epithermal gold mineralization in arid and semi-arid terrains, mainly those in the western United States (Crosta and Moore, 1989; Loughlin, 1991).

9.4.3.1 Hydroxyl-bearing clay minerals

In order to map the distribution of hydroxyl-bearing clay minerals, those reflected radiation TM bands that contain appropriate information are incorporated in a principal components (PC) image. Since iron oxides have strong reflectance in TM2 and TM3, these are omitted and the PC image for hydroxyl-bearing minerals is generated from TM1, TM4, TM5 and TM7. Hydroxyl spectra have strong absorption across TM7 and rather more reflectance across TM5. The PC image that best discriminates hydroxyl-bearing minerals is that with a high eigenvector loading, irrespective of sign, for TM7 and an eigenvector loading of opposite sign for TM5. When the eigenvector for TM7 is positive, negation is used to display hydroxyl-bearing minerals as bright pixels.

Table 9.2 shows the eigenvector loadings resulting from the principal components transformation of TM1, TM4, TM5 and TM7 of the Takab area. The highest eigenvector loading for TM7 is in PC4, which also has an eigenvector loading of opposite sign for TM5. The hydroxyl-bearing minerals are therefore best mapped by PC4. Because the eigenvector loading for TM7 in PC4 is positive, the PC image is negated to show hydroxyls as bright pixels (Fig. 9.4).

The first principal component (PC1) shows the albedo image and is therefore excluded from further consideration. Both PC2 and PC3 may contain subordinate information about hydroxyl-bearing minerals and are combined with negated PC4 to form a colour composite. Hydroxyl-bearing minerals are identified as bright pixels in this image. The Zarshuran gold deposit and Anguran lead-zinc deposit are highlighted by orange pixels, which could indicate partially-obscured hydroxyl (Fig. 9.5).

Table 9.2. Eigenvector covariance matrix of four TM Bands transformation for hydroxyl mapping

PCs	TM1	TM4	TM5	TM7	Variance %
PC1	0.24	0.36	0.79	0.46	94.58
PC2	0.88	0.30	-0.32	-0.17	3.21
PC3	0.38	-0.84	0.03	0.40	1.50
PC4	-0.14	0.29	-0.54	0.78	0.71

Ground truthing and spatial analysis indicated that most of the mapped hydroxyl zones are spatially associated with the igneous heat sources and controlled by the linear structures of the area. They are mainly argillic hydrothermal alteration (e.g., sericite, kaolinite and illite) which characterizes many of the known mineral deposits

Table 9.3. Eigenvector covariance matrix of four TM Bands transformation for iron-oxide mapping

PCs	TM1	TM3	TM4	TM5	Variance %
PC1	0.27	0.41	0.37	0.79	92.80
PC2	0.73	0.44	0.10	-0.52	5.20
PC3	0.47	-0.23	-0.79	0.33	1.45
PC4	0.42	-0.77	0.48	0.03	0.55

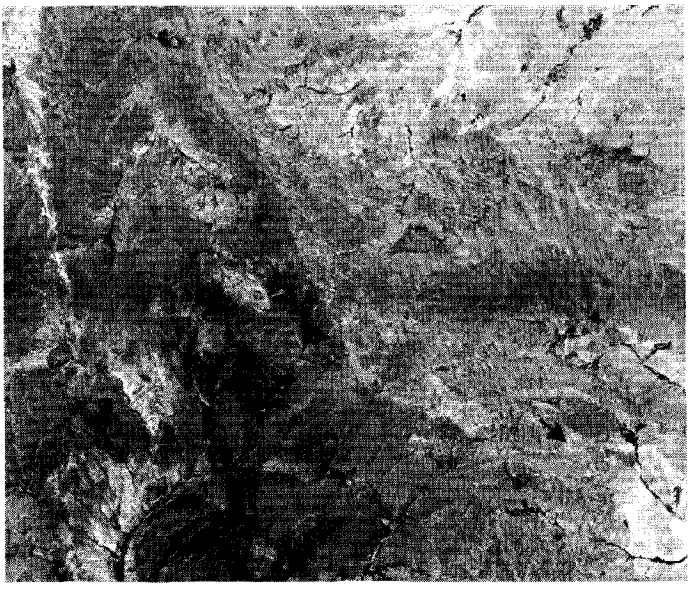

Fig.9.5. Colour composite image of negated PC4 and PC2 and PC3 showing the hydroxyl bearing minerals as bright-orange pixels, Zarshuran (central) and Anguran (southeast) are highlighted by orange pixels (see also Fig. 9.5 in colour figures).

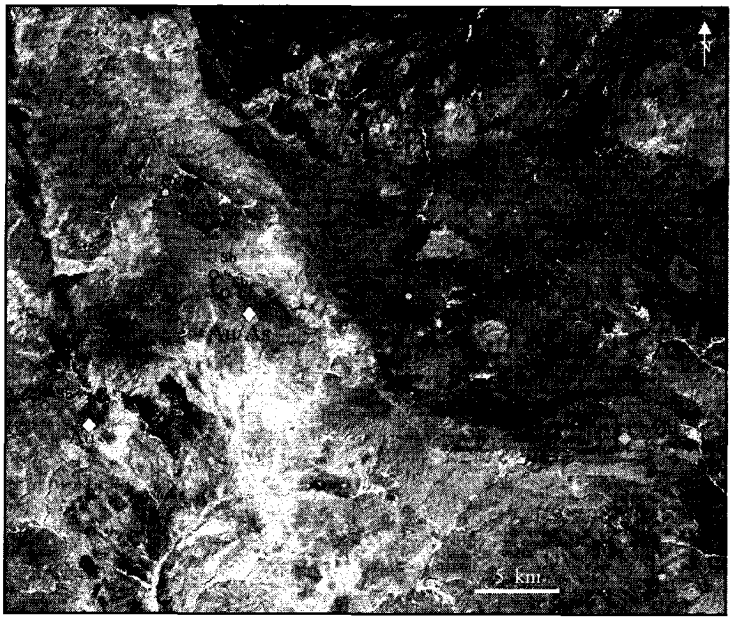

Fig. 9.7. PC1 (Iron Oxide Image) showing iron oxide as bright zones.

9.4.3.2 Iron oxide minerals

In order to map the distribution of iron oxide minerals, those reflected radiation bands that contain appropriate information are incorporated in a principal components (PC) image. Since hydroxyl has strong reflectance in TM7, this is omitted, as is TM2 which has iron oxide spectral characteristics intermediate to those of TM1 and TM3. The PC image for iron oxide minerals is generated from TM1, TM3, TM4 and TM5. Iron oxide spectra have strong reflectance across TM3 and rather more absorption across TM1. The PC image that best discriminates iron oxide minerals is that with a high eigenvector loading, irrespective of sign, for TM3 and an eigenvector loading of opposite sign for TM1. When the eigenvector loading for TM3 is negative, negation is used to display iron oxide minerals as bright pixels.

Applying this method to TM1, TM3, TM4 and TM5 of the Takab area, iron oxides are mapped in both PC3 and PC4 (Table 9.3). In order to extract the iron oxide information from both PC3 and PC4 into a single image, PC3 and PC4 are first stretched to give each similar means and standard deviations, then a pairwise principal components transformation is performed. The PC image from this transformation with two positive eigenvector loadings, in this case $PC1_p$, shows the iron oxide minerals as bright pixels (Fig. 9.7).

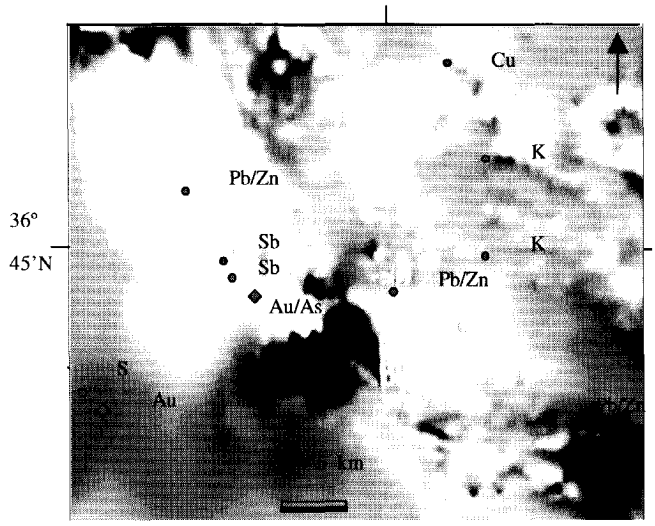

Fig. 9.8. Reduction to the pole image showing magnetic lows as dark shades.

Reduction to the pole of the total magnetic intensity data was used by Asadi and Hale (1999b) to map iron oxide hydrothermal alteration zones associated with epithermal mineralization of the Takab area. Reduction to the pole of the total magnetic field intensity data affords improved visualization of anomalously low magnetism due to the demagnetization of magnetite in contact with hydrothermal fluids, yielding epigenetic hematite and limonite (Patterson and Halof, 1991). Figure 9.8 is a map of total magnetic field intensity reduced to the pole showing anomalously low magnetic zones in black. The largest anomaly in the central part of the area coincides with the southeastern and eastern parts of the Zarshuran mining area. Another large anomaly is situated in the southeast of the area and coincides with the Anguran lead-zinc mining area. In the north anomalies surround a circular feature of high magnetic intensity, possibly representing a sub-surface intrusion. In the southwest of the area what appears as a weak anomaly characterizes Aghdarreh Au-Sb mining area. Beyond the Takab area, however, this weak anomaly is seen to be the extremity of another large anomaly extending over 20 km in a NE-SW direction.

Some of the iron oxide zones mapped by principal components are located in the southern part of the area, where there is no evidence of volcanic activity to form hydrothermal alteration. These iron oxides, associated with a Miocene red sandstone formation, are attributed to surface weathering. In order to have high confidence in a map of iron oxides from hydrothermal alteration rather

than surface weathering, the iron oxides mapped by principal components analysis and those mapped by reduction to the pole technique were crossed, and the overlapping zones extracted.

9.4.4 Map of structures

Faults trending NE-SW and NW-SE, which have a spatial association with Zarshuran and other known mineralizations in the Takab area, were digitized from the 1:100,000 geologic map. In addition, shaded relief total magnetic field intensity data and the processed Landsat-TM imagery of the area were used to map structures (i.e., surface and subsurface faults) that were not recorded on the geological map.

Successful representation of lineament features in shaded relief depends upon the choice of illumination azimuth (preferably perpendicular to the linear features), illumination angle above the horizon and exaggeration of vertical scale. For the Takab area, two different illumination angles were chosen to map the structures trending in different directions. A shaded relief map of total magnetic field intensity with an artificial illumination of azimuth of 45°, an inclination of 45° and a scale factor of 0.35 highlights the major structural features oriented in a NW-SE direction parallel to the Zagros thrust. A map with an azimuth of 315°, an inclination of 45° and a scale factor of 0.35 shows lineaments perpendicular to the major structures (Fig. 9.9). Many of the known mineral deposits of the area lie on or close to these lineaments.

Processing of the TM imagery was also carried out to map the structural controls in the Takab area. A principal components transformation was applied to the six reflected radiation TM bands of the area to produce PC images containing most of the information in the visible and near-infrared regions. The first principal component (PC1), containing the overall albedo of the area, displayed the structural features much better than the other images, and was therefore used for lineament discrimination. In addition, a colour composite image from the combination of TM7, TM2 and TM1 proved to be the best image to assist lineament discrimination. Directional filtering was applied to both the PC1 image as well as to each component of the colour composite image to enhance lineaments.

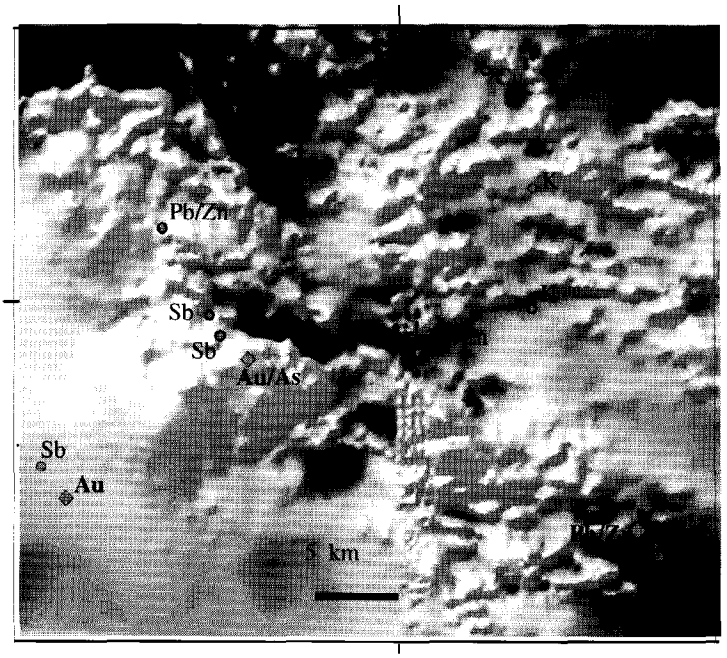

9.9. Shaded relief image of total magnetic field intensity map of Takab area (Illumination angle=315°)

Finally, on the basis of the geodynamic model of the ZOB (chapter 2), a few regional NE-SW conjugate faults that have spatial controls on known hydrothermal base-metal and epithermal precious-metal mineralization and are adjacent to outcropping volcano-plutonic rocks were added to the map of the structural controls of the Takab area.

9.4.5 Map of favourable metal sources

Genetic modelling of gold mineralization at Zarshuran indicated that metamorphosed ophiolitic rocks (e.g., serpentinites), characterized by very strong positive magnetic susceptibility, are possible sources for gold. Spatial modelling of the deposit displayed a close association between these rocks and highly mineralized zones. The Zagros suture at the boundary of the Sanandaj-Sirjan zone (SSZ) and the Urumieh-Dokhtar Magmatic Assemblage (UDMA), discussed in chapter 2, is marked by such rocks. The mapped outlines of these rocks were digitized from the 1:100,000 scale map sheet of the Takab area (Fig. 9.2).

9.4.6 *Map of geochemical signatures of gold mineralization*

Table 9.4 contains the summary statistics of the geochemical variables. All of the raw data distributions are positively skewed. By applying a natural logarithmic ($\log_e$) transformation, the asymmetry of the distributions is effectively reduced. Therefore, the statistical analyses were carried out using the $\log_e$-transformed data.

Table 9.4. Univariate statistics of the geochemical data of Takab area

Element	n	Minimum	Maximum	Mean	Std. Dev.	Skewness	Skewness ($\log_e$)
B	194	15	580	64	52	5.69	0.66
Co	194	5	73	29	12	1.12	-0.20
Pb	194	9	>1000	95	144	3.36	0.75
Zn	194	34	>1000	143	101	4.58	0.81
As	165	1.3	1946	70	183	7.46	0.69
Cd	166	1.7	4500	164	426	7.39	0.18
Sn	186	1	20	3.7	1.60	6.34	0.45
Cr	132	5	564	95	87	2.34	-0.56
Sr	194	79	1796	286	180	3.82	0.53
Ba	194	14	3247	444	404	3.48	-0.57
Cu	153	5	247	61	47	1.62	-0.41

9.4.6.1 *Filtration of effects of factors irrelevant to mineralization*

Two factors that heavily influence the stream sediment geochemistry are the composition of the non-mineralized rocks within the catchment basin and surficial chemical controls (e.g., scavenging of metal ions by oxides of Mn and Fe). These effects are predicted and filtered-out from the geochemical data to leave residuals from which the signatures of anomalous geological processes (e.g., mineralization) may be seen.

Given the observed stream sediment element contents Y_i at locality i, the areal proportions, X_{ij}, of the jth rock unit in the ith sample catchment basin attached to locality i, and the Mn and Fe contents (Mn_i, Fe_i) at locality i, the stream sediment element contents due to the lithologic and chemical controls are predicted using a simple regression model as follows:

$$\acute{Y}_i = b_o + \sum_{j=1}^{m} b_j X_{ij} + b_{Mn} Mn_i + b_{Fe} Fe_i$$

with $\sum_{j=1}^{m} X_{ij}=1.0$ for $j=1,2,....,m$ rock units in sample catchment basin i; b_o, b_j, b_{Mn} and b_{Fe} are the regression coefficients. Estimation of the element contents is accomplished by minimizing the quantity $\sum_{j=1}^{m} (Y_i - \acute{Y}_i)$ using the least squares regression procedure.

It is assumed that the predicted element content is a result of mixing of weathering products (i.e., an additive mixing model); that is, setting $b_o=0$ and interpreting b_j as background element contents of the jth rock unit, $b_{Mn}Mn$ and $b_{Fe}Fe$ as fraction of the measured metal contents due to the chemical controls. However, because the values of Y are $\log_e$-transformed, the model becomes multiplicative with respect to the raw data and the additive mixing hypothesis is not modelled (Bonham-Carter et al., 1987). Nonetheless, the $\log_e$ transforms of the original data are used and b_o is forced through the origin so that the b_j, b_{Mn} and b_{Fe} are easy to interpret (Bonham-Carter and Goodfellow, 1986).

Bonham-Carter et al. (1987) pointed out that statistical tests of significance of the regression coefficients are considered inappropriate if the individual sample points are not independent. Due to the relatively high sampling density in the Takab area, the individual sample points are expected to be autocorrelated. Consequently, statistical tests of significance of the regression coefficients are not applied. In this situation, the effectiveness of the independent variables in accounting for the variation of the dependent variables can be characterized by using R^2 (expressed as a percentage), the ratio of the sum of squares explained by the regression to the total sum of squares.

To evaluate the relative contribution of the lithologic and chemical controls to the variability of the geochemical data, the regression experiments were carried out in two steps: (1) regression against areal proportions of rock units, and (2) regression against areal proportions of rock units, Mn and Fe contents. In the first step, the explained variability in the geochemical data is attributed to the lithologic controls. In the second step, additional contribution of Mn and Fe content to the explained variability of the geochemical data is attributed to surficial chemical controls.

The results of the regression experiments are summarized in Table 9.5. For all elements, the lithologic controls explain between 89 and 99.5% of the variations in the geochemical data. For all elements, the chemical controls account for less than 2% in explained variability over that already explained by the lithologic controls. These results indicate that the stream sediment geochemistry of the study area is controlled mainly by the lithologic controls and to a minimal extent by the chemical controls.

Table 9.5. Results of regression of stream sediment element contents against areal proportions of rock units and Fe and Mn contents.

Dependent variables	% variation due to independent variables (R^2)		Additional variation due to Mn & Fe
	lithology	lithology+Fe+Mn	
B	98.70	98.75	0.05
Co	98.89	98.94	0.05
Pb	94.00	94.03	0.03
Zn	99.06	99.13	0.07
As	89.06	90.47	1.47
Cd	90.25	91.11	0.86
Sn	94.83	95.00	0.17
Cr	95.89	96.42	0.53
Sr	99.46	99.57	0.11
Ba	98.32	98.82	0.50
Cu	95.62	97.34	1.72

Based on the results of the regression analyses, element contents due to the lithologic and chemical controls are estimated according to the equation:

$$\acute{Y}_i = \sum_{j=1}^{m} b_j X_{ij} + b_{Mn} Mn_i + b_{Fe} Fe_i$$

Filtration of the predicted data from the original data (i.e., $Y_i - \acute{Y}_i$) results in residuals which may reflect other sources. In particular, positive geochemical residuals are considered to reflect enhancement in the stream sediment geochemistry caused by anomalous geological processes (e.g., mineralization). The positive geochemical residuals are, therefore, used to determine a multi-element geochemical signature for the known mineral occurrences in the Takab area.

9.4.6.2 Determination of geochemical signature of mineral occurrences

For sample catchment basins that contain outcropping mineralization, it may be expected that there is a surficial enrichment (i.e., positive residuals) in the concentrations of the suite of elements associated with the mineralization. This suite of elements with enriched concentrations in the surficial materials (in this case stream sediments) may be taken to represent the surficial geochemical signature of the mineralization.

To determine the multi-element surficial geochemical signature that characterizes known mineral occurrences in the Takab area, a variable is used to indicate whether a sample catchment basin contains a mineral occurrence (score = 1) or not (score = 0) and the positive geochemical residuals are

calculated by means of stepwise multiple regression analysis using 11 geochemical variables in the stream sediment data. The variable indicating presence/absence of mineralization is taken to represent the 'observed mineral occurrence index' of a sample catchment basin. If O_i, a binary variable denoting the observed mineral occurrence index of the ith catchment basin, is taken as the dependent variable, and if R_j (j=1,2,...,11), the positive geochemical residuals of each of the 11 geochemical variables in the ith catchment basin, are used as the predictor variables, then a 'predicted mineral occurrence index' is calculated according to the regression equation (Bonham-Carter et al., 1988):

$$\hat{O}_i = b_o + \sum_{j=1}^{11} b_j R_{ij}$$

Assuming that an absence of a positive geochemical residual represents an absence of mineral occurrence, b_o is forced through the origin and the coefficients b_j are determined through ordinary least-squares regression. The final regression equation thus means that sample catchment basins with high positive geochemical residuals for a suite of significant elements (see below) have a high 'predicted mineral occurrence index'.

A forward stepwise multiple least-squares regression is then carried out in which the positive residual for each of the 11 geochemical variables is added sequentially to the regression equation in such a way that the variable which is added (out of those not yet added) contributes significantly to the regression sum of squares (Howarth and Sinding-Larsen, 1983). If at any step a variable already included now contributes a non-significant amount to the sum of squares, it is removed. At each step, the significance of the independent variables to the regression is tested using the F-ratio which is equal to the ratio of the sum of squares due to regression with j variables to the mean squares of residuals. At each step of the regression, a F-value of 4 is used as the statistical criterion to determine whether the newly-added variable contributes significantly to the regression sum of squares. The statistical criterion, taken from a statistical look-up graph in Howarth (1983), is based on 1 and [a possible minimum of n-j-1=132-11-1=] 120 degrees of freedom at the 95% significance level.

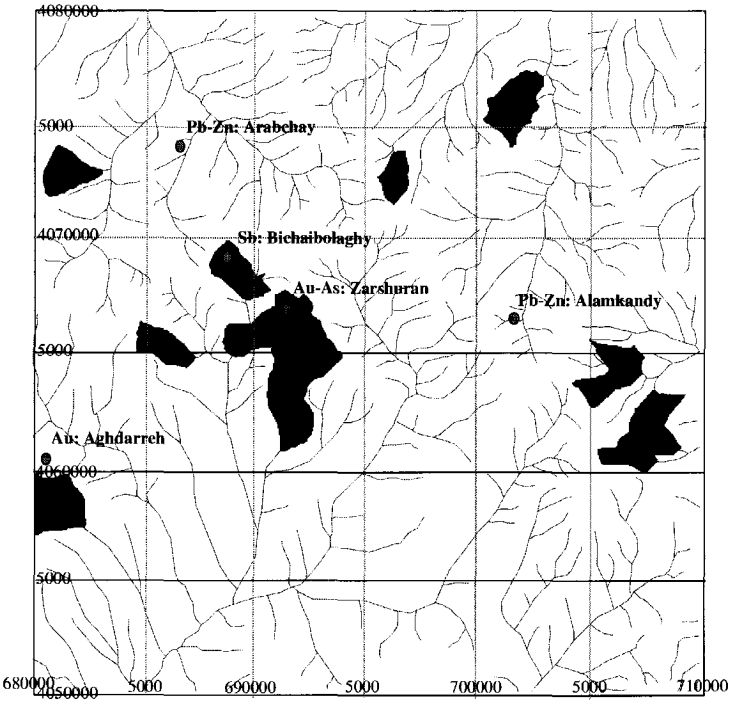

Fig. 9.10. Sample catchment basins with > 80% quantified geochemical signature of known mineralization.

Table 9.6. Significant variables for the prediction index of mineral occurrence.

Element	b	F-value
As	0.1587	8.0456
Zn	0.0857	4.1146
Cd	-0.1019	4.6864

The significant predictor variables that remain in the final regression equation (Table 9.6) are taken to represent a multi-element surficial geochemical signature that characterizes the known mineral occurrences in the Takab area. The different known mineral occurrences in the area can be collectively characterized by an As-Zn-Cd signature. The 'predicted mineral occurrence index', calculated according to the final regression equation, is taken to represent the degree of favourability of a sample catchment basin to contain a possible mineral occurrence with an As-Zn-Cd surficial geochemical signature.

The known mineral occurrences in the area are within or adjacent to sample catchment basins with a predicted mineral occurrence index >80 percentile (Fig. 9.10). This implies that sample catchment basins with predicted mineral occurrence index >80 percentile are likely to contain mineral deposits similar to the known mineral occurrences.

9.5 CONCLUSIONS

(1) Genetic and spatial models of known deposits are useful in providing deposit recognition criteria (DRC) that guide GIS investigations during regional mineral exploration.
(2) The most important DRC for epithermal gold and base-metal mineralizations in the Takab area are: (a) chemically-reactive and permeable sedimentary formations; (b) volcano-plutonic heat sources; (c) proximity to ophiolites; (d) hydrothermal alteration (argillic alteration and iron oxides); (e) proximity to NE-SW lineaments and their intersections with NW-SE lineaments; and (f) an arsenic-zinc-cadmium surficial geochemical signature.
(3) Zones of epithermal mineralization potential in the Takab area can be extracted from spatial covariations in different geodata sets using spatial features related to the Zarshuran deposit (plus spatial features related to other known epithermal deposits), genetic criteria from the Zarshuran deposit and the geodynamic setting of the Zagros Orogenic Belt.
(4) The analytical signal technique applied to the semi-high resolution aeromagnetic data of the Takab area represents an important tool for mapping subsurface high-magnetic susceptibility igneous rocks associated with the known deposits of the area.
(5) Remote sensing is an effective tool for detecting the spectral and magnetic signatures characterizing recognition criteria of epithermal mineralization in the Takab area.
(6) The principal components transformation (PC) technique applied to the Landsat TM data indicates the presence of hydrothermal alteration consisting of either iron oxides or hydroxyl-bearing clay minerals associated with the known deposits of the area.
(7) The validity of hydrothermal alteration zones identified by the PC technique can be verified by using reduction to the pole of aeromagnetic data in order to detect magnetic lows resulting from magnetite destruction by hydrothermal solutions.
(8) Shaded relief maps of total magnetic field intensity data and the directional filtering applied to the first principal component image of six

reflective Landsat-TM bands revealed several major NE-SW trending lineaments that were not mapped in the geological maps of the area; many of the known deposits of the area lie on or close to these lineaments.

(9) The major NW-SE lineaments of the area represent the major thrust of the area, at the contact of Tertiary volcano-sedimentary rocks and Precambrian metamorphics. The E-W and NE-SW trending lineaments probably represent conjugate faults generated almost perpendicular to the thrust. The known mineral deposits lie within a distance of 500 m from the E-W and NE-SW lineaments interpreted from Landsat-TM and aeromagnetic data. This implies that areas within a 500 m distance from similar trending lineaments may be favourable for the occurrence of similar mineralization

(10) Filtering high values of the stream sediment geochemical data gives an index characteristic of known mineralization. In the Takab area the sample catchment basins with a predicted mineral occurrence index of >80 percentile might contain mineral deposits similar to the known mineral occurrences.

In this chapter characteristics of known mineralization in the Takab area were chosen and converted to six evidence maps. In order to create a single map indicating potential mineralization in the Takab area, these maps are combined using a weights of evidence model in the next chapter.

Chapter 10

A PREDICTIVE GIS MODEL FOR MAPPING POTENTIAL GOLD AND BASE METAL MINERALIZATION IN THE TAKAB AREA

In chapter 9, interpretation of aeromagnetic, Landsat TM, geological, geochemical and mineral occurrence data was used to identify the geological features, spectral characteristics, and magnetic and geochemical signatures associated with the Zarshuran gold deposit and other epithermal gold, arsenic, antimony and base-metal deposits in the Takab area. Six representative maps of the deposit recognition criteria (DRC) in the Takab area were created. In this chapter, these maps are combined in a weights of evidence model which uses the spatial distribution of 19 known mineral occurrences. A predictive geographic information system (GIS) model is constructed to locate areas of interest for future gold and base metal exploration. This chapter is an edited version of a paper entitled *A predictive GIS model for mapping potential gold and base metal mineralization in Takab area, Iran*, published in the proceedings of the 4th International Conference on Geocomputation, Mary Washington College, Fredericksburg, Virginia, USA, paper No. 12 (CD ROM) and is in press in the Journal of Computers and Geosciences, Spatial Issue of the 13th Geocomputation Conference (Asadi and Hale, 1999c and 2000b).

10.1 INTRODUCTION

Genetic models are conceptual models that describe the typical characteristics of a deposit or a group of similar deposits and classify the

features that control mineralization. They are useful in providing deposit recognition criteria that can guide a GIS approach to regional mineral exploration. Chapter 9 describes how a developed gold deposit model as well as the regional mineralogical and geological background of northwest Iran are used to predict potential areas for carbonate-hosted epithermal mineralization. The spatial and genetic controls for gold, arsenic, antimony and base-metal mineralizations in the Takab area were used to select data input to a GIS, and to find out which features to enhance and extract (e.g., appropriate spectral, magnetic, geochemical and geological features) as the deposit recognition criteria. This chapter explains how to weigh the relative importance of six evidence maps representing diagnostic deposit recognition criteria for regional potential mapping in the 1782 km^2 Takab area.

10.2 WEIGHTS OF EVIDENCE METHOD

Bonham-Carter et al. (1989) and Bonham-Carter (1994) described the way in which the quantitative relationships between the data sets representing the deposit recognition criteria and known mineral occurrences is analyzed using a Bayesian statistical method. A series of binary maps is created for mineral occurrences and recognition criteria. The locations of known mineral occurrences are treated as single pixels. A pixel size representing 100 x 100 m (thus the nominal area of a mineral occurrence) is used to rasterize the mineral occurrence and deposit recognition criteria maps. The resulting binary maps are used as input maps to Bayesian statistical analysis and the end product is a sum of weights map ranking favourable areas.

Each binary map depicts areas where the test domain represented by the map is either present (D_p) or absent (D_n). Scoring is then performed using that domain and known mineral occurrences, in order to obtain a range of positive and negative weights (W+ and W-). In detail the mathematical basis for calculating weights is involved (Bonham-Carter, 1994). Turner (1997) suggested a simplified approach based on an approximation of the conditional probability.

Positive spatial
association if (% mineral occurrences in D_P) ÷ (% of total area occupied by D_p)>1

Negative spatial
association if (% mineral occurrences in D_P) ÷ (% of total area occupied by D_p)<1

No spatial
association if (% mineral occurrences in D_P) ÷ (% of total area occupied by D_p =1

In the case of positive associations, more known mineral occurrences fall in the test domain (D_P) than would be expected if the mineral occurrences and test domain are unrelated. Conversely, a negative association implies the occurrence of fewer known mineral deposits in the test domain than would be expected if the mineral occurrences and test domain are unrelated.

Since the area covered by a mineral occurrence is much smaller than the domain being considered, weights of evidence are estimated by taking the natural log of the probability ratios:

W^+ = ln ((% mineral occurrence in D_p) ÷ (% of total area occupied by D_p))

W^- = ln ((% mineral occurrence in D_n) ÷ (% of total area occupied by D_n))

These weights give unitless measures of spatial correlation between mineral occurrences and recognition criterion (i.e., test domain). The contrast, $C = W^+ - W^-$, combines these weights into an overall measure of association for a given test domain. For a positive spatial association, C is positive; C is negative in case of negative correlation.

For each test domain the maximum contrast often gives the best measure of spatial correlation with the mineral occurrence points provided there is a large area and a large number of mineral occurrences (Bonham-Carter 1994; Turner 1997; Wilkinson et al., 1999). In the case of a small area and a small number of mineral occurrences the uncertainty of the weights could be large and therefore C can be meaningless. The Studentized value of C, calculated as the ratio of C to its standard deviation, C/s(C), serves as a test of the statistical significance of the spatial correlation between the mineral occurrence points and a test domain (Bonham-Carter, 1994). The standard deviation (s) of *C* is the square root the sum of the variances of the weights:

$$s(C) = \sqrt{s^2(W^+) + s^2(W^-)}$$

The Studentized value of C is used to define the optimum cutoff.

A simplified Bayesian weights of evidence analysis approach was used by Turner (1997) to create a predictive GIS model for exploration for sediment-hosted gold deposits in a large area of north-central Nevada. Turner (1997) used the mathematical basis of Bayes' rule to calculate weights, W^+ and W^-, and contrast, C, in order to create a ranked-favourability map. Turner (1997) did not test the conditional independence of the input recognition-criteria

binary maps as explained by Bonham-Carter (1994). This approach, modified by calculating the Studentized value of C as well as by applying a conditional independence test, is used for the sediment-hosted gold and base-metal deposits of the Takab area, which appear to share several similarities with those of north-central Nevada.

10.3 WEIGHTS OF EVIDENCE ANALYSIS

For the Takab area the approach was implemented in a GIS. Six binary maps (test domains) representing the six deposit recognition criteria were generated with buffer zones at distances of 100-500 m (in increments of 100 m) away from criteria outlines. Weights were calculated at every location (pixel) for each map. The weighted binary maps were combined to create a final predictive map. The result is shown as a "sum of the weights" map (e.g., Turner, 1997), rather than as a posterior probability map as used by Bonham-Carter et al. (1989) and Bonham-Carter (1994). In terms of order of ranking relationships there is a 1:1 correspondence between the "sum of weights" map and the posterior probability map (G.F. Bonham-Carter, written communication, 1999).

10.3.1 Analysis of host lithologies domain

Favourable host rocks are exposed over 12.05% of the Takab area. These are buffered in order to include potentially-favourable lithologies that may be covered by unfavourable lithologies. The rasterized mineral occurrence map was crossed with the buffered favourable host lithology map to calculate the weights of evidence (W^+ and W^-) for cumulative distance away from the favourable host lithology (Table 10.1). The optimum cutoff distance was selected at 300 m away from the outline of the host lithology on the basis that the highest Studentized value of C (C=4.04) is estimated at this distance. Twelve out of 19 occurrences, including the two major gold deposits of the area (Zarshuran and Aghdarreh) and the largest lead-zinc mine of the area (Anguran), fall in the host lithology domain within the 300 m buffer zone (Fig. 10.1a). The weights of this favourable domain used for the final model are:

$W^+ = 1.15$ if in a favourable host rock domain;
$W^- = -0.77$ if not in a favourable host rock domain.

10.3.2 Analysis of heat-sources domain

Surface exposures of Tertiary igneous rocks and the interpreted high magnetic-susceptibility igneous rocks beneath the sediments were combined in a binary raster map to represent the heat sources driving the migration of mineralizing hydrothermal solutions. The resulting heat-source domain map was buffered at distances of 100 m to 500 m, and weights of evidence, contrast C, and Studentized value of C were calculated (Table 10.1). The optimum buffer, yielding the maximum Studentized value of C, was defined at 200 m. The resulting buffered igneous heat-source domain constitutes 31.49% of the area, and 13 out of 19 mineral occurrences are present in this domain (Fig. 10.1b). This weights of evidence analysis reveals a moderate to strong correlation between the igneous heat sources and mineral occurrences. This spatial affinity is more evident in the Zarshuran mining district in the central part of the area than elsewhere. The weights used in the final model are:

$W^+ = 0.78$ if in a favourable heat source domain;
$W^- = -0.77$ if not in a favourable heat source domain.

10.3.3 Analysis of hydrothermal alteration domain

Iron oxide and hydroxyl hydrothermal alteration occurs over 5.25% of the Takab area. In order to have high confidence that iron oxides used in the weights of evidence analysis resulted from hydrothermal alteration rather than surface weathering, the iron oxides mapped by principal components analysis and those mapped by reduction to the pole were crossed, and the overlapping zones extracted for the weights of evidence analysis. Argillic hydrothermal alteration and iron oxide hydrothermal alteration were then combined into a new map which was used as the third binary predictor input map for weights of evidence analysis. The resulting hydrothermal alteration domain map was buffered at distances of 100 m to 500 m, crossed with the raster mineral occurrence map, and weights of evidence, contrast C and Studentized values of C were calculated (Table 10.1). The optimum buffer, that yielding the maximum Studentized value of C, was defined at 300 m. The resulting buffered hydrothermal alteration domain covers 20.56% of the study area, and 12 out of 19 mineral occurrences are present in this domain (Fig. 10.1d). The

Table 10.1. Weights of evidence analysis of recognition criteria domains

Distance (m)	Mineral Co. Points	% Co.	No. of pixels in domain	% Domain	Ratio [1]	W^+	W^-	C [2]	$S^2(W^+)$ [3]	$S^2(W^-)$ [4]	S (C) [5]	C/S(c) [6]
Host lithology domain												
100	8	42.11	26234	14.70	2.86	1.05	-0.39	1.44	0.13	0.09	0.46	3.10
200	10	52.63	30805	17.26	3.05	1.11	-0.56	1.67	0.10	0.11	0.46	3.64
300	**12**	**63.16**	**35828**	**20.07**	**3.15**	**1.15**	**-0.77**	**1.92**	**0.08**	**0.14**	**0.48**	**4.04**
400	12	63.16	40006	22.42	2.82	0.39	-0.74	1.14	0.08	0.14	0.48	2.39
500	14	63.16	42874	24.02	2.63	0.97	-0.72	1.69	0.07	0.20	0.52	3.24
Heat source domain												
100	12	63.16	52300	29.30	2.16	0.77	-0.65	1.42	0.08	0.14	0.48	2.98
200	**13**	**68.42**	**56200**	**31.49**	**2.17**	**0.78**	**-0.77**	**1.55**	**0.08**	**0.17**	**0.49**	**3.14**
300	13	68.42	75207	42.14	1.62	0.48	-0.61	1.09	0.08	0.17	0.49	2.21
400	13	68.42	79358	45.14	1.52	0.39	-0.55	0.94	0.08	0.17	0.49	1.91
500	13	68.42	85358	47.83	1.43	0.36	-0.50	0.86	0.08	0.17	0.49	1.74
Hydrothermal alteration domain												
100	6	31.58	19369	10.85	2.91	1.07	-0.26	1.33	0.17	0.08	0.49	2.70
200	9	47.37	27944	15.66	3.03	1.11	-0.47	1.58	0.11	0.10	0.46	3.44
300	**12**	**63.16**	**36699**	**20.56**	**3.07**	**1.12**	**-0.77**	**1.89**	**0.08**	**0.14**	**0.48**	**3.97**
400	12	63.16	43424	24.33	2.60	0.39	-0.72	1.11	0.08	0.14	0.48	2.34
500	13	84.21	45313	25.39	3.32	1.20	-1.55	2.75	0.08	0.33	0.63	3.55
Structural domain												
100	7	36.84	29119	16.32	2.26	0.81	-0.28	1.10	0.14	0.08	0.48	2.30
200	**12**	**63.16**	**39570**	**22.17**	**2.85**	**1.05**	**-0.75**	**1.79**	**0.08**	**0.14**	**0.48**	**3.77**
300	12	63.16	64977	36.41	1.73	0.55	-0.55	1.10	0.08	0.14	0.48	2.31
400	14	73.68	73222	41.03	1.80	0.39	-0.81	1.20	0.07	0.20	0.52	2.30
500	15	78.95	81673	45.76	1.73	0.55	-0.95	1.49	0.07	0.25	0.56	2.65
Metal source domain												
100	2	10.53	2278	1.28	8.25	2.11	-0.10	2.21	0.50	0.06	0.75	2.95
200	3	15.79	3941	2.21	7.15	1.97	-0.15	2.12	0.33	0.06	0.63	3.36
300	3	15.79	4443	2.49	6.34	1.85	-0.15	1.99	0.33	0.06	0.63	3.17
400	4	21.05	6438	3.61	5.84	1.77	-0.20	1.96	0.25	0.07	0.56	3.49
500	**6**	**31.58**	**8442**	**4.73**	**6.68**	**1.90**	**-0.33**	**2.23**	**0.17**	**0.08**	**0.49**	**4.52**
Geochemical signature domain												
0	**6**	**50**	**4881**	**4.45**	**11.24**	**2.42**	**-0.65**	**3.07**	**0.17**	**0.08**	**0.50**	**6.21**

[1] = % Co. ÷ % Domain, [2] = Contrast, [3] = Variance of W^+, [4] = Variance of W , [5] = Standard deviation of contrast and [6] = Studentized value of contrast Total No. Of pixels in the area = 178476

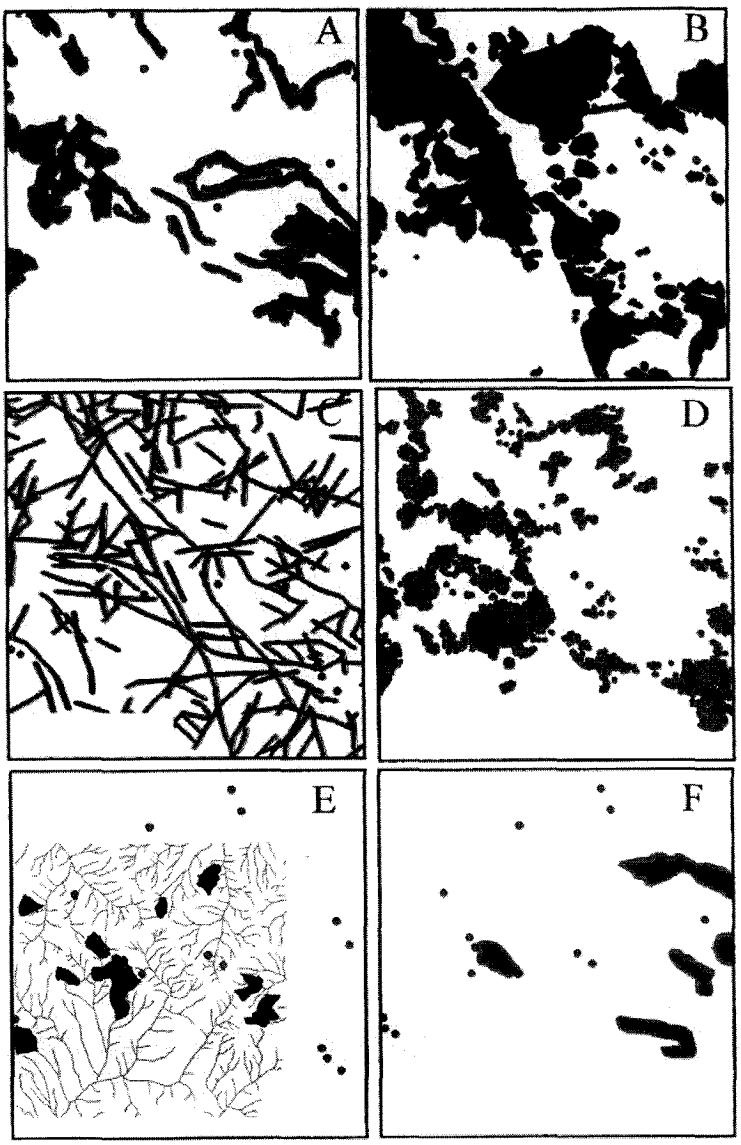

Fig. 10.1. Six evidence maps with the buffer zones used in the weights of evidence analysis: (A) host lithology (black) with 200 m buffer zone (grey); (B) igneous heat-source domain (black) with 200 m buffer zones (grey); (C) structural domain (black) with 200 m buffer zones (grey); (D) hydrothermal alteration domain (black) with 300 m buffer zones (grey); (E) predicted mineral occurrence index with > 80% (black); and (F) metamorphosed ophiolitic rocks, mainly serpentinite, (black) with 500 m buffer zones (grey).

weights of evidence analysis reveals a strong correlation between the hydrothermal alteration and mineral occurrences (Table 10.1). The weights used in the final model are:

$W^+ = 1.12$ if in a favourable hydrothermal alteration domain;
$W^- = -0.77$ if not in a favourable hydrothermal alteration domain.

10.3.4 Analysis of structures domain

Known mineralization in the Takab area is associated with linear structures trending NE-SW and NW-SE. Those digitized from the geological map were combined with those extracted from the shaded relief image of the total magnetic field intensity. The resulting structural domain was rasterized, buffered at distances of 100 m to 500 m and crossed with the raster mineral occurrence point map to estimate weights of evidence of the domain (Table 10.1). The optimum buffer was defined at 200 m. The resulting buffered structural domain covers 22.17 % of the area, and 12 out of 19 mineral occurrences are present in this domain (Fig. 10.1c). The weights of evidence analysis reveals a strong correlation between the structural domain and mineral occurrences. The weights used in the final model are:

$W^+ = 1.05$ if in a favourable structural domain;
$W^- = -0.75$ if not in a favourable structural domain.

10.3.5 Analysis of metal source domain

Metamorphosed ophiolitic rocks, possible sources for metal, are exposed over 1.28% of the Takab area. These are buffered in order to include potentially-favourable ophiolites that may be covered by unfavourable lithologies. The rasterized mineral occurrence map was crossed with the buffered ophiolite map to calculate the weights of evidence (W^+ and W^-) for cumulative distance away from the exposed ophiolites (Table 10.1). The optimum cutoff distance was selected at 500 m away from the outline of the ophiolites on the basis that the highest Studentized value of C (C=4.52) is estimated at this distance. Six out of 19 occurrences, including the Zarshuran and Aghdarreh gold deposits and Anguran lead-zinc mine, fall in the possible metal source domain within the 500 m buffer zone (Fig. 10.1f). The weights of this favourable domain used for the final model are:

$W^+ = 1.9$ if in a favourable metal source domain;
$W^- = -0.33$ if not in a favourable metal source domain.

10.3.6 Analysis of geochemical signatures of mineralization domain

In chapter 9, the significant predictor variables of stream sediment data were taken to represent a multi-element surficial geochemical signature (As-Zn-Cd) that characterizes the known mineral occurrences in the Takab area. The known mineral occurrences in the area are within or adjacent to sample catchment basins with a predicted mineral occurrence index >80 percentile. This implies that sample catchment basins with a predicted mineral occurrence index >80 percentile are likely to contain mineral deposits similar to the known mineral occurrences. Figure 10.1e is a binary map showing the sample catchment basins with a predicted mineral occurrence index >80% percentile. The catchment basins with a predicted mineral occurrence index of >80% percentile cover 4.45% of the area. This map was converted to a binary raster map and crossed with the rasterized mineral occurrence map to calculate the weights of evidence (W^+ and W^-) (Table 10.1). Six out of 12 occurrences, including the Zarshuran and Aghdarreh gold deposits and two lead-zinc mines (Alamkandi and Arpachi), fall in the geochemical signature domain (Fig. 10.1e). The weights of this favourable domain used for the final model are:

$W^+ = 2.42$ if in a favourable geochemical signature domain;
$W^- = -0.65$ if not in a favourable geochemical signature domain.

10.4 TEST OF CONDITIONAL INDEPENDENCE

Combining the foregoing six binary predictor maps first requires testing the assumption of conditional independence between all pairs of maps with respect to mineral occurrences (Bonham-Carter, 1994). Conditional independence between all pairs of binary maps is checked to identify the maps that must be used in or rejected from the combination procedure. Conditional independence was tested by formulating the null hypothesis of pairwise conditional independence of the predictor binary maps. Then the χ^2 test was run to check if the null hypothesis is rejected at the 95% significance level.

According to Bonham-Carter (1994), equation 1 defines the relationship if two binary patterns are conditionally independent with respect to a set of mineral occurrence points:

$$N\{B_1 \cap B_2 \cap D\} = \frac{N\{B_1 \cap D\}\ N\{B_2 \cap D\}}{N\{D\}}. \qquad (1)$$

where B_1 and B_2 are two binary predictor maps and D represents a mineral occurrence. The left-hand side of the equation is the observed number of deposits occurring in the overlap region where both binary patterns B_1 and B_2 are present. The right-hand side is the predicted number of deposits in this overlap zone. The relationship leads to a contingency table calculation for testing the conditional independence of two binary patterns (Table 10.2). The four cells in the table correspond to the four possible overlap conditions between two binary patterns where mineral occurrence points are present. The conditional independence is tested by calculating χ^2 as follows:

$$\chi^2 = \sum_{i=1}^{6} \frac{(observed_i - expected_i)^2}{expected_i}. \qquad (2)$$

Because the mineral occurrences are considered as points, or single unit cells, the resulting values of χ^2 are unaffected by the units of area measurement.

Table 10.2. Contingency table for testing conditional independence hypothesis. The four values within the table are either the expected values, assuming conditional independence, which are calculated from the marginal totals (Eq. 1), or the observed values measured from the maps. There is 1 degree of freedom (adapted from Bonham-Carter, 1994)

	B_1 Present	B_1 Absent	Totals
B_2 Present	$N\{B_1 \cap B_2 \cap D\}$	$N\{\overline{B}_1 \cap B_2 \cap D\}$	$N\{B_2 \cap D\}$
B_2 Absent	$N\{B_1 \cap \overline{B}_2 \cap D\}$	$N\{\overline{B}_1 \cap \overline{B}_2 \cap D\}$	$N\{\overline{B}_2 \cap D\}$
Totals	$N\{B_1 \cap D\}$	$N\{\overline{B}_1 \cap D\}$	$N\{D\}$

Table 10.3. Example of contingency table for testing conditional independence between a pair of binary maps, viz., hydrothermal alteration and the host lithology. The χ^2 values shown in the table are added to yield the total χ^2 value shown in Table 4.

	Host Lithology Present			Host Lithology Absent			Totals
	Observed	Expected	χ^2	Observed	Expected	χ^2	
Hydrothermal alteration Present	6	7.58	0.33	6	4.42	0.56	12
Hydrothermal alteration Absent	6	4.42	0.56	1	2.58	0.97	7
Totals	12	12	0.89	7	7	1.53	19

Table 10.4. Total χ^2 values for all six pairs of binary maps

Binary Map	Heat sources	Hydrothermal alteration	Lineaments	Metal source	Geochemical signature
Host lithology	0.07	2.42	1.93	0.03	1.55
Heat sources		1.54	1.12	2.65	0.8
Hydrothermal alteration			0.33	0.29	1.1
Geochemical signature			1.80	1.02	0.9
Lineaments					0.32

The calculated values can then be compared with standard values of χ^2 to verify if the conditional independence hypothesis holds at 95% probability with one degree of freedom. The χ^2 values for each pair of binary predictor maps for all the four overlap conditions can be calculated using the contingency tables (Bonham-Carter, 1994). A sum of these four χ^2 values gives the total χ^2 value for each pair of the binary pattern.

An example of such a contingency table for one pair of binary maps in the Takab area, viz., hydrothermal alteration and host lithology, is shown in Table 10.3. The total χ^2 values for each pair of binary predictor maps are shown in Table 10.4. The standard χ^2 value with one degree of freedom at the 95% significance level is 3.84 (Davis, 1986). It can be seen from Table 10.4 that the χ^2 values for all the pairs of binary predictor maps are less than 3.84. Thus, the null hypothesis of conditional independence is not rejected at the 95% probability level for any of the six pairs of maps.

10.5 PROSPECTIVITY MODEL

The predictive exploration model was generated by summing the weights of evidence of six binary maps representing the epithermal gold and base-metal recognition criteria. The various overlap combinations of the binary maps result in the highest cumulative weights for the locations where all the recognition criteria are present. The lowest weights are located where favourable conditions are scarce. The predictive weights range from a maximum of 7.1 to a minimum of –4.06, providing a relative measure for prioritizing areas of exploration potential (Table 10.5).

Based on the coincidence of the ranked criteria, the resulting predictive map was classified into four categories: low prospectivity, moderate prospectivity, high prospectivity and very high prospectivity (Fig. 10.2). The threshold between low prospectivity and moderate prospectivity zones is set by $W^+_1 + W^+_2 + W^-_1 + W^-_2$, where subscripts refer to the domains with the two lowest weights, thus +0.78 + 1.05 + (-0.77) + (-0.77) = + 0.29. The threshold between the moderate prospectivity and high prospectivity zones is set by a corresponding calculation based on the domains with the three lowest weights, thus +0.78 + 1.05 + 1.12 + (-0.77) + (-0.77) + (-0.75) = + 0.66. The threshold between the high prospectivity and very high prospectivity zones is also set by a corresponding calculation based on the domains with the four lowest weights, thus +0.78 + 1.05 + 1.12 + 1.15 + (-0.77) + (-0.77) + (-0.75) + (-0.77) = +1.04.

Table 10.5. Weights of evidence for deposit recognition criteria binary maps

Recognition Criteria	W^+	W^-
Favourable host lithology	1.15	-0.77
Igneous heat sources	0.78	-0.77
Hydrothermal alteration domain	1.12	-0.77
Favourable structural domain	1.05	-0.75
Metal source domain	1.90	-0.33
Geochemical signature domain	2.42	-0.65
Cumulative total	**7.10**	**-4.06**

The prospectivity model (Fig. 10.2) places 16 of 19 (84 %) of the known mineral deposits of the Takab area (including all the major gold deposits and base-metal mines) in the high and very high prospectivity zones, which

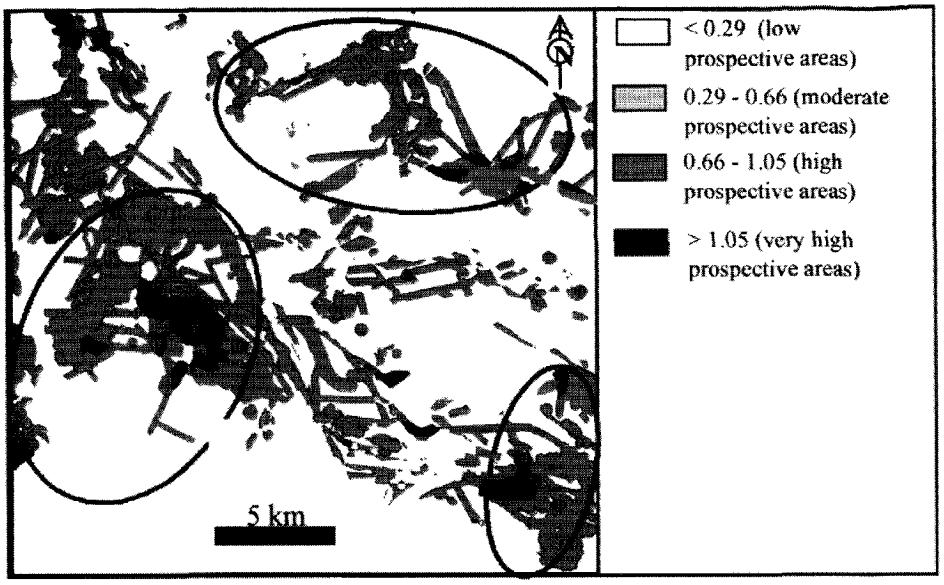

Fig. 10.2. Predictive model map outlining prospective mineralized zones in the Takab area (see also Fig. 10.2 in the colour figures).

represent 9.15% of the total area. The model places four important mining districts in the high prospectivity zone, namely Zarshuran in the central part, Aghdarreh in the southwest, Anguran in the southeast and Biche-Bagh in the northeast. In addition, the model suggests as highly prospective some areas not previously recognized as favourable in the northwest of the Takab area, the central-south part between the Zarshuran and Anguran mining districts, and some small areas in the western part. These require follow-up investigations.

10.6 CONCLUSIONS

This chapter demonstrates that successful development of a GIS model for epithermal gold and base-metal reconnaissance in a rugged terrain with difficult access, such as Takab, requires:

1) investigation of the genetic concepts of particular mineral deposit(s) and recognition of the spatial features (deposit recognition criteria) that control the known mineralizations;
2) analysis of cost-effective remotely-sensed data for a fast detection of the spectral and magnetic signatures of deposit recognition criteria; and

3) application of Bayesian theory, within a GIS framework, to quantify the spatial correlations between the deposit recognition criteria and the known mineral occurrences.

Chapter 11

CONCLUSIONS AND RECOMMENDATIONS

The research began by proposing a geodynamic model for the Zagros Orogenic Belt of Iran that, when implemented within a GIS environment, demonstrates the controls on mineralization. The research then focused on characterizing the style of gold mineralization at the Zarshuran deposit. The findings established recognition criteria for mineral potential mapping in the neighbouring areas, based on information obtained by remote sensing and a predictive GIS exploration model. Global analogues and regional metallogeny were other important components of the exploration model.

11.1 CONCLUSIONS

11.1.1 Geodynamics of mineralization

From the geodynamic model developed for the geological setting of the Zagros Orogenic Belt, the following conclusions are made.

- The evidence from data integration in a country-scale GIS supports a subduction model for the Zagros Orogenic Belt (ZOB). It implies that the suture zone, marking the closure of the Neo Tethys ocean, lies along the contact of the Urumieh Dokhtar Magmatic Assemblages (UDMA) and the Sanandaj-Sirjan Zone (SSZ), rather than along the Main Zagros Thrust.
- Closure of the Neo-Tethys oceanic basin was accompanied by subduction of oceanic crust beneath the Iranian plate. Anatexis of the subducted material led to the formation of a magmatic arc (the UDMA) with associated porphyry copper mineralization.

- Subsequent collision of the Afro-Arabian and Iranian plates resulted in southwestward thrusting and stacking of passive margin rocks forming an accretion wedge with suture materials (e.g., ophiolite fragments in the SSZ). This led to significant crustal thickening, orogenic collapse of the thickened crust along the SSZ, bi-modal magmatism and northeast-southwest and north-south extensional faulting. These provided energy, sources and pathways for hydrothermal base-metal and epithermal precious-metal mineralizing solutions, especially in the sector of the SSZ straddled by the Takab Shahin-Dez quadrangle.
- The geodynamic setting of the ZOB indicates three regional deposit recognition criteria for hydrothermal base-metal and epithermal precious-metal mineralizations in this region: (1) proximity to the NW-SE trending ophiolitic rocks along the proposed suture zone at the boundary of the SSZ and UDMA; (2) proximity to the NE-SW trending faults and their intersections with the older NW-SE trending structures; and (3) proximity to Tertiary igneous rocks extending in a NE-SW direction within the SSZ and their intersections with those igneous rocks, possibly connected to the UDMA, extending in a NW-SE direction.

11.1.2 Spatial controls on mineralization

Based on the results obtained from the interpretation of the 2D spatial data sets at Zarshuran, several conclusions relevant to a 3D geological interpretation are made.

- The NW-SE linear anomalies identified in both the geophysical and geochemical data demonstrate a stratigraphic control on mineralization at Zarshuran.
- Several NE-SW linear features terminate or displace stratigraphic trends, and are therefore interpreted as late faults.
- An exceptionally high magnetic anomaly, located in close spatial association with zones of strong mineralization, is attributed to the metamorphosed ophiolitic rocks (e.g., serpentinites).
- The high magnetic anomalies within the Zarshuran area also indicate the presence at a depth of about 25 m of a stock or dykes of intermediate-basic composition, dipping northeast at around 60°, within or at the contact of the Iman-Khan schist; these could have contributed energy or fluids to the mineralizing hydrothermal system.
- Weathering leads to a degree of surface enrichment of gold in soils. Comparison of the gold values in soils and gold assays from 12 drillholes in the same area suggests *in-situ* gold mineralization in bedrock amounts to more than 100 million tonnes grading 0.84 ppm Au.

11.1.3 Ore genesis

Within the context of conceptual modelling, Zarshuran exhibits many similarities with the sediment-hosted disseminated gold deposits of the western USA, from which it is concluded that Zarshuran is a Carlin-like deposit. There are, however, significant differences. From the results for the genetic model of mineralization at Zarshuran, the following conclusions are made.

- In general, the type of host rocks (e.g., black shale and carbonate), hydrothermal alterations (e.g., decalcification, silicification and argillization), style of mineralization (disseminated as well as vuggy and open space filling), ore related minerals (e.g. orpiment, realgar, getchellite, sulphosalts and gold-bearing arsenian pyrite) and geochemical signatures (e.g., the suite of trace elements of As, Sb, Au, Hg, Tl, and abundance of organic matter) of the Zarshuran deposit are very similar to the Carlin-type sediment-hosted disseminated gold deposits (chapters 4, 5, 6)
- Five mineral assemblages, including three of hydrothermal origin (early stage, main stage and late stage), can be distinguished at Zarshuran. Gold mainly occurs as invisible gold at the end of the main stage and during the late stage of hydrothermal mineralization (chapters 4 and 5).
- Although micron-size particles of metallic gold are observed at Zarshuran, the quantities do not account for the gold concentrations determined by chemical analyses. The occurrence of invisible gold in arsenian pyrite (up to 1300 ppm Au), associated with hydrothermal silica and orpiment, and in sphalerite (up to 390 ppm Au), associated with hydrothermal silica, explains the measured gold concentrations. The invisible gold owes its origin to solid solution deposition and/or encapsulation of submicron-size particles of metallic gold.
- In contrast to the typical Carlin-type deposits, the presence of tellurium in concentrations sufficient to precipitate coloradoite (HgTe) and the occurrence of gold-bearing colloform sphalerite (which is very abundant) are unique to Zarshuran (chapters 4, 5).
- Three assemblages of sulphosalt minerals have been identified at Zarshuran. Invisible gold is present in arsenian pyrite occurring both before and after the sulphosalt assemblages. The sulphosalt mineral sequence and its accompanying change in the As:Sb ratio suggest the evolution of a single mineralizing hydrothermal fluid. This was initially antimony rich and arsenic poor and through the main sulphosalt precipitation phase evolved to become arsenic rich. Mineral paragenesis and the temperature ranges of sulphosalt crystallization suggest two phases of gold mineralization. The first phase was derived from an antimony-rich and arsenic-poor fluid at a temperature higher than 300°C. The second phase was derived from an arsenic-rich fluid at a temperature range of 150-250°C (chapter 6).
- Metamorphosed ophiolitic rocks (e.g., serpentinite) which occur in close association with mineralization may have acted as an important source of metals at Zarshuran

(chapters 3 and 8). Although, such an association has not been reported from the typical Carlin-type deposits, it is a very important feature of the Archean-type gold deposits.

- Two types of fluids, gas-rich and aqueous-rich, were involved during hydrothermal mineralization at Zarshuran. These fluids may be formed by unmixing (or immiscibility) of a parent homogeneous H_2O-CO_2 fluid with high temperature, generated from magmatic components (chapter 7).
- The earliest hydrothermal mineralization is marked by a high temperature of ±350°C. High pressure and temperature, abundance of primary CO_2 inclusions, low salinity fluids and rarity of inclusion decrepitation (explosion) at this stage indicate that the system was under relatively high pressure, preventing mineral precipitation. This high pressure (approximately 1250 bars corresponding to a depth of 5 km) hydrothermal system provided appropriate conditions for volatile constituents to leach gold from the suitable source rocks (e.g., serpentinites and granitoids).
- Hydrothermal fluid circulation, uplift, decompression (transition from a high pressure system to a low pressure system), release of substantial amounts of carbon, and silicification leading to restoration of pressure provided favourable conditions for mineralization at Zarshuran.
- Mineralization occurred at an estimated temperature between 200 to 270°C and a fluid pressure of 250-400 bars. (chapter 7). The main mineralization was linked with fluid immiscibility, caused by a strong pressure decrease. It resulted in the destruction of metal-bearing complexes, stable in the homogeneous fluid, and metal deposition. This occurred in a temperature range of 200-270°C and at a pressure of approximately 250 bars (depth of about 1 km) in a strong reducing environment.
- Occurrence of widespread outcropping volcanics in close spatial and temporal proximity to the Zarshuran deposit (chapter 8) substantiates the implied link between mineralization and magmatism. The association of the mineralization at Zarshuran with igneous rocks (e.g., granitoid and an inferred intermediate-basic intrusion) and the presence of Te suggest a larger magmatic component in the mineralizing hydrothermal solution than is typical for most Carlin-type deposits (chapters 3, 4, 8).

11.1.4 Deposit recognition criteria

On the basis of geodynamic setting of ZOB, the geology and metallogeny of the Takab Shahin-Dez quadrangle, and the genetic and spatial models of the Zarshuran deposit, the characteristic DRC of the Takab area that could be identified using the aeromagnetic, Landsat-TM, geological, geochemical and mineral occurrence data sets, are: (1) chemically-reactive black-shale and carbonate formations; (2) Tertiary volcano-plutonic heat sources; (3) hydrothermal alteration (argillic and iron oxides); (4) proximity to NE-SW trending faults and their intersections with NW-SE trending geologic structures; (5) an arsenic-zinc-

cadmium surficial geochemical signature (6) proximity to metamorphosed ophiolites (e.g., serpentinite).

However, within the context of mapping DRC and developing a predictive GIS exploration model for mapping potential gold and base-metal mineralization in the Takab area, the following conclusions are drawn.

- Analysis of remotely-sensed data is effective for detection of the spectral and magnetic signatures characterizing recognition criteria of known mineral deposits. The analytical signal technique applied to the aeromagnetic data of the Takab area maps subsurface igneous heat sources. The principal components (PC) transformation technique applied to the Landsat TM indicates the presence of hydrothermal alteration consisting of either iron oxides or hydroxyl-bearing clay minerals associated with the known deposits of the area. The hydrothermal alteration zones identified by PC technique are verified by using reduction to the pole of aeromagnetic data in order to identify magnetic lows resulting from magnetite destruction by hydrothermal solutions.
- Shaded relief maps of total magnetic field intensity data and the directional filtering applied to the first principal component image of six reflective Landsat-TM bands revealed several major NE-SW and E-W trending lineaments in the Takab area. These are interpreted as conjugate faults generated perpendicular to the major NW-SE thrust of the area. Many of the known deposits of the area lie within a distance of 500 m from these conjugate faults.
- Filtering stream sediment geochemical data gives an index characteristic of mineralization. In the Takab area the known mineral occurrences are within or adjacent to sample catchment basins with a predicted mineral occurrence index (comprising arsenic, zinc and cadmium) > 80 percentile.
- Ground truthing was very important to validate the mapped deposit recognition criteria by remote sensing, and to refine them into a predictive GIS exploration model.
- The application of Bayesian theory within a GIS framework quantifies the spatial correlations between the deposit recognition criteria and the known mineral occurrences, and allows prediction of potentially prospective areas.

11.2 RECOMMENDATIONS

- The geodynamic model developed in this study for the geological setting of the Zagros Orogenic Belt questions the traditional models and provides new insights for regional metallogenic mapping of hydrothermal base-metal and epithermal precious-metal deposits within the SSZ. However, additional research is required to map at a smaller scale the inferred ophiolites within the SSZ and to determine their role on the metallogeny of the region. Research is also required to define the

metallogenic role of the NW-SE trending compressional faults associated with subduction and the NE-SW and N-S trending extensional conjugate faults formed by orogenic collapse during or after subduction.

- Although many researchers suggest that the gold in the Carlin-type gold deposits has been scavenged from sedimentary rocks (e.g., from the diagenetic pyrite), the favoured source at Zarshuran is metamorphosed ophiolitic rocks (serpentinites) and granitoids. An isotope analysis of the ^{34}S in arsenian pyrite, orpiment and sphalerite, the main gold-bearing minerals at Zarshuran, could provide important additional evidence. In addition, the isotopic characteristics (e.g., δD and $\delta^{18}O$ values) of the fluids and mineral separates at Zarshuran may provide additional information about the origin of the hydrothermal solutions.
- The abundance of CO_2-rich fluid inclusions, in the early and late stage hydrothermal mineralization at Zarshuran, coupled with release of a large amount of carbon by decrepitation of CO_2-rich inclusions, during the main stage, indicate the possible importance of gases and carbon in gold transportation and gold precipitation. Therefore, laboratory experiments of gas transport of Au by volatiles and scavenging properties of organic matter (black shale) should be investigated in future.
- Because of the economic importance of the Zarshuran mining district and the Takab area, further exploration and investigation should be also focused on the technological implications related to the recovery of invisible gold, as well as on the environmental impact of arsenic, mercury and other hazardous elements accompanying gold.
- The presence at surface of the epithermal element suite of As-Sb-Hg-Tl along with Zn and Te (in view of the occurrence of gold in sphalerite, presence of coloradoite) coupled with the 1-2 km depth of mineralization (inferred from fluid inclusion data) imply gold mineralization at/below the working levels at active and abandoned mines and prospects of As, Sb, Hg and Pb/Zn. These should be considered as targets for follow up gold exploration.
- The presence of tellurium in concentrations sufficient to precipitate coloradoite (HgTe) and widespread occurrence of gold-bearing sphalerite deserve further attention.
- The predictive GIS exploration model, developed for the Takab area, highlighted several potential areas of gold and base metal mineralizations. Preliminary ground truthing of some of these areas confirmed the presence of the characteristics of gold mineralization. Panned concentrate and rock samples from these anomalies were found to contain up to 600 ppb gold, a remarkably high concentration for reconnaissance exploration. These areas require systematic follow-up investigations. This approach appears to be applicable to the remainder of the western margin of the Sanandaj-Sirjan zone, especially along its contact with the Urumieh-Dokhtar Magmatic Assemblage belt.

REFERENCES

Alavi, M. (1976). Geology and petrography in the ophiolite range NW of Sabzevar with special regard to metamorphism and genetic relations in ophiolite suite. Unpublished thesis, University of Saarlande, 174 p.

Alavi, M. (1980). Tectonostratigraphic evolution of the Zagros of Iran. Geology, 8: 144-149.

Alavi, M. Hajian, J., Amidi, M. and Bolourchi, H. (1982). Geology of Takab-Shahin-Dez Quadrangle. The Ministry of Mines and Metals of Iran, Tehran, 100 p.

Alavi, M. (1993). Tectonics of the Zagros Orogenic Belt of Iran: New Data and Interpretations. Tectonophysics, 229: 211-238.

Alavi, M. (1994). Tectonic of the Zagros orogenic belt of Iran new data and interpretations. Tectonophysics , 229: 211-238.

Amidi, S.M. (1975). Contribution 'a l'e'tude stratigraphique, petrologique et petrographique des roches magmatiques de la region Natanz-Nain-Surk (Iran central). PhD thesis, University of Grenoble France.

Arehart, G.B., Chryssoulis, L.S. and Kesler, S.E. (1993). Gold and arsenic in iron sulphides from sediment-hosted disseminated gold deposits: implications for depositional processes. Economic Geology, 188:171-185.

Arehart, G.B., Foland, K.F., Naeser, C.W. and Kesler, S.E. (1993). $^{40}Ar/^{39}Ar$, K/Ar and fission track geochronology of sediment-hosted disseminated gold deposit at Post-Betz, Carlin trend, northeastern Nevada. Economic Geology, 88:622-646.

Asadi, H.H. (1995). Integrated analysis of geological data set for gold exploration in Takab Shahin-Dez quadrangle, Iran. MSc. Thesis, International Institute for Aerospace Survey and Earth Sciences (ITC), Delft, The Netherlands, 132p.

Asadi, H.H., Carranza, E.J.M. and Hale, H. (1998a). Assessment of epithermal mineralization in northwest Iran using GIS. Proceedings of the 5th International Conference on Geographic Information System, Cartographic Center of Iran, Tehran, pp. 29-47.

Asadi, H.H., Carranza, E.J.M. and Hale, M. (1998b). GIS and remote sensing for epithermal gold exploration in the northwest Iran. Proceedings of International Conference on GIS for Earth Science Applications, Lublijana, Slovenia, pp. 57-73.

Asadi, H.H., Voncken, J.H.L. and Hale, M. (1999). Invisible gold at Zarshuran, Iran, Economic Geology, 94:1367-1374.

Asadi, H.H. and Hale, M. (1999a). Magmatic contribution to the Carlin-type gold deposit at Zarshuran, Iran. Proceedings of the join SGA-IAGOD Conference at the Imperial college of Science, Technology and Medicine, London, 1:463-466.

Asadi, H.H. and Hale, M. (1999b). Integrated analysis of aeromagnetic, Landsat TM and mineral occurrence data for epithermal gold exploration in northwest Iran.

Proceedings of the 13th International Conference on Applied Geologic Remote Sensing, Vancouver, British Colombia, Canada, 1:16-24.

Asadi, H.H. and Hale, M. (1999c). A predictive GIS model for potential mapping of gold and base metal mineralization in Takab area, Iran. Proceedings of the 4th International Conference on Geocomputation, Mary Washington College, Fredrickburg, Virginia, USA, paper No. 12, CD ROM and Web: http://www.geovista.psu.edu/geocomp/geocomp99/Gc99/012/gc_012.htm

Asadi, H. H. and Hale, M. (2000a). Application of the Zarshuran Carlin-like deposit model for gold exploration GIS in NW Iran. Proceedings of The 14th International Conference on Applied Geologic Remote Sensing, Las Vegas, Nevada, 6-8 November 2000, 8 pp.).

Asadi, H.H. and Hale, M. (2000b). A predictive GIS model for mapping potential gold and base metal mineralization in Takab area, Iran. Journal of Computers and Geosciences (in press).

Asadi, H.H., Erren, H. and Westerhof, A.B. (2000a). Integrated analysis of remote sensing, aeromagnetic, geological and mineral occurrence data for the assessment of a subduction setting along the Zagros Orogenic Belt of Iran. Proceedings of. XIXth Conference of the international society for photogrammetry and remote sensing (ISPRS 2000), Amsterdam, paper TP VII-04-21, CD ROM.

Asadi, H.H., Sides, E. and Ngonzi, K. (2000b). Using 2D GIS to assist 3D modelling of the Zarshuran gold deposit, NW Iran. Proceedings of. XIXth Conference of the international society for photogrammetry and remote sensing (ISPRS 2000), Amsterdam, paper TP VII-04-22, CD ROM.

Asadi, H.H., Voncken, J.H.L., Kühnel, R.A. and Hale, M. (2000c). Petrography, mineralogy and geochemistry of the Zarshuran Carlin-like gold deposit, NW Iran. Mineralium Deposita, Springer, Issue 7, 35:672-682 (Asadi et al., 2000c).

Asadi, H.H., Voncken, J. H.L. and Hale, M. (2000d). Gold mineralization at Zarshuran, NW Iran (MSF Mini-Symposium, Espoo, Finland, Modern Approaches to Ore and Environmental Mineralogy, pp. 1-2)

Asadi, H.H., Voncken, J.H.L. and Hale, M. (2001). Sulphosalts at the Zarshuran Carlin-like gold deposit, northwest Iran, implications for gold mineralization. Trans. of Institution of Mining and Metallurgy, Transactions, Section B (in review).

Asudeh, I. (1982). Seismic structural Iran from serface and body wave data. Geophys. J.R. Astron. Sosc., 71: 715-730.

Asudeh, I. (1983). I.S.C. mislocation of earthquakes in Iran and geometrical residuals. Tectonophysics, 95: 61-74.

Bagby, W.C. and Berger, B.R. (1985). Geologic characteristics of sediment-hosted, disseminated precious metal deposits in the western United States. In: Berger, B.R., Bethke, P.M. (eds), Geology and Geochemistry of Epithermal Systems. Reviews in Economic Geology, 2: 169-202.

Bakken, B.M., Hochella, M.F., Marshall, A.F. and Turner, A.M. (1989). High-resolution microscopy of gold in unoxidized ore from Carlin mine, Nevada. Economic Geology, 84:171-179.

Bakken, B.M., Brigham, R.H. and Fleming, A.F. (1991). The distribution of gold in unoxidized ore from Carlin-type deposits revealed by secondary ion mass spectrometry (SIMS): Geological Society of America, Annual Meeting, Abstracts, 52: 228.

Bariand, P. (1962). Contribution a' la mineralogie de l'Iran, Ph.D thesis. Univ. Paris, Faculte des Sciences, Ser. A. No. 980, 235 p.

Bariand, P., Cesborn, F., Agrinier, H., Geffroy, J. and Issakhanian, V. (1968). La Getchellite, $AsSbS_3$, de Zarshuran, Afshar, Iran. Bull. Soc. Fr. Mineral Crystallography, 95:403-406.

Barrie, I.J. and and Touret, J. (1999). Fluid inclusion studies of gold-bearing quartz veins from the Yirisen deposit, Sula Mountains greenstone belt, Masumbiri, Sierra Leone, Ore Geology Reviews, Elsevier, 14:203-225.

Bate, R. L. and Jackson, J. A. (1980). Glossary of Geology. American Geological Institute, Virginia, Second Edition, 751 p.

Berberian, M. and King, G.C.P. (1981). Toward a paleogeography and tectonic evolution of Iran. Canadian Journal of Earth Sciences, 18: 210-265.

Berberian, F. and Muir, I.D., Pankhurst, R.J. and Berberian, M. (1982). Late Cretaceous and Early Miocene Andean-type plutonic activity in northern Makran and Central Iran. J. Geol. Soc. London, 139:605-614.

Berger, B.R. (1985). Geological and geochemical relationships at the Getchell mine and vicinity, Humboldt County, Nevada. In: Hollister, V.F. (ed.), Discoveries of Epithermal Precious Metal Deposits. Soc. of Mining Engineers, New York, p. 51-59.

Berger, B.R. and Henley, R.W. (1989). Advances in the understanding of epithermal gold-silver deposits- With special reference to deposits of the western United States. In: Keays, R., Ramsy, R. and Groves, D. (eds.), The geology of gold deposits: The prospective in (1988).Economic Geoligy. Monogr., 6: 405-423.

Berger, B.R. and Bagby, W.C. (1991). The geology and the origin of the Carlin-type deposit. In: Foster, R.P. (ed.), Gold Metallogeny and Exploration. Blackie, Glasgow, p. 210-248.

Bettels, K.H. (1989). Gold deposits of the Goldstrike mine, Carlin trend, Nevada. Society of Mining Engineers Preprint, 89:158, 14p.

Birnie, R.W. and Burnham, C.W. (1976). The crystal structure and extent of solid solution of geocronite. Am Mineral, 61: 963 – 970.

Bonham, H.F. (1985). Characteristics of bulk-minable gold-silver deposits in Cordilleran and island-arc settings. U.S.Geol.Survey Bull., 1646, 821-843.

Bonham-Carter, G.F. and Goodfellow, W.D. (1986). Background corrections to stream sediment geochemical data using digitized drainage and geological maps: application to Selwyn Basin, Yukon and Northwest Territories. In: Nichols, C.E. (ed.), Exploration for Ore Deposit of the North American Cordillera. Jour. Geochem. Explor., 25:139-155.

Bonham-Carter, G.F., Rogers, P.J. and Ellwood, D.J. (1987). Catchment basin analysis applied to surficial geochemical data, Cobequid Highlands, Nova Scotia. In: Garrett, R.G. (ed.), Geochemical Exploration 1985, Geochem, J. Explor., 29: 259-278.

Bonham-Carter, G.F., Agterberg, F.P. and Wright, D.F. (1988). Integration of geological datasets for gold exploration in Vova Scotia. Photogrammetric Engineering and Remote Sensing, 54:1585-1598.

Bonham-Carter, G.F., Agterberg, F.P. and Wright, D.F. (1989). Weights of evidence modelling: a new approach to mapping mineral potential. In: Aterberg, F.P., Bonham-Carter, G.F. (eds.), Statistical Applications in the Earth Sciences. Geological Survey of Canada, Paper 89-9, p. 171-183.

Bonham-Carter, G.F. (1994). Geographic Information Systems for Geoscientists, Modelling with GIS. Pergamon, Ontario, 398 p.

Callow, K.J. & Worley, B.W. (1965). The occurrence of telluride minerals at the Acupan gold mine, Mountain province, Philippines. Economic Geology, 60:251-268.

Chandra, U. (1981). Focal mechanism solutions and their tectonics implications for the eastern alpine-Himalayan , Ph.D. thesis, Massachusetts Institute of Technology, Camnridge, M.A.

Chang, L.L.Y. and Bever, J.E. (1973). Lead sulphosalts minerals: crystal structures, stability relations, and paragenesis. Mineral Sci Eng , 5: 181 –191.

Cherven, V.B. (1986). Tethys-marginal sedimentary basins in western Iran. Geological Society of American Bulletin, 97:516-522.

Cook, N.J. and Chryssoulis, S.L. (1990). Concentrations of invisible gold in common sulphides. Canadian Mineralogist, 28:1-16.

Cooke, D.R., Mcphail, D.C. and Bloom M.S. (1996). Epithermal gold mineralization, Acupan, Baguio district, Philippines: geology, mineralization, alteration, and the thermochemical environment of ore deposition. Economic Geology, 91:243-272. Couto, H., Roger, G., Moëlo, Y. and Bril, H. (1990). Le district antimoine-or Dúrico-Beirã (Portugal) : evolution paragenetique et géochimique; implication métallogeniques. Mineral Deposita 25 Suppl: S69-S81.

Crawford, A.R. (1972). Iran, Continental drift and plate tectonics. 24th Int. Geol. Congr., Montreal, 3:106-112.

Crosta, A.P. and Moore, J.M. (1989). Enhancement of Landsat Thematic Mapper Imagery for Residual Soil Mapping in SW Minas Gerais State, Brazil, A prospective Case History in Greenstone Belt Terrain. Proceedings of the 7th (ERIM) Thematic Conference on Remote Sensing for Exploration Geology, Calgary, pp. 1173-1187.

Daliran, F., Walteher, J. and Stuben, D. (1999). Sediment-hosted disseminated gold mineralization in the north Takab geothermal field, NW Iran. Proceedings of the fifth joint SGA-IAGOD international meeting, Imperial College, London, 4 p.

Davis, J.C. (1986). Statistics and Data Analysis in Geology (4th edn.). John Wiley and Sons, New York, 641 p.

Davoudzadeh, M. and Schmidt, K. (1984). A review of the Mesozoic paleogeography and Paleotectonic Evolution of Iran. N. Jb. Geol. Palaont Abh., Stuttgart, 168: 182-207.

Dehghani, G. and Makris, J. (1983). The gravity field and crustal structure of Iran. Geological Survey of Iran, Rep., 51:51-68.

Dewey, J.F., Pitman, W.C., Ryan, W.B.F. and Bonnin, J. (1973). Plate tectonics and evolution of the Alpine system. Geol. Soc. Amer. Bull., 84: 3137-3180.

Dickson, F.W., Radtke, A.S., Weissberg, B.G. and Heropoulos, C. (1975). Solid solutions of antimony, arsenic, and gold in stibnite (Sb_2S_3), orpiment (As_2S_3), and realgar (AsS): Econmic Geology, 70: 591–594.

Field, C.W. and Fifarek, R.H. (1985). Light stable isotopes systematics in the epithermal environment. In: Berger, B.R. and Bethke, P.M. (eds.), Geology and Geochemistry of Epithermal Systems. Rev. inEconomic Geology, 2: 99-128.

Forster, H. (1976). Continental drift in Iran in relation to the Afar structure. In Afar between continental and oceanic rifting. Pilger A. and Rosler A. (eds.). Schweizerbartsche Verlagsbuchhandlung, Stuttgart, p. 182-190.

Foster, R.P. (1996). Gold in the year 2000: a global overview. Australian Journal of Earth Sciences, 43:1-14.

Geological Survey of Iran (1999). Geological map of Takab area (1:100,000 scale), Tehran.

Gervilla, F., Papunen, H., Kojonen, K. and Johanson, B. (1997). Results of trace element analysis of platinum-group element arsenides and sulphoarsenides from some Finnish PGE-bearing mafic-ultramafic intrusions, in Papunen, H. (ed.), Mineral Deposits: Rotterdam, Balkema, p. 423-426.

Giesse, P., Makris, J., Akashe, B., Rower, P., Letz, H. and Mostaanpour, M. (1983). Seismic crustal studies in southern Iran between the central Iran and the Zagros belt. Geol. Surv. Iran Rep., 51:71-84.

Giggenbach, R.W. (1986). The use of gas chemistry in delineating the origin of fluids discharged over the Taupo Volcanic Zone. Proc. Symp. V, Internat. Volcanological Congress, Auckland, New Zealand, P. 47-50.

Glass, H.J., Voncken, J.H.L. (1996). The Delft Opaque Mineral Identification Program. Mineral Soc Bull, 112: 11 P.

Goldstein, R.H. and Reynolds, T.J. (1994). Systematics of fluid inclusions in diagentic minerals, Society for Sedimentary Geology, USA, 199 p.

Graham, J., Rabinson, B.W. and Walker, R.K. (1989). Gold in arsenopyrite, in Proceedings AusIMM Mineralogy-Petrology Symposium: Sydney, p. 55-57.

Grauch, V.J.S. (1988). Geophysical tools for defining covered geologic features: Significance for disseminated gold deposits in Nevada, U.S.A. In: Goode, A.D.T., Smyth, E.L. , Birch, W.D. and Bosman, L.I. (eds.), Bicentennial Gold 88, Extended Abstracts, Poster Programme, Geol. Soc. Aust. Abstr., 23(2): 527-529.

Harris, D.P. and Pan, G. (1991). Consistent geological areas for epithermal gold-silver deposits in the Walker Lake quadrangle of Nevada and California: Detailed by quantitative methods. Economic Geology, 86:142-165.

Hausen, D.M. and Park, W.C. (1986). Observation on the association of gold mineralization with organic matter in Carlin-type ores. In: Dean, W. E. (ed.), Proc. Symp. Organics and Ore Deposition, Denver Region. Exploration Geol. Soc., p. 119-136

Haynes, S.J. and McQuillan, H. (1974). Evalution of the Zagros suture zone, southern Iran.. Geol. Sos Am. Bull., 85:739-744.

Hezarkhani, A. and Williams-Jones, A.E. (1998). Control of alteration and mineralization in the Sungun porphyry copper deposit, Economic Geology, p. 651-670.

Holland, P.T., Beaty, D.W. and Snow, G.G. (1988). Comparitive elemental and oxygen isotope geochemistry of jasperoid in the northern Great Basin: Evidence for distinctive fluid evolution in gold-producing hydrothermal system.Economic Geology., 83: 1401-1423.

Hofstra, A.H., Northrop, H.R., Rye, R.O., Landis, G.P. and Birak, D.J. (1988). Origin of sediment-hosted disseminated gold deposits by fluid mixing-Evidence from jasperoids in the Jerritt Canyon gold district, Nevada, USA. Geol.Soc. Australia Abstr., 22:284-289.

Howarth, R.J. (ed.), (1983). Statistics and Data Analysis in geochemical Prospecting. Handbook of Exploration Geochemistry Govett, G.J.S. (ed.), Elsevier, Amsterdam, 437 p.

Howarth, R. J. and Sindig-Larsen (1983). Multivariate analysis. In: Howarth, R.J. (ed.), Statistics and Data Analysis in geochemical Prospecting. Handbook of Exploration Geochemistry Govett, G.J.S. (ed.), Elsevier, Amsterdam, p. 207-289.

Ilchik, R.L. and Baton, M.D. (1997). An amagmatic origin of Carlin-type deposits. Economic Geology, 92: 269-288.

Irvine, R.J. and Smith, M.J. (1990). Geophysical Exploration for Epithermal Gold Deposits, Journal of Geochemical Exploration, 36: 375-412.

Jackson, J. (1980). Reactivation of basement faults and crustal shortening in orogenic belts. Nature, 283:343-346.

Jackson, J., Fitch, T. and McKenzie, D. (1981). Active thrusting and the evolution of the Zagros fold belt. In: MaClay, K. and Price N.(ed.), Thrust and Nappe Tectonics.Geol. Soc. London, Spec. Publ., 9:371-379.

Jambor, J.L. (1967). New lead sulfantimonodes from Madoc, Ontario. Part 2 - Mineral Descriptions. Can Mineral, 9: 191 - 213.

Jambor, J.L. (1968). New lead sulphosalts from Madoc Ontario, Part 3. Synthesis, paragenesis, origin. Can Mineral , 10: 505-521.

Johansen, B. and Kojonen, K. (1996). Results of major and trace analyses of kimberlitic garnet, in Proceedings of European Microbeam Analysis Society (EMAS) 2nd regional workshop, "Electron Probe Microanalysis Today - Practical Aspects", L b r, J.L., Heikinheima, E, Nicholson, P., (eds.), Balatonf red, Hungary, p. 24 - 25.

Joralemon, P. (1975). K-Ar relation of granodiorite emplacement and tungsten and gold mineralization near the Getchell mine, Humboldt County, Nevada-a discussion.Economic Geology, 70: 405-406.

Karimi, M. (1992). Geology, petrography, and mineralogical studies of Zarshuran gold deposit: Tehran, Kansaran Engineering Consultant, 250 p. (in Persian).

Karimpour, M.H. (1989). Applied Economic Geology, Javid publication, Tehran. 264p. (in Persian).

Khakzad, A. (1991). A view to copper deposits in Kerman area, Copper industry National Co. of Iran, 23 pp.

Kojonen, K. and Johansen, B. (1997). Ore microscopy and microprobe results of invisible gold in pyrite and arsenopyrite, in: Intern. Mineral. Assoc./Comm. on Ore Mineral., Short Course on "Modern approach to ore and environmental mineralogy", Laboratorio do IGM, S. Mameda da Infesta, Portugal, p. 1-18.

Koop, W. and Stoneley, R. (1982). Subsidence history of the Middle East Zagros basin, Permian to Recent. Philos. Trans. R. Soc. London, Ser. A, 305:149-168.

Kretschmar, U. and Scott, S.D. (1973). Phase relations involving arsenopyrite in the system Fe-As-S and their application. Can Mineral, 14: 364 – 386.

Kuehn, C.A. and Rose, A.W. (1992). Geology and geochemistry of wall-rock alteration at the Carlin gold deposit, Nevada. Economic Geology, 87: 1697-1721.

Kuehn, C.A. and Rose, A.W. (1995). Carlin gold deposit, Nevada: origin in a deep zone of mixing between normally pressured and overpressured fluids. Economic Geology, 90: 17-36.

K hnel, R.A., Prins, J.J. and Roorda, H.J. (1980). The Delft System for mineral identification. Delft University of Technology, 204 p.

Lescuyer, J.L. and Rio, R. (1976). Geologie de la region de Mianeh (Azarbaijan), Contribution a' l' etude du volcanisme tertiaire de l' Iran. Theses, University of Grenoble, France.

Lindgren, W. (1933). Mineral Deposits (4th edn.). McGraw-Hill New York. 930 p.

Lugaski, T.P., Bonham, H.F., John, C.K. and William, H.A. (1990). Exploration for bulk minable precious metal deposits in the western great basin by integration of geologic, geophysical and remote sensing data. In: Remote sensing an operational technology for the mining and petroleum industries, 1990 conference. The Institution of Mining and Metallurgy, London, p. 213-221.

Loughlin, W.P. (1990). Geological exploration in the western United Sates by use of airborne scanner imagery. IMM conference: Remote Sensing, an Operational Technology for the Mining and Petroleum Industries. London, p. 223-241.

Loughlin, W.P. (1991). Principal Components Analysis for Alteration Mapping,, Photogrammetric Engineering and Remote Sensing, 57: 1163-1169.

MacMillan, S.B. and Panteleyev, A. (1988). Disseminated gold deposits. In: Roberts R.G. and Sheahan S.H. (eds.), Ore Deposit Models. p. 31-45.

Mann, C.D. and Vita-Finzi, C. (1982). Curve interpolation and folded strata. Tectonophysics, 88:T7-T15.

McKinstry, H.E. and Kennedy, G.C. (1957). Some suggestions concerning the sequence of certain ore minerals. Economic Geology, 52: 379– 390.

Mehrabi, B., Yardley, B.W.D. and Cann, J.R. (1999). Sediment-hosted disseminated gold mineralization at Zarshuran, NW Iran. Mineralium Deposita, Springer, 34: 673– 696.

Middleton, T. W. (1994). Report on exploration at Agh-Darreh west Azarbaijan province, Iran. Persian Resources company, Pert, Australia, 50 pp.

Mineral Export Company (1995). Geological map of the Agh-Darreh deposit (1:5,000 scale), Tehran.

Ministry of Mines and Metals of Iran (1994). Mineral deposits of Takab area, internal report, Tehran, 275 p. (in Persian).

Mo lo, Y. (1983). Contribution l'etude des formation des sulpures complexes d'antimoine et plomb. Documents de B.R.G.M., No. 55 (Ph.D. Thesis, Universit Pierre et Marie Curie, Paris), 207 p.

Mohajer, G., Parsaie, H., Fallah, N. and Ma'dani, F. (1989). Mercury exploration in the Saein Dez-Takab area. Tehran, Ministry of Mines and Metals of Iran, 227 p. (in Persian).

Moore, J.M. and Guo, L.J. (1990). Image enhancement of epithermal gold deposit alteration zones in southeast Spain. In: Remote sensing, an operational technology for the mining and petroleum industry, 1990 conference. The Institution of Mining and Metallurgy, London, p. 49-57.

Nabavi, M.H. (1972). Geologic map of the Yazd quadrangle, scale 1:250, 000. Geological Survey of Iran, Tehran.

Nakai, I., Yakoi, H. and Nagashima, K. (1986). Crystal chemistry of the system wakabayashilite and synthetic study on the solid solution in the system As_2S_3 - Sb_2S_3. Mineralogical Journal, Tokyo, 13(4): 212-222.

Ni, J. and Barzangi, M (1986). Seismotectonics of Zagros continental collision zone a comparison with Himalayas. J. Geophys. Ref., 91:8205-8218.

Niazi, M. , Asudeh, I. , Ballard, G., Jackson, J.,King,G. and McKenzie, D. (1978). The depth of seismicity in the Kermanshah region of the Zagros mountains, Iran, Earth planet. Sci.Lett., 40:270-274 .

Ngonzi, K. (2000). Spatial modelling of mineral exploration data from the Zarshuran gold deposit, Iran: using 2D approaches to guide 3D resource modelling. International Institute for Aerospace Survey and Earth Sciences (ITC), The Netherlands, MSc thesis, 150 p.

Northrope, H.R., Rye, R.O., Landis, G.P. Lustwerk, R., Jones, M.B. and Daly, W.E. (1987). Sediment-hosted disseminated gold mineralization at Jerrit Canyon, Nevada, V. - Stable isotope geochemistry and a model of ore deposition (abs.), Geol. Soc. Amer. Abstr. Programs, 19(7), 791.

Nowroozi, A.A. (1972). Focal mechanism of earthquakes in Persia, Turkey, West Pakistan . Bull. Seismol. Soc. Am., 62: 823-850.

Nowroozi, A.A. (1976). Seismotectonic provinces of Iran. Bull. Seismol. Soc. Am., 66: 1249-1276.

Oberthur, T., Weiser, T. and Amanor, S. L. (1997). Mineralogical setting and distribution of gold in quartz veins and sulphide ores of the Ashanti mine and other deposits in the Ashanti belt of Ghana: genetic implications. Mineralium Deposita, 32: 2-15.

Ojaghi, B. (1995). Geology of Zarshuran gold deposit. Kansaran Engineering Consultant, Tehran, 165 p. (in Persian).

Ortega, E., Artida, J., Haydn, R. and Volk, P. (1990). Remote sensing in mineral exploration- really a practical tool? Image processing and GIS applications in exploration projects. In: remote sensing an operational technology for the mining and petroleum industries, 1990 conferences. The Institution of Mining and Metallurgy, London, p. 259-262.

Paterson, N.R. and Reeves, C.V. (1985). Applications of Gravity and Magnetic Surveys: The State-of-the-Art in 1985. Geophysics, 50: 2558-2594.

Paterson, N.R. and Halof, P.G. (1991). Geophysical Exploration for Gold. In Gold Metalogeny and Exploration, ed. R.P. Foster, Blackie and Son, London, Chap. 12, p. 360.

Phllips, G. N. and Powell, R. (1993). Link between gold provinces. Economic Geology, 88: 1084-1098.

Pirajno, F. (1992). Hydrothermal mineral deposits, principal and fundamental concepts for the exploration geologists. Springer-Vorlage, New York, 709 p.

Qin, S. (1994). An analytical signal approach to the interpretation of total field magnetic anomalies, Geophysical Prospecting, 42:665-676.

Radtke, A.S. and Scheiner, B.J. (1970). Studies of hydrothermal gold at the Carlin gold deposit, Nevada: The role of carbonaceous materials in gold deposition. Economic Geology, 65: 87-102.

Radtke, A.S., Taylor, C., and Christ, C.L. (1972). Chemical distribution of gold and mercury at the Carlin deposit, Nevada: Geological Society of America, Annual Meeting, Abstracts, 4: 632.

Radtke, A.S., Taylor, C. and Heropoulos, C. (1973). Antimony-bearing orpiment, Carlin gold deposit, Nevada. Jour. Research U. S. 1: 85-87.

Radtke, A.S., Taylor, C.M., Erd, R.C. and Dickson, F.W. (1974). Occurrence of lorandite $TlAsS_2$ at the Carlin gold deposit, Nevada. Economic Geology, 69: 121-124.

Radtke, A.S., Dickson, F.W., Slack, J.F. and Brown, K.L. (1977). Christite a new thallium mineral from the Carlin gold deposit, Nevada. American Mineralogist, 62: 421-425

Radtke, S.A., Rye, R.O., and Dickson, F.W. (1980). Geology and stable isotope studies of Carlin gold deposit, Nevada. Economic Geology, 75:641-673.

Radtke, A.S. (1985). Geology of the Carlin gold deposit, Nevada: Prof. Paper 1267, U.S. Geological Survey, 124 p.

Rheault, M.M., Simard, R., Keating, P. and Pelliter, M.M. (1989). Mineral exploration: digital image processing of Landsat, Spot, magnetic and geological data. In: Agterberg F.P. and bonham-Carter G.F. (eds.), Statistical analysis in earth sciences. Can. Geol. Surv., Paper 89-9:36-46.

Richard, J.A. (1993). Remote Sensing Digital Image Analysis: An introduction, Springer Verlage, Berlin, 2nd Ed., 340 pp.

Robinson, B.W. and Graham, J. (1992). Advances in Electron Microprobe Trace Element Analysis: Journal of Computer-Assisted Microscopy, 4: 263-265.

Roedder, E. (1984). Fluid inclusions. Reviews in Mineralogy, Mineral. Soc.of Amer., Vol. 12, 644 pp.

Rye, R.O. (1985). A model for the formation of carbonate-hosted disseminated-gold deposits as indicated by geologic, fluid inclusion, geochemical, and stable-isotopes studies of the Carlin and Cortez deposits, Nevada. In: Tookers, E. W. (ed.) Geologic characteristics of the sediment- and volcanic-hosted disseminated gold deposits, search for an occurrence model. U.S. Geol. Soc., Bull., 1646:35-42.

Sabzehie, M. (1974). Les melanges ophiolitique de la region d'E Sphandagheh (Iran meridional). Etude petrologique et structurale, Interpretation dans le carde Iranien. These Doctorat Etat, Grenoble, France, 306p.

Sabzehie, M. (1992). Geologic map of the Neyriz quadrangle, scale 1:250,000. Geological survey of Iran, Tehran.

Samimi, M. (1992). Reconnaissance and preliminary exploration in the Zarshuran area. Kavoshgaran Engineering ConsultantS, Tehran, 47 p. (in Persian).

Schroder, J.W. (1944). Essai sur la structure de l'Iran. Eclogae Geol. Helv., 37:37-81.

Sengor, A.M.C. (1990). A new model for the Late Palaeozoic- Mesozoic tectonic evolution of Iran and implication for Oman. In the geology and tectonics of the Oman region, Robertson, A.H.F., Searle, M.P. and Ries, A.C. (eds.) Geological Society of London Special Publication , 49: 797-831.

Shahpour, J. (1994). Post mineralization breccia dyke for the Sar Cheshmeh porphyry copper deposits, Kerman, Iran, Exploration and Mining Geology, 3: 39-43.

Shepherd, T.J., Rankin, A.H. and Alderton, D.H.M. (1985). A practical guide to fluid inclusion studies. Blackie, 239 p.

Sillitoe, R.H. and Bonham, H.F.J. (1990). Sediment hosted gold deposits: Distal products of magmatic-hydrothermal systems. Geology. 18:157-161.

Sillitoe, R.H. (1993). Gold rich porphyry deposits: Geological model and exploration implications.Geological Association of Canada, Spatial Paper, 40: 465-478.

Stocklin, J. (1968). Structural history and tectonics of Iran: A review, American Association of Petroleum Geologist (AAPG) Bulletin, 52:1229-1258.

Stocklin, J. (1974) Possible ancient continental margins in Iran. In: Burk, C.A. and Drake, C.A. (eds.), The Geology of Continental Margins. Springer, New York, p. 837-887.

Stocklin, J. (1977). Structural correlation of the Alpine ranges between Iran and central Asia. Mem. Horse-serie Soc. Geol. Fr. , 8: 333-353.

Taddaion, A.H. (1991). Detailed geochemical prospection in Zarshuran mine area, Takab, Ministry of Mines and Metals, Zarshuran gold project, 79p. (in Persian).

Takin, M. (1972). Iranian geology and continental drift in the middle East. Nature, 235: 147-150.

Tanaka, S.M. and Segal, D.B. (1990). Integrated remote sensing/vector-based GIS technology for gold exploration, Round Mountain district, Nevada, USA.

Proceeding of the Twenty-third international symposium on remote sensing of environment, Bangkok, 2:747-753.

Taylor, B.E. (1986). Magmatic volatiles: Isotopic variations of C, H and S. In: Valley, J. W. Taylor, H. P. and O'Neil J.R. (eds.), Stable Isotopes. Mineralogical Society of America, 16: 185-226

Thorman, C.H. and Christensen, O.D. (1991). Geologic settings of gold deposits in the Great Basin, western United States. In: Ladira, E. A. (ed.), Brazil Gold'91, Balkema, Rotterdam, p. 65-75.

Titly, S.R. and Beane, R.E. (1981). Porphyry copper deposits: Part I. Geologic settings, petrology and tectonogenesis. Economic Geology, 75: 214-243.

Touret, J. (1977). The significance of fluid inclusions in the metamorphic rocks, in Fraser, D.G. (ed.), Thermodynamics in Geology, p. 203-227.

Turner, D.D. (1997). Predictive GIS model for sediment-hosted gold deposits, north-central Nevada, U.S.A. Proceedings of Exploration 97: Fourth Decennial International Conference on Mineral Exploration. p. 115-126.

Watson, G.P. and Rencz, A. (1989). Data integration in northern New Brunswick. In: Agterberg, F.P. and Bonham-Carter, G.F (eds.), Statistical analysis in earth sciences. Can. Geol. Surv., Paper 89-9: 185-191.

Wells, J.D., and Mullens, T.E. (1973). Gold-bearing arsenian pyrite determined by microprobe analysis, Cortez and Carlin gold mines, Nevada: Economic Geology, 68: 187-201.

Weissberg, B.G (1965). Getchellite, $AsSbS_3$, from Humboldt County, Nevada. Am. Mineral, 50:1817–1826.

White, N.C. and Hedenquist, J.W. (1990). Epithermal environments and styles of mineralization: variations and their causes, and guidelines for exploration. Journal of Geochemical Exploration, 36: 445-474.

Wilkinson, L., Harris, J. and Kiarsgaard, B. (1999). Searching for kimberlite: preliminary weighhts of evidence modeling of the Lac De Gras area, NWT, using GIS technology. Thirteenth international conference on applied geologic remote sensing, Vancouver, 1:263-271.

Zanjani, A. (1945). Biche-Bagh copper mine. Internal report, Tehran, Ministry of Mines and Metals of Iran, 15 p. (in Persian).

Zieboldt, T.O., (1967). Precision and sensitivity in electron microprobe analysis: Analytical Chemistry, 39: 858-861.

COLOUR FIGURES

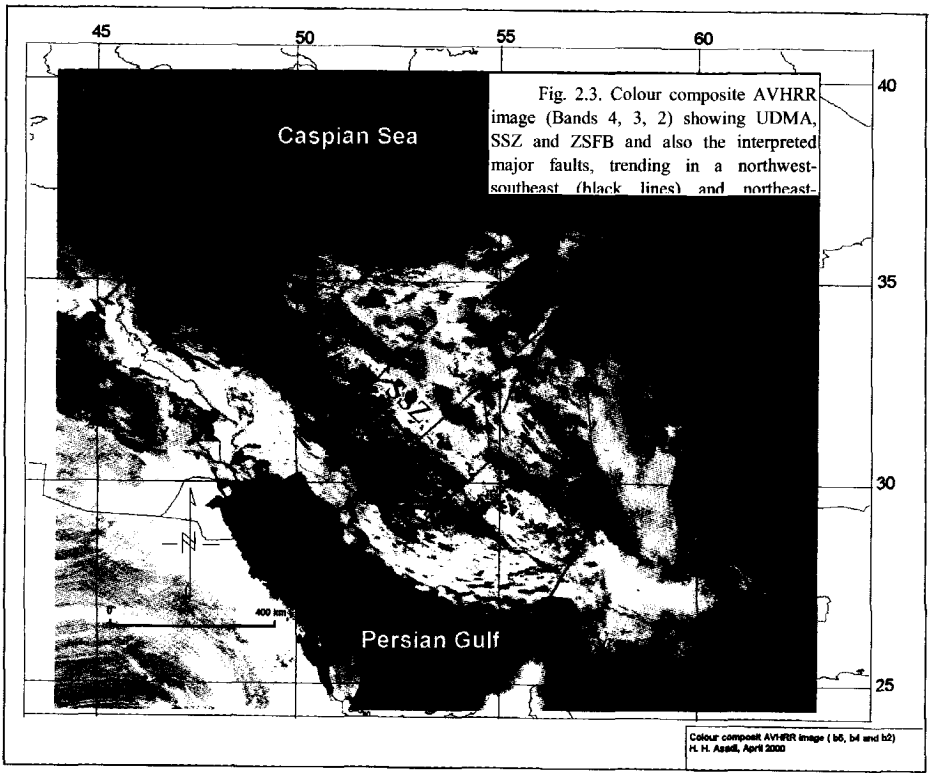

Fig. 2.3. Colour composite AVHRR image (Bands 4, 3, 2) showing UDMA, SSZ and ZSFB and also the interpreted major faults, trending in a northwest-southeast (black lines) and northeast-

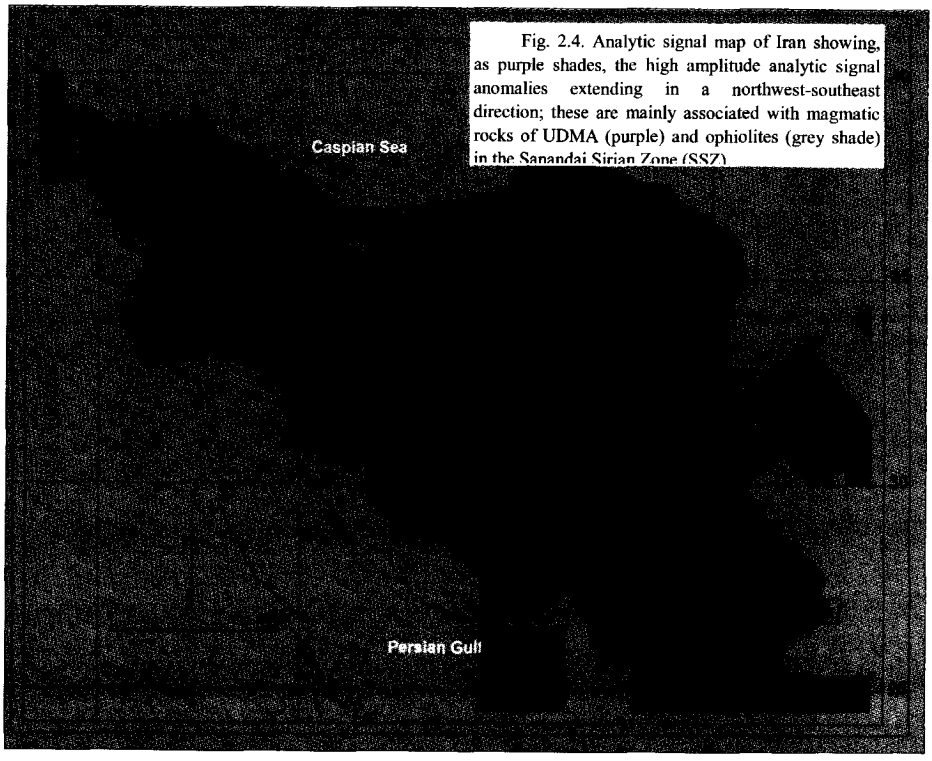

Fig. 2.4. Analytic signal map of Iran showing, as purple shades, the high amplitude analytic signal anomalies extending in a northwest-southeast direction; these are mainly associated with magmatic rocks of UDMA (purple) and ophiolites (grey shade) in the Sanandaj Sirjan Zone (SSZ)

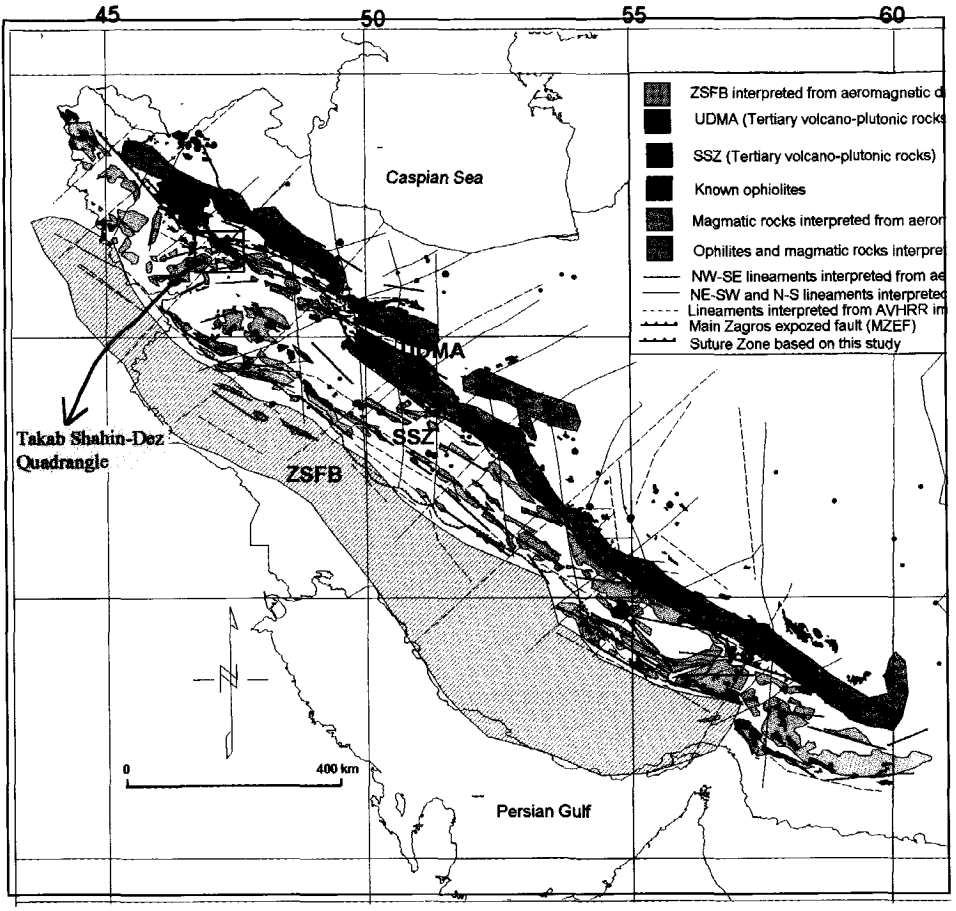

Fig. 2.7 Component elements of the ZOB based on integration of the results from analysis of AVHRR imagery, aeromagnetic, geological and mineral occurrence data.

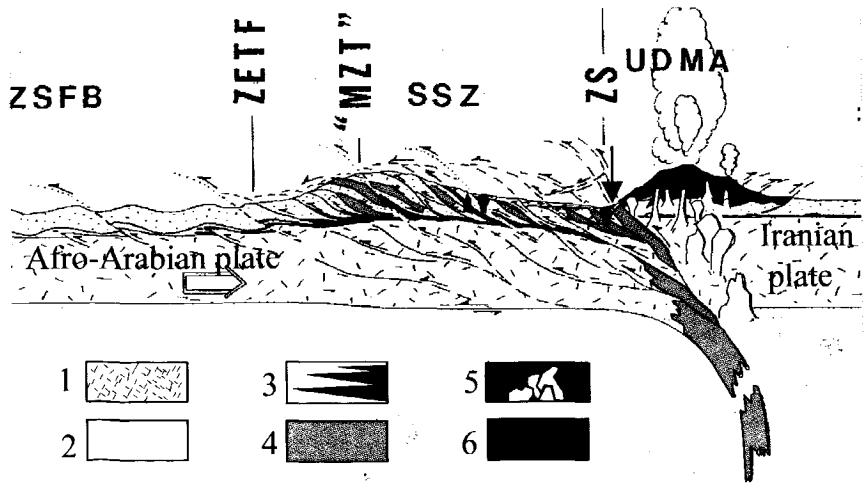

Fig. 2.8. Schematic cross-section across the ZOB (Fig. 2.7). 1 = Continental crust; 2 = Phanerozoic sedimentary cover; 3 = evaporates (white) and dolomites (black) at the base of the sedimentary cover; 4 = oceanic crust; 5 = intrusive and extrusive rocks

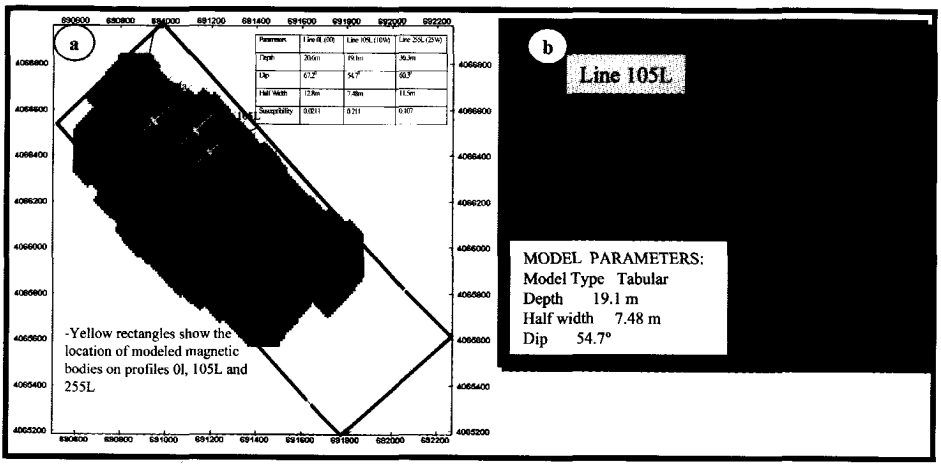

Fig. 3.3. Processed total magnetic field intensity data at the Zarshuran deposit: (a) analytic signal map overlain with Iman-Khan metamorphics (IM-Meta); (b) profile of results for quantitative modelling and inversion on survey line 105L.

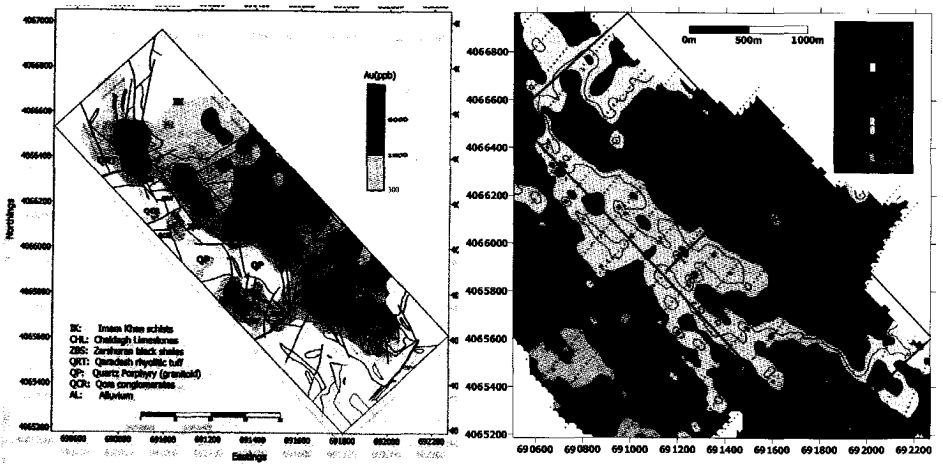

Fig. 3.5. Gold in soils at the Zarshuran deposit: (a) grid plot of three classes separated by the 300 ppb, and the 95th and 99th percentile Au concentration values, superimposed on geology; (b) colour-shaded contour plot with contours at regular $\log_e$ ppb intervals.

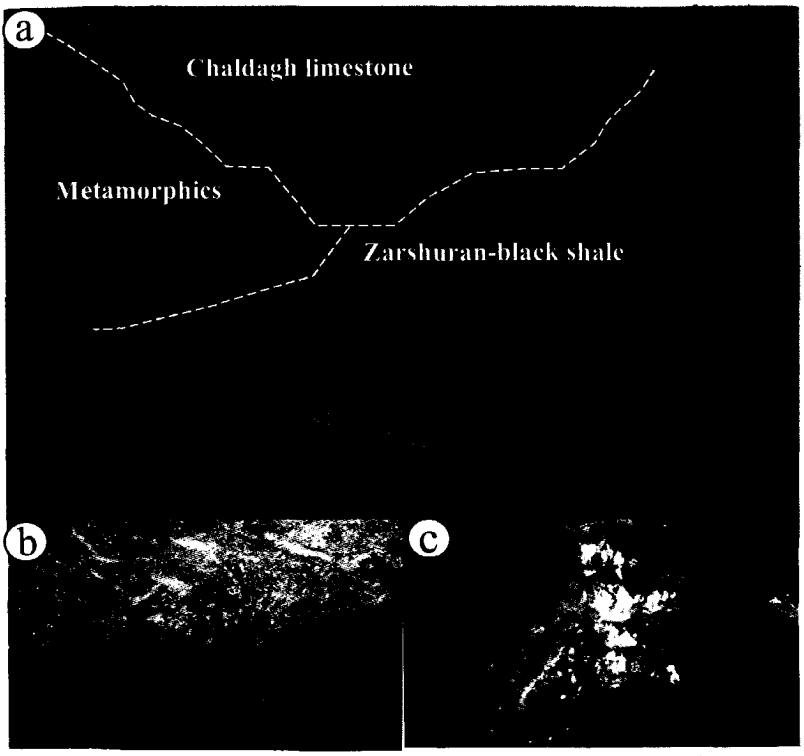

4.1 Photographs of geology, mineralogy and alteration at Zarshuran: (a) part of the Zarshuran deposit showing the three major rock types (view to the northeast); (b) arsenic ore of mainly orpiment within the jasperoids rich in organic matter; and (c) hydrothermal alteration

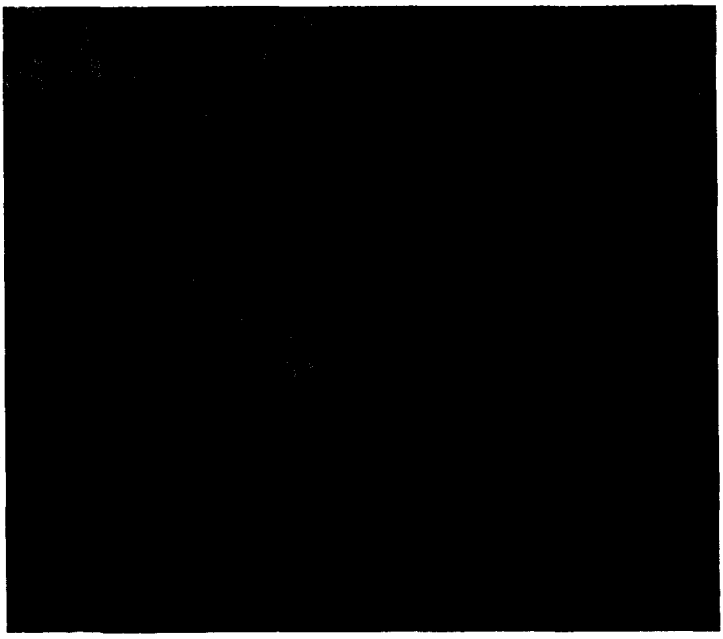

Fig. 9.3. Colour shaded relief map of the analytical signal of the total magnetic field intensity with the known deposits of the Takab area overlaid.



Fig.9.5. Colour composite image of negated PC4 and PC2 and PC3 showing the hydroxyl bearing minerals as bright-orange pixels, Zarshuran (central) and Anguran (southeast) are highlighted by orange pixels.

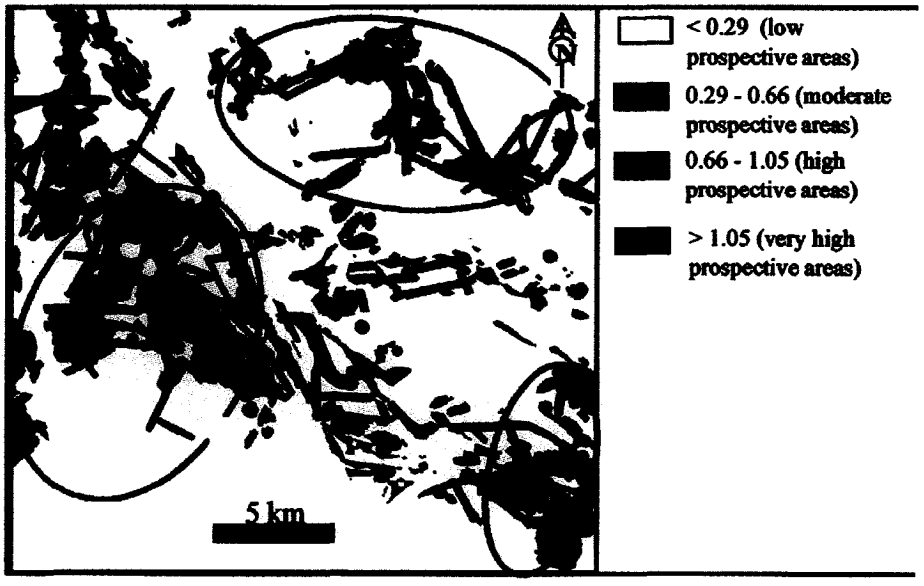

Fig. 10.2. Predictive model map outlining prospective mineralized zones in the Takab area

Curriculum vita

Hooshang Asadi haroni was born on 23 July 1967 in Shahrekord, a small town near Isfahan, Iran. He is married and has two children. He completed his high school in Isfahan and in Tehran in the period of 1981 to 1985. Asadi Haroni obtained a B.Sc. in Geology from the Shahid Beheshti University in Tehran in 1991. His post-graduate studies at ITC (International Institute of Aerospace Survey and Earth Sciences (ITC) in the Netherlands led to a M.Sc. degree in Mineral Exploration in 1995. He is expected to complete his Ph.D. research on the 21st of November 2000 at ITC in cooperation with the Delft University of Technology Delft and the Free University of Amsterdam. Asadi Haroni has published 13 papers in the International Conferences and Peer-reviewed Journals (refer to the reference list).